Erbium doped materials for bulk and waveguide laser sources emitting around 2.8um

Liza Basyrova

To cite this version:

Liza Basyrova. Erbium doped materials for bulk and waveguide laser sources emitting around 2.8um. Inorganic chemistry. Normandie Université, 2023. English. NNT : 2023NORMC218 . tel-04226866

HAL Id: tel-04226866

https://theses.hal.science/tel-04226866

Submitted on 3 Oct 2023

Normandie Université

UNIVERSITÉ
CAEN
NORMANDIE

THÈSE

Pour obtenir le diplôme de doctorat

Spécialité PHYSIQUE

Préparée au sein de l'Université de Caen Normandie

Erbium doped materials for bulk and waveguide laser sources emitting around 2.8um

Présentée et soutenue par
LIZA BASYROVA

Thèse soutenue le 25/09/2023
devant le jury composé de

MME BRIGITTE BOULARD	Maître de conférences HDR, UNIVERSITE LE MANS	Rapporteur du jury
M. FREDERIC DRUON	Directeur de recherche, Université Paris Saclay	Rapporteur du jury
M. RÉMY BOULESTEIX	Maître de conférences, Université de Limoges	Membre du jury
M. PAVEL LOIKO	Chercheur, ENSICAEN	Membre du jury Co-encadrant
M. BRUNO VIANA	Directeur de recherche au CNRS, UNIVERSITE PARIS 6 PIERRE ET MARIE CURIE	Président du jury
M. PATRICE CAMY	Professeur des universités, Université de Caen Normandie	Directeur de thèse

Thèse dirigée par PATRICE CAMY (Centre de recherche sur les ions, les matériaux et la photonique (Caen))

ED 591 PSIME

CIMAP

UNIVERSITE DE CAEN NORMANDIE

DOCTORAL THESIS

Erbium doped materials for bulk and waveguide laser sources emitting around 2.8 µm

Author	**Director**
Liza BASYROVA	Prof. Patrice CAMY
	Co-supervisors
	Dr. Pavel LOIKO Dr. Gurvan BRASSE

A thesis submitted in fulfilment of the requirements
for the degree of Doctor of Philosophy
in the

Centre de recherche sur les Ions, les Materiaux et la Photonique
U.F.R. des Sciences

25 September 2023

Acknowledgments

This doctoral study was conducted at the Centre de recherche sur les Ions, les MAtériaux et la Photonique in Caen. These three years of doctoral research were pivotal in my life. The results of this doctoral thesis are not only research papers, but more importantly, the transformation of my thoughts and actions in academia, which inevitably determines my future trajectory.

The realization of this doctoral thesis was made possible through the collaborative efforts of many people. I wish to express deep gratitude to my supervisors, colleagues, friends, and family for their invaluable support.

First and foremost, I am deeply grateful to my PhD co-supervisors, Dr. Pavel LOIKO and Dr. Gurvan BRASSE, for their direct assistance in lab experiments and for their invaluable support, guidance, and discussions throughout my graduate studies. I am grateful to my PhD thesis director, Prof. Patrice CAMY for the time and effort, he dedicated to ensuring the success of my PhD study.

I would like to thank other researches, engineers and technicians of the OML team, in particular, Dr. Jean-Louis DOUALAN and Prof. Alain BRAUD for their immense knowledge and plentiful experience that helped me during my thesis. I'm also very grateful to Dr. Abdel BENAYAD for the single-crystal elaboration, to Vivien MENARD for the polishing of the epitaxial layers, and for teaching me about laser crystal polishing and to Philippe LEPRINCE for providing mechanical assistance. I would like to thank Dr. Simone NORMANI for his help with lab experiments and valuable advices in writing my manuscript.

Afterwards, I want to thank all other the members of the OML team with whom I have actively interacted over these years: Amandine, Ahmed, Esrom and Lauren, the administration staff represented by Sarah COLINEAUX and Delphine HASLEY and the other members of the CIMAP lab.

In addition, I would like to express my gratitude to all our collaborators and partners responsible for the fabrication of the transparent ceramics and the extra measurements needed to complete this study. I address my thanks to Dr. Stanislav BALABANOV (G.G. Devyatykh Institute of Chemistry of High-Purity Substances, Nizhniy Novgorod, Russia), Dr. Roman MAKSIMOV (Institute of Electrophysics, Ekaterinburg, Russia), Dr. Wei JING (Institute of Chemical Materials, China Academy of Engineering Physics, Mianyang, China), Dr. Xavier MATEOS and Dr. Rosa-Maria SOLÉ (Universitat Rovira i Virgili, Tarragona, Spain).

I would like to offer my special thanks to the people who have become my friends during my years of PhD studies: Anya, Kirill, Kirill M, Massimo, Min, Kou, Parameshwari, Lucas Brazilian, Lucas French, Cintia, Alina and Clara. I had a wonderful opportunity to enjoy memorable moments with all of you outside the lab spending crazy nights out and cozy gatherings. I want to express my gratitude not only for the assistance and support I received from you but also for the cherished experiences we shared. I will forever hold these memories close to my heart.

I would like to express my sincere gratitude to my old and beloved friends Pasha and Tanya for their enormous encouragement in hard times for me, for their love and acceptance of me as I am.

Finally, I would like to thank my parents for their belief in me, their sacrifices, and their unconditional love. From the earliest days to the significant milestones I have reached, their presence and support have been a constant source of strength and motivation. From the bottom of my heart I want to thank my husband Denis for his endless love, patience and support no matter what.

Contents

Chapter II Materials and methods..62

Chapter III Erbium-doped $LiYF_4$ and CaF_2 layers elaborated by Liquid Phase Epitaxy 100

Introduction

Since its invention in 1960 by Theodore H. Maiman by using a synthetic ruby crystal, the laser, which is the acronym used for "Light Amplification by Stimulated Emission of Radiation" has led to a ground-breaking moment in the history of science and technology. Indeed, since their inception, laser sources have become indispensable and unavoidable tools in a large field of scientific and technological applications, thanks to their properties in terms of density of energy, monochromaticity, low divergence or spatio-temporal characteristics for examples, being not exhaustive.

The last decade has especially seen a significant surge of interest for laser sources emitting in the mid-infrared (mid-IR) spectral range, which extends from the NIR-MIR area about 2 µm to the terahertz (THz) region. Covering the most important atmospheric windows, the mid-IR range exhibits the distinctive spectroscopic fingerprints of numerous elements such as traces of number of gases, toxic substances, air and water pollutants, as well as components of human breath, biological tissues or various explosives and drugs. Absorption bands of a sample of important molecules and materials are shown in Figure 1. Given the remarkable characteristics of the mid-IR range, it plays a key role in various fields, including environmental monitoring, free space transmission, non-invasive disease diagnosis, breath-based therapy, minimally invasive surgical procedures, food quality control, imaging, safety and security systems, as well as for quantum information technologies.

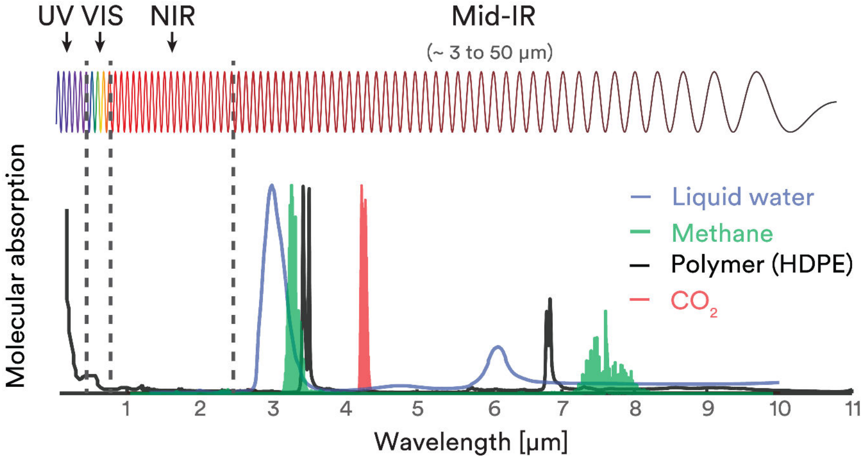

Figure 1: Absorption bands of important molecules and materials. Image taken from: https://femtum.com/mid-infrared-lasers-applications-overview/

A key element for the developments of innovatives applications and devices in the mid-infrared spectral range is the creation of new laser sources with continuously improving characteristics in terms of wavelength coverage, spectral and spatio-temporal quality, power, efficiency, and stability of the output signal. Material science is in the heart of the laser developments in the sense that the main element of lasers is the active medium that emits light, which is in most of cases a material, except for gas based and liquid based lasers. This active material can be of different natures: it can be based on semiconductors or on rare-earth (RE) doped or on transition-metals doped dielectric materials. These dielectric matrices can present a crystalline nature, an amorphous nature like glasses or even a ceramic nature and can take various shapes like bulk crystals and glasses, crystalline or glassy thin films or optical fibers. The material research concerning the development of such a material presenting the suited structural, microstructural, physico-chemical, spectroscopic properties and optical quality has been in the first place of considerations and importance since the invention of laser, being their elementary bricks. At the same time, deep research activities concerning the different ways to synthesize such laser materials have been carried out all over the world especially for the growth of bulk crystals and epitaxial crystalline thin films, but also in the glass technology to develop novel glass compositions or new processes for elaborating complex optical fibers compositions and design. So, the advances in materials science are essential to enlarge the offer in terms of new crystal gain media for solid-state and fiber lasers, but also for semiconductors, waveguides, chip-based nanostructures and nonlinear crystals operating for the mid-IR.

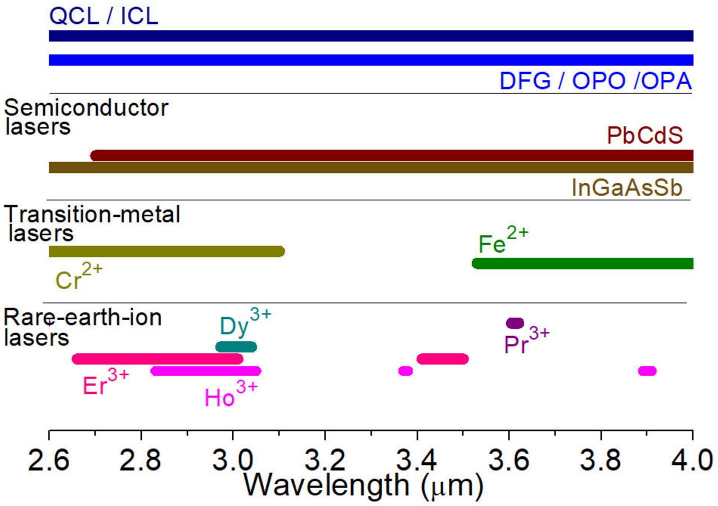

Figure 2: Laser sources covering the spectral range of 2.6 - 4.0 μm.

There are multiple laser sources covering the mid-wave infrared (MWIR) spectral range, as shown in Figure 2. These include frequency-converting laser sources such as Raman-shifted lasers and optical parametric oscillators (OPOs) but both suffer from poor beam quality and complex laser architectures. Despite a broadband tuning to the mid-IR range, OPOs are complex and expensive systems that require pump sources with a high optical intensity, as well as nonlinear crystals that must be cut along the phase-matching directions. Progress are currently made in exploring alternative laser technologies, such as quantum cascade lasers (QCLs) and novel semiconductor diode lasers, to provide more compact, efficient and higher-quality solutions for MWIR applications. The main drawbacks of such laser sources are related to the limited output power in the short-wavelength range near 3 µm and its sensitivity to environmental factors, affecting their output performances. The spectral range of 2.8- 3 µm, is meanwhile well addressed by rare-earth doped solid-state lasers, namely lasers based on Er^{3+}, Ho^{3+} and Dy^{3+} ions, as well as lasers based on transition-metal ions such as Cr^{2+}.

This doctoral research work was carried out within the framework of the SPLENDID2 ANR project (**S**hort **P**ulse Solid State **L**as**e**rs a**nd** Ampl**i**fiers beyon**d** **2** µm). The main goal of this project is to create, to develop and to explore innovative active inorganic materials in both bulk and crystalline thin films shape. This study aims to demonstrate the suitability and the use of these materials in high-power ultrafast lasers and amplifiers operating in the mid-infrared spectral range beyond 2 µm. In particular, this PhD study is devoted to the exploration, the study and the development of various materials doped with Er^{3+} ions, presenting different shapes (bulk and thin films), different structural natures (crystalline and ceramics), as well as different chemical natures and compositions (oxides, fluorides), which seem very well suited for efficient laser operation in the 2.8 µm region, related to the $^4I_{11/2} \rightarrow {}^4I_{13/2}$ electronic transition, which has been deeply investigated in these works. This wavelength is indeed of a paramount importance for medical applications because of the strong absorption of water by biological tissues, resulting in shallow penetration and high precision in surgical incisions for example.

This PhD thesis is structured in five chapters that are organized as follows:

The discussion in Chapter I begins with an overview of lasers operating around 3 µm and their potential applications in mid-infrared. It discusses the available laser sources to cover these needs. The fundamental properties of Er^{3+} ions are then considered. Additionally, the Chapter reviews the state-of-the-art of materials developed for efficient erbium emission around 2.8 µm.

Chapter 2 focuses on providing general information on the studied host matrices for Er^{3+} doping and their elaboration methods and processes, including a presentation of the Liquid Phase Epitaxy (LPE) growth of crystalline thin films for waveguides elaboration; The gowth methods of bulk single-crystals and transparent ceramic for bulk solid-state lasers are also presented. The methods for their structural and spectroscopic characterization are discussed as well.

Chapter 3 goes on to present the results on a comprehensive study of the homoepitaxial growth by the liquid phase epitaxy method of Er^{3+}-doped fluoride single-crystalline layers, with a focus on $LiYF_4$ and CaF_2 compositions. Our investigations and research works specifically emphasizes on heavily doped compositions of Er^{3+}:$LiYF_4$/$LiYF_4$ epitaxies, which play a crucial role to enable laser emission at 2.8 µm. An important research work has also been lead concerning the growth of Er-doped CaF_2 epitaxial layers, on the improvement of their structural and optical quality by varying and testing different experimental parameters, completed by a deep investigation of their microstructural and thermo-mechanical properties to understand and explain the observed results.

In Chapter 4, we present the results of a systematic study focusing on the spectroscopic properties and mid-infrared laser performances of various cubic Er^{3+}-doped fluorite-type single crystals. Our investigation included fluorite-type crystals Er^{3+}:MF_2 (where M = Ca, Sr, Ba, and their mixtures: Ca/Sr, Ba/Sr), Er^{3+}:$Na_5Y_9F_{32}$, and Er^{3+}:KY_3F_{10}. Throughout the chapter, we delve into the detailed analysis of these crystals, aiming to gain valuable insights into their optical characteristics and their potential as efficient mid-infrared laser sources.

Chapter 5 provides results of comprehensive investigation on compositionally "mixed" transparent sesquioxide ceramics doped with Er^{3+} ions, with a particular focus on their mid-infrared emission properties and the inhomogeneous spectral line broadening resulting from compositional disorder. We conducted a thorough study of four binary systems: lutetia-scandia (Lu_2O_3 – Sc_2O_3), lutetia-yttria (Lu_2O_3 – Y_2O_3), yttria-lantana (Y_2O_3 – La_2O_3), and yttria-scandia (Y_2O_3 – Sc_2O_3).

Chapter I

Erbium-doped materials for mid-infrared lasers at ~2.8 µm: State-of-the-art [Literature review]

1 Lasers emitting around 3 µm: Application and solutions

The development of modern mid-infrared laser systems has been driven by many factors, particularly scientific advances, and demand in applications. In terms of their applications, we are dealing with a wide range of uses in gas sensing, spectroscopy, defense, and medicine. These specific areas will be discussed in detail further below.

1.1 Possible applications

Currently, more than 40 years after the invention of laser light sources, various suitable coherent light sources (gas, chemical, semiconductor, etc.) are available in the ultraviolet (UV) to infrared range.

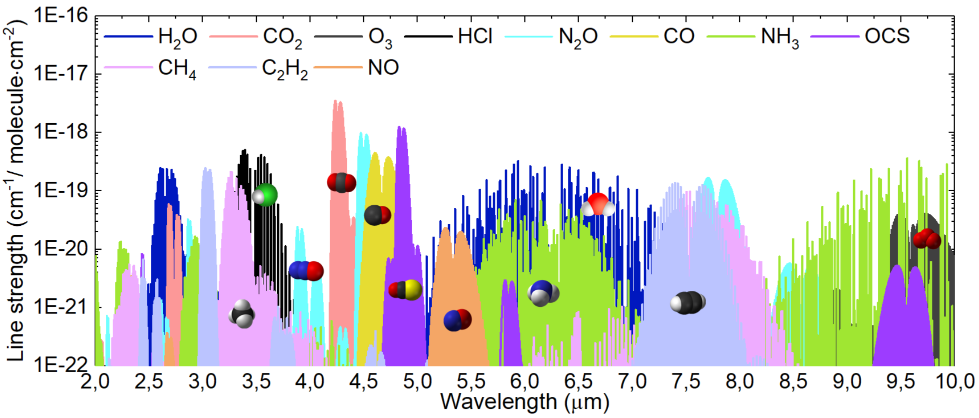

Figure I.1: Characteristic mid-infrared absorption bands for major atmospheric species, the spectra were taken from HITRAN database **https://hitran.org/.**

The origins of infrared radiation or so-called "calorific rays" (calor is a heat from Latin) go back to 1800, when astronomer William Herschel discovered the infrared region of the electromagnetic spectrum beyond the red edge of the visible range [Gil17]. The mid-IR spectral range of wavelengths is currently attracting the attention of scientists. This is because it contains the so-called fingerprint region (approximately 2 – 10 µm) associated with the stretching, vibration, and rotation of the molecules. The spectral emission pattern, or 'molecular fingerprint', is unique to each specific molecule. The transition strength in this spectral band can be more than thousand times stronger than that in the near-infrared region, which increases the detection sensitivity by a similar amount. The mid-infrared region also has several transparency windows in the Earth's atmosphere (e.g., 8 – 14 µm and 3 – 5 µm), which are important for ambient gas-sensing applications [Pic19]. Figure I.1 shows the characteristic absorption bands in the spectral range of 2 – 10 µm for several atmospheric species.

1.1.1 Lasers for gas trace detection

With the onset of climate change and significant environmental issues, it is impossible to manage real-time pollution monitoring without sensors. Many dangerous gases (so-called greenhouse gases), such as CH_4, SO_2, NO_2, NO, and H_2S, have a strong absorption capacity in the mid-infrared spectral region (Figure I.1). LIDAR technique ("Light Detection and Ranging (LIDAR) technique is a powerful remote sensing tool for environmental monitoring, especially in polluted areas such as industrial and urban areas, where the timing and spatial distribution of exhaust sources are highly variable. The basic principle of this technique is as follows: a laser source emits a pulse of light (typically a few nanoseconds), and as the pulse propagates, photons interact with particles in the atmosphere. Some of these interactions, such as Min and Rayleigh scattering, result in backscattered photons. Photons are collected by the detector and recorded as a function of time. These time-of-flight data have a direct correspondence with the range (distance) at which the scattering event occurs.

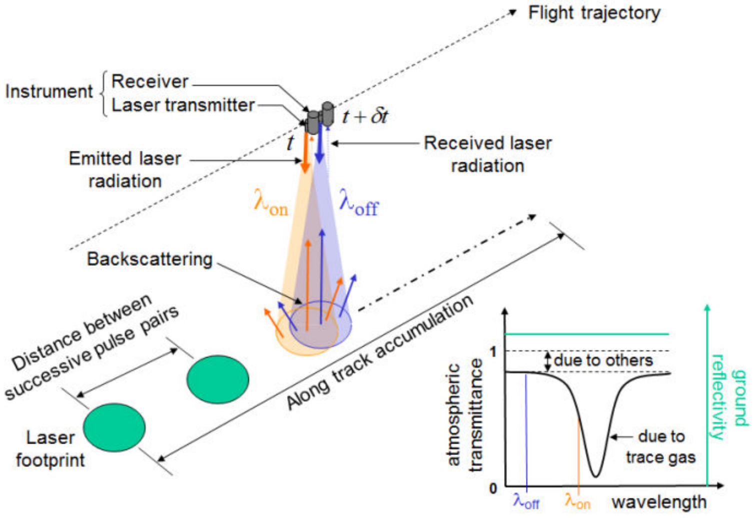

Figure I.2: Schematic illustration of IP-DIAL system [Ehr17].

The differential absorption LIDAR (DIAL) method works on the same principle as LIDAR but uses two different wavelengths, with the first being in resonance with the absorption line peak (λ_{ON}) of the species under study, and the second being tuned to the wing of the (λ_{OFF}); therefore, the backscattered signals obtained at (λ_{ON}) and (λ_{OFF}) have different intensities, and the ratio of the corresponding signals allows us to estimate the concentration of the investigated species [Amb00]. The DIAL is more often used in ground-based studies. It allows the visualization of fine atmospheric structures (tens to hundreds of meters). In addition, the integrated path differential absorption (IP-DIAL) method is preferable for investigations on a global scale (for example, from aircraft or satellites) because it provides a large signal and high measurement accuracy, despite the beam propagation distance. A schematic illustration of the IP-DIAL system is shown in Figure I.2. This system was used in the Franco-German space lidar mission for methane remote sensing (MERLIN) [Ehr17].

Another laser-assisted method tool quantitative sensitive remote gaseous analysis is open path differential optical absorption spectroscopy (DOAS). Typical commercial mid-IR DOAS open path systems include an infrared incoherent optical source, an angular cube, and a telescope coupled to a Fourier transform spectrometer. There is a great deal of interest in incorporating the advanced MWIR lasers into DOAS systems. Table I.1 shows the characteristics of some MWIR laser sources recently described in the literature [Lam15].

Table I.1: A summary of the recently studied MWIR DOAS systems.

System	**FTS**	**TLAS**		**SAS**	**QCL**	**OPG**	
Laser	fs comb	OPO	OPO+OPA	SC	QCL (DFB)	OPG	
λ, μm	2.8-4.8	2.5-3.7	3.3-3.7	2.53	7.69-7.71	1.475-3.8	
Emission bandwidth, nm	~100-300	~5	~0.004	>4000	~0.05	~10-200	
Rep. rate, kHz	136,000	150	2000	2000	20	4	0.15
Power, mW	>1000	80	4-10	4000	0.6	70	2.25
Energy, μJ	0.007/pulse	0.5	2-5	2	0.03	17.5	15

FTS - Fourier transform spectroscopy, TLAS- tunable laser absorption spectroscopy, SAS - supercontinuum absorption spectroscopy, QCL - quantum cascade laser, DFB - distributed-feedback laser, OPG- optical parametric generation.

Apart from monitoring the atmosphere globally from both Earth and space, infrared sensors have also become a part of our everyday lives. These in-situ sensors are utilized in various medical applications, such as identifying gases (biomarkers) in breath diagnostics [Kim10, Tut19, Sel20] and noninvasive measurement of blood glucose levels in patients with diabetes [Pet01]. Figure I.3 displays the absorption ranges of some biomolecules in the human body that can be detected using these sensing techniques in the mid-IR region, particularly around 3 μm, where water molecules and functional C-H groups present in proteins can be observed. Table 1.2 summarizes the available techniques for detecting biomarkers of different diseases in the mid-IR region.

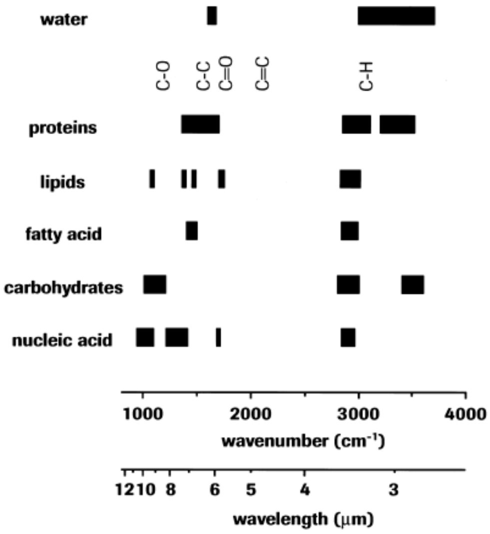

Figure I.3: Schematic illustration of mid-infrared ranges, which are characteristic for water (*top*) and some biomolecules (*bottom*) [Pet01].

Table I.2: A summary of laser techniques employed to detect biomarkers of a few human diseases; data is taken from [Sel20].

Disease	Biomarker	Technique	Laser source and wavelength
Colorectal cancer	Methane (CH_4) from high lipid	CALOS	EDCL 800nm, Nd:YAG 1064nm with PPLN
		CEAS	Tunable laser system at 3.35µm
		TDLAS	ICL at 3.34µm
Scleroderma, cystic fibroma	Ethane (C_2H_6)	HCF	3.4 µm
		MPAS	QCL at 7.874µm
Diabetes	Acetone $CO(CH3)_2$	WMS	DFB – ICL at 3.367µm

Technique abbreviations: CEAS - cavity-enhanced absorption spectroscopy, CALOS - cavity leak-out absorption spectroscopy, TDLAS - tunable diode laser absorption spectroscopy, MP – multipass absorption spectroscopy, WMS - wavelength modulation spectroscopy; *Laser source abbreviations:* ECDL - external cavity diode laser, DFB-ICL - distributed feedback-intracavity laser, HCF - hollow core fiber, PPLN - periodically poled lithium niobate.

1.1.2 Lasers for medical applications: surgery & biopsy

At the beginning of this chapter, it was noted that the absorption of mid-infrared radiation by many molecules is a crucial aspect in the application of IR lasers in medicine. These lasers are commercially available and offer a less invasive alternative to surgical scalpels [Pol01]. Laser surgery involves using the cutting power of a laser beam to make bloodless incisions, with the principle of selective photothermolysis at its core. The laser beam passes through the skin until it encounters a chromophore that absorbs the beam, releasing heat and causing coagulation and necrosis of the target tissue, which is subsequently removed. Chromophores in biological tissues can include water molecules, hydroxyapatite (a component of dental enamel), and various proteins, such as collagen [Par20]. In fact, water absorption in biological tissues increases by almost six orders of magnitude in the mid-IR spectral region compared to the visible range [Vog03]. Figure I.4 displays the mid-infrared absorption spectra of water, collagen, and hydroxyapatite in human tissues.

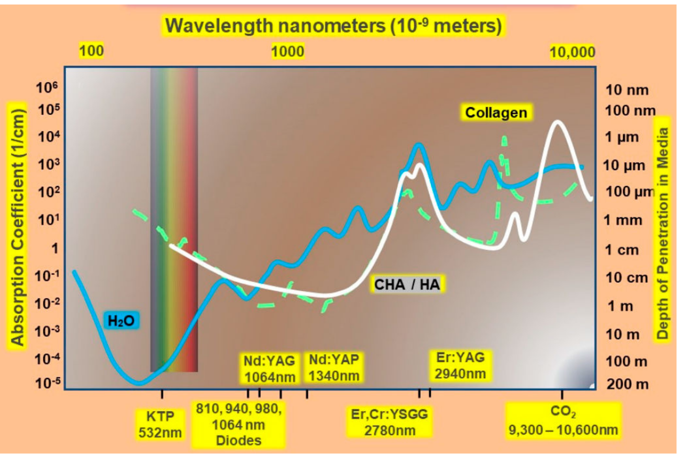

Figure I.4: The absorption spectra of major tissue elements relevant to bone and dental hard tissue management, with absorbance shown relative to irradiation wavelength. Key tissue components include water *(blue)*, collagen *(green)*, and hydroxyapatite (HA) and carbonated HA *(white)*. Image source: [Par20].

Erbium lasers emitting at 2.8 µm occupy a key position in this medical field due to the perfect overlapping of laser wavelengths with maximum peak of water absorption around 3 µm. To date, many papers are devoted to skin surgery and laser resurfacing using 2.9 µm erbium laser [Luk08, Bel05, and Hoh97].

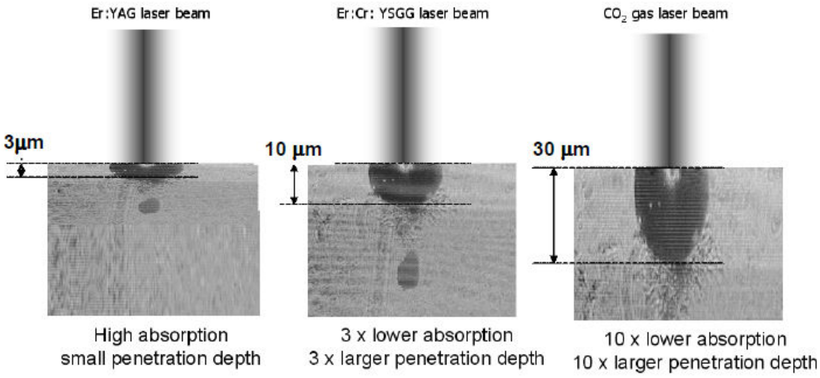

Figure I.5: The optical penetration depths in skin for the three ablative lasers, namely for the Er:YAG, Er,Cr:YSGG and CO_2 lasers [Luk08].

In the literature, it is often compared to CO_2 lasers which emit around 10.6 µm [Luk08]. In Figure I.5, it has been shown that erbium laser is gentler than the CO_2 laser allowing a very superficial epidermal ablation with a minimal thermal effect, and a limited area of necrosis [Hoh97] and on some evidence, it can even stimulate the production of your own collagen [Bel05]. The clinical effects of Er:YAG lasers on the soft tissues of the oral cavity during biopsy have been demonstrated by Chen *et al.* [Che13]. The gentle and painless effect of the laser on the keratotic tissues of the buccal area and tongue made it possible to dispense with needle-free anesthesia.

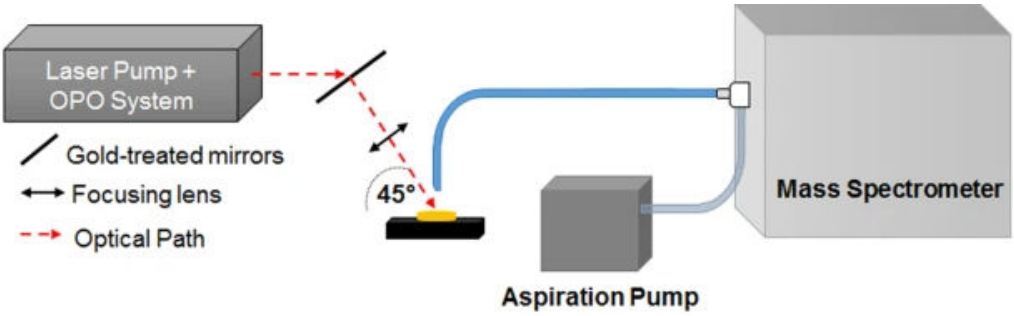

Figure I.6: Schematic representation of the SpiderMass instrument [Fat16].

More sophisticated mass spectrometry instruments assisted by a 3 µm laser radiation have also been developed for tumor biopsy. These include systems such as SpiderMass [Fat16, Sau18] and PIRL [Fra09, Woo17], which can be used for both *ex vivo* conditions [Sau18] and *in vivo* real-time analyses under minimally invasive conditions. For example, in paper [Fat18] the SpiderMass instrument set-up was equipped with an infrared OPO pumped by a 4 ns Nd:YAG laser operating at 1064 nm with a repetition rate of 10 Hz in order to be able to finely tune the laser wavelength to match the most intense water absorption band within their biological environment. The scheme of SpiderMass set-up is shown in Figure I.6. Authors have demonstrated an instrument based on laser ablation and mass spectrometry allowing real-time analysis and with the ability to provide molecular characteristic data on samples *in vivo* [Fat18].

1.1.3 Lasers for infrared countermeasures

There are two transparency windows in the Earth's atmosphere located between 3 and 5 µm and 8 and 12 µm, respectively. This allows light to propagate over long distances and, hence, enables applications in infrared countermeasures [Mah07] and free-space optical communications (FSOC) [Kau17]. Defense and security applications are particularly interesting because of the overlap of the blackbody radiation emitted by aircraft turbines, Figure I.7(a), with those windows of atmospheric transmission [Mah07]; therefore, lasers emitting in this spectral region are of great interest for infrared countermeasures [Eld10].

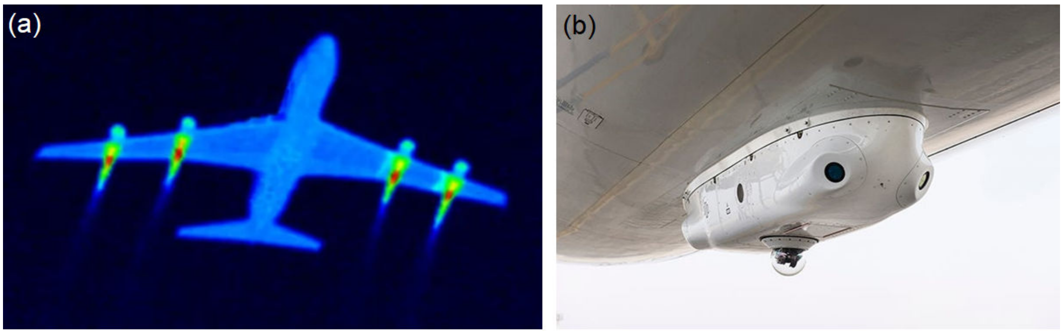

Figure I.7: (a) A typical infrared pattern in the range of Earth transparency window (3 - 5 µm) of commercial aircraft showing strong infrared emission from turbines represents a target for heat-seeking missiles. https://www.laserfocusworld.com/lasers-sources/article/16548073/photonics-applied-defense-ir-countermeasures-aim-for-safer-flights; (b) An example of DIRCM system (Elbit Systems C-Music DIRCM) https://www.airforce-technology.com/news/elbit-dircm-ew-asia-pacific/

In the FSOC region, the range from 3 to 5 µm exhibits much less atmospheric turbulence and is therefore of particular interest compared with other transmittance windows [Luz15]. The example of Directed Infrared Countermeasure (DIRCM) systems protecting airborne vehicles from heat-seeking ground-to-air missiles (MANPADS) is shown in Figure I.7(b). They present the compact minimized systems which feature an open architecture design and can be seamlessly integrated on any type of aircraft with any type of MWS (missile warning systems) and other defensive aids. These systems have been successfully used by the Israeli government to protect Israeli commercial airliners, by the Israeli Air Force to protect military platforms, by NATO to protect the A330 MRTT multinational fleet program, etc.

1.1.4 Lasers at 3 µm for pumping other laser systems

- **For pumping lasers based on iron ions (Fe^{2+})**

Iron (Fe^{2+}) doped binary (e.g., ZnSe, ZnS, CdSe, CdS, ZnTe) and ternary (e.g., CdMnTe, CdZnTe, ZnSSe) chalcogenide crystals are known for their intense and broadband absorption and emission in the mid-infrared originating from the $^5E \leftrightarrow {}^5T_2$ (5D) transitions of Fe^{2+} ions in tetrahedral (T_d) crystal field [Mir10]. They represent promising material for tunable solid-state lasers operating over the 3 – 8 µm spectral range due to high ground-state absorption (GSA) cross sections ($\sigma_{GSA} = 0.97 \times 10^{-18}$ cm^2 for Fe^{2+}:ZnSe) and the lack of excited-state absorption [Dor16, Fir15, Dor09]. Figure I.8(a) shows the absorption cross-sections of the Fe:ZnSe and Fe:ZnMgSe crystals.

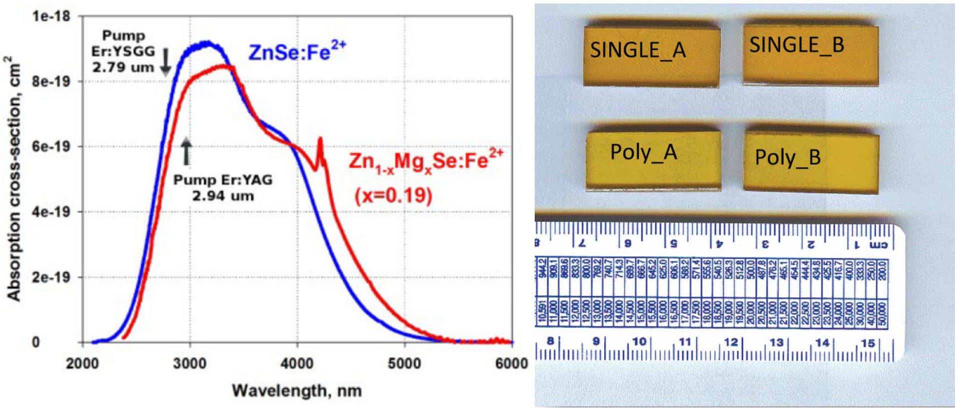

Figure I.8: (a) Absorption cross-sections of the Fe^{2+}:ZnSe and Fe^{2+}:ZnMgSe crystals [Jel15]; (b) Photograph of Fe^{2+}:ZnSe single and polycrystalline saturable absorbers (https://www.ipgphotonics.com/en/products/components/mid-ir-crystals).

The development of room-temperature (RT) Fe^{2+} - lasers strongly depends on the availability of high-energy nanosecond pump lasers operating near the maximum of the Fe^{2+} absorption band (2.7 - 3.2 µm). The fluorescence lifetime of the Fe^{2+}:ZnSe crystal originating from the $^5E \rightarrow {}^5T_2$ (5D) mid-IR transition experiences intense multiphoton quenching, resulting in a shortened lifetime of 300 ns at room temperature. This imposes specific requirements on pumping sources, such as pulse duration comparable with fluorescence lifetime [Fed06]. Recently, the following laser sources have been used as a pump: Er lasers operating at 2.9 µm, Cr^{2+} laser emitting at 2.6 – 2.9 µm, D2 Raman shifted Nd:YAG laser 2.92 µm emission and HF laser operating at 2.6 µm [Mir18]. For example, the output energy of the Fe:ZnSe laser at RT reached 1.4 J at a pulse duration of ~150 ns when pumped by HF laser radiation [Dor16]. However, the toxicity of HF chemical lasers to humans limits a number of their possible applications. Erbium laser operating around 2.8 - 2.9 µm is convenient and commonly used pump source for such lasers [Vor08, Eva12, Eva15, Mar17, Pus18, Jel15, Li21]. Its laser wavelengths nicely overlap with the absorption band of Fe^{2+} ions in II-VI materials, as shown in Figure I.8(a). In paper [Li21], Li *et al.* demonstrated high-efficient CW Fe^{2+}:ZnSe laser pumped by Er:YAP laser at 2.92 µm. The home-constructed pump laser generated an output power of 3.6 W with an average slope efficiency of 36.6%. The Fe^{2+}:ZnSe laser produced a maximum output power of 1 W at 4.06 µm *vs*. 2.1 W of absorbed pump power corresponding to an average slope efficiency of 48.8%. This result proofs that Er^{3+} laser can be a reliable pump source for lasers based on Fe^{2+} ions. Figure I.9 shows the experimental set-up used in abovementioned work.

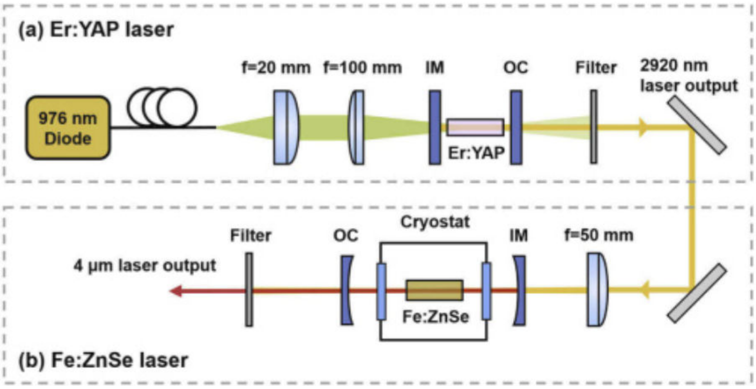

Figure I.9: Experimental set-up of Fe:ZnSe laser pumped by erbium laser: (a) Er:YAP laser; (b) Fe:ZnSe laser [Li21].

Moreover, these Fe^{2+} based materials are interesting as saturable absorbers (SA) for generation of short pulses in mid-infrared lasers based on Er^{3+} and Tm^{3+} ions [Can08, Den18]. Figure I.8(b) shows a photograph of the Fe^{2+}:ZnSe single and polycrystalline saturable absorbers offered by the IPG Photonics company. Fe^{2+}:ZnSe boasts exceptional optical-mechanical characteristics, including a damage threshold of approximately 2 J/cm^2 and a relatively low saturation intensity that allows it to be used for the low-threshold operation of pulsed lasers [Zha19]. Zhang *et al.* achieved a passively Q-switched operation by utilizing polycrystalline Fe^{2+}:ZnSe as a saturable absorber, resulting in the shortest pulse width of approximately 14.6 ns. This is believed to be the shortest pulse for passively Q-switched mid-infrared Er^{3+} lasers obtained so far. The maximum pulse energy and peak power produced are 5.05 µJ and 345.8 W, respectively.

- For pumping lasers based on dysprosium ions (Dy^{3+})

Lasers doped with rare-earth elements are becoming promising powerful laser sources in the mid-infrared region of 2.6-3.0 µm and 3.3-3.8 µm based on Er^{3+} and Ho^{3+} ions. However, the region between 3 and 3.3 µm, which is important for manufacturing and defense applications, currently has a limited number of suitable options as shown in Figure I.10. To address this problem, the potential of dysprosium-doped fibers has been demonstrated to date. Owing to the transition from the first excited manifold to the ground state ($^6H_{13/2} \rightarrow {}^6H_{15/2}$), Dy^{3+} ions exhibit a broad emission cross section from 2.6 to 3.4 µm [Woo18].

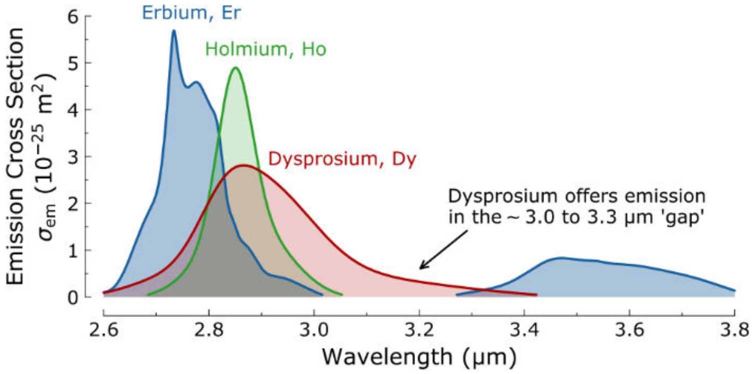

Figure I.10: The emission cross-sections for existing mid-IR fiber lasers based on Er^{3+}, Ho^{3+}, and Dy^{3+} ions covering a spectral range of 2.6 to 3.8 µm [Woo18].

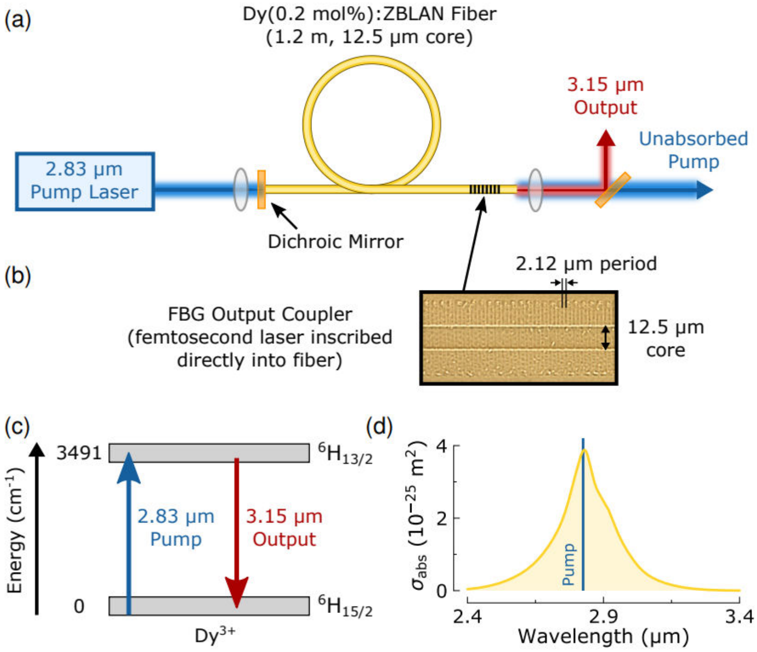

Figure I.11: (a) Scheme of Dy^{3+} fiber laser cavity; (b) Micrograph showing direct-written FBG structure in doped core fiber; (c) Energy level scheme of Dy^{3+} ions in ZBLAN fiber; (d) Absorption cross-section of Dy^{3+}:ZBLAN. Image taken from paper [Woo18].

The in-band pumping at 2.8 µm proved to be the most promising scheme for Dy^{3+} lasers emitting at 3.15 µm owing to $^6H_{13/2} \rightarrow {}^6H_{15/2}$ transition, as shown in Figure I.11(c,d). Recently, Woodward *et al.* reported the first watt-level fiber laser in the 3.0–3.3 µm region by employing a dysprosium-doped ZBLAN fiber. Using a simple in-band pumped linear cavity with a grating stabilized Er^{3+}:ZBLAN fiber laser as a pump source at 2.85 µm, Figure I.11(a), they achieved 1.06 W at 3.15 µm with 77% slope efficiency (relative to absorbed power) [Woo18]. A year later, using a similar pumping scheme, the scientific group of Real Vallée demonstrated a system delivering 10.1 W at 3.24 µm in continuous wave operation, a record for fiber oscillators in this range of wavelengths [For19].

- **For pumping optical parametric oscillators (OPO)**

The principle of nonlinear frequency conversion involves a process called parametric amplification, where the energy of the pump laser with frequency ω_p is converted into two lower frequencies (ω_s, ω_i), known as the signal and idler wavelengths. The sum of the output frequencies is equal to the input wave frequency: $\omega_s + \omega_i = \omega_p$ and $k_s + k_i = k_p$. These wavelengths are typically different from the pump wavelength and can be adjusted by choosing an appropriate nonlinear crystal and adjusting the angle of the crystal. Principle of optical parametric frequency conversion is shown in Figure I.12.

In recent decades, significant progress has been made in the development of novel non-oxide nonlinear optical (NLO) crystals in the mid-infrared region. They consist of sevelal crystal families: phosphides (P), sulfides (S), selenides (Se), arsenides (As), and tellurides (Te). However, only a few crystals have been commercially realized and are widely used as NLO crystals, including AgGaS2 (AGS), AgGaSe2 (AGSe), and ZnGeP2 (ZGP). The first two represent benchmarks for laser pumping near 1 and 1.6 µm, respectively, for generating longer wavelengths in the mid-IR range, that is, for frequency down-conversion [Pet21]. Despite this, these materials still suffer from high dual-photon absorption, chemical instability, low thermal conductivity, and low optical damage thresholds, which limits their use in practical applications. Among commercial NLO crystals, the ZGP crystal has the best characteristics owing to its higher nonlinearity, thermal conductivity, and damage threshold. However, its pump wavelength should be 2 µm or more owing to residual absorption near IR. Consequently, 2-µm Ho and Tm or 3-µm Er lasers are suitable candidates for this purpose [All97, Bud00, Vod00, Vod01, Der08 Cre08, Yao14]. For example, Vodopyanov *et al.* demonstrated ZGP OPO with wide mid-IR tunability (3.8 - 12.4 µm) pumped by 100-ns Er laser pulses at $\lambda = 2.93$ µm with the quantum conversion efficiency of 35% [Vod00]. The OPO type-I idler energy is shown in Figure I.13(a) as a function of the wavelength. They also demonstrated the sensitive detection of N_2O gas with a narrow linewidth (<0.5 cm^{-1}) using this OPO system, Figure I.13(b).

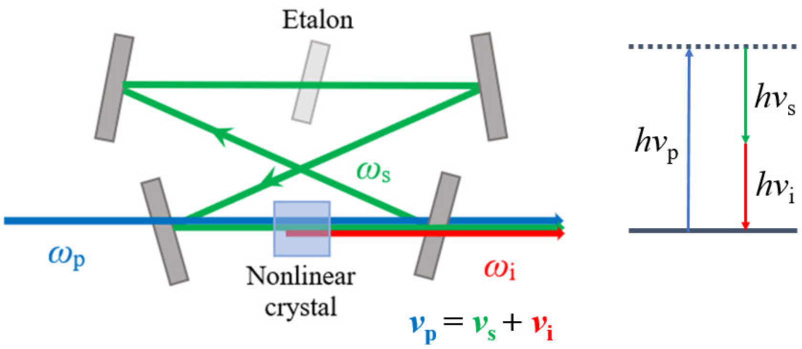

Figure I.12: Principle of optical parametric frequency conversion.

Pulsed 2.8 μm Er lasers have recently been shown to be suitable for pumping OPOs based on a new generation of NLO crystals such as $BaGa_4S_7$ (BGS), $BaGa_4Se_7$ (BGSe), $BaGa_2GeS_6$ (BGGS) and $BaGa_2GeSe_6$ (BGGSe) [Hu19]. Hu *et al.* demonstrated the mid-infrared BGSe optical parametric oscillator with high conversion efficiency and beam quality, which is pumped by 2.79-μm electro-optically Q-switched Cr,Er:YSGG laser. A pulse energy of 3.5 mJ with a pulse duration of 21 ns at 10 Hz is obtained in the range of 3.94 - 9.55 μm.

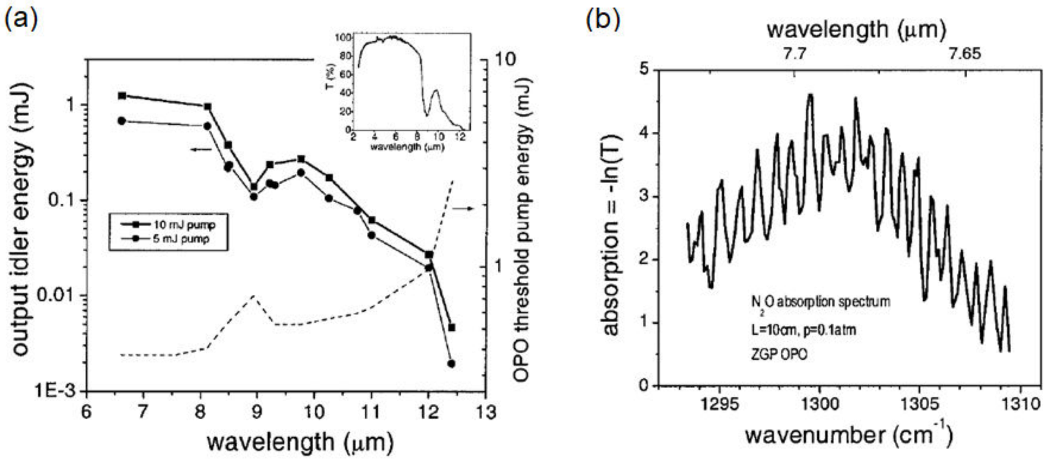

Figure I.13: (a) OPO output as a function of λ_{idler} for two pump energies: 5 and 10 mJ. *Dashed curve* - the OPO pump threshold dependence. *Inset* - transmission spectrum of the antireflection-coated 2-cm ZGP crystal; (b) Absorption spectrum of N_2O gas obtained from the OPO transmission experiment [Vod00].

- **For pumping supercontinuum sources**

Supercontinuum generation involves the use of nonlinear optical effects, such as self-phase modulation, the Raman effect, four-wave mixing, modulation instability, soliton splitting, and dispersion wave generation, to extend the spectral range of the laser beam, which is initially nearly monochromatic [Dud10]. This can be achieved by directing a short and powerful stream of light through a photonic crystalline optical fiber. Supercontinuum sources provide superior brightness and beam quality compared to thermal sources, such as blackbody and solar radiation, producing a broad and relatively even spectrum of a few microns in the mid-infrared region [Mic16]. Figure I.14 illustrates the principle of supercontinuum generation.

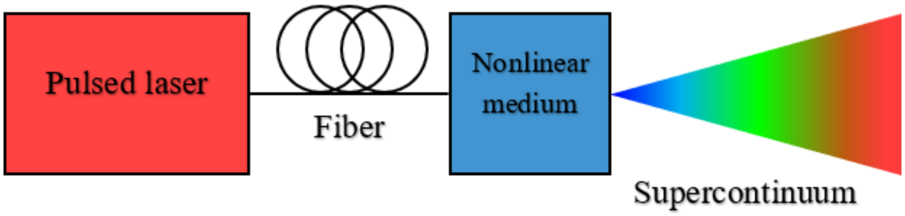

Figure I.14: Schematic representation of the supercontinuum generation principle.

Although commercial fiber-based supercontinuum (SC) systems have become more reliable, their energy conversion in the mid-infrared region is still lacking, typically producing wavelengths no longer than 4.7 µm due to the trigger laser wavelength is too far from the desired spectral region. Previous methods have utilized nanosecond/picosecond initial pulses of 1.55 or 2 µm that are amplified in doped silicon dioxide and expanded in undoped fluoride fibers [Ale12, Yin17, Hei13]. However, Gauthier *et al.* proposed amplifying picosecond seed pulses at a wavelength of 2.8 µm in an erbium-doped fluoride fiber amplifier to achieve a maximum SC power beyond 3 µm [Gau15, Gau18]. The experimental setup for this approach is illustrated in Figure I.15.

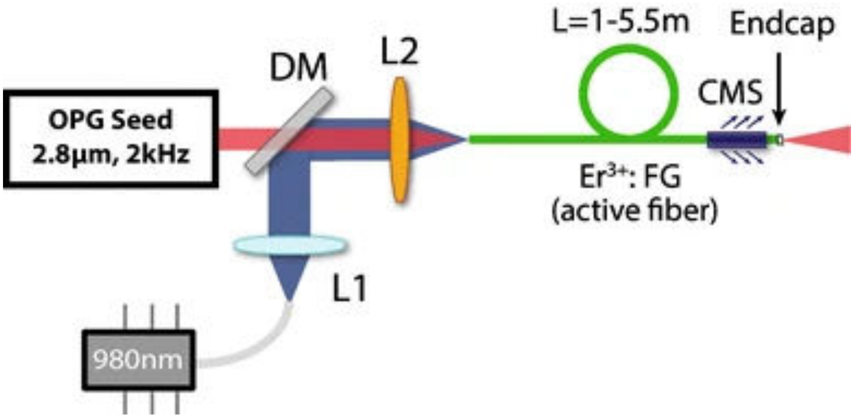

Figure I.15: Experimental set-up scheme for the SC generation [Gau18].

This method allowed to achieve a mid-infrared conversion efficiency of up to 95% and spectral coverage up to transparency limits of 4.2 µm for ZrF_2 and 5.5 µm for InF_3 fibers. Figure I.16 shows power density spectra of SC for three different amplifier lengths. It is shown that increasing the amplifier length enhances the spectral broadening in the SC by increasing the nonlinear interaction length. This resulted in a 30 mW SC extending from 2.7 to 4.2 µm at less than a watt pump power (830 mW) using a 5.5 m amplifier length, wider than was possible with a 1 m amplifier at 2.13 W pump power.

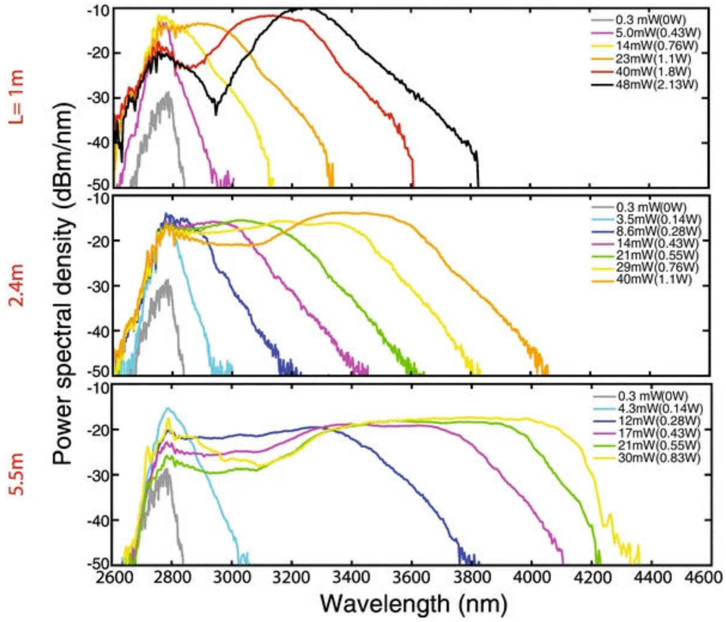

Figure I.16: Power spectral density of the SC generated with three different amplifier lengths [Gau18].

1.2 Existing sources around 2.8 µm

Various MIR laser technologies are now available for 2.7 - 3 µm laser generation, including rare-earth-doped crystalline and fiber lasers, semiconductor laser diodes (LDs), quantum and interband cascade lasers, Raman lasers, nonlinear optical frequency converters, etc.

1.2.1 Semiconductor lasers

In order to achieve mid-infrared wavelengths using semiconductor sources operating at ambient temperature, it is necessary to have materials with a small bandgap energy, which has not been available for a long time. Wavelengths above 4 µm have been achieved by using transitions within the conduction band. Such lasers are called quantum cascade lasers (QCLs). Unlike traditional semiconductor materials, QCLs present superlattices - a series of thin layers - in their optically active region. These layers are quantum well barrier systems that are spaced equidistantly from each other, resulting in multiple quantum wells (MQWs) and one-dimensional confinement. Figure I.17 illustrates the concept of quantum cascade laser.

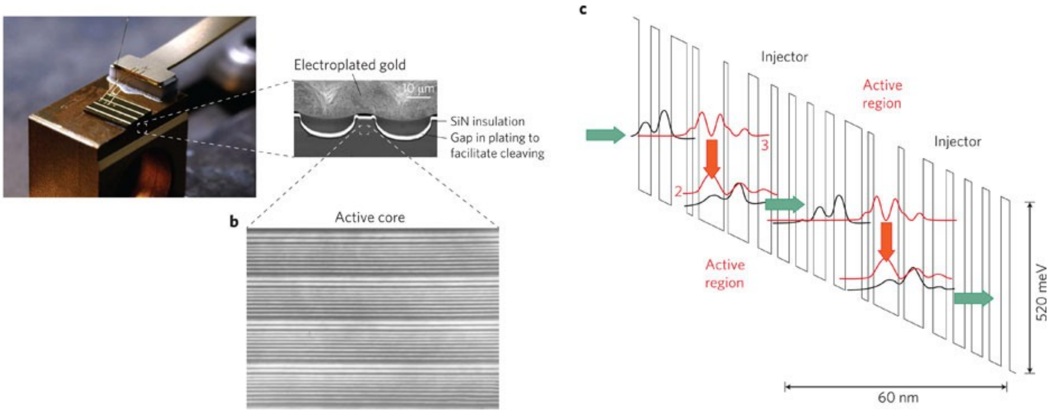

Figure I.17: Concept of a QC laser: (a) Photograph of a laser bar with four QC lasers *(left)* and SEM image of the front facet of the QC laser *(right)*; (b) TEM image of QC laser showing four periods of active regions and injector; (c) Schematic representation of the conduction band structure for a basic QC laser, where the laser transition is between sub-bands 3 and 2 [Yao12].

First attempts to break the "3µm barrier" and reach the wavelengths near 3 µm where the absorption lines of important molecules such as H_2O and CO_2 are presented, were undertaken by Lin *et al.* In order to decrease the bandgap, they increased the In and As contents in GaInAsSb quantum well. However, this approach led to a degradation of the laser performance due to the thermal escape of holes from the quantum well into the waveguide where they recombined [Tou12]. In 2006 - 2007, significant progress was made in three distinct technologies that approached the 3 µm wavelength mark. These included an InGaAs/AlAsSb lattice matched on InP, strained (Ga)InAs/Al(In)As heterostructures grown on InP, and InAs/AlSb on an InAs substrate [Dev06, Rev07 and Sem07].

Another possibility to cover the spectral range below 3 µm is the use of optically pumped semiconductor disk lasers (OPSDLs). They are also known as the vertical-external-cavity surface-emitting lasers (VECSELs). The OPSDL operation at 2.65–3.1 µm with an output power exceeding 2 W was achieved by Ishida *et al.* [Ish11]. The laser structure was grown epitaxially on a BaF_2 (111) substrate and consisted of an optical excitation (OE) layer made of short-period PbSrS superlattices, active PbSrS/PbS MQW layer, and an SrS/PbSrS Bragg reflector mirror structure. The OE layer absorbed most of the pump light, generating electrons and holes that diffuse into the active QW layer with the smallest bandgap. Furthermore, the use of a single-mode distributed feedback (DFB) interband cascade laser allowed to achieve a 2.8 µm laser emission with an output power of several milliwatts at ambient temperature, Figure I.18. This device was a waveguide consisting of 200 nm wide GaSb separate confinement layers (SCLs) on both sides of the active region. It was embedded between 2.5 µm lower and 1.5 µm upper InAs/AlSb superlattice cladding layer [Sch15].

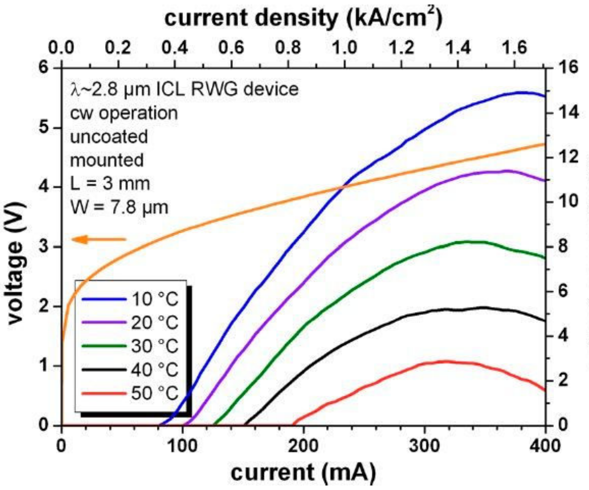

Figure I.18: Output characteristics of an ICL DFB device at temperatures ranging from 0°C to 20 °C in CW operation [Sch15].

To date, commercially available laser diodes based on ICL, DFB ICL and Fabry-Perot resonators operating in the 2.6-3.0 µm range have a limited output power of several tens of milliwatts. An example of such laser diode offered by Tharlabs Company is shown in Figure I.19.

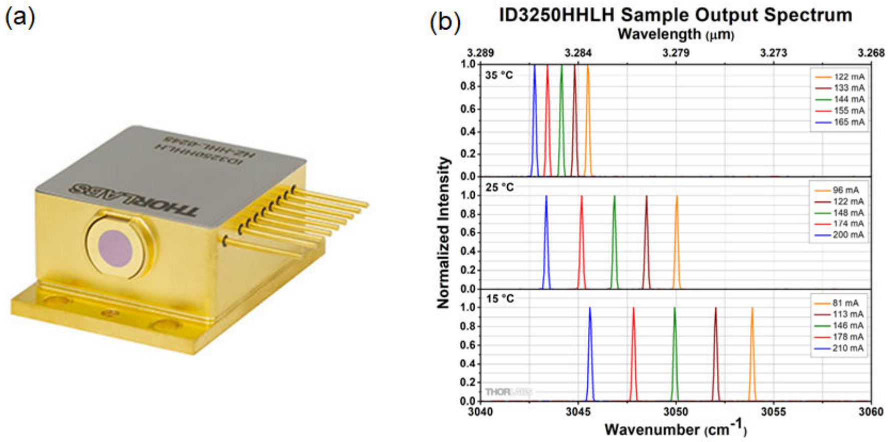

Figure I.19: An example of commercially available ICL laser operating at 3.00 - 3.50 µm: (a) Photograph of DFB ICL (model: ID3250HHLH, Thorlabs); (b) Spectral output chracteristics at different temperatures (15-35°C). Information taken from https://www.thorlabs.com/thorproduct.cfm?partnumber=ID3250HHLH

In summary, semiconductor lasers are a beneficial technology that is ideally suited for use in miniaturized devices owing to their compact size, low power consumption, high conversion efficiency, and reliability. In addition, their high-speed modulation ability makes them a suitable choice for communication systems. However, these methods have certain disadvantages. Its limited output power in short-wavelength range near 3 μm, and its sensitivity to environmental factors, such as temperature changes, humidity, and dust, which can affect performance. Furthermore, its wide spectral width may limit its use in applications that require narrow spectral widths. Finally, the production cost of semiconductor lasers can be relatively high compared to that of other types of lasers.

1.2.2 Raman lasers

A coherent light source called a Raman frequency converter (or Raman laser) employs a stimulated Raman scattering (SRS) amplifier medium, which is a third-order nonlinear optical process [Vod20]. Using the Raman effect, one can obtain the emission of a wavelength shift from that of a pump laser. Because the shift is based on inelastic scattering and not on discrete electronic transitions, there is great flexibility in the tunability. The shift between the two wavelengths depends on the material; for example, in silica fibers, it is approximately 100 nm [Gui21]. For example, Raman shifted Nd:YAG laser at 2.92 μm (2nd Stokes) has been used as pump sources for Fe^{2+}:ZnSe laser system [Fed06].

1.2.3 Nonlinear optical frequency convertors (DFG, OPOs, OPGs)

Optical parametric sources (OPSs), such as optical parametric oscillators (OPOs), optical parametric generators (OPGs), or difference frequency generators (DFGs), offer a versatile solution for generating coherent light at wavelengths where other lasers unavailable or have limitations. Principle of nonlinear frequency conversion was described in Sub-section 1.1.4. They allow to reach output characteristics that cannot be realized by traditional lasers and has many advantages, such as a wide tuning range, relatively simple structure, high output power, narrow linewidth, etc.

Despite the unique capabilities offered by parametric oscillators, their commercial realization is extremely limited due to the complexity and cost compared to pure laser systems, as they require the use of multiple pump lasers and sometimes a thermostabilizing crystal oven. The nonlinear conversion cascades in these systems are particularly sensitive to phase matching, in contrast to laser amplifiers which are more forgiving of crystal temperature. In addition, some nonlinear crystal materials are prone to hygroscopicity or grey tracking (i.e. increased parasitic losses), while others are difficult to apply strong anti-reflection coatings due to non-isotropic thermal expansion.

1.2.3 Solid- state lasers (SSLs)

- **Cr^{2+}-doped II–VI chalcogenide lasers**

The absorption bands of Cr^{2+} ions in II-VI chalcogenides are broad and cover the range of 1.5-2.2 µm, which allows the use of different pump sources, as shown in Figure I.20. These crystals have also wide emission bands, which is an advantage for tuning in the mid-IR range and generation of ultra-short pulses. In contrast to Fe^{2+} ions, in Cr^{2+} doped ZnSe crystal, no luminescence quenching is observed at room temperature, and the quantum yield of luminescence in these crystals is close to unity. This property is one of the reasons why Cr^{2+}:ZnSe and similar crystals serve as gain medium for effective RT lasers operating in the 2 - 3 µm range. It is noteworthy that the peak absorption and emission cross sections of Cr^{2+} in all II-VI chalcogenide media are about two orders of magnitude larger than those of the rare-earth ions [Vod20].

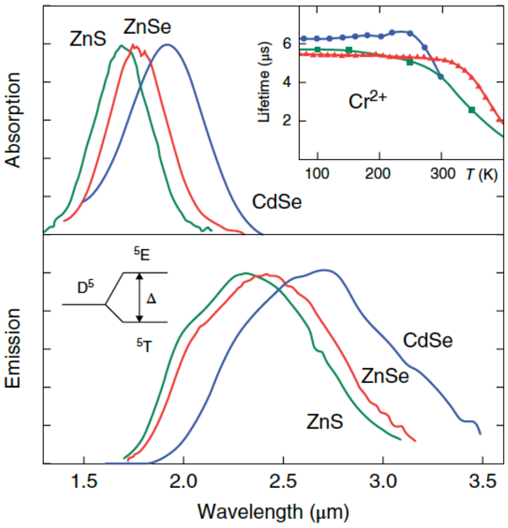

Figure I.20: Normalized RT absorption *(top)* and emission spectra *(bottom)* of Cr^{2+} ions in ZnS, ZnSe, and CdSe crystals. Image taken from [Vod20].

However, despite the wide tuning range from 1.9 to 3.3 µm, in Figure I.21, Cr^{2+}-doped chalcogenide thin disk lasers have limited power outputs of about 10 W and 2 W for 2.4-2.5 µm and 2.94 µm lasers, respectively [Sch05]. The main factors limiting the high output power in Cr^{2+}:ZnS and Cr^{2+}:ZnSe lasers with typical slab gain media or thin disk geometry are strong thermal lensing effects and a low optical damage threshold. To manage thermal effects in thin disks, smaller thickness is required, resulting in lower optical density and hindering power scaling efforts [Mos16].

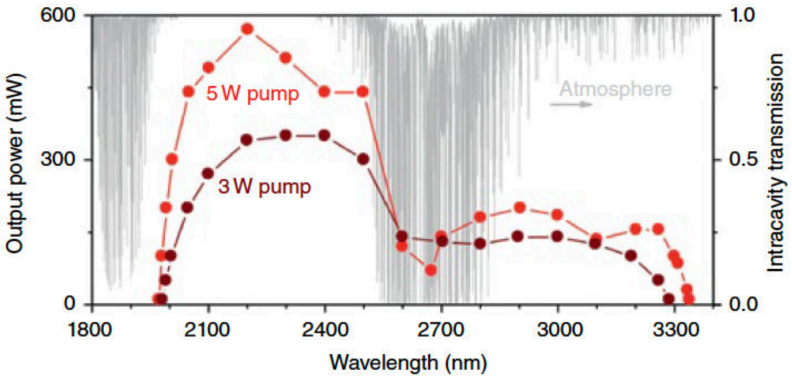

Figure I.21: Tunability range of a CW Cr:ZnSe laser. Transmission of the atmosphere is shown in the background. Taken from [Vod20].

- **Holmium (Ho^{3+}) solid-state lasers**

Among the RE^{3+} ions, only Ho^{3+} and Dy^{3+} ions provide laser generation in the 2.7 – 3 µm region, similar to that of Er^{3+} ones. Simplified energy-level diagrams for these lasers is shown in Figure I.22.

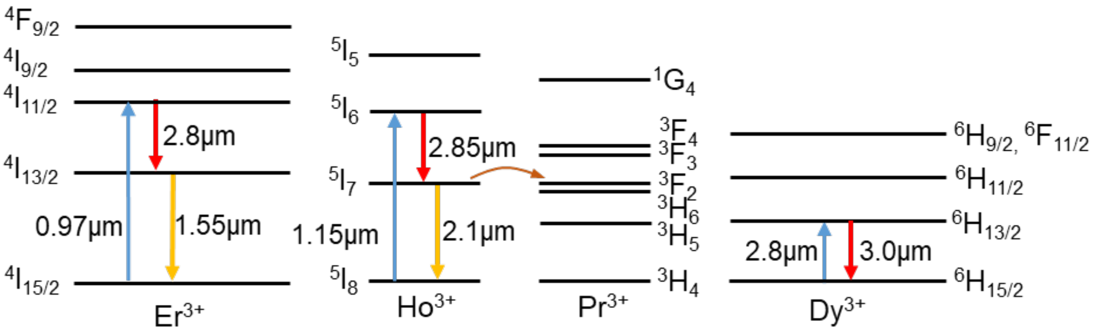

Figure I.22: Simplified energy-level diagram for Er^{3+}-doped laser at 2.8 µm *(left)*, Ho^{3+}, Pr^{3+}-codoped laser at 2.85 µm *(middle)*; a Dy^{3+}-doped laser at 3.0 µm *(right)*.

Lasers based on Ho^{3+} ions emitting in the 2.7 – 3 µm spectral region are poorly studied compared to lasers emitting around 2.1 µm. The main limiting problems are the pump wavelength of approximately 1150 nm (commercially unavailable LD wavelength) and the self-quenching effect occurring at the $^5I_6 \rightarrow {}^5I_7$ transition (5I_7 has a longer lifetime than $^5I_6$). The saturation of the $^5I_6 \rightarrow {}^5I_7$ transition can be suppressed by two approaches: cascade generation or by co-doping with sensitized (usually Yb^{3+} ions) [Umy96] or deactivated (usually Nd^{3+} and Pr^{3+}) ions [Mac87, Zha12, and Nie18]. Cascade lasing involves the simultaneous oscillation on both transitions of the Ho^{3+} ions ($^5I_6 \rightarrow {}^5I_7$ and $^5I_7 \rightarrow {}^5I_8$ transitions) in the same resonator. This cascade oscillation scheme has been successfully demonstrated Cr^{2+},Yb^{3+},Ho^{3+}:YSGG [Zav93]. However, using a deactivator, such as Pr^{3+}, simplifies the laser resonator and provides a single-emission output as compared to cascade lasing.

In addition, lasers doped with Ho^{3+} ions require specific and sometimes complex pump sources, such as a flash lamp [Mac87, Umy96, Bow90], a Raman fiber laser emitting at 1150 nm [Nie18, Xu22], or a combination of a $Ti:Al_2O_3$ laser and 970 nm LD [Die98]. Using a power-scalable Yb^{3+} fiber-laser-pumped 1150-nm Raman fiber laser as the pump source, Crowfard *et al.* achieved maximum average output power of 7.2 W with slope efficiency of 29% and the broadest tuning range of 150 nm (2825~2975 nm) in Ho^{3+}/Pr^{3+}-codoped ZBLAN fiber [Cra15], as shown in Figure I.23.

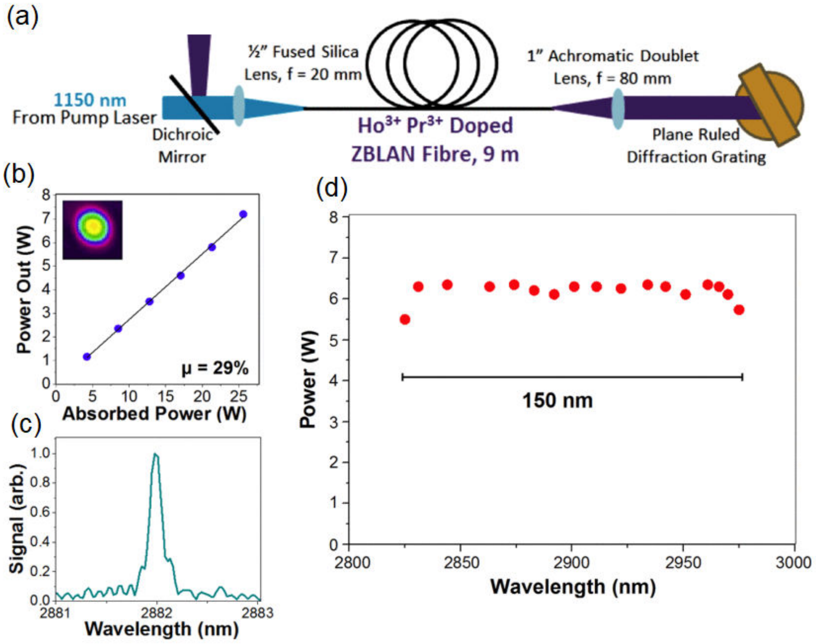

Figure I.23: (a) Schematic diagrams of the Ho^{3+}, Pr^{3+} codoped ZBLAN fiber laser used in [Cra15]; (b) output power at 2882 nm as a function of absorbed power; (c) spectrum of laser emission at 2882 nm, and (d) wavelength tuning.

• Dysprosium (Dy^{3+}) solid-state lasers

Another candidate for generating a 2.7 – 3 µm emission is the laser based on Dy^{3+} ions; this emission originates from the $^6H_{13/2} \rightarrow {}^2H_{15/2}$ transition. At present, 3 µm Dy^{3+}-doped lasers have been poorly studied. This is because of the lack of high-quality crystals and suitable pump sources. Thus far, laser emission originating from the $^6H_{13/2} \rightarrow {}^2H_{15/2}$ transition has been achieved mostly in fluoride fibers and some bulk crystals [Joh73, Dje97]. Recently, Dy^{3+}-doped ZBLAN fiber lasers have demonstrated CW operation, emitting an output power of more than 10 W [For19], a slope efficiency of up to 77% [Woo18], and a tuning range wider than 500 nm [Maj18]. Pulse lasers have been demonstrated in the gain switching [Paj19, Luo19a], Q-switching [Luo19b, Yan20, Woo19], and mode-locking regimes [Woo18, Wan19]. As mentioned before in Sub-section 1.1.4, given the exceptional output characteristics, the most suitable pump for such lasers are Er^{3+} lasers emitting at 2.8 μm.

Despite the advantages offered by fiber-based sources, their output energy and peak power are limited by the dimensions of the fiber core. This limitation results in extremely high-power density within the gain medium, leading to significant non-linear or damaging effects.

- **Erbium (Er^{3+}) solid-state lasers**

Erbium-doped crystal and fiber lasers have emerged as promising candidates for efficient laser operation at the 3 μm wavelength. Since this is the main objective of this thesis, we will discuss erbium-doped solid-state lasers in detail in the following sections.

2 Trivalent erbium ions (Er^{3+})

2.1 General information about rare-earth ions

The rare earth elements (REEs) are a group of 15 elements placed in the sixth period of the periodic table and designated as the lanthanide series. Scandium and yttrium are included in this category because they exhibit similar characteristics to the lanthanides and occur in the same mineral ores. REEs are the key components of many electronic devices that we use in our daily life, as well as in various industrial applications.

Electrons in the rare-earth atom occupy orbitals of either $[Xe]4f^{n}5d^{1}6s^{2}$ or $[Xe]4f^{(n-1)}5d^{0}6s^{2}$. Here, [Xe] represents a ground state configuration of a xenon nucleus, namely:

$$[Xe] = 1s^{2}2s^{2}2p^{6}3s^{2}3p^{6}3d^{10}4s^{2}4p^{6}4d^{10}5s^{2}5p^{6} \tag{I.1}$$

and n – number of electrons filling the $4f$ orbital, which varying from 0 to 14. The filling and spatial extent of the outer electron orbitals, $5d$- and $6s$-, which are most important for chemical bonding, practically do not change in the entire rare-earth series. With the increase of lanthanide number, the completing of inner $4f$- orbital by the electrons is initiated from cerium to lutetium. The $4f$-electrons are more localized spatially being held closer to the nucleus and shielded from the coordination environment by the outer $5s$- and $5p$- electrons. The shielding effect originates from the inner electrons and decreases according to $s > p > d > f$. As a result, the interaction between $4f$-electrons and the environment is very weak. Therefore, as the atomic number increases the effective attraction between the nucleus and the outer electrons increases. This increased attraction leads to a reduction in the atomic and ionic radii. The lanthanum ion, La^{3+}, has ionic radius of 1.061Å, whereas the heavier lutetium ion, Lu^{3+}, has a radius of 0.850 Å. This phenomenon is called "lanthanide contraction".

Each of the n electrons of the $4f^{n}$ configuration is associated with one of seven $4f$ wavefunctions and can have a spin of ½. There are several ways to assign n electrons to $4f$ orbitals, considering spin; this number corresponds to the multiplicity (or degeneracy) of the configuration and is given by the following formula:

$$\mathrm{d}\left(4f^{n}\right) = C_{14}^{n} = \frac{14!}{n!\left(14-n\right)!} \tag{I.2}$$

The energy levels of electronic configurations can be labeled by L, M_L, S, and M_S quantum numbers, where L is the total orbital angular momentum and its projection along the z-axis, M_L is the total magnetic orbital angular momentum, S is the total spin angular momentum, which is often indicated as the spin multiplicity, $2S+1$, as well as its projection along the z-axis, and M_S is the total magnetic spin quantum number. In the case of heavy atoms, such as lanthanides, the Russell-

Saunders coupling formalism with an additional quantum number J describes the spin-orbit coupling and is calculated as $L+S$. According to this formalism, the wavefunction associated with the energy levels of free ion can be written as a linear combination of Russell-Saunders states $|4f^n\alpha SLJ>$:

$$\left|4f^n\alpha[SL]J\right\rangle = \sum_{\alpha',L',S'} C(\alpha',L',S')\left|4f^n\alpha'S'L'J\right\rangle \quad \text{(I.3)}$$

where $C(\alpha',L',S')$ are the coefficients calculated by diagonalization of the Hamiltonian of the ion. More extensive calculations are presented in the following works [Wyb65, Hen89].

Over the years, numerical analysis techniques have been developed to calculate the energy states of free RE ions (i.e., for ions outside a ligand or crystal-field environment). The perturbation of the Ln $4f$ levels caused by the crystal field is rather weak compared to the Coulomb interaction between the electrons and the spin-orbit coupling. The Coulomb interaction between the electrons within the $4f$ shell has the largest contribution to energy splitting; it produces different SL terms separated from each other on the order of 10^4 cm^{-1}, but independent of the total angular momentum J. Each of these terms is then split further on the order of 10^3 cm^{-1} into SLJ multiples by the spin-orbit interaction. These levels form the $4f$ configuration of the free Ln ions, and each level can be labeled by the symbol $^{2S+1}L_J$. Finally, when the RE^{3+} ion is placed into host matrix, the crystal-field interaction splits the multiples into mixtures of $|\alpha SLJM>$ basis states (Stark sublevels), split by the order of 10^2 cm^{-1}. The energy-level scheme of the Er^{3+} ions, indicating the splitting of the $4f^{11}$ configuration by Coulomb interaction, spin-orbit coupling, and Stark splitting by the crystal-field of the host material is shown in Figure I.24. Since the surrounding ions in the crystal lattice have a clearly defined symmetry the degeneracy depends on the local symmetry of the site occupied by the RE^{3+} ion.

The complete arrangement of energy levels can be easily understood by examining the electronic configuration of RE^{3+} ions. Gerhard Dieke extensively studied the various combinations of electronic $4f^n$ configurations and derived the potential terms. In the 1960s, Dieke pioneered the development of energy level diagrams for all $4f^n$ configurations, covering the infrared, visible, and ultraviolet regions of the spectrum (up to 40000 cm^{-1}). These diagrams, known as Dieke diagrams, remain applicable to RE^{3+} ions in different crystal structures due to the minimal impact of crystal field splitting.

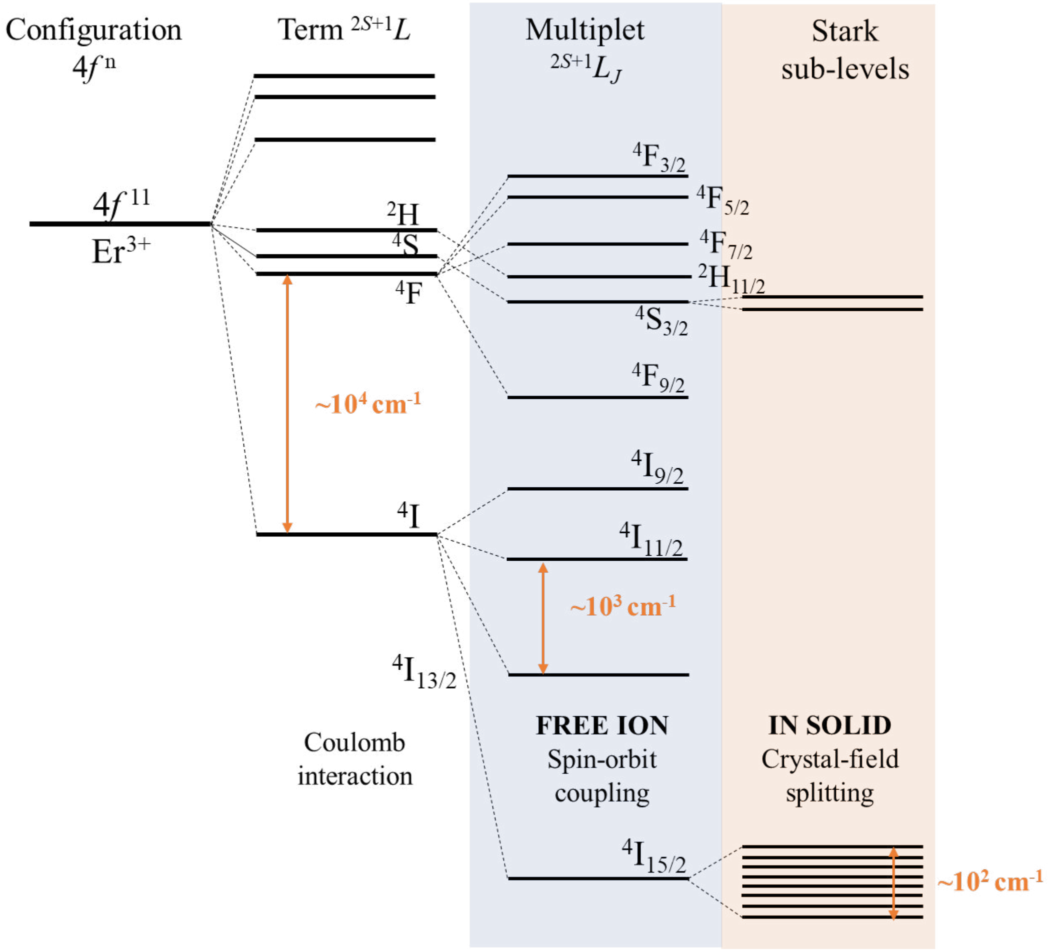

Figure I.24: Energy-level scheme of Er^{3+}indicating the splitting of the $4f^{11}$ configuration by Coulomb interaction, spin-orbit coupling, and Stark splitting by the crystal-field of the host matrix.

• Spectral behavior of rare –earth ions in solids

Any influence on the emitting system leads to the broadening of the spectral lines, which can appear as homogeneous or inhomogeneous broadening. Homogeneous broadening results in uniform line broadening for individual atoms as well as for the entire system. The individual atoms emit the same spectrum with the same center frequency, ν0. However, inhomogeneous broadening occurs when the resonant frequencies of individual atoms are distributed over the frequency range, resulting in line broadening for the entire system, even if the line of each atom remains unaffected. Homogeneous broadening is described by a Lorentz function, whereas inhomogeneous broadening is described by a Gaussian function. Figure I.25 provides a graphic representation of these two types of broadening.

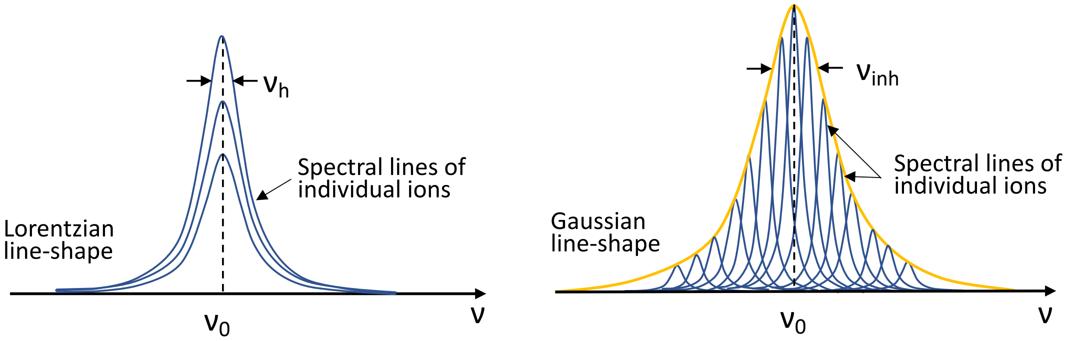

Figure I.25: Spectral broadening behavior: (a) homogeneous and (b) inhomogeneous.

Let us consider this in detail. If the activator ion is incorporated isomorphically into a compound with an ordered structure and replaces the matrix ions located in equivalent positions, such a compound can be called an ideal simple single-center crystal. In this case, all the interaction centers are identical, and the spectral line associated with each center is a set of lines identical in position and shape. Such lines in the spectra are called homogeneously broadened lines. However, in real crystals, even in simple crystals, because of the small defects in the host matrix structure, the activator centers may differ slightly from each other, especially at low temperatures. In this case, the observed lines are a superposition of lines that are slightly shifted in terms of frequency.

Several mechanisms of inhomogeneous spectral broadening of activator ions in a crystalline matrix can be distinguished:

1. Crystals with a structure disorder;
2. Crystals with heterovalent activation leading to various charge compensation mechanisms;
3. Solid-solution (compositionally “mixed” crystals).

Structural disorder in the crystals can occur for two reasons. First, activator ions can occupy several non-equivalent crystallographic positions, leading to a multisite behavior. In some crystals, such as cubic sesquioxides such as Y_2O_3, rare-earth cations occupy two non-equivalent sites with C_2 and C_{3i} symmetry, leading to different crystal field strengths and even different selection rules for electric and magnetic dipole transitions [Kra15]. Second, structural disorder can be caused by the random distribution of two or more host cations at one or more crystallographic sites, and sometimes, activator ions do not replace all host cations. In such cases, inhomogeneous broadening of the spectrum occurs because of the variations in the composition of the second coordination sphere around the activator ions. This leads to several families of site geometries, resulting in a spectroscopic behavior similar to that of glasses. As an example, is the tetragonal crystal $CaGdAlO_4$, in which Ca^{2+} and Gd^{3+} cations are randomly distributed on identical lattice sites with C_{4v} symmetry [Pet08a].

A different scenario arises for crystals that involve *heterovalent activation*. This occurs when ions with different charges but similar sizes replace each other within the crystal lattice. In such cases, the arrangement of centers is influenced by how charge compensation is achieved to maintain local electrical neutrality. Heterovalent isomorphism can result in two types of crystals: those with a single center and those with multiple centers. An example of the latter type is found in rare-earth-doped cubic CaF_2 and its fluorite-type counterparts, such as SrF_2 and BaF_2.

Solid-solution crystals, also known as compositionally "mixed" crystals, refer to third type of inhomogeneous broadening mechanisms. They involve host materials forming substitutional isostructural series referred to as A1-xBx, where A and B compounds serve as parent elements. Due to their compositionally disordered structure, these crystals give rise to various types of centers. In contrast to simple multicenter crystals, where optical spectra exhibit distinct lines for each center type, "mixed" systems do not display well-defined line resolution, even at very low temperatures. Instead, their spectra are characterized by broad bands that result from the overlapping of numerous lines. In essence, the spectral lines corresponding to activator impurities in mixed crystals always possess inhomogeneous broadening. Notable examples of such crystals include the cubic Y_2O_3 - Lu_2O_3 - Sc_2O_3 solid-solutions.

In this PhD thesis, we examine materials featuring all the above-mentioned mechanisms of inhomogeneous line broadening.

2.2 Interaction of light and matter

2.2.1 Intraionic processes

The intraionic processes in rare- earth ions, which include ground-state absorption (GSA), stimulated emission (SE), spontaneous emission, and multiphonon relaxation are shown in Figure I.26.

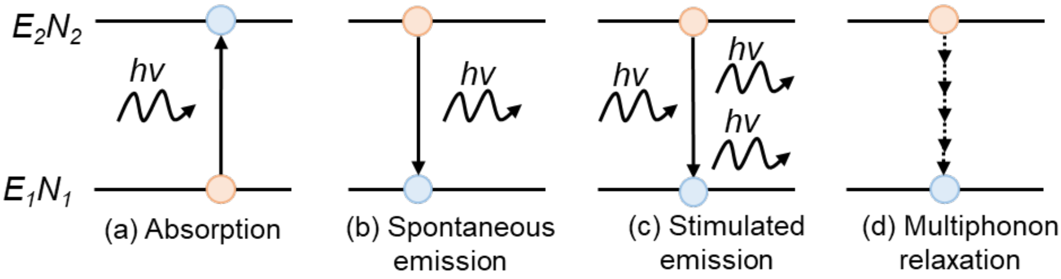

Figure I.26: Intraionic processes occurring in a two-level system.

- **Absorption & Stimulated emission**

When a photon with energy $E_{phot} = hv$ interacts with an ion that has two energy levels as shown in Figure 1.26(a), absorption can occur if the condition $E_{phot} = E_2 - E_1$ is satisfied. This results in the ion being excited, and this process is referred to as ground state absorption (GSA). The change in the population N_1 can be expressed as follows:

$$\left(\frac{dN_1}{dt}\right)_{abs} = -W_{12}N_1 = -\sigma_{12}FN_1 \qquad (I.4)$$

The transition probability between 1 and 2 levels is given by W_{12}, whereas F is the photon flux, and σ_{abs} is the GSA cross-section.

If an ion is already in an excited state, it can emit a photon exhibiting properties identical to those of the absorbed photon (same frequency, propagation direction, and polarization). This process is called stimulated emission (SE), Figure I.26(c). The population N_2 of the excited state changes as:

$$\left(\frac{dN_2}{dt}\right)_{SE} = -W_{21}N_{21} = -\sigma_{21}FN_2 \qquad (I.5)$$

where W_{21} is the transition probability from 2 to 1 level, and σ_{SE} is the SE cross-section.

The radiative transitions also include the process of excited-state absorption (ESA). In this case, within a three-level scheme the following condition must be fulfilled: $E_3 - E_2 = E_2 - E_1$. This means that a photon with given energy can be further absorbed by the already exited ion.

- **Spontaneous emission**

If no photon is present to induce stimulated emission, an excited ion can decay via spontaneous emission of a photon, Figure I.26(b). This decay is characterized by a time constant τ rad which is called the radiative lifetime of the respective excited state. The probability A of this decay is given by $A = 1/\tau_{rad}$. It allows the calculation the change of the population of N_2 caused by this process via:

$$\left(\frac{dN_2}{dt}\right)_{spon} = -AN_2 \tag{I.6}$$

The absorption cross section, denoted as σ_{abs}, can be determined by absorption measurements. On the other hand, the emission cross section, σ_{SE}, can be calculated by applying the Füchtbauer-Ladenburg theory to the measured emission spectrum. Finally, the relation between the absorption cross-section and the emission cross-section can be established by using McCumber's theory (the so-called reciprocity method).

Significant progress in the quantitative description of the transition intensities for RE^{3+} ions in crystals and glasses was achieved by Judd and Ofelt [Jud62, Ofe62]. *Judd-Ofelt analysis* is a method used to study the properties of electronic states in a $4f^n$ shell, which have wavefunctions described by spherical harmonics and exhibit a definite parity corresponding to the angular quantum number. In a free ion, electric dipole (ED) transitions ($f - f$ transitions) are prohibited by parity; however, this restriction is removed when a noncentrosymmetric perturbing field (e.g., a crystal field) is present. The crystal field mixes the states of excited configurations with opposite parity (e.g., $4f^{n-1}5d^1$) into the ground configuration $4f^n$, enabling electric dipole transitions.

The calculation of electric dipole operator matrix elements involves treating the crystal field as a first-order perturbation. The process is simplified by assuming that: (i) the ground $4f^n$ configuration states are represented as linear combinations of Russell-Saunders coupled states, (ii) the ground $4f^n$ and the excited $4f^{n-1}5d^1$ configurations are completely degenerate with the excited one being much higher in energy, (iii) all the Stark sub-levels of the ground configuration are equally populated, and (iv) the local field approximation holds. Under these assumptions, the line strengths of electric dipole $f - f$ transitions can be described using an Equation (I.8) and a set of intensity parameters (Ω_k), which are assumed to be identical for all transitions, representing weak configuration interaction (WCI) or standard Judd-Ofelt theory.

$$S^{ED}_{JJ'} = \sum_{\lambda=2,4,6} \Omega_\lambda |\langle 4f^n\alpha[SL]J \| U^{(\lambda)} \| 4f^n\alpha' J[S'L'] \rangle'|^2 \tag{I.7}$$

In this equation, $\langle 4f^n\alpha[SL]J||U^\lambda||4f^n\alpha'[S'L']J'\rangle$ are reduced matrix elements of electric-dipole transition $J \rightarrow J'$ provided in literature. They are calculated for all RE^{3+} ions and their transitions and Ω_λ, are the intensity parameters (so-called Judd-Ofelt parameters). They involve the odd-order parameters of the crystal field, radial integrals of wavefunctions from the ground $4f^n$, perturbing configurations, and other factors. Although it is possible to calculate these parameters from first principles (*ab initio*), they are commonly treated as phenomenological parameters that are adjusted to fit the experimental absorption data.

The absorption oscillator strengths are related to the line strengths:

$$f^{\Sigma}_{calc}(JJ') = \frac{8}{3h(2J+1)\langle\lambda\rangle^3} n\left(\frac{n^2+2}{3}\right)^2 S^{ED}_{calc}(JJ') + f^{MD}_{calc}(JJ') \tag{I.8}$$

where h is the Planck constant, n is the refractive index of the crystal at $\langle\lambda\rangle$ and the superscript "Σ" stands for the total (ED + MD) value. In the standard J-O theory, there are three free parameters, (Ω_2, Ω_4, Ω_6).

The probabilities of radiative spontaneous transitions for emission channels $J \rightarrow J'$ are then determined from the corresponding line strengths in emission:

$$A^{\Sigma}_{calc}(JJ') = \frac{64\pi^4 e^4}{3h(2J+1)\langle\lambda\rangle^3} n\left(\frac{n^2+2}{3}\right)^2 S^{ED}_{calc}(JJ') + A^{MD}_{calc}(JJ') \tag{I.9}$$

Using the A_{calc} values, we have further determined the total probabilities of spontaneous radiative transitions from the excited states A_{tot}, the corresponding radiative lifetimes τ_{rad} and the luminescence branching ratios for the particular emission channels $B(\mathrm{JJ'})$:

$$\tau_{rad} = \frac{1}{A_{tot}} \tag{I.10a}$$

$$A_{tot} = \sum_{f'} A^{\Sigma}_{calc}(JJ') \tag{I.10b}$$

$$B(JJ') = \frac{A^{\Sigma}_{calc}(JJ')}{A_{tot}} \tag{I.11}$$

• Multiphonon relaxation

In addition to radiative processes, non-radiative relaxation processes occur in the crystal due to the interaction with lattice vibration. This process is illustrated in Figure I.26(d). The rate of a multiphonon relaxation W_{NR}, decreases exponentially with the energy gap ΔE to the lower state and with order of the process (number of high energy phonons, p required to fill the energy gap):

$$W_i = Ce^{-p\beta} \tag{I.12}$$

$$p = \frac{\Delta E}{h\nu} \tag{I.13}$$

where C and β characteristic constants for the host matrix. The rate of multiphonon relaxation increases with temperature. The electron-phonon interaction does not change the exponential character of the emission decay, however, reduces its lifetime:

$$\frac{1}{\tau_{lum}} = \frac{1}{\tau_{rad}} + W_{NR} \tag{I.14}$$

2.2.2 Interionic processes

The Er^{3+} ion has a rich structure of energy levels, which are separated by spin-orbit interaction to several almost equidistant crystal-field manifolds. With the increasing concentration of Er^{3+} ions and their spatial proximity, energy transfer processes can occur between neighboring ions. In particular, the laser transition at 2.8 μm results from the transition from the $^4I_{11/2}$ manifold to the $^4I_{13/2}$ state and is affected by various interionic (so-called multiple-ion) processes. Figure I.27 shows the important interionic processes, including both radiative and non-radiative processes.

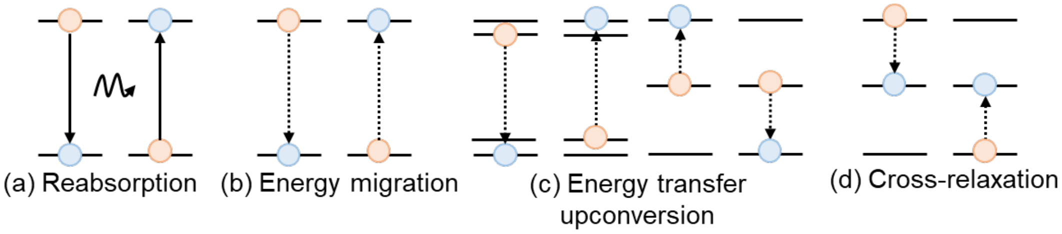

Figure I.27: Possible interionic processes in Er^{3+} ions.

- **Reabsorption**

Reabsorption refers to the process in which a photon emitted by a donor ion is subsequently absorbed by an acceptor ion in a material or crystal, Figure I.27(a). This phenomenon is a resonant process that can occur several times before the photon eventually emits and leaves the material. It can have notable effects on spectroscopic properties, such as the effective lifetime or luminescence spectra of the material.

- **Energy migration**

In the energy transfer process shown in Figure I.27(b), energy is transferred from the excited ion (called the donor) to the neighboring ion, which is initially in the ground state. The donor ion then relaxes back to its ground state, while the second ion becomes excited. This phenomenon is known as donor-donor transfer because the newly excited ion can subsequently act as a donor for another energy transfer event. This sequential process of energy transfer can continue, with each excited ion acting as a donor for the next ion, forming a chain of energy transfer. However, this chain of events can eventually lead to the loss of excitation through energy dissipation at an impurity, such as an OH- group.

- **Energy transfer upconversion**

Donor-acceptor transfer, known as energy transfer upconversion (ETU) between ions, refers to the process when energy is transferred from an excited ion, called a donor, to a neighboring ion, called an acceptor, which is also initially in an excited state. During this transfer, the donor ion undergoes relaxation and returns to its ground state, while the acceptor ion absorbs energy and goes to an even higher energy state. This process is shown in Figure I.27(c).

- **Cross-relaxation**

In the process of cross-relaxation, the donor ion is initially excited, while the acceptor ion remains in the ground state. The excited donor transfers a part of its energy to the acceptor, causing both ions to be in the excited state, Figure I.27(d). If the cross-relaxation process results in both ions being in the same final excited state, a unique phenomenon called the “two-for-one process” can occur. In this process, the absorbed energy of one pump photon is shared between the donor and acceptor ions, resulting in the emission of two photons with the same energy.

2.3 Laser transitions occurring in Er^{3+}ions

Possible laser transitions between the energy levels of the Er^{3+} ions are shown in Figure I.28. Of particular interest for laser operation are the 1.55 μm and 2.8 μm wavelengths. The former is considered “eye-safe” because it is absorbed at the front of the eye without reaching the retina, and finds applications in LIDARs, range finders, and free-space communications. The second, which is within the water absorption maximum of 3 μm, is useful mainly for medical applications. More potential applications are discussed at the beginning of this Chapter. Other Er^{3+} lasers can be generated at wavelengths of 0.55 μm, 0.85 μm, 1.3 μm, 1.7 μm, and 3.5 μm [Din94, Pol97, and San99].

2.3.1 Transition $^4I_{13/2} \rightarrow {}^4I_{15/2}$ at 1.55 μm

The laser emission at 1.55 – 1.65 μm originating from a quasi-three-level transition $^4I_{13/2} \rightarrow {}^4I_{15/2}$ can be used for telecommunications, since it matches the absorption minimum in glass fibers. Although the most common pumping scheme is based on the $^4I_{15/2} \rightarrow {}^4I_{13/2}$ transition with a wavelength of about 0.9 – 1 μm, in-band pumping at 1.54 μm is also possible. However, effective pump absorption at the $^4I_{15/2} \rightarrow {}^4I_{13/2}$

transition can be complicated owing to the small absorption cross-section ($\sigma_{abs} \approx 5\times10^{-21} cm^2$) and limited doping concentration. Co-doping with Yb^{3+} sensitizer ions is a common solution to effectively absorb pump radiation at 980 nm and transfer energy to Er^{3+} ions in the ground state manifold. Er-Yb co-doped fibers are widely used in erbium fiber amplifiers and short fiber lasers.

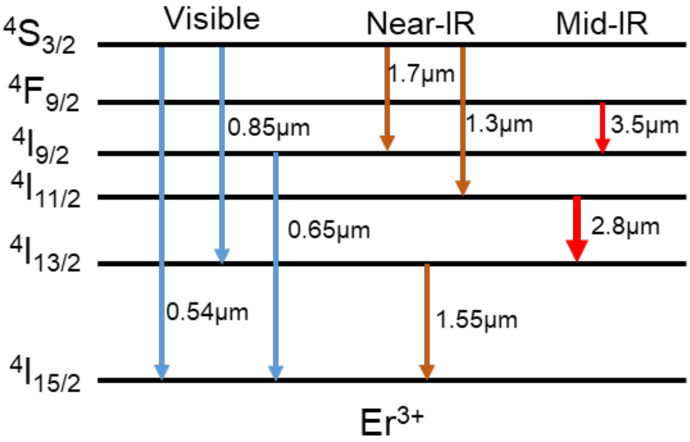

Figure I.28: Energy level scheme of Er^{3+} ions and possible laser transitions occurring in visible, near- and mid- infrared spectral range.

2.3.2 Transition $^4I_{11/2} \rightarrow {}^4I_{13/2}$ at 2.8 µm

Simultaneously, many scientists have been puzzled by the mechanism of stimulated emission from the $^4I_{11/2} \rightarrow {}^4I_{13/2}$ transition. Because the luminescence lifetime of the lower laser level, $^4I_{13/2}$, is typically longer than that of the upper level, $^4I_{11/2}$ (the so-called "bottleneck effect") and leading to self-termination of this laser transition. A schematic illustration of the "bottleneck effect" is shown in Figure I.29(a).

Although many mechanisms operate spontaneously in the erbium ion system, the 2.8 µm laser behavior is mainly explained by four principal processes. These are illustrated in Figure I.29(b). The GSA of the pump (~0.97 µm directly populates the upper laser level, $^4I_{11/2}$. Once this level is completed, there are two main depopulating mechanisms, stimulated emission (SE) and ETU2 ($^4I_{11/2}$, $^4I_{11/2}$) → ($^4F_{7/2}$, $^4I_{15/2}$), which are proportional to the squared population. This induces a more significant loss impact on the laser channel than ESA ($^4I_{11/2} \rightarrow {}^4F_{7/2}$). Both ETU2 and ESA eventually populate the $^4S_{3/2}$ state after nonradiative relaxation, from which energy is redistributed to the upper and lower levels by cross-relaxation. ETU1 ($^4I_{13/2}$, $^4I_{13/2}$) → ($^4I_{9/2}$, $^4I_{15/2}$) depopulates the terminal laser level by transferring energy to the ground level and back to the emitting level. This ETU is the main mechanism responsible for the continuous-wave (CW) laser operation at 2.8 µm in Er^{3+}. This phenomenon (the so-called "two-to-one" process) provides two photons at the laser wavelength for each absorbed pump photon. When a large number of ions are involved in this process, the slope efficiency, η is twice that of Stokes, $\eta_{St} = \lambda_p/\lambda_l$, because the quantum efficiency $\eta_q = n_l/n_p$ of the pump photons converted into laser photons increases from 1 to 2 (λ and n are the wavelength and photon number of the laser and pump transitions, respectively). Direct pumping into the upper laser level, $^4I_{11/2}$, offers the highest slope efficiency of $^4I_{11/2} \rightarrow {}^4I_{13/2}$ laser transition up to 50%, exceeding the Stokes efficiency of 35% [Pol05].

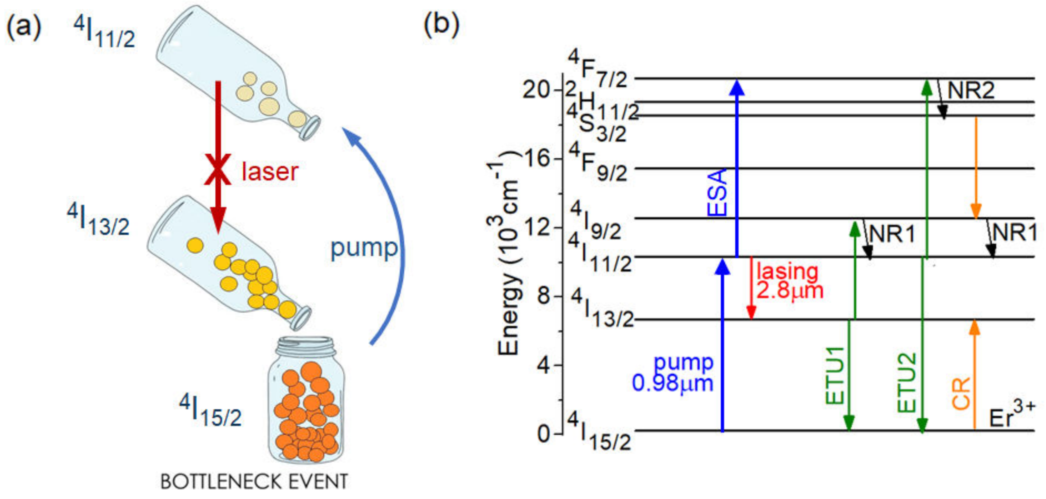

Figure I.29: Energy level scheme of Er^{3+} ions and possible laser transitions occurring in visible, near- and mid- infrared spectral range.

3 Materials for the efficient erbium mid-infrared emission

3.1 Criteria for erbium doped host matrices

The vibrations, or phonons, in a material can indeed influence the transparency of the material in the longwave limit. This phenomenon is known as phonon-photon coupling or phonon-induced transparency. In certain cases, when the energy of the photon matches the energy of a phonon mode, the presence of the phonon can modify the refractive index of the material at that particular energy. This modification can result in a transparency window in the absorption spectrum of material. Solid-state laser media materials generally have a *wide transparency range in the infrared*; as shown in Figure I.30

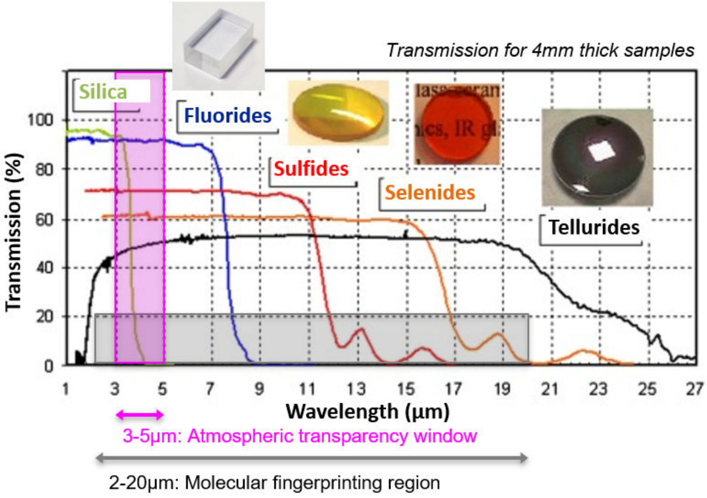

Figure I.30: Transparency ranges for several crystal families: silica, fluorides, sulfides, selenides, and tellurides. Le verre fluore https://leverrefluore.com/scientific-world/fluoride-glasses/

As previously discussed, the implementation of a 2.8 µm Er^{3+} laser is challenging owing to various energy-transfer processes that are highly dependent on the Er^{3+} doping level and the type of matrix used. The selection of a host matrix is also driven by *low phonon energy*, which is not present in commonly used garnet matrices such as $Y_3Al_5O_{12}$ (YAG). The high phonon energy of 800 cm^{-1} in YAG causes strong multi-phonon quenching of the upper laser level, $^4I_{11/2}$, resulting in fast decay and an upper-to-lower lifetime ratio of approximately 1:50 [Bag83, Geo91]. Figure I.31 provides a clear understanding of this concept.

When the energy gap decreases, there is a significant increase in the multiphoton non-radiative relaxation (MNR) rate, which is exponential in nature, as shown in Figure I.31(b). This indicates that the MNR is prevalent when the energy gap between the Ln^{3+} 4*f* states is small. In such systems, a new relationship between MNR rate and the number of phonons (p) was established, Figure I.31(c). The value of p is determined by dividing the energy gap by the highest phonon frequency ($h\omega_{\text{max}}$) of the host lattice. The results indicate that this process becomes dominant for electron de-excitation when the energy gap is less than five phonons. This "five phonons" criterion has now become a standard way to evaluate the relaxation probability of Ln^{3+} $4f$ state. [Shi22]. The phonon energies of certain host matrices are listed in Table I.3.

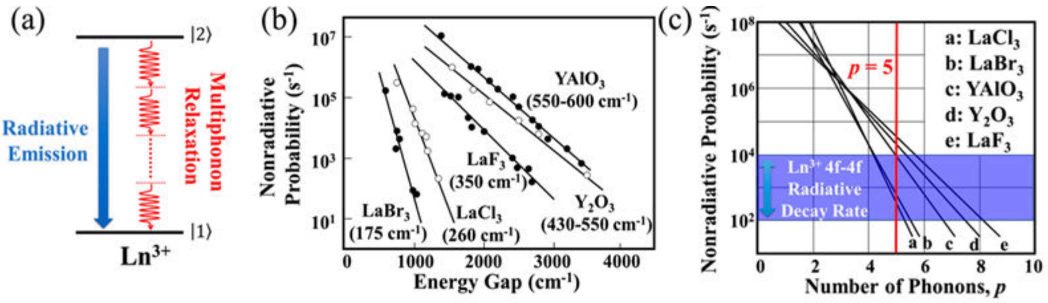

Figure I.31: (a) Graphical representation of the non-excitation of the Ln^{3+} electron state via the radiation or MPR process; (b) NR relaxation probabilities of the Ln^{3+} $4f$ states in various crystal lattices as a function of the energy gap to the next lower-lying state: (c) Plots of these exponential lines as a function of the number of phonons involved in the relaxation process. The purple-blue region denotes the range of typical rates of radiative decay of Ln^{3+} $4f \rightarrow 4f$ transitions in crystal lattices. Image is taken from [Shi22].

The second approach to reduce the self-termination effect is to use materials with *high Er^{3+} doping concentrations* to improve the efficiency of the ETU ($^4I_{13/2} + {^4I_{13/2}} \rightarrow {^4I_{15/2}} + {^4I_{9/2}}$), which quickly depletes the terminal level in favor of the emitting laser level and allows the population to be effectively inverted. However, the multi-phonon relaxation from the $^4I_{9/2}$ state following ETU produces a significant amount of heat, making the 2.8 μm Er^{3+} laser vulnerable to thermal and thermo-optic effects [Pol05].

Another problem related to the *thermal-mechanical properties* is the reduction of thermal conductivity in heavily doped active media. In dielectric materials, such as laser gain media, the thermal conductivity is mainly determined by phonon propagation. A heavy doping ion replacing the host-forming cation acts as a phonon-scattering center. Consequently, the thermal conductivity can be significantly reduced by increasing the concentration of doping ions [Kra22]. As shown in Figure I.32, this effect becomes stronger as the atomic mass difference between the doping ion and the host cation increases. In sesquioxides, the lightest host cation Sc^{3+} exhibits a large mass difference compared to the substituting ion Yb^{3+}, leading to a significant reduction in thermal conductivity from from 17.3 W/(m·K) in the undoped host to about 7 W/(m·K) at an Yb-density of $8 \cdot 10^{20}$ cm^{-3} (~2.4 at.% Yb) can be observed. In contrast, for Lu^{3+} ions being similar in term of masses and ionic radii to dopant ions (Yb^{3+}, Er^{3+}, Tm^{3+} and Ho^{3+}

[Koo12]), the thermal conductivity remains nearly constant. Thus, sesquioxides offer favorable thermal conductivity, even at high doping concentrations, which qualifies them as perfect candidates for high-power solid-state lasers.

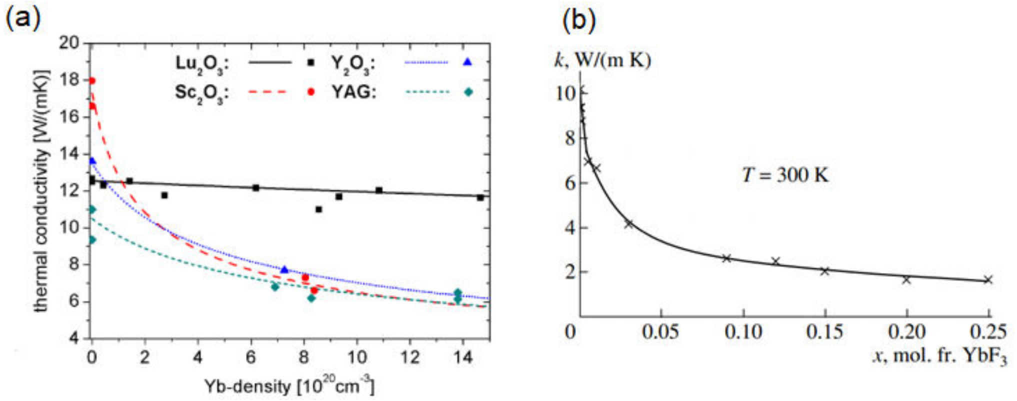

Figure I.32: Thermal conductivity *versus* Yb^{3+} doping concentration for some crystals of (a) sesquioxides and garnets between 0 and $15 \cdot 10^{20}$ cm^{-3} (corresponding to Yb:YAG (10.9 at.%), Yb:Lu_2O_3 (5.3 at.%), Yb:Sc_2O_3 (4.5 at.%), and Yb:Y_2O_3 (5.6 at.%); and (b) fluorides, namely in CaF_2 crystal. Images are taken from [Pet11, Pop08].

In the case of fluorides, the effect of high doping is achieved through the clustering effect in fluorite-type crystals. The distance between the dopant ions is reduced in clusters, which can be advantageous for ion-ion energy transfers. In CaF_2, for example, the clusters appear even at low Er^{3+} doping levels of few at. % (above 0.1at.% Er^{3+}). Therefore, efficient laser emission at 2.8 μm can be achieved at lower Er^{3+} doping concentrations without significantly sacrificing thermal conductivity. Another advantage of fluorides is their low refractive index and negative thermo-optic effect. A *low refractive index* benefits high stimulated emission cross-sections and a low laser threshold. A *negative thermo-optic coefficient, dn/dT* compensates for the thermal lensing effects that appear in most laser materials at a high pump power [Mon13]. This makes the laser resonator more stable with diode pumping, without requiring of additional compensating optics.

In conclusion, we summarized the key criteria for a host matrix for implementing an Er^{3+} laser operating at a wavelength of 2.8 μm:

- Broad transparency range;
- Low phonon energy, which ensures a relatively long luminescence lifetime τ_{lum} of the upper laser level, $^4I_{11/2}$;
- High Er^{3+} doping concentrations to force the ETU1 process depleting the lower laser level, $^4I_{13/2}$, and refilling the upper one, $^4I_{11/2}$;
- High thermal conductivity as energy transfer processes in Er^{3+} are accompanied by strong heat release;
- Low refractive indices providing high stimulated emission cross-sections;

- Negative thermo-optic coefficient, which compensates the thermal lensing effect.

3.2 State-of-the-art: 2.8 µm Er bulk lasers

3.2.1 Host matrices

Robinson and Devor reported the first observation of laser action at a wavelength of 2.8 µm originating from the $^4I_{11/2}\rightarrow{}^4I_{13/2}$ transition in Er^{3+} in 1967. Their study focused on energy transfer from Er^{3+} to Tm^{3+} in a CaF_2:ErF_3:TmF_3 crystal [Rob67]. The introduction of Tm^{3+} ions was aimed at decreasing the lifetime of the $^4I_{13/2}$ state owing to non-radiative energy transfer from Er^{3+} to Tm^{3+}. This transfer was previously investigated and documented by Johnson *et al.* [Joh72]. Laser emission was achieved at room temperature, and the threshold was reported to be 10 J. Shortly thereafter, in 1975, Zharikov *et al.* first demonstrated laser emission in the mid-infrared at 2.94 µm in an Er^{3+}-doped YAG crystal [Zha75]. Most of the literature prior to 1994 was devoted to flashlamp-pumped Er:YAG (2.94 µm) and Er:YSGG (2.8 µm) lasers. To date, solid-state Er lasers relying on the transition of $^4I_{11/2} \rightarrow {}^4I_{13/2}$ in the 3 µm spectral region have been widely studied in various host matrices such as garnets, fluorides, sesquioxides, aluminates and etc. Figure I.33(a) summarizes the highest output slope efficiencies of ~3 µm Er lasers over the last 33 years (1990 – 2023) in the CW regime.

- **Oxide-based matrices (garnets, sesquioxides and aluminates)**

Being a “classical” host matrix for laser media, garnets have been extensively investigated for Er^{3+} doping, particularly $Y_3Al_5O_{12}$ (YAG). Owing to their excellent thermal conductivity and thermo-optical properties, garnet crystals have been demonstrated as promising candidates for high-power lasers. Nevertheless, the high phonon energy of 800 cm^{-1} increases the nonradiative relaxation, reducing the lifetime of the $^4I_{11/2}$ level. To achieve a continuous population inversion, a high concentration of Er^{3+} ions (50 at. %) is needed for the energy-transfer upconversion effect (ETU). However, this high doping concentration results in unfavorable conditions for continuous-wave (CW) operation because of the high thermal density in the crystals resulting from significant absorption. Consequently, Er:YAG lasers are typically operated in the quasi-continuous-wave (QCW) regime. Only a few reports exist on CW 2.94 µm Er:YAG lasers, because they require better thermal management. For example, Chen *et al.* demonstrated a diode-pumped CW 2.94 µm laser based complex crystal composed of Er:YAG bonded to undoped YAG generating 1.15 W of output power with a slope efficiency of 34% [Che99]. To reduce the probability of NR relaxation from the $^4I_{11/2}$ level, the emphasis has shifted to “mixed” garnet analogous to YAG such as Y/GSGG [Sto92, Din94, Hu19], Ga/Y/LuGG [Din94, You18, You19], GAGG [Sve18], which exhibit lower phonon energies and offer inhomogeneous spectral broadening owing to the partial or full substitution of Al^{3+} ions by Sc^{3+} or Ga^{3+}, resulting in distortion of the crystal lattice. Moreover, calcium niobium gallium garnets (CNGG) and calcium lithium niobium gallium garnets (CLNGG) are promising alternatives to conventional ordered garnet crystals similar to YAG because of their lower melting point and disordered structure. The lower melting point allows for the easier production of high-quality, large-sized crystals using the Czochralski method. The disordered structure results in inhomogeneous broadening of the spectral bands, making it suitable for ultrashort pulse generation. Very recently, Normani *et al.* reported the first laser operation at 2.8 μm in Er:CLNGG crystal [Nor23b].

Among the various oxide-based materials, cubic sesquioxides A_2O_3 (where A stands for Y, Sc, Lu or their combination) were found to be very suitable for Er^{3+} doping with the aim of ~2.8 μm laser operation [Li12]. These crystals provide good thermal properties such as high thermal conductivity with weak concentration-dependence and positive thermo-optic coefficients, low phonon (cf. Table 1.3) and easy doping with Er^{3+} ions in high concentrations. In addition, sesquioxides provide high crystal-field strength resulting in large total Stark splitting of the $^4I_{13/2}$ multiplet leading to structured but relatively broad emission bands [Tra10]. Using a high-brightness pump source (an optically pumped semiconductor laser, OPSL), Li *et al.* achieved an output power of 1.4 W at ~2.85 μm from an $Er:Lu_2O_3$ single-crystal laser operating with a slope efficiency as high as 36 %, while using a laser diode, the output was scaled up to 5.9 W at the expense of lower slope efficiency [Li12]. First laser operation in "mixed" sesquioxide crystal were published not in 2021, an Er^{3+}-doped $(Sc_{0.46}Y_{0.54})_2O_3$ crystal pumped at 970.5 nm by an OPSL delivered a maximum output power of 0.44 W with a slope efficiency of up to 19% in qCW regime [Hul21]. Very recently, a continuous wave output power of 579 mW with a slope efficiency of 16.6% was obtained in "mixed" sesquioxide crystal of $Er:(Gd,Sc)_2O_3$ [Hou23].

So far ~2.8 μm laser emission from Er^{3+} sesquioxide ceramics based on Lu_2O_3 [Ueh18, Yao20b] and Y_2O_3 [San11, Din22] has been also studied. Very recently, Yao *et al.* reported on a diode-pumped $Er:Lu_2O_3$ ceramic laser delivering 6.7 W at 2845 nm with a slope efficiency of 30.2 %, representing record-high results in terms of output power and efficiency. Er^{3+}-doped Sc_2O_3 transparent ceramics have been also reported [Heu18]. In framework of this PhD thesis, the record-highly efficient 2.8 μm laser based on "mixed" sesquioxide ceramics have been demonstrated [Bas21a, Bas22a].

- **Fluoride matrices**

Among the host matrices for Er^{3+} doping, fluoride materials, such as glasses and single-crystals, appear attractive for mid-infrared lasers. CW lasing on the $^4I_{11/2} \rightarrow {}^4I_{13/2}$ transition has been demonstrated in Er:ZBLAN glasses [San99, New21] and $Er:LiYF_4$ [Jen96, Wys97 and Der00], $Er:BaY_2F_8$ [Pol96], $Er:KY_3F_{10}$ [Bas21b], $Er:CaF_2$ [Lab02], $Er:SrF_2$ [Bas06], and $Er:BaF_2$ [Nor23a] single-crystals. Wyss *et al.* reported on an $Er:LiYF_4$ laser operating at 2809 nm with a record-high slope efficiency of 50% well exceeding the Stokes limit and evidencing efficient ETU for optimized Er^{3+} doping [Wys97]. Dergachev *et al.* reported on power scaling of a diode-pumped Er:$LiYF_4$ laser delivering up to 1.8 W at ~2810 nm at the expense of a lower slope efficiency of 13%. Among the above-mentioned fluoride crystals, Er^{3+}-doped CaF_2 attracts attention due to a unique combination of high thermal conductivity, broadband emission properties and efficient ETU even at low doping levels [Lab02]. This crystal features a very strong clustering of rare-earth dopants (including Er^{3+} ions) already for >0.5 at.% doping leading to a significant inhomogeneous spectral line broadening resulting in smooth and broad spectral bands (a glassy-like spectroscopic behavior) and efficient energy-transfer processes among the clustered dopants [Ren08, Pet08]. Being the pioneering laboratory, the first tunable CW Er:CaF_2 laser has demonstrated in CIMAP [Lab02].

CaF_2 belongs to the family of divalent metal fluorides, MF_2 (where M = Ca, Sr, Ba, Cd, or Pb). Compared to CaF_2, other MF_2 crystals are less studied for RE^{3+} doping but they are also attractive as laser host media as they benefit from either a lower melting point, or better thermal properties, or lower phonon energies. Fluorite-type crystals can also form substitutional solid-solutions $(M1_{1-x}M2_x)F_2$ for the entire range of $0 < x < 1$ [Fed05, Pop21 and Kuz20]. For such “mixed” compositions, the melting point is expected to decrease further as compared to the parent compounds [Kli08]. An additional spectral broadening is also expected due to the compositional disorder. The growth and laser operation of some RE^{3+}-doped “mixed” fluorite-type crystals were reported mainly focusing on $(Ca,Sr)F_2$ [Dou10, Lui18 and Ves20]. Liu *et al.* realized an efficient CW laser performance of a diode-end-pumped Er:CaF_2-SrF_2 crystal with an output power of 712 mW and a slope efficiency of 41.4%. To date, this is the record high slope efficiency ever achieved for Er lasers emitting at a 2.8 μm wavelength, based on MF_2-type crystals. Within the scope of this thesis, the first laser generation has been demonstrated in several fluorite-type crystals, namely in Er:KY_3F_{10} [Bas21b], Er:BaF_2 and “mixed” Er:$(Ba,Sr)F_2$ [Nor23a] single-crystals.

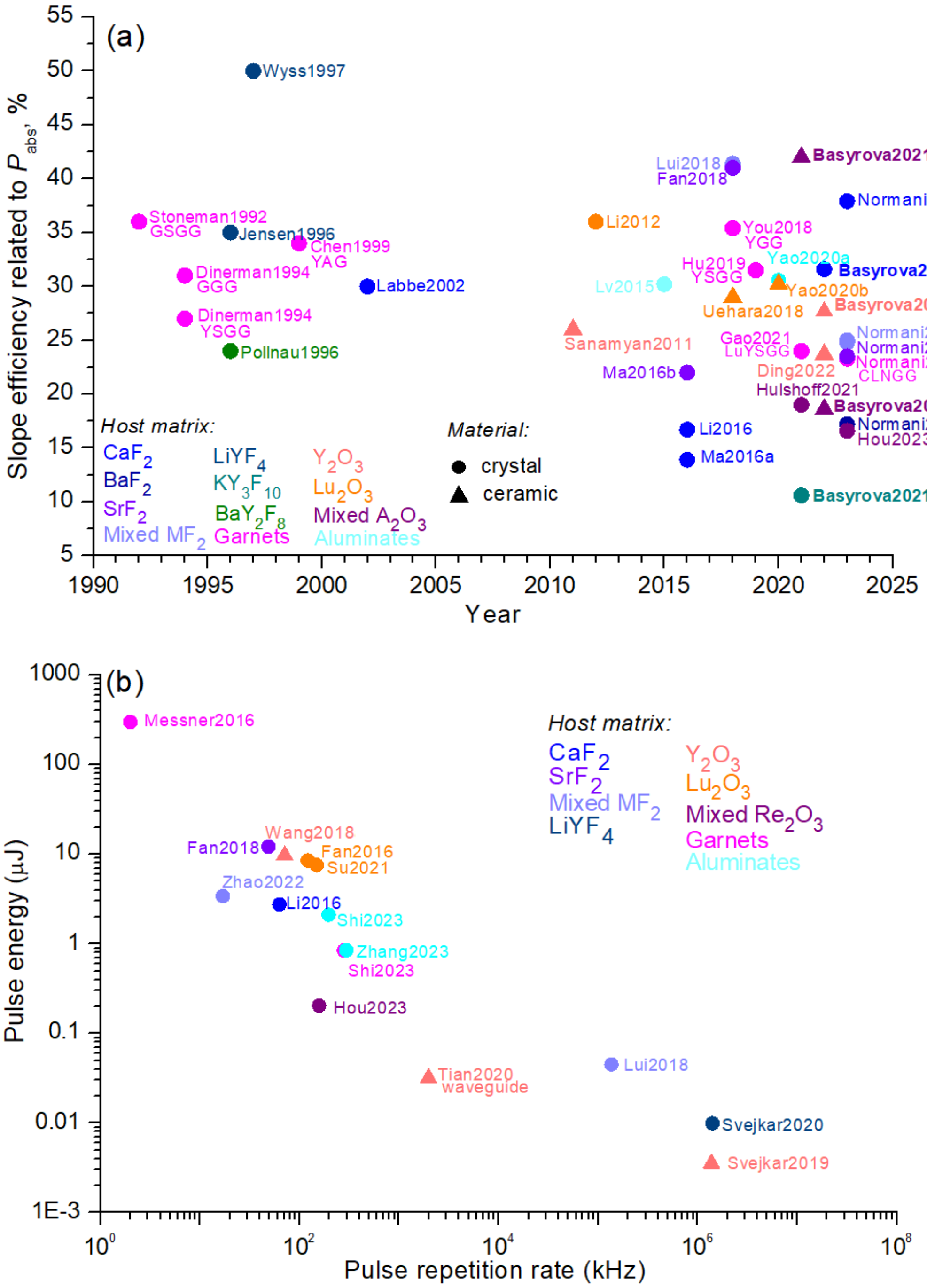

Figure I.33: State-of-the-art of Er^{3+} lasers emitting at 2.8 µm: (a) Evolution of the highest output slope efficiencies over the last 33 years (1990 – 2023) in CW regime; (b) Q-switched (QS), Q-switched mode-locked (QML) and mode-locked (ML) Er laser reported very recently. Different colors indicate the material of host-matrix and symbols the type of material: (●) – crystals, (▲) – transparent ceramics. Shown references: Stoneman1992

[Sto92]; Dinerman1994 [Din94]; Pollnau1996 [Pol96]; Wyss1997 [Wys97]; Chen1999 [Che99]; Labbe2002 [Lab02]; Sanamyan2011 [San11]; Li2012 [Li12]; Lv2015 [Lv15]; Fan2016 [Fan16]; Ma2016a [Ma16a]; Ma2016b [Ma16b]; Li2016 [Li16]; Messner2016 [Mes16]; Lui2018 [Liu18]; Fan2018 [Fan18]; You2018 [You18]; Uehara2018 [Ueh18]; Hu2019 [Hu19]; Svejkar2019 [Sve19]; Svejkar2020 [Sve20]; Tian2020 [Tia20]; Yao2020a [Yao20a]; Yao2020b [Yao20b]; Gao2021 [Gao21]; Hulshoff2021 [Hul21]; Su2021 [Su21]; Basyrova2021a [Bas21a]; Basyrova2021b [Bas21b]; Zhao2022 [Zha22a]; Ding 2022 [Din22]; Basyrova2022a [Bas22a]; Basyrova2022b [Bas22b]; Basyrova2022c [Bas22c]; Normani2023a [Nor23a]; Normani2023b [Nor23b]; Hou2023 [Hou23]; Shi2023 [Shi23]; Zhang2023 [Zha23].

3.2.2 Perspertives of ultrashort pulse generation

The use of ultrashort mid-IR pulses is essential in medical procedures, particularly for tissue removal with 3-µm lasers. As discussed earlier in Section 1, these pulses facilitate quick ablation or cutting processes, preventing thermal effects and shock wave propagation, and avoiding plasma formation or ionizing radiation effects. Such pulsed lasers are especially useful for PIRL scalpels.

Until now, pulsed Er lasers operating at 2.8 µm have primarily been demonstrated in Q-switched and Q-switched mode-locked modes using flash lamp or diode as a pump source. These lasers can produce pulse energies ranging from 5 to 300 mJ with pulse durations of up to sub-100 ps. Figure I.33(b) provides an overview of the recently demonstrated pulsed 2.8 µm Er laser. Svejkar *et al.* achieved the shortest pulse duration at 2.8 µm in bulk Er^{3+}-doped fluoride materials with their SESAM mode-locked compact Er:YLF laser, which produced picosecond pulses of 72 ps and a high repetition rate of 1.41 GHz with a mean energy per pulse of 9.9 nJ. Liu *et al.* also demonstrated a Q-switched mode-locked laser with their $Er:CaF_2-SrF_2$ laser, which had a repetition rate of the Q-switched envelope of 4.17 kHz and mode-locked pulses in the Q-switched pulse envelope with a repetition rate of 136.3 MHz and an estimated duration of approximately 1.78 ns. Among the oxide based lasers, best results have been achieved by Svejkar *et al.* in compact passively Q-switched mode-locked $Er:Y_2O_3$ laser. The pulse duration of 86 ps with a repetition rate of 1.38 GHz, pulse energy of 3.55 nJ and the corresponding peak power at 2.74 µm of 12 W were achieved [Sve19].

For further development of ~3 um lasers in order to generate the ultrashort pulses, we aimed to study the materials exhibiting the inhomogeneous spectral broadening. Since the laser crystals can be divided into simple materials and "mixed" systems based on their spectroscopic properties, they can have identical active centres and homogeneously broadened lines, whereas in "mixed" systems inhomogeneous line broadening occurs due to structural distortion. There several mechanisms of inhomogeneous broadening exist: (i) structural disordering induced by the multisite nature of the material; (ii) compositionally "mixed" solid-solutions; (iii) crystals offering the strong RE ion clustering (so called "glassy-like" spectral behaviour). The some of these mechanisms can be combined to obtain additional inhomogeneous broadening. The schematic representation of the inhomogeneous spectral broadening mechanisms in crystals and transparent ceramics is shown in Figure I.34.

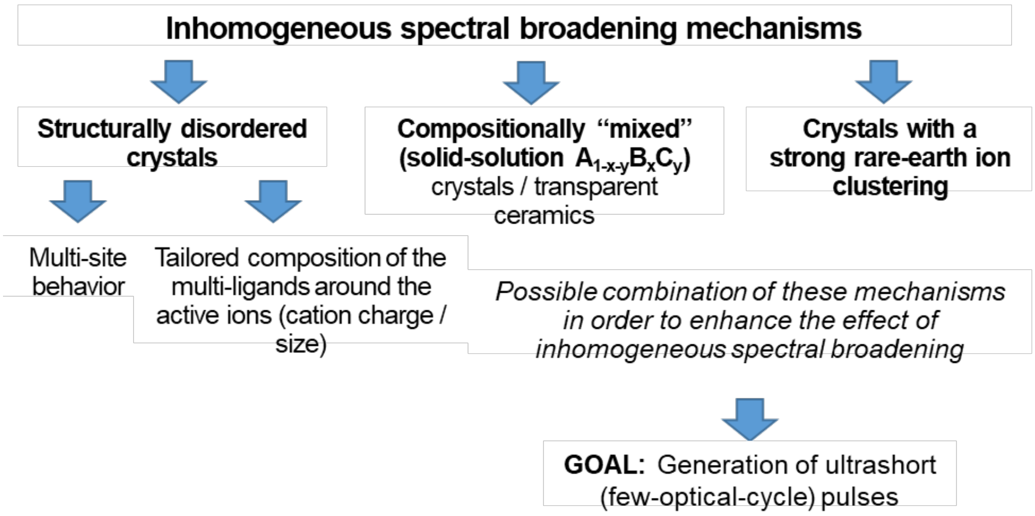

Figure I.34: Mechanisms of inhomogeneous spectral broadening in crystals and transparent ceramics.

3.2.3 Waveguide approach

In recent years, there has been a growing trend towards the development of compact high-brightness laser sources. One approach to achieve this is through the use of waveguide (WG) lasers and amplifiers, which serve as essential components in integrated photonics. They are of particular interest in mid-infrared sensing applications. Optical waveguides can be classified into two types based on their geometry: planar waveguides and channel waveguides. A planar waveguide comprises a thin active layer, usually ranging from a few micrometers to hundreds of micrometers thick, placed on a substrate and containing luminescent centers such as RE^{3+} ions. To enhance mode confinement, reduce propagation loss, and protect the waveguide surface, a cladding layer can be added. By exploiting the difference in refractive indices between the layer and substrate/cladding, optical modes can be guided vertically perpendicular to the plane of the layer. This technique offers better index control than thermal effects, such as thermal lensing, which can significantly impact mode formation in solid-state lasers.

Several methods are available for fabricating waveguide thin films, including Liquid Phase Epitaxy (LPE) [Fer99], Molecular Beam Epitaxy (MBE) [McF95], Pulsed Laser Deposition (PLD) [Gra16], and reactive co-sputtering [Ber11]. Channel waveguides can be created by microstructuring planar structures using techniques such as reactive ion etching [Ges10] or mechanical dicing [Kif19]. An alternative approach involves the direct formation of waveguides in bulk materials using femtosecond laser inscription [Tia20].

One of the most common ways to produce planar WGs based on single-crystalline layers is Liquid Phase Epitaxy growth well-developed in CIMAP for fluorides materials such as $LiYF_4$ and CaF_2. So far, single-crystalline oriented thin films of $LiYF_4$ doped with various rare-earth ions (RE^{3+}) such as Yb^{3+} [Bol13], Tm^{3+} [Loi18], Ho^{3+} [Loi18a], or Pr^{3+} [Sta13] were grown on bulk undoped $LiYF_4$ substrates using LiF as a solvent. In these LPE experiments, relatively low propagation losses (down to 0.2 dB/cm at ~1 μm [Bol13] and 0.11 dB/cm at ~2 μm [Bol12]) were achieved as well as efficient laser operation was demonstrated in these epitaxial films [Bol13, Sta13, Loi18, and Loi18a]. The possibility of incorporating high concentrations of RE^{3+} ions (up to 20 at. %) has been proven in the case of Yb^{3+} dopants [Bra21] and Tm^{3+} [Sou19], which is highly pertinent for the realization of efficient Er^{3+} ion-based lasers operating at 2.8 μm. To date, there are no reports on the fabrication of highly Er^{3+} doped $LiYF_4$ epitaxial layers featuring ~2.8 μm emission. Rogin and Hulliger described in general the growth of RE^{3+}-doped $LiYF_4$ epitaxial films with Nd^{3+} and Er^{3+} dopants at low concentrations (1–3 at.%) [Rog97]. To enhance the refractive index contrast between the substrate and the layer, optically "passive" Gd^{3+}ions (~10 at.% in the melt) were added to the films. For this, (101) and (100) oriented $LiYF_4$ substrates were used. However, in [Rog97], very little information was given about the Er:$LiYF_4$ films.

Epitaxial growth of CaF_2 thin films has not been studied extensively to date. The first studies involved the growth of underdoped CaF_2 films on semiconductor substrates (such as Si, GaAs, or InP [Fat84, Sch85 and Sin85]) by molecular beam epitaxy because of the similarity of the lattice constants of Si and CaF_2, which makes it suitable as a buffer layer for subsequent deposition. Later, RE^{3+}:CaF_2 (RE = Nd, Er, Yb or Pr) films were grown on (100)-oriented CaF_2 substrates by the MBE method; however, they were relatively thin. The use of liquid phase epitaxy (LPE) to grow Yb^{3+}- and Tm^{3+}-doped CaF_2 layers [Ren06, Bra19] and successful laser operation on Yb:CaF_2 thin films using planar waveguide geometry have also been reported.

4 Conclusion of Chapter I

The aim of this PhD study is to develop functional materials (laser gain media) for laser sources emitting at 2.8 µm based on low phonon energy matrices including fluoride single-crystals and epitaxial thin films, as well as transparent polycrystalline ceramics. By the development of laser materials, we understand both fabrication, in particular, the growth of single-crystalline layers by liquid phase epitaxy, as well as detailed characterization of spectroscopic properties essential for mid-infrared laser operation and for materials coming from external collaborations. In general, this PhD thesis aims at extending the family of existing materials providing efficient and low threshold laser action around 2.8 µm. In particular, a special attention is paid to the development of materials featuring inhomogeneous spectral broadening with broad and smooth emission bands around 2.8 µm which are of practical importance for broadly tunable and potentially femtosecond mode-locked lasers.

This aim is envisioned to be reached by addressing the following goals:

1. To elaborate heavily Er^{3+}-doped $LiYF_4$ single-crystalline layers by liquid phase epitaxy and to study their structure, morphology, vibronic and spectroscopic properties, as well as to assess their potential for the development of mid-infrared lasers. Moreover, the suitability of Er^{3+}-doped CaF_2 for the liquid phase epitaxy growth of waveguiding thin films will be explored.
2. To perform a detailed study of Er^{3+}- doped fluorite-type crystals MF_2 (where M stand for Ca, Sr, Ba and their combinations) focusing on the inhomogeneous spectral line broadening induced by rare-earth ion clustering, the effects of compositional disorder on the spectroscopic properties will be explored.
3. To demonstrate efficient laser operation of several Er^{3+}-doped fluoride single-crystals (MF_2 type, KY_3F_{10} and $Na_5Y_9F_{32}$). To study heat loading and thermal lensing in $Er:CaF_2$ crystals with different pumping schemes to demonstrate power scaling of $Er:CaF_2$ lasers at 2.8 µm.
4. To investigate Er^{3+}-doped compositionally "mixed" transparent sesquioxide laser ceramics in binary systems (Y_2O_3-Sc_2O_3, Lu_2O_3-Sc_2O_3 and La_2O_3-Y_2O_3) and a ternary one: (Y_2O_3- Lu_2O_3- La_2O_3). To study mid-infrared emission properties of Er^{3+} ions in such ceramics, inhomogeneous spectral broadening and to demonstrate first laser operation of these ceramic materials at 2.8 µm.

Chapter II

Materials and methods

1 Overview of the studied materials

Table II.1: Erbium-doped materials studied in the framework of this PhD thesis.

Crystal family	**Chemical formula**	**Crystal class (sp. gr.) & Optical property**	**Synthesis method**	**Source**
Epitaxial layers				
Fluorides	$LiYF_4$ 11 at.% Er (#1) * 7 at.% Er^{3+}, 5 at.% Gd^{3+} (#2) *	tetragonal ($I4_1/a$) uniaxial	LPE (LiF solvent)	CIMAP*
	CaF_2 11.25at.% Er *	cubic ($Fm\bar{3}m$) isotropic	LPE (LiF solvent)	CIMAP*
Crystals				
Fluorides	CaF_2, SrF_2 BaF_2 $Ca_{0.05}Sr_{0.05}F_2$ $Ba_{0.05}Sr_{0.05}F_2$ (5at.% Er)	cubic ($Fm\bar{3}m$) isotropic	Bridgman	CIMAP
	$Na_5Y_9F_{32}$ (0.22, 1.16, 2.0, 5.59 and 9.63 at.% Er)	cubic ($Fm\bar{3}m$) isotropic	Czochralski	CIMAP
	KY_3F_{10} (15at.% Er)	cubic ($Fm\bar{3}m$) isotropic	Czochralski	CIMAP
Transparent ceramics				
Sesquioxides	$(Er_{0.07}La_{0.10}Y_{0.83})_2O_3$ $(Er_{0.07}La_{0.05}Y_{0.25}Lu_{0.63})_2O_3$ La_2O_3 acted as a sintering additive	cubic ($Ia\bar{3}$) isotropic	Vacuum sintering	ICHPS RAS
	$Er_{0.14}(Sc_xY_{1-x})_{1.86}O_3$ (where $x = 0$, 0.125, 0.25 and 0.5) ZrO_2 used as a sintering additive	cubic ($Ia\bar{3}$) isotropic	Vacuum sintering	IE RAS
	$(Er_{0.07}Lu_{0.78}Sc_{0.15})_2O_3$	cubic ($Ia\bar{3}$) isotropic	Vacuum + HIP	ICM CAEP

* For the concentrations in the bath
** Grown by me

Collaborators providing transparent ceramics:

ICHPS RAS - G.G. Devyatykh Institute of Chemistry of High-Purity Substances of the RAS, Nizhniy Novgorod, Russi
IE RAS - Institute of Electrophysics, Ural Branch of the RAS, Ekaterinburg, Russia
ICM CAEP - Institute of Chemical Materials, Chinese Academy of Engineering Physics, China

2 Material elaboration

This section is devoted to the chemical aspects of the elaboration methods used to synthesize the materials studied in this PhD thesis. We consider single-crystal growth methods, namely the Czochralski and Bridgman techniques for the growth of bulk single-crystals, the Liquid Phase Epitaxy (LPE) technique for the growth of single-crystalline epitaxial thin films and transparent ceramic technology as an alternative approach for the fabrication of bulk laser materials.

2.1 Growth of fluoride single-crystals

Currently, there are three general approaches for the growth of bulk inorganic single crystals: growth from the melt, solution growth techniques also called flux growth and vapor phase deposition. Growth from the melt is the most used method and is based upon the solidification and crystallization of a melted material. The Czochralski (Cz) and Bridgman methods are the two most used melt-growth techniques. Fluoride single-crystals studied within this PhD have been elaborated in CIMAP laboratory by Dr. Abdelmjid Benayad.

2.1.1 Fluorination stage

To optimize the optical quality of the grown materials, it is preferable to use precursors of ultra-high purity. In this respect, the fluorination of oxides precursors are suitable alternatives to prepare the precursors for single-crystals and LPE growth due to their better purity (4N) and lower cost compared to fluoride precursors (Y_2O_3 instead of YF_3, for example). The fluorination of oxide precursors can be achieved through different methods. One approach involves a heat treatment under a gas flow of a fluorinating agent like hydrofluoric acid, HF(gas). Another method involves a chemical solution process, which is favored for safety reasons [Rig21].

The fluorination process occurs in presence of a large excess of molten ammonium hydrogen bifluoride (NH_4HF_2) solution as a fluorinating agent under mechanical stirring and heating at 180 °C for 20 h in a glassy-carbon crucible, following the chemical equation:

$$Y_2O_3 + 6NH_4HF_2 \rightarrow 2YF_3 + 6NH_4F + 3H_2O\ (g)\ (T = 180\ °C).$$

In addtion, this chemical equation can be complete by the chemical equations describing the decomposition of the NH4HF2 under heating:

$$\mathbf{NH_4HF_2} \rightarrow NH_4F + HF\ (g)\ \text{(under heating)}$$

$$NH_4F \rightarrow \mathbf{NH_3\ (g) + HF\ (g)}\ \text{(under heating)}$$

In the next step, the so obtained dry cake should be annealed at 650 °C during 4 h in an oxygen free controlled Ar atmosphere, in order to remove the residual

NH_4HF_2, NH_4F and moisture of the fluorinated precursors. By this way, the excess of NH_4HF_2 and NH_4F are vaporized and condensed on the cold wall of a water-cooled condenser, as shown Figure II.1.

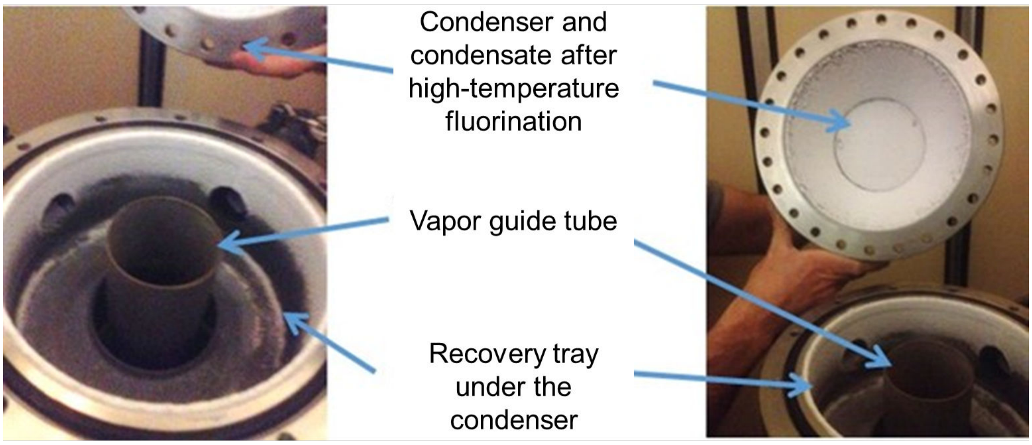

Figure II.1: Observation of the condenser on the upper part of the fluorination furnace after a fluorination at 650°C – the excess of NH_4F and NH_4HF is condensed onto the inner wall of the water-cooled condensor.

2.1.2 Czochralski (Cz) technique

The Czochralski (Cz) method, initially developed by Jan Czochralski in 1916 and later modified by various researchers, has become a widely adopted technique for growing large, high-quality single crystals for a broad range of commercial and technological applications. This method is particularly crucial for the production of single crystals employed in electronics, optics and materials science such as sapphire, silicon, germanium, fluoride and oxide crystals [Rub66, Shi01 and Dep06]. The Czochralski method offers advantages in terms of efficiency and scalability, enabling the production of large size single crystals with excellent quality in relatively short time frames compared with alternative growth methods. Figure II.2 shows a schematic representation of the Czochralski furnace which has been used in CIMAP for the growth of bulk fluorides crystals like $LiYF_4$ for example.

In the Czochralski process, a cylindrical crucible containing the starting material is heated using resistive or radiofrequency heaters until it fully melts. Once the material is molten, a seed crystal, typically a few millimeters in diameter, is gradually approached to the surface of the molten bath from above, creating a meniscus at the melt surface. After a small portion of the seed crystal dissolves and re-solidifies, it is slowly pulled out of the melt, often accompanied by rotation. As the seed crystal is withdrawn, the melt crytsallizes at the interface, continuing the growth of the seed, following the same crystallographic orientation, into a bulk crystal. Precise control of the crystal shape, especially the diameter and the neck, was achieved by carefully adjusting the heating power / temperature of the furnace, pulling speed and rotation speed during the growth process. Automatic diameter control mechanisms, which control the meniscus shape or employ weighting techniques with a crystal or melt, are typically employed. To regulate convective heat transfer and the distribution of species within the melt, which significantly influence the crystal quality, an appropriate combination of crystal and crucible rotation can be applied throughout the process in the most evoluted growth setups [Cap17].

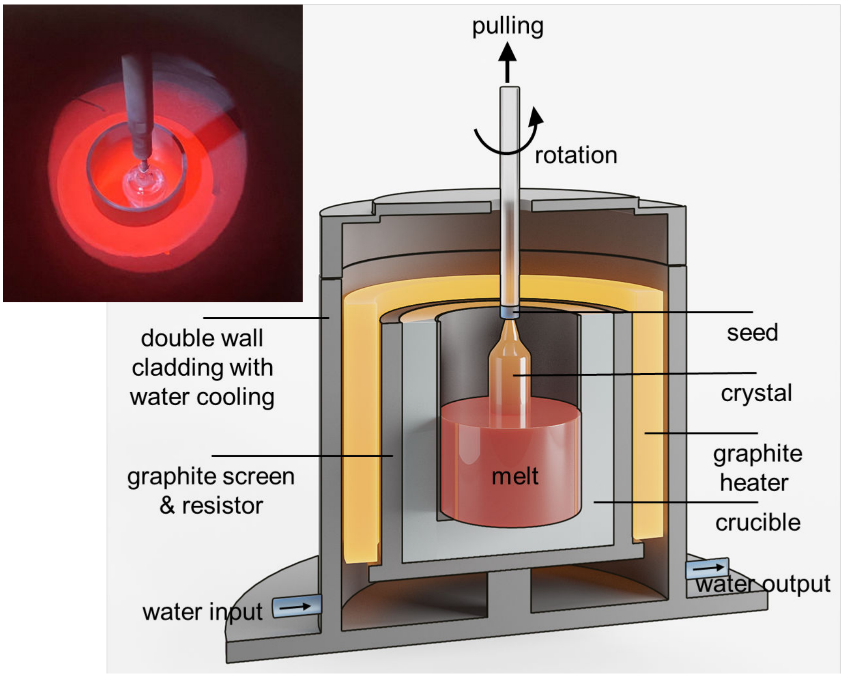

Figure II.2: Schematic representation of the Cz furnace; *insert* - a photograph of the undoped $LiYF_4$ crystal inside the furnace.

• Cz growth of undoped $LiYF_4$ substrates for LPE use

The high optical quality of $LiYF_4$ crystals used as a substrate for LPE growth were grown in CIMAP by the Cz method. The reagents LiF (Alfa-Aesar, optical grade 99.95%) and Y_2O_3 (Alfa Aesar, 4N-REO) in the molar ratio 52% LiF - 48% YF_3, according to the phase diagram of the LiF-YF_3 binary system, were used as raw materials. The oxide precursor Y_2O_3 was fluorinated, as it has been described previously in Sub-section 2.1.1. The growth process of bulk $LiYF_4$ crystal is carried out in a glassy carbon crucible under an oxygen-free Ar atmosphere at ~810 °C using a [001]-oriented seed of undoped $LiYF_4$. The pulling rate was fixed at 0.5-1 mm/h. The crystal growth duration was around 1 week. A photograph of Cz grown $LiYF_4$ crystal is shown in Figure II.3(a).

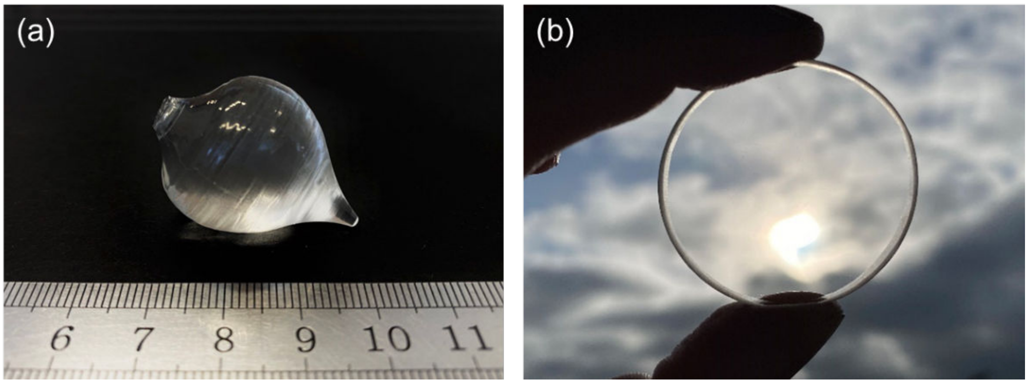

Figure II.3: (a) A photograph of an as-grown undoped $LiYF_4$ crystal; (b) a photograph of the substrate disk polished from both sides.

For the substrate preparation, even if the bulk crystals are grown on an oriented seed, the as-grown crystal ingot was further oriented post-growth along the (001) crystallographic plane using a Laue diffractometer (Thermo Scientific ARL EQUINOX) for a better accuracy on their orientations for the cutting stages. This method involves exposing a collimated X-ray beam to a crystal, resulting in a diffraction pattern that is dependent on the crystal's symmetry and orientation. In order to analyze the Laue diffraction pattern of the crystal, we used the CLIP4, also known as the Cologne Laue Indexation Program, an open-source software tool designed for the analysis and simulation of Laue X-Ray patterns. It offers a semi-automatic indexing feature, enabling the efficient determination of crystal orientations. Additionally, CLIP4 allows for further refinement of the indexing solution and provides calculations for the necessary rotations to reorientate the crystal accurately. Figure II.4 shows the simulated pattern superimposed on the measured pattern of an undoped $LiYF_4$ substrate. A slight deviation of the diffraction pattern obtained on the sample from the simulation can be noticed, it can be explained and solved by a better adjustment and accuracy of the simulation parameters in CLIP4, especially the X-ray beam size, the distance between the detector and the crystal area probed by the X-Ray beam, as well as the exact dimensions of the films detector of the camera, in order to fit better the simulated patterns with the real ones. Anyway, in this case this slight deviation with the simulated pattern has no incidence on the precision of the crystal orientation.

This substrate orientation was chosen mainly to access to the **π** and **σ** polarization in a waveguide configuration of the epitaxial layer. Furthermore, it appears that the growth of $LiYF_4$ crystals along the [001] axis, which is also the optical axis of the crystal, is preferential. Moreover, we can also notice that the thermo-mechanical properties of $LiYF_4$ in the ***a-b*** plane are isotropic, thus it is an advantage to perform good quality epitaxial layers by LPE. The substrates are then polished from both sides with good flatness ($\lambda/4$ in wave transmission), parallelism (about 10') and a very low surface roughness (<2 nm), as shown in Figure II.4(b).

The latter point is known to be a critical parameter for the growth of high optical quality RE^{3+}-doped $LiYF_4$ layers.

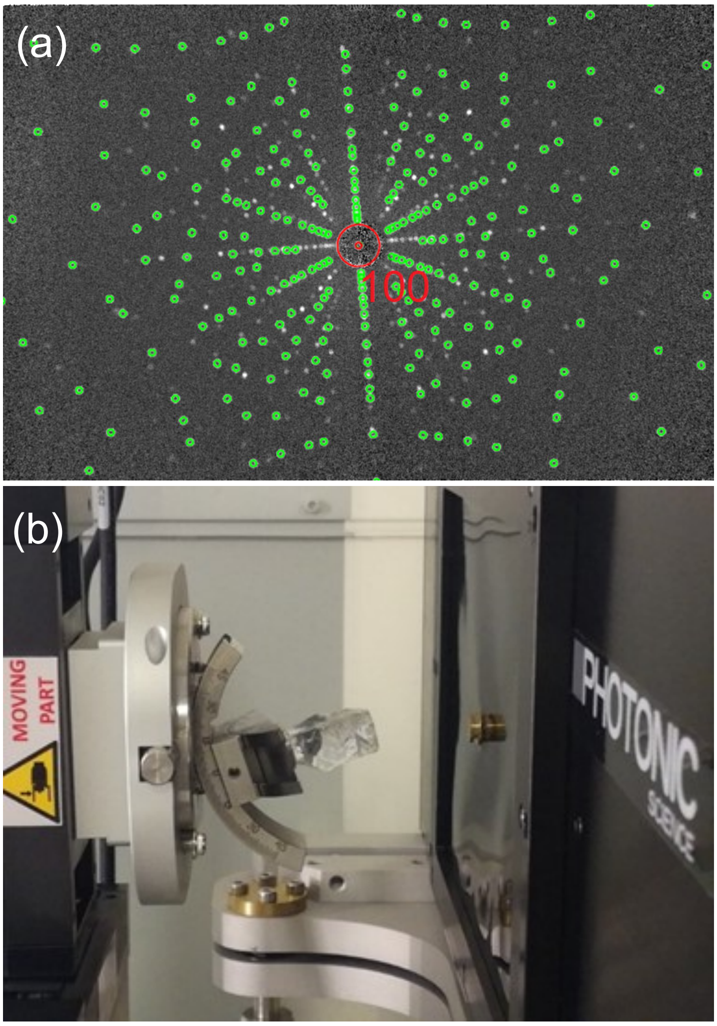

Figure II.4: (a) The Laue diffraction pattern of an undoped $LiYF_4$ substrate analyzed using the CLIP4 software. *Green circles* – simulated Laue pattern of the $LiYF_4$ crystal, *red circles* – position of the X-ray beam. (b) A $LiYF_4$ single crystal mounted onto a 3 circles goniometer support under orientation in front of the X-Ray beam and detector.

- ## Cz growth of $Er:Na_5Y_9F_{32}$ crystals

Single-crystals of $Na_5Y_9F_{32}$ ($5NaF{\cdot}9YF_3$) doped with 0.2 – 10 at.% Er^{3+} (with respect to Y^{3+}, initial composition) were grown by the Cz method using the composition 36%NaF – 64%$(Y,Er)F_3$ (mol.%). This composition is plotted on the phase diagram, Figure II.5. The letter **F** on the phase diagram indicates the phase we aimed to crystalize.

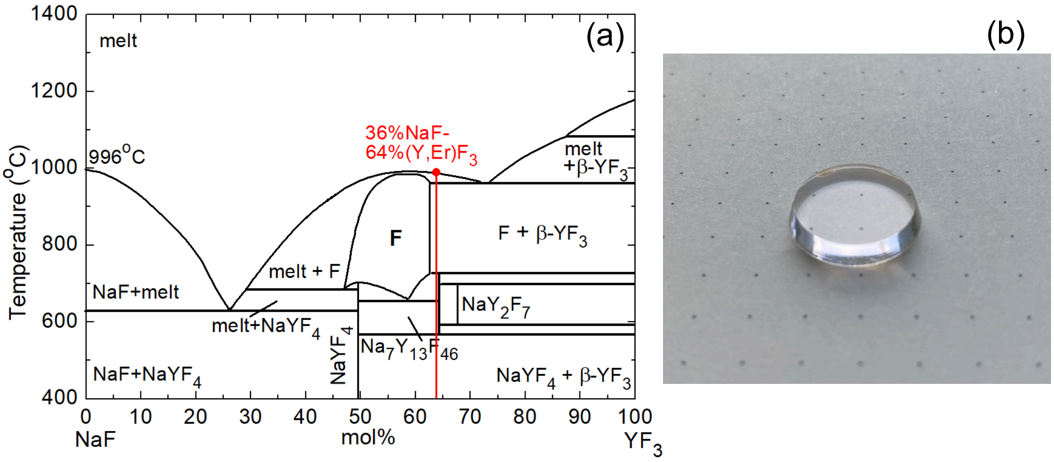

Figure II.5: (a) Phase diagram of the NaF – YF_3 binary system [Fed79]; (b) A photograph of a polished 2.0 at.% Er:$Na_5Y_9F_{32}$ crystal.

The growth charge was prepared from a stoichiometric mixture of NaF (purity: 2N), YF_3 and ErF_3 reagents. The rare-earth fluorides (REF_3) were obtained via fluorination of the corresponding oxides (RE_2O_3, 4N) using an excess of NH_4HF_2 solution under heating at 180 °C and the dry cakes were annealed at 650 °C for 4 h under Ar atmosphere to remove the residual NH_4F and moisture. The growth charge was well degassed in a vacuum furnace (10^{-5} mbar) by gradual heating up to 300 °C. The crucible was then heated to the temperature slightly higher than the melting point of $Na_5Y_9F_{32}$ (975 °C) to ensure that the raw materials are completely molten and under an Ar + CF_4 atmosphere to prevent oxyfluoride phase formation. For the crystal growth, an oriented seed from undoped $Na_5Y_9F_{32}$ was used. The pulling rate was 3 mm/h.

The as-grown crystals had a cylindrical shape with uniform cross-section (⌀12-15 mm, length: 20 - 25 mm). All the crystals, except the one with the highest doping (10 at.% Er^{3+}), were transparent and free of cracks and inclusions. The crystals had a rose coloration due to the Er^{3+} dopant. The actual Er^{3+} doping level was determined by atomic emission spectroscopy (AES): five crystals doped with 0.22, 1.16, 2.0, 5.59 and 9.63 at.% Er^{3+} were studied. E.g., for the 5.59 at.% Er^{3+}-doped crystal, the corresponding ion density N_{Er} was 8.23×10^{20} at/cm^3.

• Cz growth of 15 at. % Er:KY_3F_{10} crystal

The Czochralski (Cz) method using an induction heating furnace was used to grow a 15at.% Er:KY_3F_{10} crystal. The congruent melting temperature of the KY_3F_{10} compounds is approximately 1030 °C. Powders of KF, YF_3 and ErF_3 (purity 4N) were mixed according to the composition 22 KY - 78 (YF_3 + ErF_3) in molar % and placed in a glass-carbon crucible. The crucible was evacuated to 10^{-5} mbar and heated to 450 °C for 24 hours to remove oxygen impurities. Then high-purity gases argon (Alfagaz 1) and CF_4 were added until atmospheric pressure was reached and the crucible was heated to the melting temperature for several hours to prevent the formation of unwanted oxyfluoride phases. The crystal was grown using [100]-

oriented seed from undoped KY_3F_{10} at a growth rate of 2-4 mm/h. After growth the crystal was slowly cooled down to room temperature. The nominal Er^{3+} doping level was 15 at.% and the actual doping concentration (in bulk crystal) of N_{Er} determined by inductively coupled plasma mass spectrometry (ICP-MS) was 22.7×10^{20} cm^{-3} (segregation ratio was close to unity, ~0.98).

2.1.3 Bridgman technique

The Bridgman method, also known as the Bridgeman-Stockbarger method, is an old approach for crystal growth from a molten state. In this method, the crucible containing the molten material is moved along a temperature gradient in the furnace. The process is illustrated in Figure II.6.

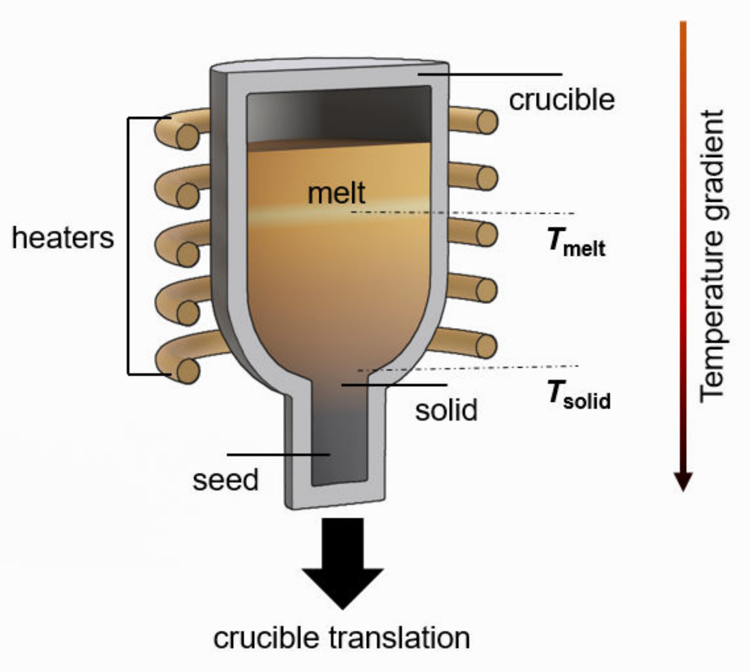

Figure II.6: Schematic representation of the vertical Bridgman technique.

The fundamental principle of the Bridgman method is a directional solidification, which is achieved by moving a molten material from the hot zone to the cold zone of the furnace. Initially, the material powder in the crucible is completely melted in the hot zone and comes into contact with a non melted seed crystal located in the neckof the crucible at the bottom. This seed is a single-crystal, which has been orientated and cored in bigger bulk crystal, allows the growth of a single crystal structure with a specific crystallographic orientation. Upon contact with the melt, a crystallization occurs on the seed crystal, creating a fresh interface for crystal growth. The crucible is then moved gradually to the cooler part of the furnace. When the temperature at the bottom of the crucible drops below the solidification temperature, crystal growth begins at the interface between the molten material and the seed crystal. The seed crystal acts as a catalyst, guiding crystal growth in a monocrystalline form along the desired crystallographic orientation. The movement of the crucible through the cold zone continues until the entire crucible has passed through it. As a result, the growth front is propagated along the crucible, such as the molten material solidifies progressively to form a solid single-crystal. Careful control of parameters such as the temperature gradient and transfer rate is necessary to ensure uniform and desired crystal growth. In this method, the shape of the crystal is imposed by the shape of the crucible, that can lead to stresses in the crystals. In addition, we can also note that it is possible to grow crystal by the Bridgman technique without using a seed, only by spontaneous crystallization. In this case, the crystals are often less stressed but it is required to orientate them post-growth by X-Ray diffraction.

- **Bridgman growth of Er:MF$_2$ (M = Ca, Sr, Ba) crystals**

The Er^{3+}:MF$_2$ (M = Ca, Sr, Ba) crystals were grown by the Bridgman method using graphite crucibles (⌀7-8 mm, height: 40 mm). The MF$_2$ (M = Ca, Sr, Ba) powders (purity: 4N, Sigma-Aldrich) and ErF$_3$ powder obtained by fluorination of the Er$_2$O$_3$ precursor (4N, Alfa Aesar). Five compositions were tested: M = Ca, Sr, Ba, Ca$_{0.5}$Sr$_{0.5}$ and Sr$_{0.5}$Ba$_{0.5}$. The doping level was 5 at.% Er^{3+} (with respect to M^{2+} cations). The optical quality and spectroscopic properties of RE^{3+}-doped MF$_2$ crystals are sensitive to even small pollution of oxygen / water in the growth chamber as they can lead to the presence of oxygen-assisted sites for the dopant ions or even formation of a translucent oxyfluoride phase. To avoid that, the growth chamber was sealed to vacuum (<10^{-5} mbar) and refilled with a mixture of Ar + CF$_4$ gases. The starting reagents were well mixed and placed into the crucible which was then heated slightly above (~30-50 °C) the melting point and the solution was homogenized for 3-4 h. The growth was ensured by a vertical translation of the crucible in a vertical temperature gradient of 30-40 °C/cm. After the growth was completed, the crystals were cooled down to room temperature (20 °C) within 48 h. The photographs of the grown crystals are shown in Figure II.7.

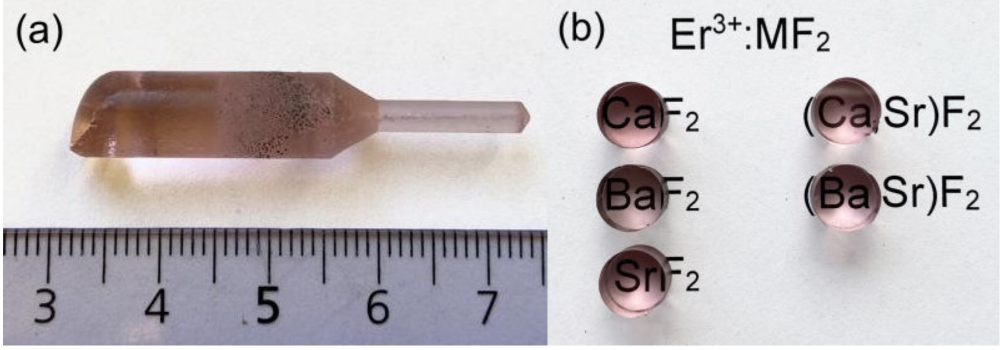

Figure II.7: Photographs of Er^{3+}:MF$_2$ crystals: (a) an as-grown Er^{3+}:CaF$_2$ crystal boule; (b) cut and polished Er^{3+}:MF$_2$ samples.

2.2 Growth of fluoride films by Liquid Phase Epitaxy

In the following paragraphs, the main principles, the kinetic aspects and experimental set-up of LPE growth of fluoride thin-films will be discussed. Fluoride single-crystalline epitaxial thin-films have been elaborated and characterized with the guidance of Dr. Gurvan Brasse.

2.2.1 Theoretical aspects LPE growth

Liquid-phase epitaxy (LPE) is a flux-growth method used to grow crystalline thin films based on the solubility of a solute in a solvent. This is based on the following principle: the solubility of the solute in the solvent increases with increasing temperature. This property allows the crystallization of the solute at temperatures well below its theoretical melting point. This method is particularly advantageous for growing films of materials with high melting points, such as oxides and fluorides. The driving force for epitaxial growth by LPE is directly correlated to the level of supersaturation of the solute in the solvent. When the substrate is introduced into the molten solution, it disrupts the supersaturated state, which is metastable, leading to the crystallization of the solute on the substrate as a seed. Successful management of the LPE process requires careful control of solution supersaturation, which requires a good understanding of the thermodynamics and growth mechanisms involved in the epitaxial growth. One of the most important point in the LPE process is the choice of the solvent and of the chemical composition of the initial mixture, in order to crystallize the desired phase at temperatures compatibles with the experimental setup. Moreover, the chosen solvent should also be the most inert as possible in front of the integrity of the setup.

- **Solvent selection in case of homoepitaxy RE^{3+}:CaF_2/CaF_2**

The choice of an appropriate solvent for LPE is influenced by several factors: (i) Phase diagram of the chemical system ('solute + solvent'): understanding the solubility behavior is crucial for successful crystal growth; (ii) Volatility: it is essential to select a solvent with low volatility to minimize evaporation during the process. This helps maintain a stable growth environment and prevent solvent loss; (iii) Working temperature: the ideal solvent should allow for the lowest possible working temperature. This is important for reducing the reactivity of the growth bath, limiting the risk of contamination, and protecting the experimental setup from damage; (iv) Solvent removal/cleaning: consideration should be given to the method of removing or cleaning the residual solvent left on the grown layer. An appropriate solvent facilitates the removal process without adversely affecting the crystal quality; (v) Chemical composition: The chemical composition of the solvent is critical for promoting efficient crystal growth and anticipating any chemical changes that may occur during the experiment.

The LPE process usually takes several days or even weeks, which creates problems in controlling evaporation and maintaining a constant chemical composition of the bath and saturation temperature depending on the chosen solvent. When working in a sealed chamber in a controlled atmosphere, controlling the composition of the bath during the experiment becomes difficult owing to the lack of control over mass loss in the crucible. While the control of solvent evaporation can be achieved in an open plant typically used for oxides, this approach is not suitable for the epitaxy of fluoride materials. This is primarily due to the high sensitivity of fluorides to oxygen contamination, which can lead to the formation of undesirable oxyfluoride phases, making them unsuitable for laser applications.

In this PhD study, lithium fluoride (LiF) was used as a solvent for the homoepitaxy of Er^{3+}:CaF_2 films on a CaF_2 substrate at temperatures lower than the melting point of CaF_2 (~1418 °C) [Nas61]. According to the phase diagram of the CaF_2–LiF binary system shown in Figure II.13, CaF_2 can be grown from a molten solution at temperatures lower than 900 °C. This solvent has previously been used for Tm^{3+}:CaF_2/CaF_2 epitaxy [Bra19]. In this study, it was shown that the LiF solvent does not cause corrosion and makes it possible to obtain crack-free thin films with good reproducibility over a wide range of growth temperatures.

Other possible solvents werer tested in order to select the appropriate one, namely calcium chloride ($CaCl_2$), magnesium floride (MgF_2) and sodium floride (NaF). The behavior of these solvents during epitaxial growth are described in Table II.2.

Table II.2: Characteristics of other solvents tested for the epitaxial growth of RE^{3+}:CaF_2/CaF_2 thin films

Solvent	**$CaCl_2$**	**MgF_2**	**NaF**
Solvent characteristics in the LPE experiment	• Very soluble in water, easy to clean with ultrasound • Extremely corrosive to metallic parts of the set-up (rod, valves, airlock…) • Intermediate compound CaFCl can crystallize	• Require high temperature (1100°C) for complete melting if the mixture and homogenization • Limited working temperatures (due to the material of the set-up parts: silica tube, substrate holder and stirrer made from Inconel alloy based on nickel-chromium) • Hybrid material of translation crane (alumina) is required.	• Partially soluble in water, facilitates the removal of residual solvent crystallized on the substrate; • Very viscous bath due to epitaxy at a temperature quite close to solidus (2-3°C). It is difficult to homogenize the bath.

2.2.2 Optimization of LPE growth conditions

The LPE growth process always begins with the determination of the epitaxial growth temperature. First, we determine the liquidus temperature T_{liq} for the studied composition from the phase diagram to approximate the range of the working temperatures (metastable zone), as shown in Figure II.8. The metastable zone is the temperature range (typically in the order of 0.5-1°C) where crystallization does not occur without seed, even if it is thermodynamically favorable. The width of the metastable zone, also called Ostwald-Meier zone, is mostly dependent of the nature of the solvent.

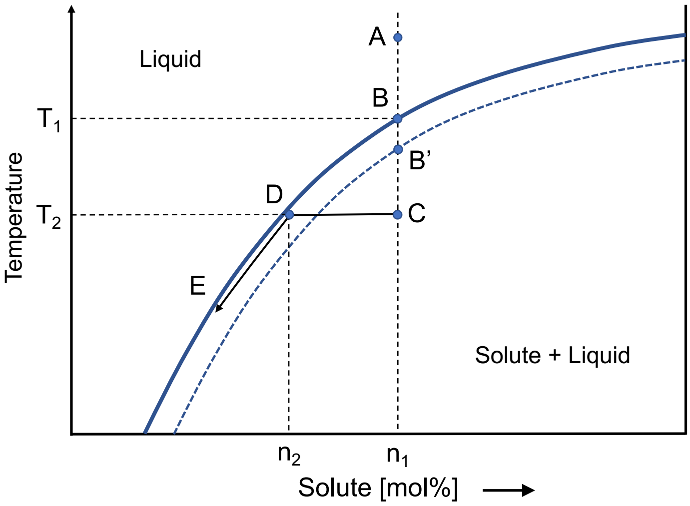

Figure II.8: Graphic illustration of the metastable zone in the Ostwald-Meier diagram for a solute/solvent system.

Let us consider the solubility curve in Figure II.8 in more details. Initially, the liquid solution contains n_1 mol% of solute and is maintained at a specific initial temperature (point A), corresponding the temperature well above the crystallization temperature (all components are in liquid state). As the system is cooled progressively to temperature T_2, the solution intersects the liquidus curve at temperature T_1 (point B), entering the two-phase region (solute-liquid) and becoming supersaturated with respect to the solute. This creates a driving force for the precipitation of the solute. The solute continues to crystallize until reaching point D on the liquidus curve, resulting in a decrease in the solute fraction from n_1 to n_2. Further cooling moves the solution from point D to point E if more solute is crystallized and so on.

It is important to note that in the absence of a seed crystal or other crystallization centers (such as crucible walls or impurities), spontaneous precipitation does not occur until the solution reaches point B' on the dashed line. The region between the liquidus line and the dashed line is known as the metastable or Ostwald-Miers (OM) region. Although the solution is supersaturated in the OM region, crystallization does not initiate spontaneously because the existing atomic clusters are still smaller than a critical size called r^*. However, when a substrate is introduced to the supersaturated solution remaining in the OM region, the substrate acts as a large nucleation center, allowing the excess solute to crystallize onto it. Therefore, only a slight supercooling below the saturation temperature T_1 is necessary to achieve controlled and gradual growth along the B-D-E liquidus curve. This characteristic is crucial in the context of Liquid Phase Epitaxy (LPE) [Rom06].

There are three modes to achieve supersaturation: ramp (or equilibrium) cooling, step cooling, and supercooling, as shown in Figure II.13. In ramp cooling, the epitaxial layer is grown as the temperature decreases at a constant rate (the substrate is introduced into the saturated bath at the equilibrium temperature, T_{liq}, and cooled at a constant rate for time t). In the step-cooling technique, the growth temperature was rapidly reduced to obtain large supersaturation (the substrate is soaked at a constant T_0 in a supersaturated bath at $T_0 = T_{\text{eq}} - \Delta T$). In the supercooling technique, the epitaxial layer is first grown from a highly supersaturated bath and a constant cooling rate is then imposed to force the crystallization on the substrate / the seed (an intermediate technique between ramp and step cooling). Being almost an equilibrium process, LPE growth requires a very low level of supersaturation on the order of a few Kelvin [Cap07].

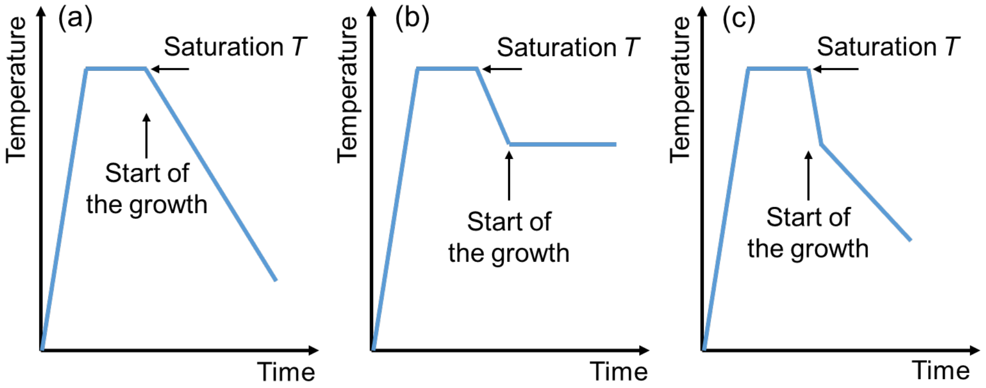

Figure II.9: LPE cooling modes to obtain supersaturation: (a) ramp cooling; (b) step cooling and (c) supercooling [Cap07].

In our point of view, the most effective ways to achieve supersaturation in the conditions of our experimental setup are the step cooling and supercooling modes, in the sense that it is difficult to determine accurately the exact equilibrium temperature. By this way, we are most often in a supersaturated regime when the substrate is dipped in the bath. Otherwise, when the temperature is too high, the substrate is significantly dissolved or slightly dissolved depending on the conditions, while there is neither dissolution nor crystallization on the substrate when we are in the considered equilibrium temperature.

We also attempted to grow films in the supercooling mode, however this growing regime is more difficult to control and could lead to the formation of polycrystalline layers or strong anarchic crystallization of a mixture of solvent and solute onto the top surface of the substrate, which is damageable for the targeting applications, due to a too high level of supercooling, as well as a too high growth rate. In our case this growth mode has been tested but did not lead to exploitable samples, even if such a process has already allowed the growth of good quality epitaxial layers of RE-doped $LiYF_4$ in the past.

To determine experimentally the apparent onset of crystallization temperature, we slightly decrease the temperature of the furnace towards the expected liquidus temperature and observe crystallization on the bath surface (visually, by the appearance of a thin crystalline film on the bath surface or by dipping a platinum wire into the molten bath as shown in Figure II.13). However, Pt wire is only suitable for a rough estimation of the crystallization temperature because of the different surface qualities and nature of the material from those of the substrates. Empirically, when the Pt wire is twisted after dipping, it means that the surface of the bath is solidified, and it indicates thus the lowest bound of the working temperatures range. When, a slight crystallization is observed onto the Pt wire it means that we are quite close the temperature of epitaxy. Nevertheless, let us note that the crystallization behaves quite differently onto the substrate and onto the wire.

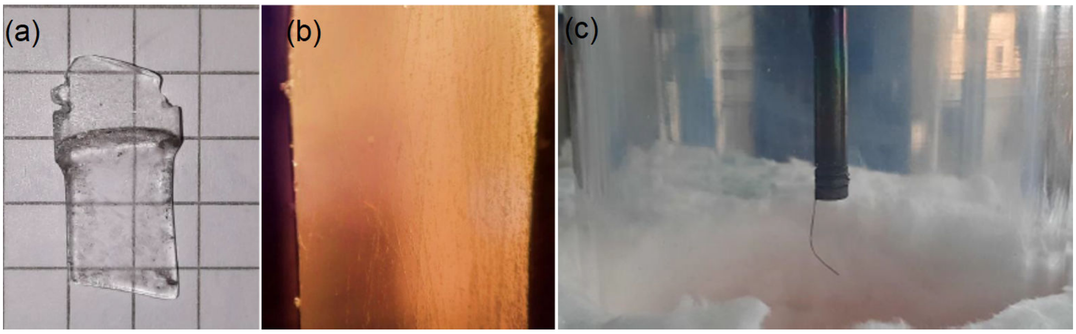

Figure II.10: (a) Substrate significantly dissolved, (b) Transverse observation in optical polarized microscopy of a slightly dissolved substrate, (c) The platinum wire fixed to the sample holder using for the empiric determination of the crystallization temperature, i.e equilibrium temperature.

Thus, the experimental process of homoepitaxial growth of the layers consists of the following stages:

(i) Growth of undoped substrates of $LiYF_4$ by the Czochralski method (Cz) in case of $Er:LiYF_4$ / $LiYF_4$ epitaxy, for $Er:CaF_2$ / CaF_2 epitaxy, it is reasonable to use high optical grade polished and oriented commercial substrates as they are available in different crystallographic orientations and dimensions for a reasonable price;

(ii) Crystal orientation, shaping / cutting and polishing of the required oriented substrates for Er:LiYF$_4$ / LiYF$_4$ epitaxial growth;
(iii) Epitaxial growth of Er: LiYF$_4$ and Er:CaF$_2$ layers on oriented substrates;
(iv) Epitaxy preparation / shaping / polishing to achieve the required dimensions and optical quality for potential laser waveguide applications.

2.2.3 Experimental set-up

Figure II.15 shows the scheme of the LPE setup. It consists of a two-zone vertical tubular furnace and a quartz tube (the growth chamber). The crucible is placed inside the quartz tube in the furnace zone presenting the lowest vertical temperature gradient. On top of the growth chamber, a sample exchange chamber is positioned. It allows to exchange the samples and if needed, to install a stirrer in maintaining the temperature and atmosphere of the growth chamber. The two chambers are separated by an electro-valve. Both the growth and the sample exchange chambers are first pumped to high secondary vacuum (10^{-5}-10^{-6} mbar) and then refilled with high purity Ar gas (Alfagaz 1). The latter is done to avoid the formation of unwanted oxyfluoride phases onto the surface of the bath and in the epitaxial layers.

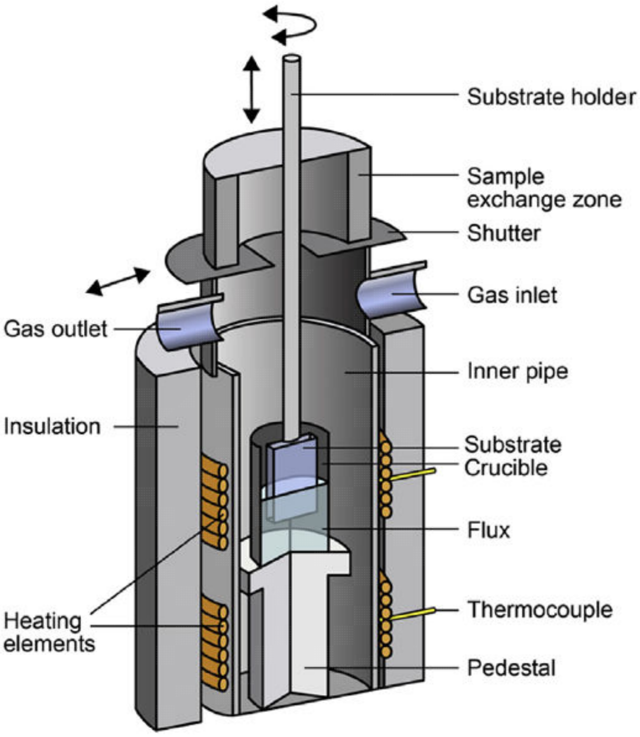

Figure II.11: Scheme of experimental set-up for Liquid Phase Epitaxy growth [Bra19].

2.2.4 LPE growth of highly doped Er^{3+}:$LiYF_4$ layers

Single-crystalline layers of $LiYF_4$ doped with Er^{3+} ions are grown on bulk substrates of undoped $LiYF_4$ by LPE. Lithium fluoride (LiF) is used as a solvent but in the case of $LiYF_4$, it is a self-flux compound because it enters also in the chemical composition of the solute. The initial composition of the growth batch is set to 73 LiF – 27 YF_3 (mol%), i.e., relatively far from the $LiYF_4$ peritectic which present the composition about 51mol.% LiF – 49mol.% YF_3, as shown on the phase diagram of the LiF – YF_3 binary system [Tho61] presented in Figure II.12. this composition has been chosen first to reduce the growth temperature and then to anticipate the vaporization of LiF that leads to a shift of the bath composition on the phase diagram. Let us indicate that a LPE run is conducted over few weeks, typically between 4 and 6 weeks, where the furnace is maintained in temperature, hence the significant vaporization of solvent. Two compositions of the layer are studied, singly doped with 11 at.% Er^{3+} (composition #1) and codoped by 7 at.% Er^{3+}, 5 at.% Gd^{3+} (composition #2, for the concentrations in the bath). In both cases, Er^{3+} and Gd^{3+} ions are introduced to substitute the Y^{3+} cations. The Gd^{3+} cations are optically “passive”, and they are added to enhance the refractive index contrast between the layer and the substrate.

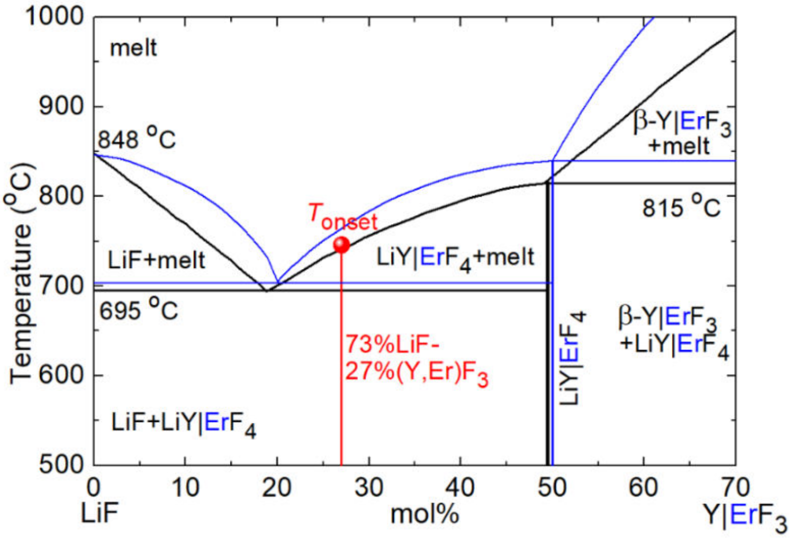

Figure II.12: Phase diagram of the LiF – YF_3 (*black*) and LiF – ErF_3 (*blue*) binary systems, *bold black line* - the $LiYF_4$ peritectic, *red line* - the composition selected for the LPE growth, *red circle* – apparent onset of crystallization. The indicated temperatures correspond to the LiF – YF_3 diagram.

The reagents used are lithium fluoride LiF (Alfa-Aesar, 99.5% optical grade) and rare-earth oxides RE_2O_3 (RE = Y, Gd, Er, Alfa Aesar, 4N-REO). The oxide precursors are fluorinated following the procedure described in Sub-section 2.1.1. This is done to obtain the REF_3 (RE = Y, Gd, Er) reagents with higher purity than that for the commercial ones. The starting powders, 73 mol% LiF – 27 mol% REF_3 (with REF_3 taken according to the doping levels described above), are placed in a glassy carbon crucible. The total mass of the growth bath is 160 g. The crucible is placed in the growth chamber which is well degassed to a pressure of 10^{-4} mbar and then refilled with pure Ar. The growth charge is superheated ~20 °C above the expected liquidus temperature (~741 °C) and kept at this temperature for a few hours under mechanical stirring using an Inconel alloy-based stirrer leading to homogenization of the melt. Then, the temperature is slowly reduced towards the expected liquidus temperature, and the apparent onset of crystallization is determined in a series of test growth experiments using small (lateral size: 15 × 5 mm^2) substrates. The growth duration for the test experiments is 30 – 45 min. The layer growth / substrate dissolution is directly observed on a polished side surface of the test substrate using an optical microscope.

After the apparent onset of crystallization is determined, larger substrates (thickness: 3 mm, lateral size: 30 (height) × 11 (width) mm^2) were used. The growth is performed at well controlled supercooling. The samples are placed vertically in the solution. During the growth, the sample is rotated at a speed of 10 rev / min in one direction. After the growth is completed, the sample is removed from the solution and slowly (during 20 - 40 min.) moved towards the sample exchange chamber. The sample is cooled to room temperature within minimum 1 hour. No annealing is applied to the as-grown epitaxies.

2.2.5 LPE growth of the Er^{3+}:CaF_2 layers

Single-crystalline thin films of calcium fluoride (CaF_2) doped with Er^{3+} ions were grown on (100) - oriented substrates of bulk CaF_2 by Liquid Phase Epitaxy using lithium fluoride (LiF) as a solvent. The molar composition 0.65% LiF – 0.35% CaF_2 was used. The molar ratio of ErF_3 was fixed to be 4.5 mol% which corresponds to an atomic ratio of 11.25 at.% with respect to Ca^{2+} considering the segregation coefficient (or sharing coefficient to be more rigorous), K_{seg} = 0.4 previously reported for Tm^{3+} in CaF_2 [Bra19]. The selected composition represented on the phase diagram is shown in Figure II.13. An expected growth temperature is ~850°C. The starting reagents were LiF (purity: >99.5%), CaF_2 (99.95%) and Er_2O_3 (4N). ErF_3 was obtained by fluorination of Er_2O_3 precursor. The fluorination process of rare-earth oxides is described in Sub-section 2.1.1.

In LPE experiments, good surface-state Er^{3+}:CaF_2 layers were obtained in the temperature range between 738.5°C and 741°C for growth durations between 40 and 70 min. In previous work of Renard *et al.* the Tm^{3+}, Er^{3+}:CaF_2 epitaxial layers were grown at higher temperature of 875°C using $CaCl_2$ as a solvent [Ren06]. Nevertheless, after experimenting with $CaCl_2$ as a solvent to grow CaF_2 epitaxial layers several times with various compositions, it was decided not to use this solvent because of its extremely high corrosive character against the metallic parts of the setup, as indicated in Table II.2. Indeed, only a few days and even a few tens of hours are sufficient to corrode the different metallic parts of the setup, especially the pulling cane, exchange chambers, primary pumping system, turbomolecular pump, and pressure gauge. The corrosion of the pulling cane also leads to damage to the vacuum seals, which ensures the sealing of the setup to prevent contamination of the growth atmosphere by moisture and oxygen.

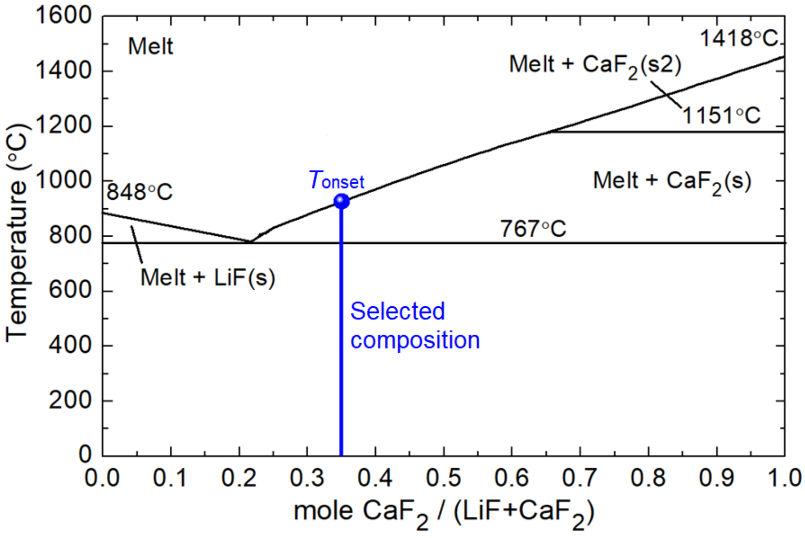

Figure II.13: Phase diagram of the CaF_2 – LiF binary system taken from [Bra19].

2.3 Transparent ceramic technology

Transparent ceramics belong to a class of inorganic materials that have both transparency and ceramic properties. In contrast to conventional ceramics, which are usually opaque, transparent ceramics allow light to pass through while retaining the desirable properties of ceramics, such as high hardness, high melting point and excellent resistance to deterioration, corrosion, and high temperatures. Scattering centers in ceramics result from refractive index variations caused by different factors. These include the presence of (1) grain boundaries; (2) residual pores, (3) secondary phases formed from sintering aids such as ZrO_2, SiO_2, LiF, and La_2O_3 which are usually localized near grain boundaries [Bal20, Bal21, Bas19 and Yan16], (4) multiple refraction on the boundaries, (5) impurities and (6) surface scattering due to roughness, as shown in Figure II.14. The formation of scattering centers is highly influenced by the fabrication process, so it is crucial to select a preparation/sintering method with carefully optimized parameters. The availability of technologies for producing transparent ceramics with near perfect optical homogeneity and microstructure could pave the way for ceramics with extremely low scattering losses. This, in turn, could lead to highly efficient ceramic laser gain media that would compete with single crystals.

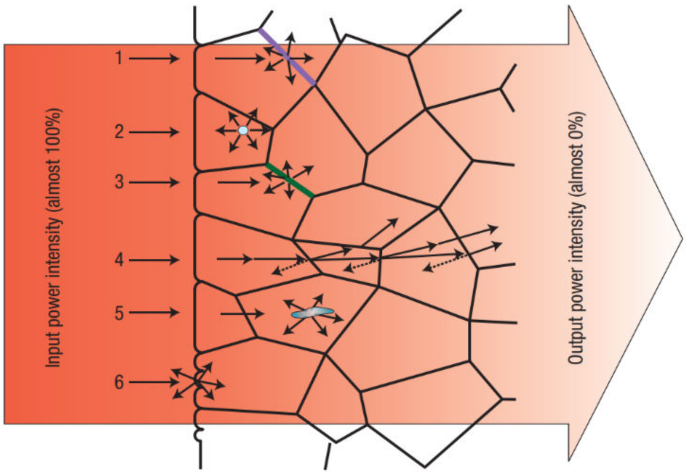

Figure II.14: A schematic representation of the microstructure of transparent ceramics and the light scattering centers: (1) grain boundary, (2) residual pores, (3) secondary phase, (4) double refraction, (5) inclusions and (6) surface roughness in ceramics [Ike08].

Transparent ceramics have emerged as a viable option for host materials to replace single crystal and glass technologies, especially for high-melting point materials such as sesquioxides. The growth of sesquioxide A_2O_3 single crystals is complicated because of their extremely high melting temperatures (over 2400 °C). In the most developed heat exchanger growth method (HEM), the use of rhenium (Re) crucibles frequently results in uncontrolled Re impurities and coloration of crystals [Pet08]. On the other hand, cubic sesquioxides are very suitable for the technology of transparent polycrystalline ceramics [Lu02, Lu03 and Tak05]. Their advantages include:

1. The lower synthesis temperatures (<1800 °C, depending on the method);
2. The well-preserved spectroscopic and thermal properties;
3. The easier fabrication of solid solution compositions $(A_{1-x}B_x)_2O_3$ [Jin17,Toc21];
4. Well-controlled doping at high levels and (v) size-scalable production. The main challenge is reaching low optical losses and good homogeneity.

- **Solid- solution (so-called “mixed”) compositions**

Solid solutions are phases in which one of the components of the composition retains its crystal lattice and the atoms of the other component are located in the lattice of the first component (solvent), changing its lattice parameter. Thus, a solid solution consisting of two or more components has one type of lattice and represents a single phase. Depending on the size ratio of the solvent atoms (component A) and the solute atoms (component B), the formation of solid solutions can occur in two ways: substitutional and interstitial solid solutions.

In a substitutional solid solution, the atoms of the solute element replace or substitute for the atoms of the solvent (matrix) metal in the crystal lattice. This occurs when the atomic sizes of the solvent and solute are relatively similar, allowing substitution without significant disruption of the crystal structure. The solute atoms occupy lattice positions that are normally occupied by solvent atoms, resulting in a homogenous solid solution.

In an interstitial solid solution, solute atoms occupy interstitial or empty spaces between the atoms of the solvent. This type of solid solution occurs when the solute atoms are significantly smaller than the solvent atoms. The small size of the solute atoms allows them to fit into the interstitial spaces in the crystal lattice without disrupting their overall structure.

There are several empirical rules, postulated by Hume-Rothery, which enable to qualitatively determine the order of the solubility limit and the existence of a solid solution:

- The crystal structures of the solute and solvent are identical.
- The atomic radius of the solute and solvent atoms do not differ by more than 15%.
- The solute and solvent do not differ greatly in electronegativity (typically within ±0.4).
- The solute and solvent have the same valence.

Substitutional solid solutions with a chemical formula $A_{1-x}B_x$ ($0 < x < 1$) are the most common type of solid solution. The crystalline structure remains largely unchanged, but the lattice parameter varies depending on the concentration of solute atoms (B). In some cases, the solute atoms are randomly distributed throughout the lattice sites, resulting in a disordered solution. This occurs when the two elements have similar crystalline structures and nearly identical atomic dimensions. However, in other instances, there may be a tendency towards order, leading to an ordered solution or atoms of the same type of form clusters, as illustrated in Figure II.15.

The value of x in $A_{1-x}B_x$ substituted solid solutions is not universally accepted when it is necessary to distinguish between a "doped" and a "mixed" crystal or solid solution. This distinction is crucial in heavily doped materials. From an optical point of view, this can be regarded as the minimum value at which a noticeable change in spectroscopic properties occurs. In highly doped crystals (on the order of tens of atomic percent), the addition of a doping element can have a significant effect on the lattice parameter and crystal field strength around the active ions, similar to what occurs in solid solution ("mixed") matrices.

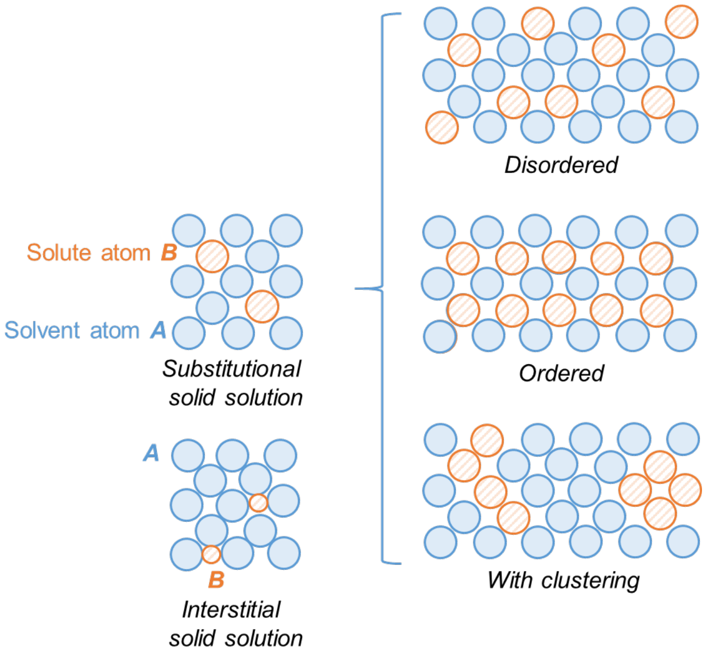

Figure II.15: Schematic representation of two types of solid solutions: substitutional and interstitial. The former is classified as disordered, ordered and with clustering.

- ### Fabrication of ceramics studied within this PhD thesis

The sesquioxide solid-solution ceramics studied within this PhD thesis were elaborated by our colleagues from the following institutes: Institute of Chemical Materials, Chinese Academy of Engineering Physics, China (ICM CAEP); Institute of Electrophysics, Ural Branch of the RAS, Ekaterinburg, Russia (IE RAS); and G.G. Devyatykh Institute of Chemistry of High-Purity Substances of the RAS, Nizhniy Novgorod, Russia (ICHPS RAS). Figure II.17 shows the ceramic production approaches of these groups.

As a rule, transparent ceramic technology includes three principal steps: synthesis of powders (precursors), green body formation and ceramic sintering as shown in Figure II.16.

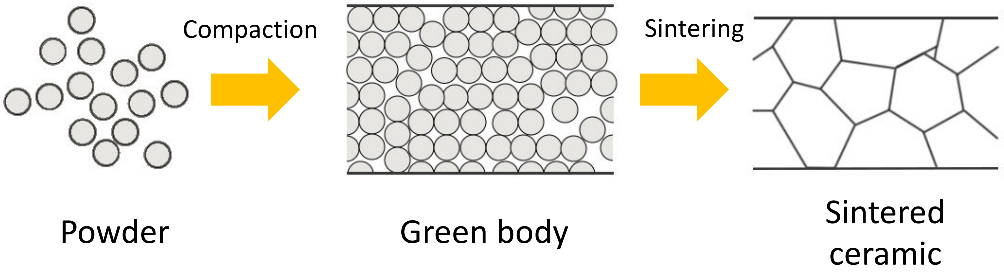

Figure II.16: Scheme of ceramic fabrication process.

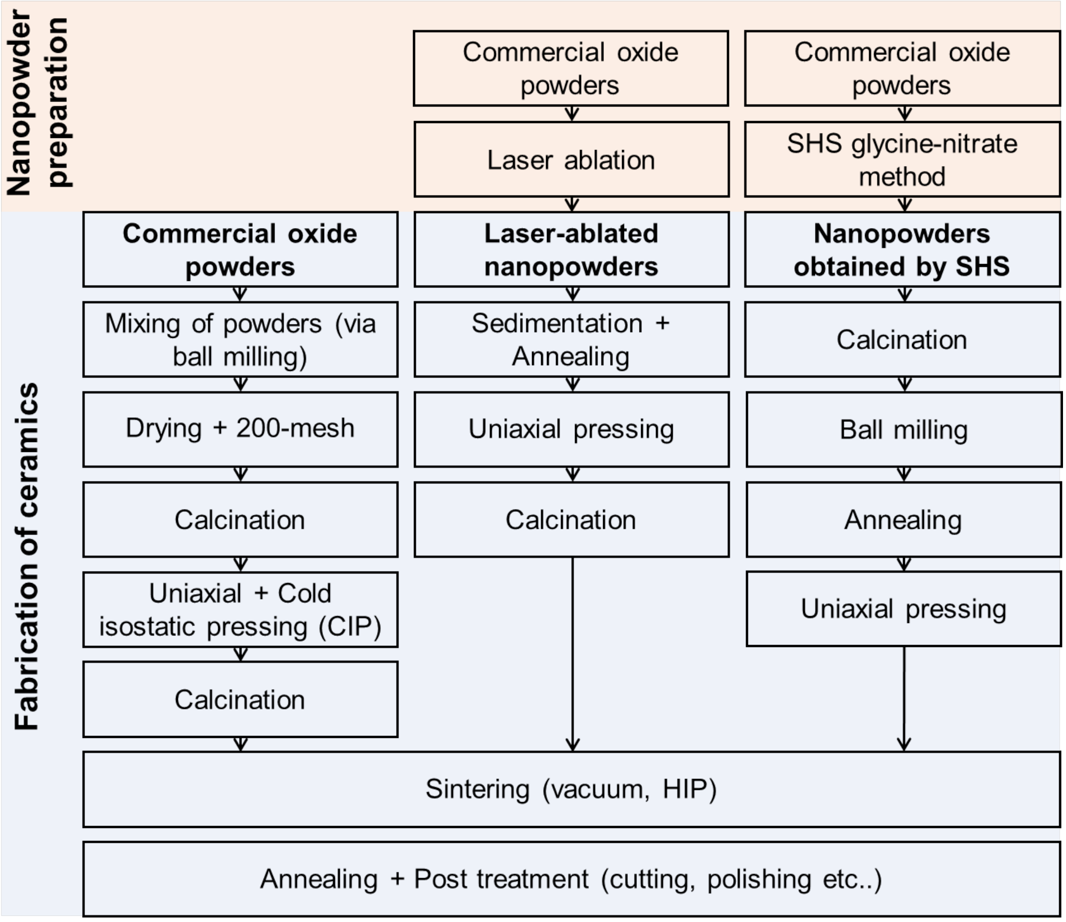

Figure II.17: Ceramic fabrication processes used by different groups provided us the materials: *left column*– ICM CAEP; *middle column*– at IE RAS; *right column* – at ICHPS RAS.

The first step can be missed if the approach implies the direct use of commercial powders. Powders with sub-µm and nm particle size are usually used as starting materials for ceramic production. Laser ablation is considered a highly promising method for obtaining oxide nanoparticles. This technique involves the use of a high-power laser to vaporize a solid target material, followed by the condensation of the resulting vapor in a buffer gas flow. Laser ablation is particularly advantageous for creating solid-solution compositions as it ensures homogeneous mixing of rare-earth radicals and enables rapid crystallization of the vapors into nanosized particles with a uniform distribution of chemical elements throughout their volume. Furthermore, the laser-ablated nanopowders exhibit high sintering activity, allowing for complete densification of the initial green bodies through conventional vacuum sintering. This eliminates the need for expensive post-treatments such as hot isostatic pressing (HIPing) that are typically employed in the fabrication of "mixed" sesquioxide transparent ceramics with laser quality [Zha22]. Thus, laser ablation offers a cost-effective approach to achieving full densification and high-quality transparent ceramics without the requirement for additional processing steps. This method is used by our colleagues from IE RAS (middle column, Figure II.20). Another way to produce the nm-sized precursors is synthesis from aqueous solution. At present, sesquioxide ceramics were produced using powders prepared by co-precipitation [Kim11], sol–gel processing [Pan06], spray pyrolysis [Bak12], and self-propagating high-temperature synthesis (SHS) [Per18]. In particular, our colleagues from ICHPS RAS (right column, Figure II.17) use the self-propagating high-temperature synthesis (SHS) because of its high productivity, simple apparatus, and good reproducibility of powder characteristics.

The next step of ceramic fabrication involves the pressing and sintering. The most common method of compaction ceramic tablets before sintering is the simple uniaxial pressing. It can also be accompanied by a cold isostatic pressing (CIP) to increase the density of the material, as it was done by our colleagues from ICM CAEP (left column, Figure II.17). In all three cases, the ceramics were fabricated using a vacuum sintering or / and hot isostatic pressing (HIP). The sesquioxide ceramics fabricated for this PhD thesis are listed in Table II.1. Details of the precursor synthesis are not presented.

3 Overview of characterization techniques

Various techniques have been applied to study the properties of materials, including physico-chemical and microstructural characterizations, as well as optical spectroscopy. They are listed in Table II.3

Table II.3: Summary of characterization methods used to study Er^{3+}-doped materials in this thesis.

Method	**Abbrev.**	**Purpose**	**Partner**
Material characterization			
• Powder X-ray diffraction	XRPD	Phase identification	URV, IE RAS, ICHPS RAS
• Rietveld analysis		Structure refinement	URV
• Temperature-dependent XRD		Thermal expansion	URV
• Differential thermal analysis	DTA	Thermal behavior	URV
• High Resolution X-Ray Diffraction: 2θ-ω scans, Reciprocal space mapping, Rocking Curves	HR-XRD / RSM / RC	Microstructural characterizations: Phase and crystallographic orientation confirmation / lattice parameters and Lattice mismatch, mosaïcity (epitaxial layers)	CIMAP
• Energy-Dispersive X-ray spectroscopy	EDX	Element mapping	CIMAP*
• Scanning electron microscopy	SEM	Morphology and Structural study	CIMAP*, ITMO*
• Confocal and Interferometric laser microscopy		Morphology and Structural study / Roughness measurements	ITMO*, CIMAP*
• Raman spectroscopy		Vibronic properties	ITMO*, CIMAP*

Table continued

Optical spectroscopy			
• Absorption spectroscopy		Absorption cross-sections	CIMAP*
• Lumimescence spectroscopy		Stimulated emission cross-sections	CIMAP*
• Lumimescence kinetics		Lumimescence lifetimes	CIMAP*
• Low-temperature spectroscopy	LT	Crystal-field splitting	CIMAP*
• Judd-Ofelt analysis	J-O	Transition probabilities	VSTU

* Performed by me
Partner institutions:
URV – Universitat Rovira i Virgili, Tarragona, Spain
ITMO –ITMO University, Saint-Pertersburg, Russia
VSTU - Vitebsk State Technological University, Vitebsk, Belarus

3.1 Material characterization methods

- **X-ray diffraction (XRD)**

XRD is a nondestructive analytical technique used to investigate the atomic structures of crystalline materials. When X-rays of a specific wavelength irradiate a crystal, they interact with regularly spaced atoms in the crystal lattice. The incident X-rays cause atoms to vibrate, and these vibrations produce scattered X-rays. The scattered X-rays interfere constructively and destructively, resulting in a unique diffraction pattern that contains information regarding the arrangement of atoms within the crystal. The diffraction pattern appears as a series of spots or peaks on a detector , in the manner that the position and intensity of these spots / peaks provide valuable informations about the lattice parameters, symmetry and crystallographic orientation of the crystal. By analyzing the diffraction pattern, researchers can determine the crystal structure, unit cell dimensions and atomic positions, which are essential for understanding the properties and behavior of the material. XRD can be broadly categorized into three main types: single-crystal diffraction, powder X-ray diffraction or Laue diffraction:

- High Resolution X-ray diffraction: High Resolution XRD provides detailed informations about the arrangement of atoms within the crystal, including precise bonding / interreticular distances, angles and molecular conformations. By rotating the crystal and collecting data from various crystallographic orientations. Typically, HR-XRD is commonly used to determine the lattice parameters of crystals, their mosaïcity (crystalline quality), to determine the crystalline nature and crystallographic orientation. The HR-XRD is particularly pertinent tu study the microstructure of single-crystalline epitaxial layers regarding their substrates. Furthermore, HR-XRD require a highly monochromatic X-Ray beam.

- Powder X-ray Diffraction (XRPD): XRPD is used to achieve a phase analysis of crystalline samples in terms of crystalline nature, dosage of the phases and size measurements of the crystalline grains. This technique requires a polycrystalline sample presenting small grain sizes which are randomly distributed. So, a fine powder of the studied material containing a multitude of microcrystalline domains with random orientations is used and obtained in milling finely the crystalline samples to be studied. When X-rays pass through a powder sample, they are diffracted by various crystalline domains, producing a diffraction pattern of rings on the detector. These rings correspond to the different crystallographic planes within the powder. By analyzing the pattern, researchers can extract information regarding the crystal microstructure and the phase composition of the material (nature, dosage, size of the crystallites). For powder X-Ray diffraction, it is common that the X-Ray beam is not perfectly monochromatic and that the $K_{\alpha 1}$ and $K_{\alpha 2}$ rays are not separated, to have a more intense incident beam.
- The Laue diffraction method is mainly used for the cristallographic orientation of single crystals essential for their preparation and/or for checking this cristallographic orientation. A description of the Laue diffractometer used in this PhD work and the method are described in Section 2.1.2. The specificity of this method is the use of a white X-Ray beam, it means a polychromatic beam. The so obtained diffraction patterns are collected in reflection on the detector and appear as a distribution of spots in the reciprocal space, each spot corresponding to the reflection of a cristallographic planes family identified by their Miller Indices (hkl).

In the course of this thesis, both X-ray diffraction methods were used. In In the course of this thesis, all of these X-ray diffraction methods were used. In particular, XRPD was employed to identify/check the phases in the crystallized molten bath of the used for the LPE growth of $Er:LiYF_4$ layers, as well as in transparent ceramics. For the former, XRPD patterns were obtained using a Bruker-AXS D8 Advance diffractometer with a vertical θ–θ goniometer. The measurements were carried out using $CuK_{\alpha 1}$ radiation ($\lambda = 0.15406$ nm) obtained from a Cu X-ray tube. The diffractograms were recorded in the 2θ range of 10–80° with an angular step of 0.02° and a step time of 0.5 s. In the case of transparent ceramics, X-ray diffraction analysis was performed by colleagues who supplied us with ceramic samples for this study.

For HR-XRD of the epitaxial crystalline $Er:LiYF_4$ layers, we used a Bruker AXS D8 Discover diffractometer with a four-circle goniometer, a line focus Cu X-ray source, a Goebel mirror and an asymmetric Ge (220) double-bounce monochromator resulting in a parallel and monochromatic X-ray beam ($CuK_{\alpha 1}$). A Ge (220) crystal analyzer was used as a secondary optics to filter the reflected beam. A 2D map was then obtained by taking a series of 2θ-ω at successive ω values to study the mosaicity out of plane and the crystalline quality of the epitaxial layers; the open source DxTools viewer was used for representation of the reciprocal space mapping (RSM) of the considered planes family. Poles figures were also done on Er:CaF_2 epitaxial layers to characterize the mosaicity in plane.

Temperature-dependent XRD was used to determine the thermal expansion coefficient of the Er:CaF_2 single crystal. This was performed to predict the thermal expansion behavior of Er:CaF_2 epitaxial layers and to better understand the causes of the crazing effect in Er:CaF_2 / CaF_2 epitaxies.

- **Confocal and interferometric laser microscopy**

The confocal and interferometric microscopic observations have been carried out by using a Sensofar S-Neox microscope. This hybrid profiler microscope is polyvalent: it allows observations in bright or darkfield, the measure of 2D profiles and acquisition of 3D topographies on a large field of view depending on the used objective. Thus, the confocal observation mode is used to observe quite rough surfaces or microstructures with peak-valleys in the order of few microns until few tens of microns, typically the observation of raw and unpolished epitaxial crystalline layers. On the contrary, the interferometric observation mode is used to characterize very smooth surfaces presenting surface profile or roughness in the nanometer range.

Briefly, the confocal principle is described in Figure II.18(a,b). Confocal technology is able to measure the surface height converting conventional images into optical sections where the signal is preserved for those areas within the depth of focus of the objective, improving the image contrast and the lateral resolution and system noise. For 3D imaging it is necessary to obtain data from all the pixels of the camera. That means: to reconstruct a confocal image. To do that, the multiple slit image is shifted one pixel as many times as necessary to fill the camera. In each of the shifted multiple slits, one image of the camera is taken and the confocal algorithm is applied on the pixels illuminated at that moment.The confocal scanning technique implemented in Sensofar's systems is a Microdisplay Scan Co Microscope. The microdisplay creates a rapidly switching device with no moving parts, making data acquisition fast, reliable and accurate. Due to this and the associated algorithms, Sensofar's Confocal technique yields a class-leading vertical resolution, better than other Confocal approaches. Three confocal objectives have been used for these confocal microscopic observations, presenting respectively a magnification of 10x, 20x, 100x and 150x.

The interferometric microscopic observations have been achieved in a phase-shift configuration (PSI). The working principle of Interferometry technology, consists on a splitting of the light into two beams that travel different optical paths and are then combined to produce interference. Interferometric objectives allow the microscope to operate as interferometer; fringes are observed in the sample when it is in focus. The PSI technique uses narrowband light source (red, green or blue) to measure the phase of the interferogram. A vertical resolution in the order of 0.1 nm can be reached, the equipment does not benefit of a vertical PZT moving. The general optical scheme for PSI present the same configuration than in a confocal configuration, but in using interferometric objectives instead of bright field ones. Let us note here, that the S-Neox microscope in CIMAP is equipped with three interferometric objectives, which present a magnification of 10x, 50x and 100x. To obtain a topography the sensorhead is scanned along the Z direction. For PSI, few microns are scanned and the phase is retrieved. With Interferometry, the 3D measurement is performed with the maximum accuracy. It is possible to scan along the z axis to obtain fringes on the complete sample, obtaining height information from the phase of the interferogram for PSI and reconstruct a 3D image with the obtained heights for the different pixels.

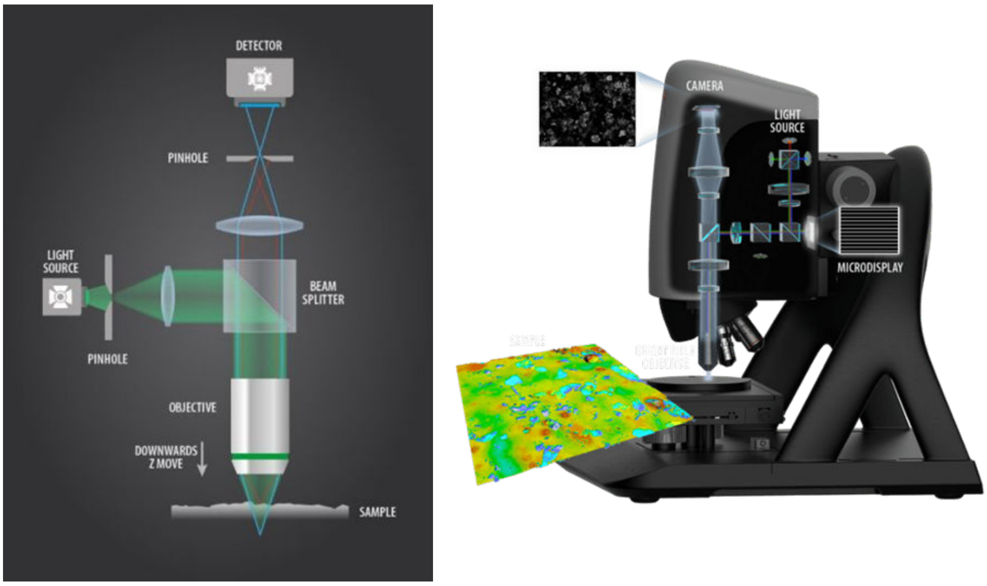

Figure II.18: (a) Optical scheme of the confocal principle, (b) General scheme of the microscope in a confocal mode.

• Scanning electron microscopy (SEM) & Energy-Dispersive X-ray spectroscopy (EDX)

SEM / EDX is a widely used surface analytical technique, known for obtaining high-resolution images of surface topography with excellent depth of field. This technique involves utilizing a highly-focused, scanning primary electron beam, which enters the surface with an energy range of 0.5 – 30 kV. Upon interaction, numerous low energy secondary electrons are generated and their intensity is heavily influenced by the sample surface topography. By measuring the intensity of these secondary electrons in response to the position of the scanning primary electron beam, an image of the sample's surface can be built. In addition to generating low energy secondary electrons, primary electron bombardment also produces backscattered electrons and X-rays. The intensity of backscattered electrons is related to the atomic number of the elements present within the sampling volume. As a result, this allows for obtaining qualitative element informations about the sample. The basic SEM set-up is shown in Figure II.19.

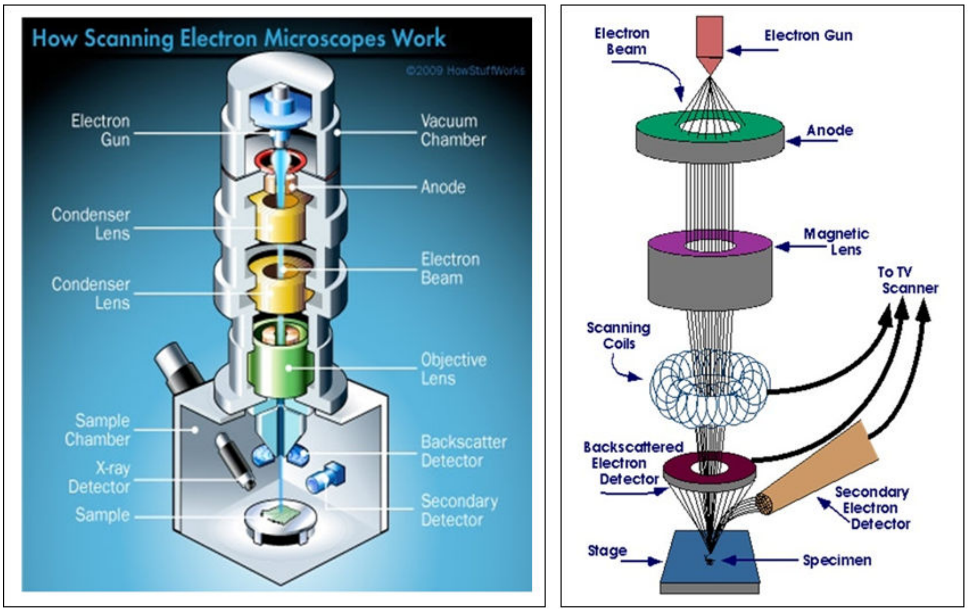

Figure II.19: Basic SEM set-up and its electron path. Image taken from http://emicroscope.blogspot.com/2011/03/scanning-electron-microscope-sem-how-it.html

Within this PhD study, the SEM / EDX was applied for the morphological and microstructural study of epitaxial layers and transparent ceramics, as well as chemical composition analysis. The Er:$LiYF_4$ epitaxies were studied by SEM in CIMAP using a JCM-7000 NeoScope Benchtop microscope (Jeol) with an integrated Energy Dispersive X-ray (EDX) module. The accelerating voltage was 15 kV, the working distance was 13 mm and the measurements were performed in a high-vacuum mode.

The microstructure of the polished Er:$(Lu,Sc)_2O_3$ ceramic surface was studied with a scanning electron microscope (SEM) MERLIN (Carl Zeiss) at ITMO University. The grain size distribution was determined by direct counting method (for >100 grains) in the ImageJ software (the shape factor of 1.2 was applied).

3.2 Optical spectroscopy methods

• Raman spectroscopy

Raman spectroscopy is an analytical technique that involves using scattered light to analyze the vibrational energy modes of a sample. When light interacts with molecules, it induces the polarization of the molecular electron cloud, leaving the molecule in a higher energy state. This process is known as the formation of a short-lived complex, called the virtual state. The virtual state is unstable, and the photons are re-emitted as scattered light almost immediately.

The dominant scattering process in most cases is elastic scattering, also known as Rayleigh scattering, where the energy and wavelength of the scattered photon remain the same as the incident photon. Raman scattering is a rare inelastic process (approximately 1 in 10 million photons)[2], involving energy transfer between the molecule and scattered photon. Stokes Raman scattering occurs when the molecule gains energy and its wavelength increases, while Anti-Stokes Raman scattering happens when the molecule loses energy, leading to a decreased wavelength for the scattered photon. Quantum mechanically they are equally likely processes. In practice, Stokes scattering is more likely because the majority of molecules are at the ground vibrational level (according to Boltzmann distribution). Consequently, Stokes Raman scattering is more intense than Anti-Stokes, making it the primary process measured in Raman spectroscopy. FigureII.20 describes the origin of Rayleigh, Stokes and Anti-Stokes Raman Scattering.

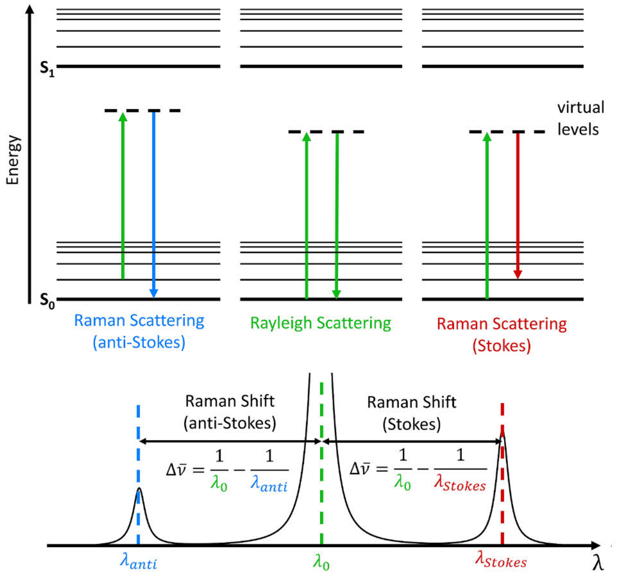

Figure II.20: Jablonski diagram showing the origin of Rayleigh, Stokes and Anti-Stokes Raman Scattering. Image taken from https://www.edinst.com/blog/what-is-raman-spectroscopy/.

Within this PhD study, the Raman spectra of materials were measured using a confocal Raman microscope (inVia, Renishaw) equipped with a × 50 objective (Leica) and an Ar^+ ion laser (457.0 nm). Schematic and instrumental images of the InVia Raman spectrometer are shown in Figure II.21. It consists of a light source for providing an excitation radiation; a detector for detecting Raman scattered light; and an optical system for directing the excitation radiation toward the sample, receiving Raman scattered light from the sample and providing the Raman scattered light to the detector. The choice of the excitation wavelength of 457.0 nm was conditioned by the absence/weak absorption of this wavelength by the erbium-doped matrices; otherwise, there could be a strong overlap of the Raman spectra with the upconversion luminescence of Er^{3+} ions (excitation at 488.0 and 514.0 nm).

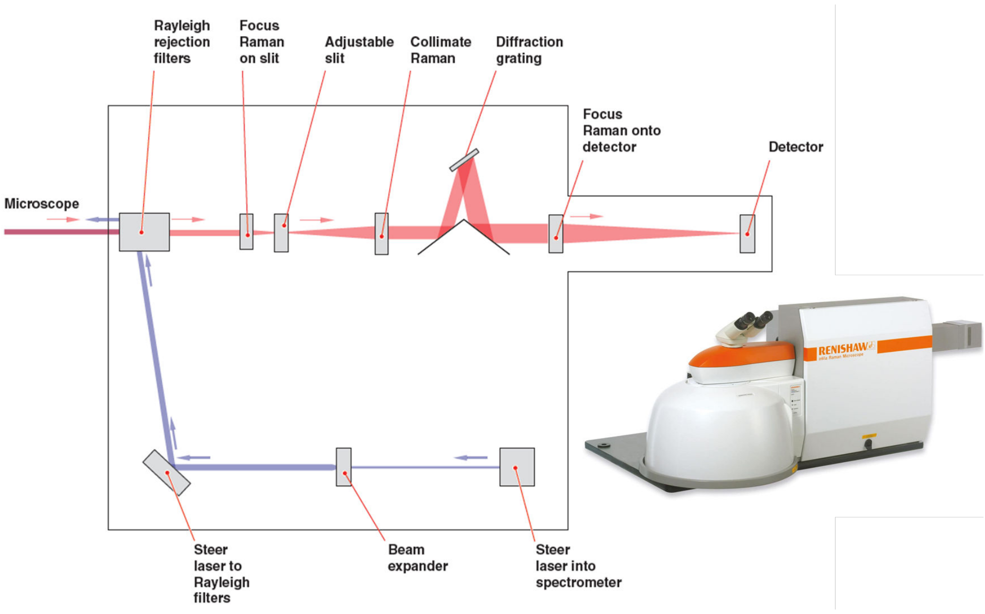

Figure II.21: InVia Raman spectrometer schematic and instrumental images from the Renishaw manual.

• Absorption

The evaluation light absorption capability of the material is commonly achieved through absorption spectroscopy. This analytical technique involves comparing the intensity of a monochromatic light beam passing through the sample with that of an unabsorbed reference beam of the same wavelength. By systematically adjusting the wavelength to cover the desired spectral range, absorption measurements can be obtained. Absorption spectroscopy serves multiple purposes, such as determining the optimal pump wavelength and calculating absorption cross sections. It also offers insights into the lattice structure by studying the distribution of Stark sublevels observed within the absorption bands. Notably, the shape, width, and to some extent, the spectral position of rare-earth absorption bands arise from the interaction between the energy levels of the rare-earth ions and the local crystal field in which they are embedded. This coupling plays a significant role in shaping the absorption characteristics of the material.

To evaluate the transparency and the ground-state absorption (GSA) of the studying materials (epitaxial layers, crystals and ceramics), transmission spectra were measured from UV to near-IR range using a dual-beam UV/Vis/NIR spectrometer (Lambda 1050, PerkinElmer); the resolution (spectral bandwidth, SBW) was 0.25 nm in the visible and 0.7 nm in the near-IR. From the obtained transmission spectra, the absorption spectra were recalculated using the Beer-Lambert law [Bee52, Lam60]:

$$I(\lambda, d) = I_0(\lambda)e^{-\alpha(\lambda)d} \tag{II.1}$$

where I is the transmitted intensity, I_0 is the incident intensity, α and d are the absorption coefficient and the sample thickness, respectively. Thus, the absorption coefficient can be expressed as follows:

$$\alpha(\lambda) = \frac{1}{d} ln \frac{I_0(\lambda)}{I(\lambda, d)} \tag{II.2}$$

With the doping concentration N_{dopant}, the absorption cross-section can be determined as follows:

$$\sigma_{abs}(\lambda) = \frac{\alpha(\lambda)}{N_{dopant}} \tag{II.3}$$

• Lumimescence spectroscopy

For most of the materials studied, luminescence spectra of Er^{3+} ions in the 2800 nm region corresponding to the $^4I_{11/2} \rightarrow {}^4I_{13/2}$ transition were measured using an optical spectrum analyzer (Yokogawa AQ6376) purged with N_2 gas to eliminate the structured absorption of water vapor in air and zirconium fluoride (ZrF_4) fiber.

Another set-up we built for similar measurements consisted of a 0.6 m monochromator (HRS2, Jobin-Yvon), lock-in amplifier (SR810 DSP, Stanford Research Systems), and InSb detector (J10D series, Judson Infrared) cooled with liquid nitrogen with SBW = 4 nm. The monochromator was purged with nitrogen to reduce the effect of the water vapor absorption. A Ti:Sapphire laser (model 3900 S, Spectra Physics) tuned to 960–980 nm, depending on the absorption peak of the material, was used as the excitation source. The calibration of both systems was performed using a Hg lamp (Schwabe).

For some of the studied materials, we also measured the luminescence spectra around 1550 nm, corresponding to the $^4I_{13/2} \rightarrow {}^4I_{15/2}$ transition, using an optical spectrum analyzer (AQ6375B, Yokogawa) with SBW = 0.5 nm.

- **Luminescence kinetics**

The luminescence dynamics was studied using a ns optical parametric oscillator (Horizon, Continuum), a 1/4 m monochomator (Oriel 77200), a photomultiplier (PMT) tube (for luminescence in visible spectral range), an InGaAs detector (near-infrared luminescence) and an 8 GHz digital oscilloscope (DSA70804B, Tektronix). To avoid the effect of reabsorption (radiation trapping) on the measured lifetimes, finely powdered samples were used.

- **Low-temperature spectroscopy (LT)**

For low-temperature (LT, 12 K) studies, the samples were mounted on an APD DE-202 closed-cycle cryo-cooler equipped with an APD HC 2 Helium vacuum cryo-compressor and a Laceshore 330 temperature controller. The cryo-system is shown in Figure V.22.

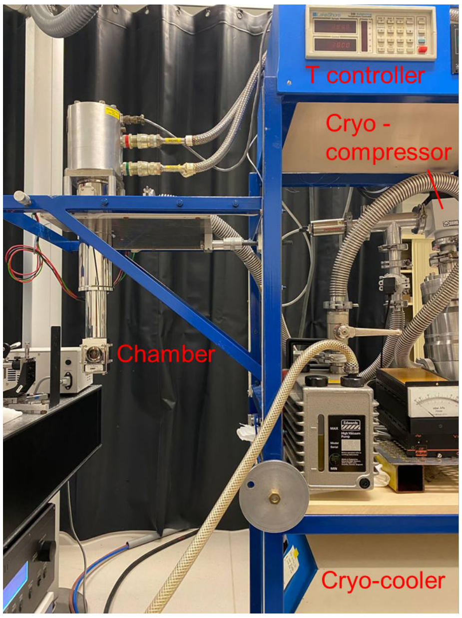

Figure II.22: Experimental set-up for spectroscopic measurements at cryogenic temperatures (12 K).

4 Conclusions Chapter II

Targeting the efficient laser operation of Er^{3+}-doped materials in the mid-infrared region and a detailed spectroscopic study should be performed, focusing on the key spectroscopic parameters relevant for laser development. These parameters include the absorption cross-sections, stimulated emission cross-sections, luminescence lifetimes, and phonon energies. To determine the parameters of the studied materials, we employed a set of spectroscopic methods including absorption and emission spectroscopy, luminescence dynamics, spectroscopy at cryogenic temperature (12 K), and Raman spectroscopy.

With the goal of producing heavily Er^{3+}-doped waveguiding single-crystalline fluoride layers, we identified $LiYF_4$ as the most promising system. A bath composition of 51 LiF – 49 YF_3 (mol.%) was selected to reduce the growth temperature and a growth set-up featureng well-controlled atmosphere was employed. For the growth of bulk udoped $LiYF_4$ single crystals intended for use in substrate fabrication, we selected the Cz growth method. The orientation of these substrates was provided by Laue diffraction. To characterize the morphological and structural properties of the epitaxies we employed scanning electron microscopy combined with energy dispersive x-ray spectroscopy, confocal laser microscopy and single-crystal and powder X-ray diffraction.

With the goal of growing the Er^{3+}-doped CaF_2 epitaxial layer, we selected lithium fluoride as the most promising solvent because, contrary to calcium chloride solvent, which was previously used by our group for the growth of Yb^{3+}:CaF_2 epitaxies, this solvent is less corrosive and aggressive and provides lower growth temperatures. The substrates for CaF_2 epitaxial growth are commercially available and represent a significant potential benefit for the fabrication of such devices.

With the goal of studying Er^{3+}-doped fluoride single crystals as promising gain media for 2.8 µm lasers, several fluorite-type crystals were identified, including MF_2-type crystals (M = Ca, Ba, Sr, and their mixture), $Na_5Y_9F_{32}$, and KY_3F_{10}. These crystals were grown by Bridgman (for MF_2 crystals) or Cz (for $Na_5Y_9F_{32}$ and KY_3F_{10}) under a well-controlled atmosphere. Fluoride materials are very sensitive to even small oxygen impurities, which can form oxygen-assisted optical centers, as well as oxyfluoride phases, which are detrimental to both the spectroscopic behavior of these materials and their optical properties.

The ceramic technology for transparent sesquioxides offers a number of important advantages; in particular, it offers lower synthesis temperatures and is more important for the present work well-conrolled fabrication of "mixed" compositions, contrary to the single-crystal growth, which suffers from the segregation of rare-earth ions. These well-conrolled ratios of host-forming cations are important for succesfully design of the emission banwiths of "mixed" materials. The samples of Er^{3+}-doped transparent sesquioxide ceramics were obtained within existing collaborations while we have identified a number of promising compositions including lutetia-scandia (Lu_2O_3 – Sc_2O_3), lutetia – yttria (Lu_2O_3 –

Y_2O_3), yttria – lantana (Y_2O_3 – La_2O_3), and yttria – scandia (Y_2O_3 – Sc_2O_3) which will be studied in the present study.

Chapter III

Erbium-doped $LiYF_4$ and CaF_2 layers elaborated by Liquid Phase Epitaxy

1 Erbium-doped LiYF$_4$ epitaxy

This Section focuses on the epitaxial growth of the Er^{3+}, Gd^{3+}:LiYF$_4$ layers. Sub-section 1.1 discusses the results on the epitaxial growth, namely the study of the structure and phase transformation of the crystallized molten bath, apparent supercooling effect on the layer growth behavior and improvement of the layer quality by optimization of cooling conditions. Sub-sections 1.2 & 1.3 are devoted to the detailed characterization of the grown Er^{3+}, Gd^{3+}:LiYF$_4$ epitaxial thin films: their structure, morphology, and spectroscopic properties.

1.1 Epitaxial growth of the Er, Gd:LiYF$_4$ layers

Three sets of Er^{3+}:LiYF$_4$ epitaxial layers with the compositions listed in Table III.1 were grownwithin the LPE experiments. For each composition, the brief description of study carried out for them is given.

Table III.1: Summary of LPE-grown LiYF$_4$ layer compositions and studies performed for them.

Composition		**Doping, % (concentration in the bath)**	**Studies performed for an appropriate composition /** ***purpose***
#1	73 LiF – 27 YF$_3$ (mol%)	11 at.% Er^{3+}	-
#2		7 at.% Er^{3+}, 5 at.% Gd^{3+}	1. Structural & thermal analysis of crystallized molten bath / *Verification of purity and determination of the relative temperature of phase transformation occurring in heating and cooling of the bath* 2. Effect of the apparent supercooling on the growth behavior / *optimization of the growth conditions*
#3		1 at.% Er^{3+}, 0.5 at.% Gd^{3+}	Elimination of layer cracking by optimization of cooling regime / *improvement of the layer quality*

1.1.1 Structure & Thermal analysis of the crystallized molten bath

To study the composition of the bath and verify the absence of pollution (oxyfluoride phase), we performed structural analysis by powder XRD of a small quantity of matter taken in different areas of the solidified bath. In addition, to better understand the thermal behavior of the molten bath, the phase transitions that occur, and their relative temperatures, thermal analysis by DSC was performed on small powder quantities taken in the translucent and transparent parts of the crystallized (upon fast cooling) molten bath have been used. Indeed, because of the use of a quaternary chemical system (LiF-YF_3-ErF_3-GdF_3), a shift in the typical temperature range was expected with respect to the reference system (LiF-YF_3), as represented in Figure III.1. To avoid overloading the phase diagram of LiF - GdF_3 is not shown.

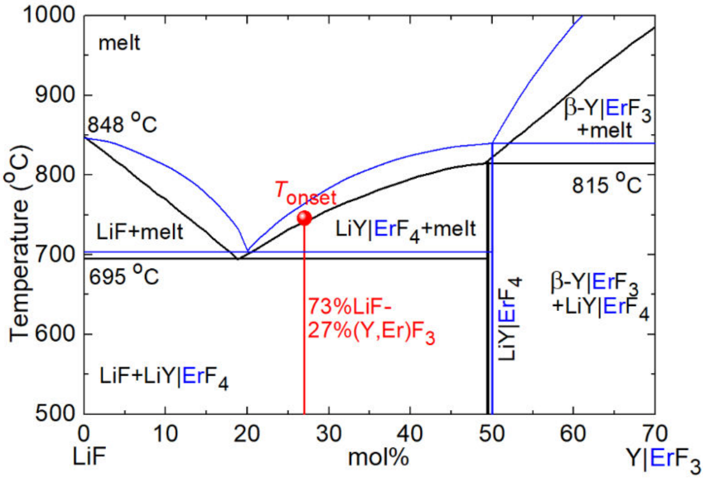

Figure III.1: Phase diagram of the LiF – YF_3 (*black*) and LiF – ErF_3 (*blue*) binary systems (according to our data and [Tho61,Fed02]), *bold black line* - the $LiYF_4$ peritectic, *red line* – the composition selected for the LPE growth, *red circle* – apparent onset of crystallization. The indicated temperatures correspond to the LiF – YF_3 diagram.

Figure III.2(a) shows a photograph of the crystallized molten bath of $Li(Y,Er,Gd)F_4$ that was removed from the crucible after the quartz tube was dismantled. Two types of materials were observed in the bath: transparent rose-colored single crystals with a volume of a few mm^3 and white-colored translucent polycrystallites, indicating a phase separation. Possible reasons for this can be: (1) a phase separation which occurs progressively in the liquid state during the cooling without stirring; (2) the predominantly peritectic composition $Li(Y,Er,Gd)F_4$ crystallizes at higher temperatures and then owing to rapid cooling melt progressively transforms into a solid polycrystalline LiF+ $Li(Y,Er,Gd)F_4$ mixture following the liquid curve until complete freezing at the solidification temperature. The latter is confirmed by the presence of transparent $Li(Y,Er,Gd)F_4$ crystals in the bottom and central parts of the bath, in Figure III.2(b), where the temperature in the crucible is usually slightly higher owing to the thermal gradient in the furnace, i.e., in the tube, but also due to the convection flux in the crucible.

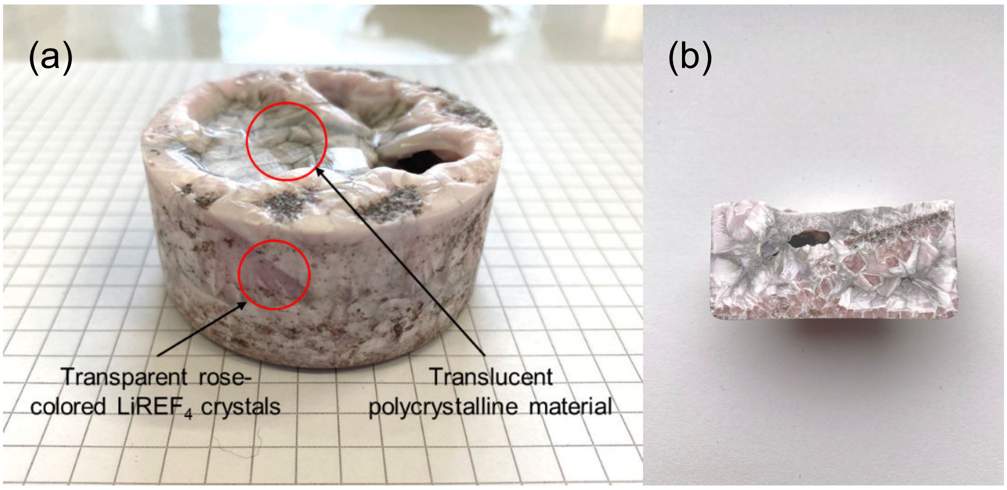

Figure III.2: Photographs of (a) the entire crystallized molten bath of Li(Y,Er,Gd)F_4 used for the LPE experiments, (b) its side slice; the both show phase separation in the liquid state.

First, the material from the crystallized molten bath with the composition #2 was studied by powder XRD. The XRD patterns, Figure III.3, indicate that transparent crystals have single-phase nature (tetragonal, $LiYF_4$-type structure with lattice constants a = 5.1704 Å and c = 10.7472 Å) and the translucent material is composed of LiF (29.4 wt%) with a cubic structure, a = 4.0304 Å and a similar $LiYF_4$-type phase (70.6 wt%). By converting this into a molar fraction, this ratio confirms the presence of a phase separation that occurs during the fast cooling of the bath and explains a local composition that is slightly different from the global composition. This phenomenon, which is observed in the solidified bath, reflects a typical behavior of solid-state matter, by considering the fast cooling of a melt, kinetic, and thermodynamic considerations, leading to a non-uniform polycrystalline phase. Moreover, the XRD patterns for both types of materials confirm the absence of an unwanted oxyfluoride phase, which is essential to achieve high-quality laser crystals, that is, epitaxial layers of Er^{3+},Gd^{3+}:$LiYF_4$.

The corresponding DSC curves are shown in Figure III.4. For the translucent material, Figure III.4(a), a single endothermic peak on the heating curve (onset temperature: T_{on} = 699 °C, peak temperature: T_p = 713 °C) corresponds to the eutectic temperature for the LiF – YF_3 diagram, Figure III.1. The difference between this eutectic temperature and that reported by Thoma *et al.* (695 °C) is probably due to the used composition with Er^{3+} doping which is not negligible. Upon cooling, the onset of crystallization is observed at T_{on} = 744 °C in agreement with the LPE experiment (apparent onset T_{on} = 746.6°C for the composition#2). In the LPE setup, the temperature is measured by thermocouples positioned in the refractory wall of the furnace, very close to the side of the inner tube, i.e., the growth chamber [Bra19]. For this purpose, there is a slight uncertainty of the absolute value of the temperature in the crucible, especially since there are convection fluxes in the melt as well as in the tube, i.e., in the growth chamber, above the molten bath. The second exothermal peak on the cooling curve (T_{on} = 689°C and T_p = 686 °C) corresponds to the eutectic temperature when the melt completely solidifies, forming a mixture of LiF + $LiREF_4$ phases. The shift toward a lower eutectic temperature between the temperature revealed in the experiment and that proposed in the literature [Tho61, Fed02] is explained by the presence of Gd^{3+} ions in our chosen composition. Fedorov *et al.* provided the eutectic temperature of 765°C for the LiF-GdF_3 phase diagram.

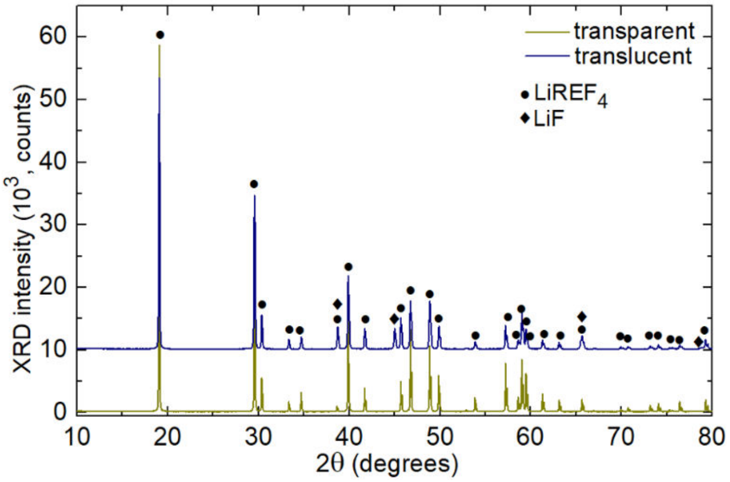

Figure III.3: Powder X-ray diffraction (XRD) patterns of the crystallized molten bath of the LPE experiment: translucent polycrystalline material and transparent rose-colored single crystals.

Figure III.4(b) shows the DTA curves for the transparent crystals, the eutectic temperature is T_{on} = 698 °C (corresponding to melting of LiF-rich eutectic) and the melting point of the $LiREF_4$-type phase is T_{on} = 820 °C on the heating curve for the peritectic composition. It confirms our suggestion about the increase of the melting temperature for $Li(Y,Er,Gd)F_4$ as compared to pure $LiYF_4$. However, upon cooling the incongruent character of melting can alternates with congruent solidification. It means that phase transformations are described by the following patterns:

1. melt ↔ $LiREF_4$ + REF_3 (eutectic, congruently melting $LiREF_4$)
2. melt + REF_3 ↔ $LiREF_4$ (peritectic, incongruently melting $LiREF_4$).

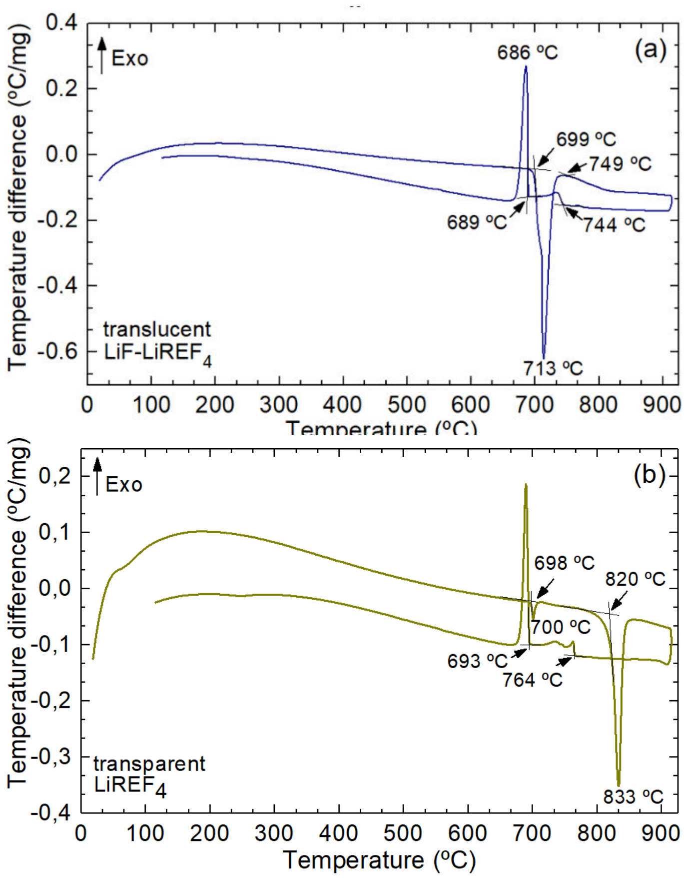

Figure III.4: Differential thermal analysis curves for the crystallized molten bath of the LPE experiment: (a) translucent polycrystalline material; (b) transparent rose-colored $LiREF_4$ crystals.

This system is vulnerable to external disturbances (impurities, cooling rate, etc.) that can shift the phase equilibrium and even a small redistribution of the liquid phase components, that is, evaporation of LiF can lead to a change in the solidification patterns [Fed02]. According to the cooling curve, the onset of crystallization is observed at T_{on} = 764 °C. Complete solidification of the melt takes place below the temperature of T_{p} = 693°C.The difference between the compositions of the liquid phase corresponding to the two patterns lies in a concentration range of less than 1 mol % [Fed02].

Thus, the study shows that the bath contained no traces of impurity phase formation, such as oxyfluoride phase, there is only the components forming the layer, namely the solvent LiF and crystallizing material $Li(Y,Er,Gd)F_4$. In the bath, phase separation was observed to be associated with the lack of mechanical stirring in the liquid state and a rapid cooling rate of the molten bath, which resulted in the formation of polycrystalline matter at the solid state. Such phase separation is typical of an LPE bath under fast cooling.

1.1.2 Effect of the apparent supercooling on the growth behavior

As mentioned in Chapter II, one of the driving forces behind nucleation and epitaxial growth is the solution supersaturation. The control of supersaturation is key to achieve the desired parameters of the epitaxial layer, that is, the growth rate, thickness, and single crystallinity. Supersaturation, in turn, is achieved by a certain cooling mode, i.e., supercooling. Other types of supersaturation methods are described in Section 2.2 of Chapter II. In order to optimize the growth conditions, we investigated the effect of solution supercooling on the growth behavior of the Er^{3+}, Gd^{3+}:$LiYF_4$ layers.

The effect of the apparent supercooling on the growth behavior of the layers was studied using batch composition #2, as shown in Figure III.5. For a small supercooling of ~0.5 °C, the film is uniform and transparent. By increasing the supercooling to 1 – 2 °C, the growth rate increases, the film surface exhibits anarchic crystallization, cracks propagating into the substrate and surface “ripples”; moreover, the deposition of solvent is enhanced. Finally, for a large supercooling of ~6 °C, the layer becomes polycrystalline and is completely covered by the crystallized solvent on the whole surface.

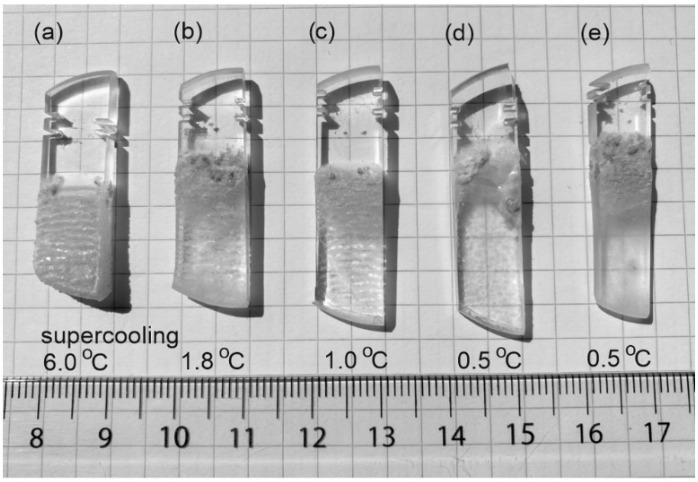

Figure III.5: Effect of the apparent supercooling on the growth behavior of Er,Gd:$LiYF_4$ layers on (001)-oriented $LiYF_4$ substrates: the supercooling is (a) 6.0 °C, (b) 1.8 °C, (c) 1.0 °C, (d) 0.5 °C (direct growth) and (e) 0.5 °C (growth after pre-dissolving the substrate at 760 °C during 5 min). The growth duration is 45 min.

Thus, for further experiments, a supercooling of less than 1 °C was selected. The duration of growth was 45 – 90 min. and the obtained layer thickness was 30 – 90 μm (on each side of the substrate), corresponding to a growth rate of 0.8 – 1.6 ± 0.5 μm/min. These values only account for the uniform thickness of the layer without the surface-deposited solvent. The observed growth rates agree with the data from Rogin *et al.* and indicate that the growth mechanism relies on the attachment of new building units anywhere at the layer edge [Rog97].

We also tested a growth regime in which the substrate was first kept inside the solution and maintained at a higher temperature (760 °C) for a few minutes resulting in healing imperfections on its surface with a subsequent growth at small supercooling (0.5 °C), Figure III.5. This significantly reduced the surface roughness of the layer. However, some curvature of the substrate / layer interface was observed due to a slight dissolution of the substrate under conditions of a vertical thermal gradient in the melt. This method seems promising for substrates with a tolerable polishing quality; however, further optimization of the high-temperature hold is required in order to activate surface without curvature formation.

1.1.3 Elimination of layer cracking by optimization of cooling regime

Another factor that determines the quality of the obtained layers is the mode of cooling during their removal from the crucible. The cooling mode is determined by the translation speed of the pulling cane, that is, the sample, in the thermal gradient of the furnace, as well as by the step duration at different stages. This defines the cooling rate of the sample. Often, owing to rapid cooling, the epitaxial layer experiences thermal shock, leading to the crack apparition on the surface. To eliminate the layer cracking effect and improve its quality, we optimized the cooling mode.

The set of samples obtained using batch composition #3 was cooled for different durations and this different cooling rates, as shown in Figure III.6(a). This was adjusted by optimizing the translation speed of the substrate holder. All the compared samples were grown at a temperature of T_{on} = 700.6 °C for 45 – 60 min. For cooling durations of 22 min and 24 min, the layers exhibited strong surface cracking. The samples were most vulnerable when moving from the furnace to the exchange chamber. This is where the layers experienced the greatest thermal shock. As the duration of cooling increased and thus the growth rate decreases, the surface became more transparent and uniform without cracks propagating into the layer, and the substrate was preserved. It has been chosen to use a 3 mm-thick substrate to avoid substrate destruction owing to thermal stress. Figure III.6(b) shows the differences in the surface quality of the samples cooled for 22 min and 810 min of translating duration. Moreover, note that some substrates present their top part cracked, which is where the substrate is fixed on the holder with a Pt wire. Being more brittle because of the dicing of small cuts to maintain the substrate in contact with the holder, the substrate is more stressed and is more sensitive to thermal shocks.

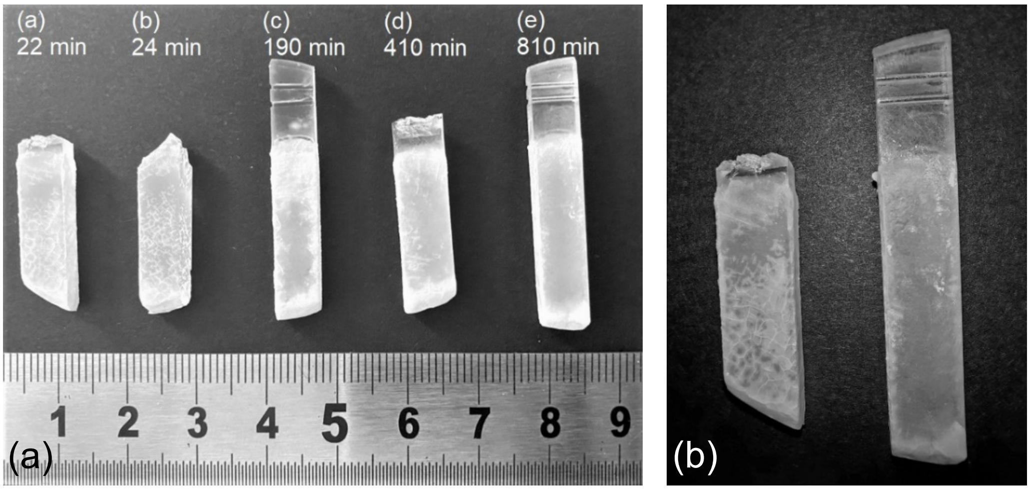

Figure III.6: Effect of cooling duration on the quality of Er^{3+},Gd^{3+}:$LiYF_4$ layers on (001)-oriented $LiYF_4$ substrates: (a) cooling duration is (a) 22 min, (b) 24 min, (c) 190 min, (d) 410 min, and (e) 810 min; (b) close look to samples (a) and (e).

1.1.4 Layers doped with Er^{3+} and Gd^{3+} ions: optimized growth conditions

To summarize, the layer parameters that define the optimal conditions for their growth are:

(i) Surface condition, namely the absence of defects on the layer surface, including cracks due to rapid cooling; excess of solvent crystallized on the surface resulting from strong supercooling of the melt;
(ii) Layer transparency (absence of crystallized solvent) and its uniformity;
(iii) Layer thickness: the minimum thickness required to fabricate a waveguide is 60-70 μm, considering further polishing steps that reduce this thickness to 20-30 μm.

Thus, the optimized LPE growth temperatures were 746.0 °C and 746.6 °C (± 0.5 °C, for batch formulations #1 and #2, respectively). These temperatures were slightly higher than those expected from the phase diagram of the LiF - YF_3 binary system proposed by Thoma *et al.* (741 °C), which is explained by the presence of ErF_3 in the composition. Fedorov *et al.* reported a higher melting point of $LiErF_4$ (840 °C) compared to $LiYF_4$ (815 °C) [Tho61, Fed02]. The transition from growth to dissolution was observed in the range less than 1 °C, which requires great stability of the furnace.

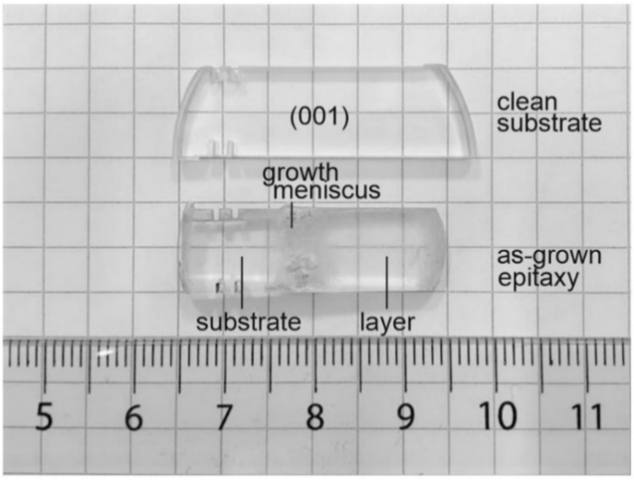

Figure III.7: Photograph of the as-grown Er:LiYF$_4$ / LiYF$_4$ epitaxy grown at 745.5 °C for 45 min. and (001)-oriented LiYF$_4$ substrate.

Figure III.7 presents photographs of a clean substrate (LiYF$_4$) and as-grown epitaxy (Er:LiYF$_4$ / LiYF$_4$) obtained using batch composition #1. The growth temperature was 745.5 °C (an apparent supercooling of 0.5 °C) and the growth duration was 45 min. The film was clean and transparent and covered approximately 2/3 of the substrate. The growth meniscus contains a much thicker layer, and it is strongly covered by the crystallized solvent owing to the thermal discontinuity related to the molten bath surface and the growth atmosphere.

1.2 Material characterization of the Er, Gd:LiYF$_4$ epitaxy

1.2.1 Structural study

The layers grown using the batch composition #1 with a clean surface were studied by high-resolution XRD, as shown in Figure III.8. Considering the X-ray absorption by the LiYF$_4$ phase and its density, the depth probed during the XRD measurement was in the 5-30 μm range, less than the film thickness. Thus, mainly the diffraction from the film was measured. The layer exhibits only two intense diffraction peaks at 2θ = 33.36° and 70.08° both corresponding to (00*l*) reflections of the LiYF$_4$ phase, namely, the (004) and (008) reflections, respectively, Figure III.8(a). This confirms a good orientation of the film with respect to the substrate, i.e., the growth along the [001] direction. To determine the lattice constants for the layer, a high-resolution XRD pattern was also measured for a tilted geometry revealing the (103) diffraction peak, Figure III.8(b). A 2D map of this (103) reflection in the reciprocal space, Figure III.9, shows a thin intense node that is slightly spread out, indicating a well-oriented layer without fluctuation of the lattice parameters. These measurements resulted in the average lattice constants for the tetragonal phase of a = 5.1696 Å and c = 10.7339 Å. A comparison of the layer XRD pattern with the standard one for undoped $LiYF_4$ indicates that the layer is isostructural to $LiYF_4$. It corresponds to the tetragonal crystal class (space group C^6_{4h} - $I4_1/a$, No. 88). It is difficult to determine a reliable value of the lattice mismatch between the layer and the substrate for batch #1 as it is within the error of calculation of the lattice constants.

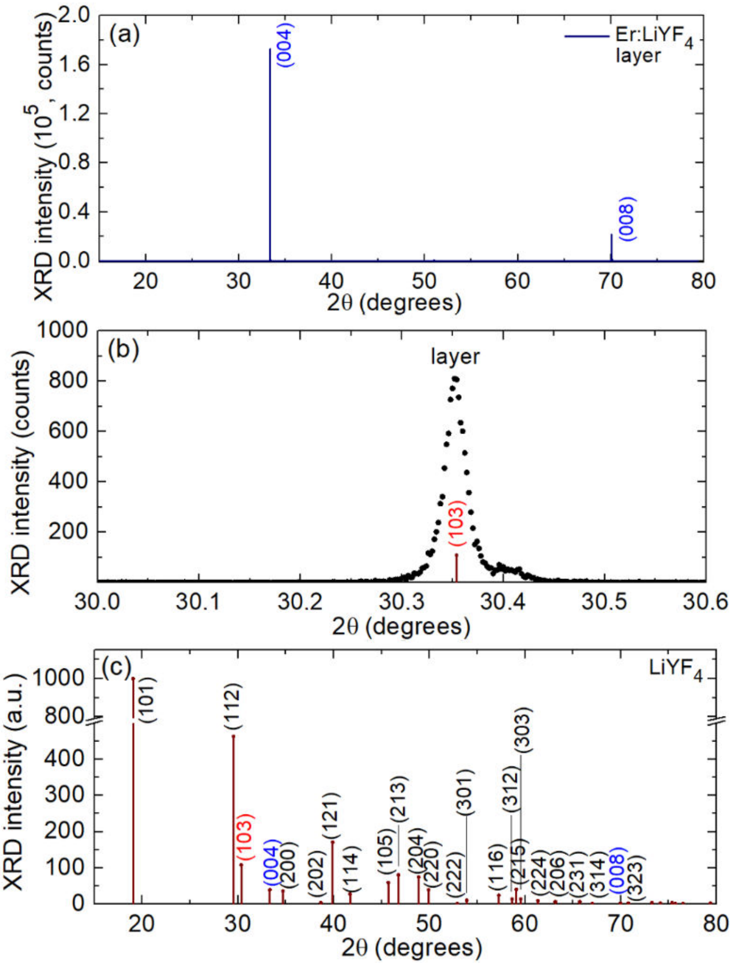

Figure III.8: High resolution X-ray diffraction (XRD) study of the Er:$LiYF_4$ / $LiYF_4$ epitaxy: (a,c) measured XRD patterns of the layer, symmetric 2θ - ω scans: (a) typical sample orientation and (b) tilted sample in skew geometry revealing the (103) reflection; (c) standard pattern of undoped $LiYF_4$ (ICSD card No. 02-7896), numbers indicate the Miller's indices, (*hkl*).

The lattice constants for the Er:$LiYF_4$ and Er,Gd:$LiYF_4$ phases should be compared with those for undoped $LiYF_4$ (a = 5.164 Å and c = 10.740 Å [Gar93]). In the $LiYF_4$ structure, there exists a single rare-earth site with S_4 symmetry and a VIII-fold fluorine coordination representing a slightly distorted dodecahedron [YF_8]. Both the Er^{3+} and Gd^{3+} cations are expected to replace for the Y^{3+} ones. The corresponding ionic radii are $R_Y = 1.16$ Å, $R_{Er} = 1.14$ Å and $R_{Gd} = 1.20$ Å [Kam13]. The larger ionic radius of Gd^{3+} explains a slight increase of the lattice constants for the Er,Gd:$LiYF_4$ phase, the corresponding lattice mismatch with respect to the substrate is $\Delta a/a_{subst} = 0.12\%$ and $\Delta c/c_{subst} = 0.07\%$.

The $LiYF_4$, $LiErF_4$ ($a = 5.162$ Å, $c = 10.706$ Å [Abe77]) and $LiGdF_4$ ($a = 5.225$ Å, $c = 10.987$ Å [Ran04]) crystals are isostructural (sp. gr. $I4_1/a$) and can form continuous solid solutions $LiY_{1-x-y}Er_xGd_yF_4$. A linear variation of the lattice constants is expected in this case. Thus, we obtain $\Delta a/a_{subst} = 0.04\%$ and $\Delta c/c_{subst} = 0.06\%$ for the codoped layer 6.9 at.% Er, 3.5 at.% Gd:$LiYF_4$ (batch #2) which reasonably agrees with the experimental values.

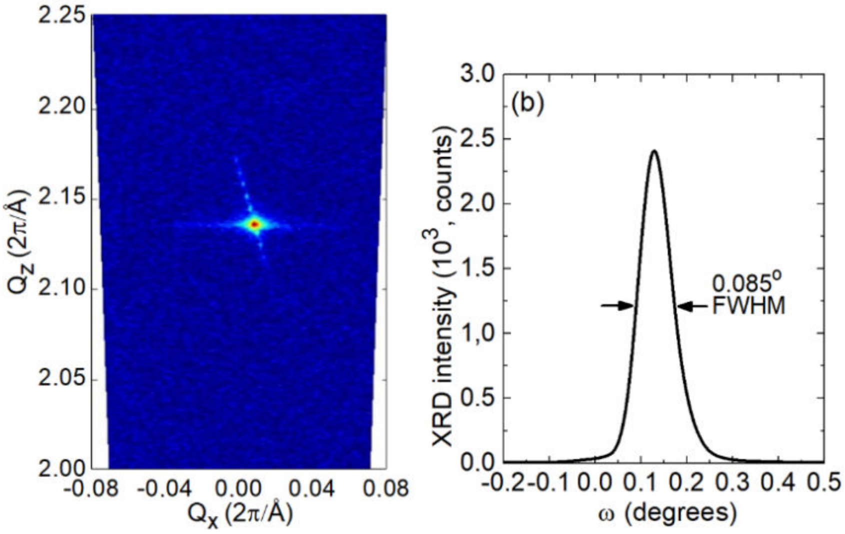

Figure III.9: (a) Reciprocal space mapping of the (103) node for the Er:$LiYF_4$ layer; (b) the rocking curve of this node.

1.2.2 Layer topography

The surface morphology of the as-grown films was studied employing a confocal and scanning electron microscopy.

A brightfield image of the raw top surface of an Er:$LiYF_4$ thin film grown at 745.5 °C is shown in Figure III.10. The central part of the epitaxy was studied. It presents smooth clean areas of the film itself, as well as sharp surface deposited dendritic structures assigned to crystallization of the residual solvent (LiF). The surface of the film is not perfectly flat at the micrometer scale, but it presents irregular “hills” and “valleys”. Very similar growth behavior was observed before for other epitaxial fluoride films ($LiYF_4$ [Bra21], CaF_2 [Bra19]).

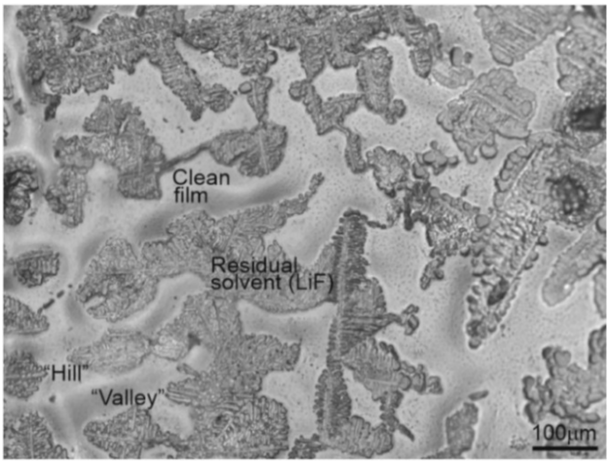

Figure III.10: Observation of the top surface of as-grown Er:$LiYF_4$ thin film. Microscope objective 20×, bright field, reflection mode, $\lambda = 405$ nm.

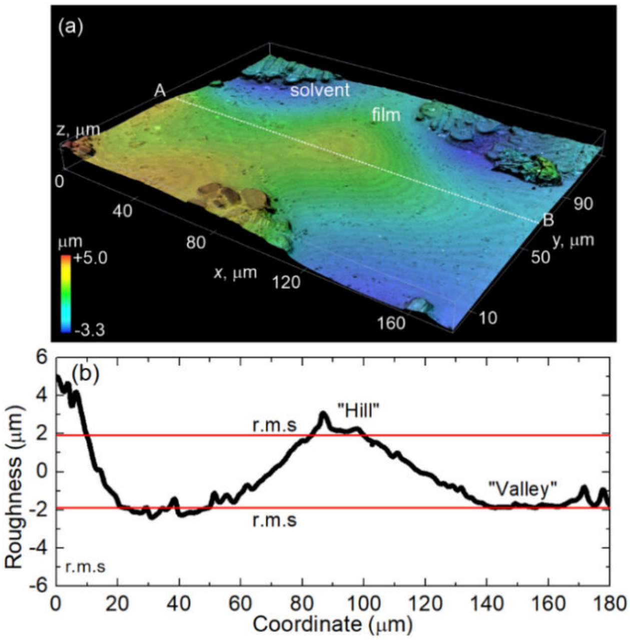

Figure III.11: Surface topography of the as-grown Er:$LiYF_4$ thin film: (a) 3D plot, (b) surface roughness profile along the A – B line, rms – root mean square deviation.

The surface roughness, as well as the remaining LiF on the surface is not critical for potential WG applications. Prior to WG experiments, the epitaxies are subjected to mechanical polishing of both the side and top surfaces. This is needed to precisely control the layer thickness for the desired modal behavior and simultaneously allows for reducing the scattering losses at the input and top surfaces. The as-grown top and polished side surfaces of the Er:$LiYF_4$ film were further studied by SEM, as shown in Figure III.12. Figure III.12(a) reveals polycrystalline LiF partially covering the surface of the film. Figure III.12(b) shows one of the polished side faces. It reveals a clean and flat substrate / layer interface, a uniform and single-crystalline layer without secondary phases, inclusions or cracks, and a small surface deposition of LiF. The layer thickness is measured to be 40 ± 2 μm and it is uniform across the central part of the epitaxy.

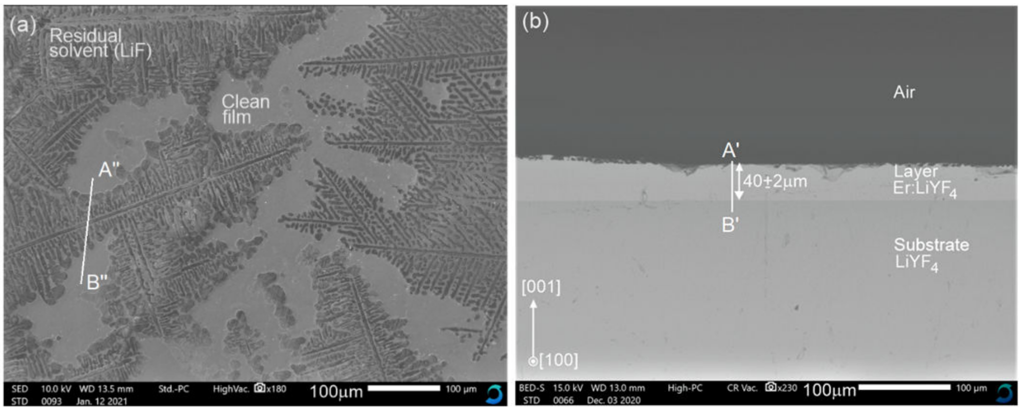

Figure III.12: (a,b) Scanning Electron Microscope (SEM) images of (a) the as-grown top surface and (b) polished end-facet of the Er:LiYF$_4$ / LiYF$_4$ epitaxy.

1.2.3 Compositional analysis

The composition of the films was confirmed by EDX analysis. The EDX spectra of both the substrate (LiYF$_4$) and the layer (Er:LiYF$_4$) were measured, Figure III.13. Both spectra reveal the presence of host-forming elements (Y and F, Li is too light to be detected by EDX). Only in the spectrum of the layer, Er is clearly detected (Mα1, Lα1,2 and Lβ1,2 lines). Other impurity elements in negligible quantities are Si, O and C. The former two elements may originate from the silica tube, while C is a contamination probably coming from the glassy carbon crucible. The fraction of oxygen in the films is too low to cause the formation of an oxyfluoride phase, in agreement with the XRD findings.

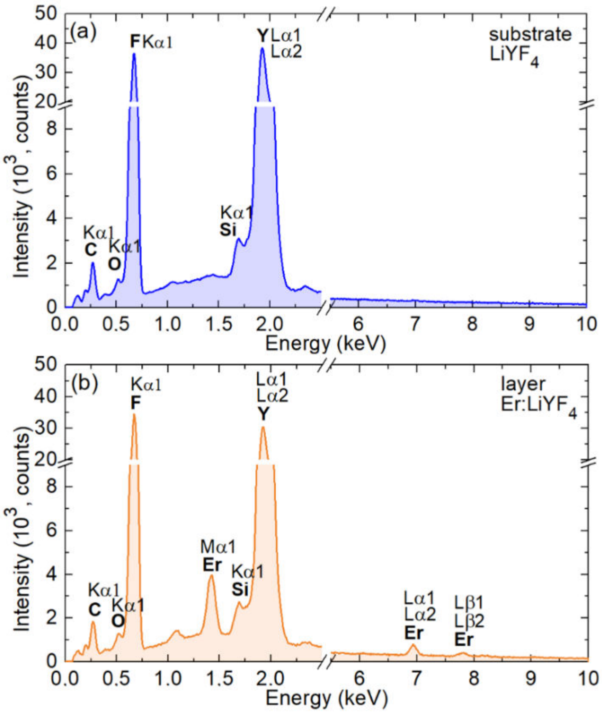

Figure III.13: Energy-dispersive X-ray (EDX) spectra of (a) the Er:LiYF$_4$ epitaxial layer and (b) the LiYF$_4$ substrate (measured in the lateral geometry).

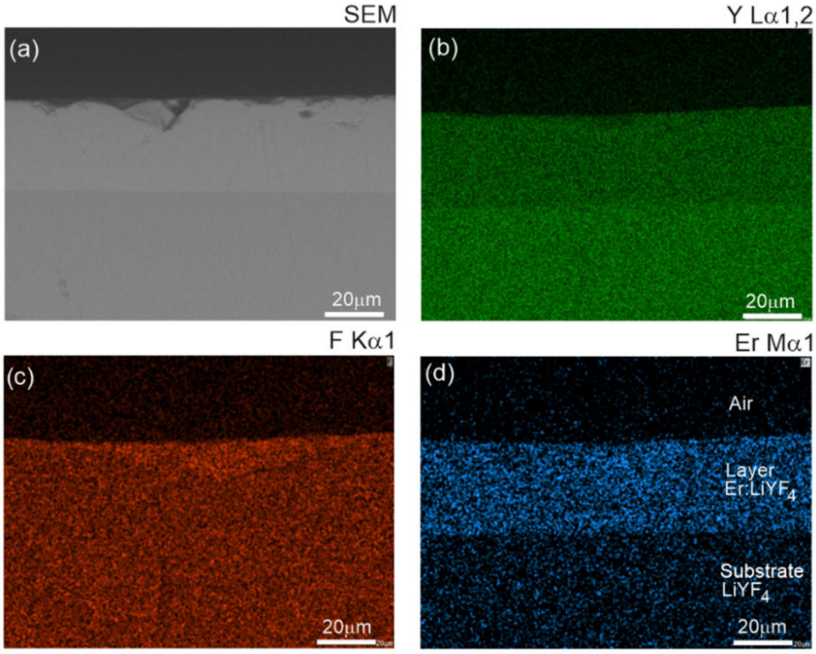

Figure III.14: Element mapping for the Er:LiYF$_4$ / LiYF$_4$ epitaxy (transversal observation): (a) SEM image, (b-d) element maps: (b) Y Lα1,2, (c) F Kα1 and (d) Er Mα1.

EDX-based element mapping was applied to reveal the distribution of Y, Er and F elements on the polished side face of the epitaxy, as shown in Figure III.14. Here of most interest are Figures III.14(c) and (d), illustrating the homogeneous substitution of Y^{3+} ions by Er^{3+} ions. In Figure III.14(c), we observe that the Er:$LiYF_4$ layer is less contrasting owing to depletion by Y^{3+} ions. On the contrary, in Figure III.14(d), the layer area is clearly observed owing to enrichment by Er^{3+} ions.

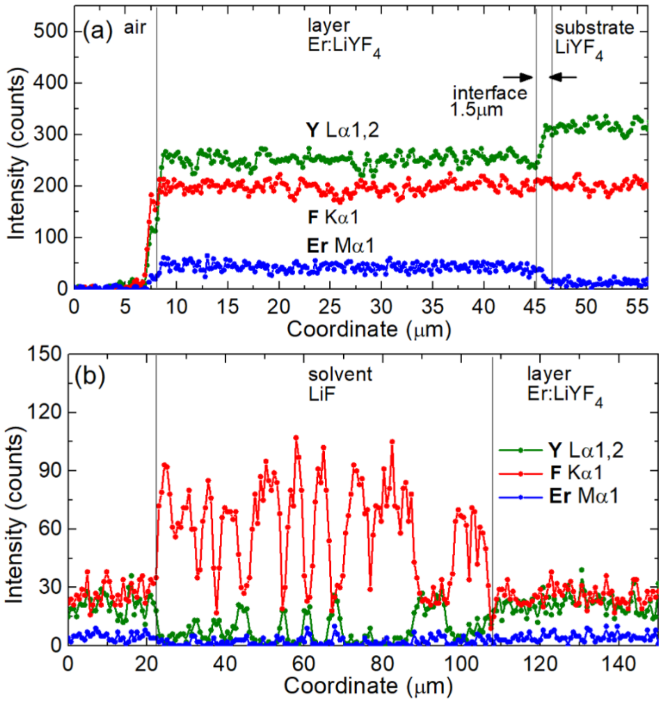

Figure III.15: Element line profiles for the Er:$LiYF_4$ / $LiYF_4$ epitaxy: (a) across the polished side face, A' – B' line, Figure 3.12(b); (b) along the raw top surface, A" – B" line, Figure III.12(a).

The corresponding line element profiles across the layer are shown in Figure III.15(a). The Y content in the layer decreases with respect to the substrate while the Er content increases representing the $LiY_{1-x}Er_xF_4$ substitution. The F content is the same in the substrate and the layer indicating no deviation from the stoichiometry in the layer. The Er^{3+} ions are uniformly distributed in the layer. The upper limit for the substrate / layer interface, estimated from the element line profile of Y, is less than 1.5 μm. A similar analysis was applied to the raw top surface of the epitaxy. The line element profiles of Y, Er and F were analyzed along a line crossing the surface dendritic structures; as shown in Figure III.15(b). A strong enhancement of the F signal and a corresponding decrease of the Y and Er signals were detected for spatial positions corresponding to such structures. This clearly confirms that these structures contain no Y and Er elements and are composed of LiF likely.

1.3 Spectroscopic characterization of the Er, Gd:$LiYF_4$ epitaxy

1.3.1 Polarized Raman spectroscopy

The polarized Raman spectroscopy were measured using a polished end-facet of the epitaxy in the ***a(ij)a*** configuration (where both *i, j* = π or σ), according to the Porto's notations [Dam66]. The studies were performed for both the $LiYF_4$ substrate and the Er^{3+}:$LiYF_4$ layer in the frequency range 100-500 cm^{-1}. The results are shown in Figure III.16.

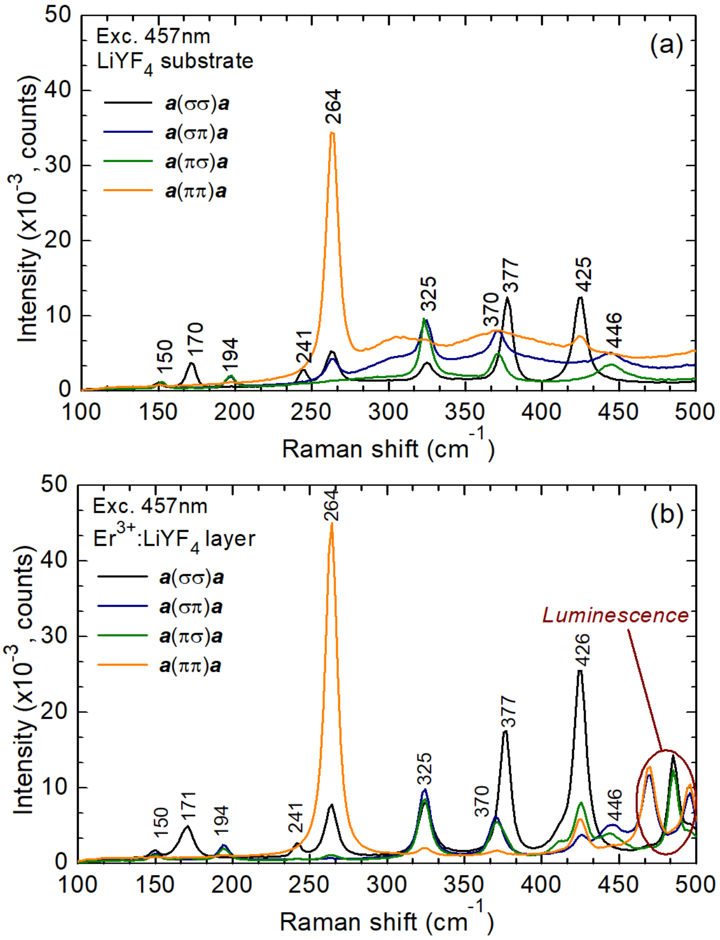

Figure III.16: Polarized Raman spectra of the undoped $LiYF_4$ substrate (a) and the LPE-grown 11 at.% Er:$LiYF_4$ layer (b) in the ***a***(*ij*)***a***, where *i*, *j* = π, σ, configuration (Porto's notations), *numbers* indicate Raman frequencies in cm^{-1}, λ_{exc} = 457 nm.

$LiYF_4$ crystallizes in scheelite-type structure having 2 formula units per unit cell. Its primitive cell has 36 vibrational modes. At the center of the Brillouin zone Γ ($\boldsymbol{k}$ = 0), these vibrational modes are distributed over the irreducible representations of C_{4h} as follows: $3A_g + 5B_g + 5E_g + 5A_u + 3B_u + 5E_u$ [Mil70]. One A_u and one E_u modes correspond to *rigid* translations of the whole crystal, and other A_u and E_u modes are IR-active. The *gerade* (g) modes ($3A_g$+$5B_g$ + $5E_g$) are Raman-active and the remaining modes (B_u) are silent.

In the Raman spectra of the substrate, Figure III.17(a), the most intense mode at 264 cm^{-1} is assigned as A_g. The highest energy vibrations are observed at 426 (B_g) and 446 (E_g) cm^{-1}. These two are related to the Li motions. In $LiYF_4$, the internal binding of the $[LiF_4]^-$ tetrahedra does not differ too much from other ionic forces in the crystal, so it is difficult to assign the internal and external vibrations [Mil70]. Observed Raman frequencies for the substrate and layer are summarized in Table III.2.

Table III.2: Frequencies of Raman active phonon modes in scheelite-type $LiYF_4$ and $LiErF_4$.

Phonon symmetry	**This work**		**Miller *et al* [Mil70] $LiYF_4$**	**Salaun *et al* [Sal97] $LiErF_4$**	
	Substrate	**Layer**			
A_g (cm^{-1})	150	150	-	151	
	264	264	264	270	
	425	426	425	430	
B_g (cm^{-1})	170	171	177	153	
	241	241	248	215	
	325	325	329	326	
	377	377	382	378	
	425	426	427	430	Li motion
E_g (cm^{-1})	150	150	153	129	
	194	194	199	179	
	325	325	329	330	
	370	370	368	368	
	446	446	446	450	Li motion

In the Er^{3+}:$LiYF_4$ layer, the polarized Raman spectra are shown in Figure III.16(b). The Raman spectra measurement is not trivial in case of Er^{3+} ions, only the excitation at 457 nm gives rise to convenient spectra. Otherwise, additional luminescence lines as intense as the Raman lines are observed in the spectra. Especially, at λ_{exc} = 514 nm, the broad luminescence bands coming from upconversion transition $^4S_{3/2} \rightarrow {}^4I_{15/2}$. Only slight shifts in the position of the band peaks (within 1 cm^{-1}) are observed. This agrees with the Raman observations for stoichiometric $LiErF_4$ [Sal97]. Maximum phonon energy of Er^{3+}:$LiYF_4$ layer are observed at 446 cm^{-1} as for the substrate. Therefore, given energy gap of

~3500 cm^{-1} for the $^4I_{11/2}$ – $^4I_{13/2}$ transition, the probability of non-radiative multi-phonon relaxations from upper laser level is low according to energy gap law.

The primary distinction between $LiYF_4$ and $LiErF_4$ crystals in terms of their dynamic properties is the mass of trivalent ions. Because the weight of the Er^{3+} ion is approximately twice that of Y^{3+}, the modes involving trivalent ion displacements should experience a significant decrease in frequency. In Table III.2, we observe this shift for the E_g and B_g symmetry modes at low frequencies. Only the Raman-active modes with E_g and B_g symmetries may involve lanthanide motion. Furthermore, it can be inferred that heavy lanthanide ions primarily vibrate at low frequencies [Sal97].

1.3.2 Absorption

• Room-temperature absorption

The results of the room temperature absorption measurements are displayed in Figure III.17. The Figure III.17(a) shows the overview absorption spectrum 10.8 at.% Er^{3+}:$LiYF_4$ epitaxy in the near IR and visible spectral range. The absorption coefficient was calculated by Equation (III.1):

$$\alpha_{\mathrm{abs}} = \frac{-\ln\left(\frac{T}{T_0}\right)}{t} \qquad \text{(III.1)}$$

The observed absorption bands are owing to transitions of Er^{3+} ions from the ground-state ($^4I_{15/2}$) to various excited-states ranging from $^4I_{13/2}$ up to $^4G_{9/2}$ and $^2K_{15/2}$.

The absorption cross-section, σ_{abs}, spectra for transitions of Er^{3+} ions from the ground-state $^4I_{15/2}$ to the excited-states $^4I_{13/2}$ and $^4I_{11/2}$ are shown in Figures III.17(b,c) for σ-polarization. The absorption cross-sections were calculated as:

$$\sigma_{\mathrm{abs}} = \alpha_{\mathrm{abs}} / N_{Er} \qquad \text{(III.2)}$$

where $N_{\mathrm{Er}} = 14.96 \times 10^{20}$ cm^{-3} is the Er^{3+} ion density. This value was estimated by comparison with the absorption cross-section, σ_{abs}, spectra for a 4.75 at.% Er^{3+}:$LiYF_4$ single-crystal with determined Er^{3+} ion density given in thesis of Christophe Labbe [Lab99]. For Er^{3+}:$LiYF_4$ layer only σ-polarization ($\boldsymbol{E} \perp \boldsymbol{c}$, $\boldsymbol{k} \perp \boldsymbol{c}$) is available due to the layer orientation. For the $^4I_{15/2} \rightarrow {}^4I_{13/2}$ transition (which corresponds to in-band pumping for 1.6 μm lasers and terminal level pumping for ~2.8 μm lasers), the maximum σ_{abs} is 0.97×10^{-20} cm^2 at 1490.8 nm and the absorption bandwidth is 7.3 nm (full width at half maximum, FWHM). For the $^4I_{15/2} \rightarrow {}^4I_{11/2}$ one (upper laser level pumping for ~2.8 μm lasers), σ_{abs} is 0.47×10^{-20} cm^2 at 972.6 nm.

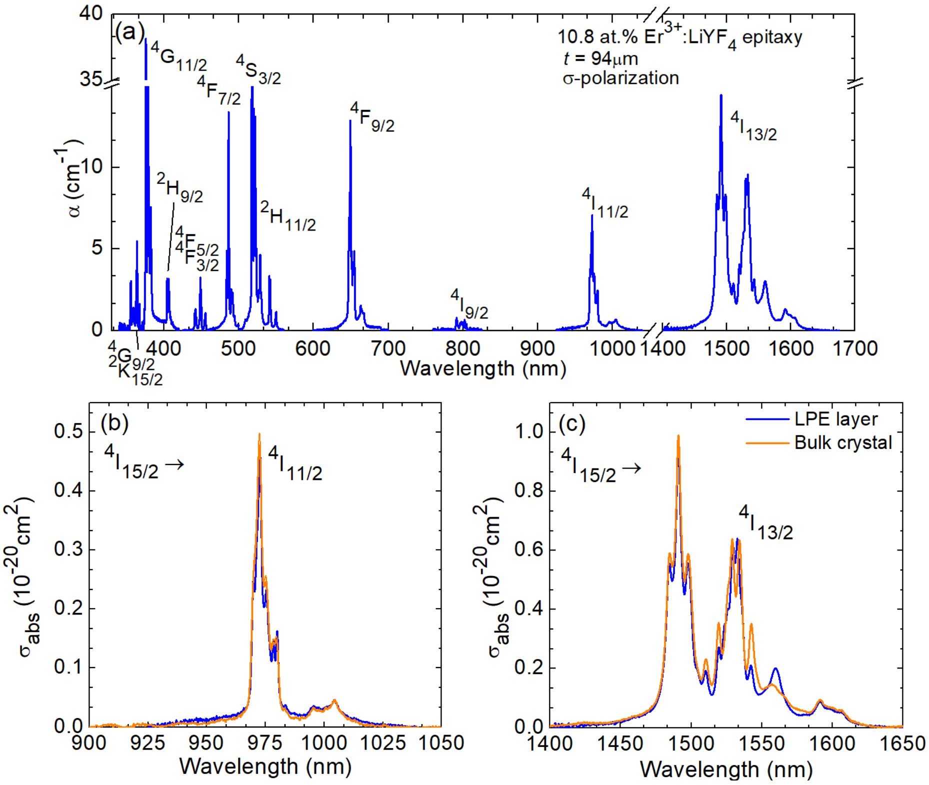

Figure III.17: Optical absorption of Er^{3+}:$LiYF_4$ epitaxy: (a) Overview absorption spectra in the visible and near IR spectral range; (b,c) Absorption cross-section spectra for: (b) $^4I_{15/2} \rightarrow {}^4I_{11/2}$, (c) $^4I_{15/2} \rightarrow {}^4I_{13/2}$ transitions compared with the absorption cross-section, σ_{abs}, spectra for a 4.75 at.% Er:$LiYF_4$ single-crystal (in *orange*), both for σ-polarization.

The actual concentration of Er^{3+} ions in the layer was determined from optical absorption measurements using known absorption cross-sections for Er^{3+} ions in $LiYF_4$ [Pay92]. For the 11 at.% Er:$LiYF_4$ layer (the starting composition), the actual doping level amounted to 10.8±0.7 at.% Er, so that the segregation coefficient for Er^{3+} ions, $K_{Er} = C_{layer}/C_{solution}$, where C is the doping level, was 0.98±0.06. Close to unity value of K_{Er} is due to the closeness of ionic radii of Y^{3+} and Er^{3+} ions for VIII-fold fluorine coordination. The segregation coefficients for various RE^{3+} ions in $LiYF_4$ epitaxial films [Loi18] are summarized in Figure III.18.

They are plotted versus the ionic radius. According to the Onuma's principle, this dependence can be expressed using the following equation: $K_{RE} = 1 - C(R_{RE} - R_Y)^2$, where C is a material-dependent constant [Sub20]. The points in Figure 19 are well fitted using this dependence yielding $C = 58 \pm 5$ Å^{-2}. According to the previous study, $K_{Gd} = 0.70$, so that the actual doping levels for the layer grown using the batch composition #2 are 6.9 at.% Er, 3.5 at.% Gd.

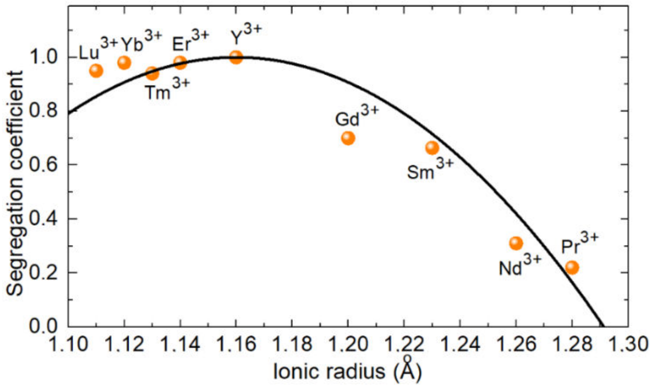

Figure III.18: Segregation coefficient of the rare-earth ions, RE^{3+} in $LiYF_4$ epitaxial films as a function of their ionic radii for VIII-fold fluorine coordination: *symbols* – experimental data ([Loi18] and this work), *curve* – their parabolic fit (see explanations in the text).

The refractive index difference between the layer and the substrate, $\Delta n = n_{\mathrm{layer}} - n_{\mathrm{substrate}}$, can be estimated from the refractive indices of the parent compounds, $LiYF_4$, $LiErF_4$ and $LiGdF_4$. All these crystals are optically uniaxial (positive, $n_o < n_e$). For the films grown on (001) oriented $LiYF_4$ substrates, both principal light polarizations, π and σ (corresponding to the refractive indices n_e and n_o, respectively), are available for light propagating in the plane of the layer (i.e., in the WG configuration).

By using the following values (taken at ~1.06 µm, due to the data availability): $n_o = 1.4480$, $n_e = 1.4702$ ($LiYF_4$ [Bar80]), $n_o = 1.466$, $n_e = 1.492$ ($LiErF_4$ [Vas12]) and $n_o = 1.474$, $n_e = 1.502$ ($LiGdF_4$ [Web18]), we obtain $\Delta n_o = 1.9\times10^{-3}$ and $\Delta n_e = 2.4\times10^{-3}$ for the singly-doped epitaxy 10.8 at.% Er:$LiYF_4$ (batch #1) and $\Delta n_o = 2.2\times10^{-3}$ and $\Delta n_e = 2.6\times10^{-3}$ for the codoped one 6.9 at.% Er, 3.5 at.% Gd:$LiYF_4$ (batch #2). Here, we assumed a linear variation of the refractive index for the solid-solution $LiY_{1-x-y}Er_xGd_yF_4$. For the calculated values, it is clear that π-polarization (TM, in the WG geometry) provides higher refractive index contrast. Single Er^{3+} doping in high concentrations (~10 at.% and above) provides relatively high Δn values, so that Gd^{3+} codoping, which may increase the risk of layer fracture due to the stronger lattice distortion, is not necessary.

• Low-temperature spectroscopy

The crystal-field splitting for Er^{3+} multiplets in Er^{3+}:$LiYF_4$ epitaxial layer was revealed under cryogenic temperature (12K) from LT absorption and emission spectra. We determined experimentally the Stark energies for all Er^{3+} multiplets ranging from $^4I_{15/2}$ up to $^4G_{9/2}$ as shown in Figure III.19. Due to the layer orientation, only σ-polarization was available.

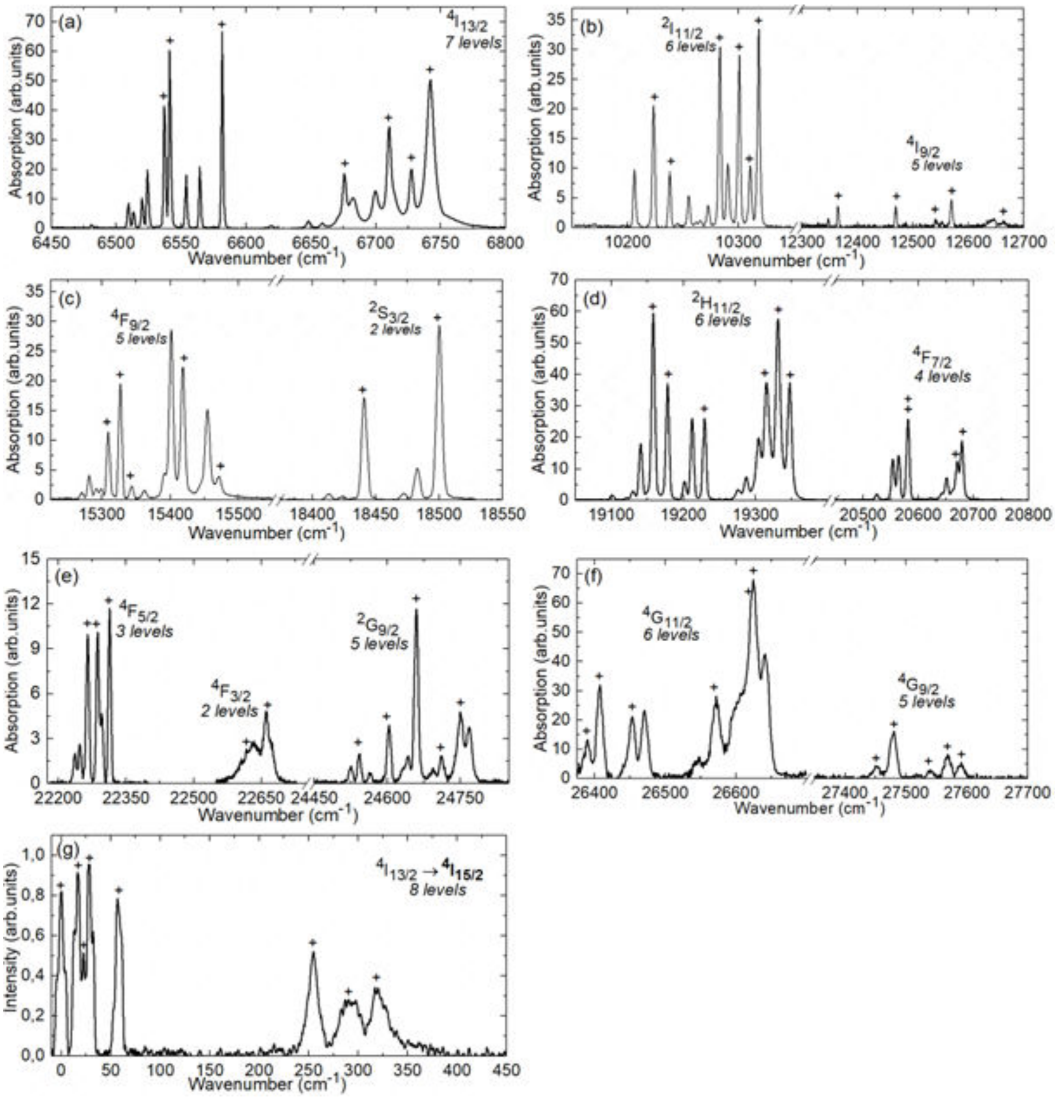

Figure III.19: LT (12 K) spectroscopy of Er^{3+} ions in $LiYF_4$ epitaxial layer for σ-polarization: (a-f) absorption spectra; (g) emission spectra for the $^4I_{13/2} \rightarrow {}^4I_{15/2}$ transition.

All Stark components of Er^{3+} multiplets in $LiYF_4$ layer are listed in Table III.3. There is a slight variation in the position of the Er^{3+} Stark sub-levels as compared to that taken from the literature [Jay89]. This is probably caused by the polarization chosen, namely by differences in the selection rules for MD and ED transitions.

Table III.3: Crystal-field splitting for Er^{3+} ions in Er:$LiYF_4$ epitaxial layer obtained in this work and in Er: $LiYF_4$ bulk crystal taken from the literature [Jay89].

Manifold	**Stark components, cm^{-1}**
$^4I_{15/2}$	0, 16, 23, 28, 57, 255, 291, 319
	0, 15, 23, 53, 247, 286, 325, 352*
$^4I_{13/2}$	6537, 6541, 6581, 6675, 6710, 6728, 6742
	6536, 6540, 6579, 6672, 6696, 6725, 6739*
$^4I_{11/2}$	10223, 10238, 10283, 10300, 10310, 10318
	10222, 10239, 10285, 10303, 10320, 10355*
$^4I_{9/2}$	12364, 12469, 12541, 12568, 12665
	12369, *missing*, 12549, 12575, 12671*
$^4F_{9/2}$	15309, 15469, 15344, 15418, 15471
	15314, 15333, 15349,15425, 15477*
$^2S_{3/2}$	18441, 18500
	18238, 18497*
$^2H_{11/2}$	19158, 19179, 19229, 19314, 19331, 19348
	19157, 19176, 19228,19313, 19330, 19346*
$^4F_{7/2}$	20581, 20584, 20669, 20679
	20576, *missing,* 20666, 20674*
$^4F_{5/2}$	22265, 22287, 22314
	22226, 22259, 22306*
$^{k4}S_{3/2}$	22621, 22660
	22609, 22306*
$^2H_{9/2}$	24541, 24601, 24659, 24710, 24749
	24523, 24584, 24640, 24695, 24750*
$^4G_{11/2}$	26390, 26408, 26453, 26571, 26620, 26625
	missing, 26407, 26464, 26565, 26593, 26636*
$^4G_{9/2}$	27450, 27480, 27538, 27568, 27590

"*" indicates the crystal-field splitting for Er^{3+} ions in Er:$LiYF_4$ taken from [Jay89]

1.3.3 Polarized luminescence

The stimulated-emission (SE) cross-sections, σ_{SE}, for the $^4I_{11/2} \rightarrow {}^4I_{13/2}$ transition of Er^{3+} ions in the Er:$LiYF_4$ epitaxial layer were calculated using the Füchtbauer–Ladenburg equation, Figure. III.20. The considered transition has both electric-dipole (ED) and magnetic-dipole (MD) contributions, so that three polarization states were considered: σ ($\boldsymbol{E} \perp \boldsymbol{c}$, $\boldsymbol{k} \perp \boldsymbol{c}$), α ($\boldsymbol{E} \perp \boldsymbol{c}$, $\boldsymbol{k} \parallel \boldsymbol{c}$) and π ($\boldsymbol{E} \parallel \boldsymbol{c}$, $\boldsymbol{k} \perp \boldsymbol{c}$). Here, ***E*** and ***k*** are the light polarization and propagation direction, respectively.

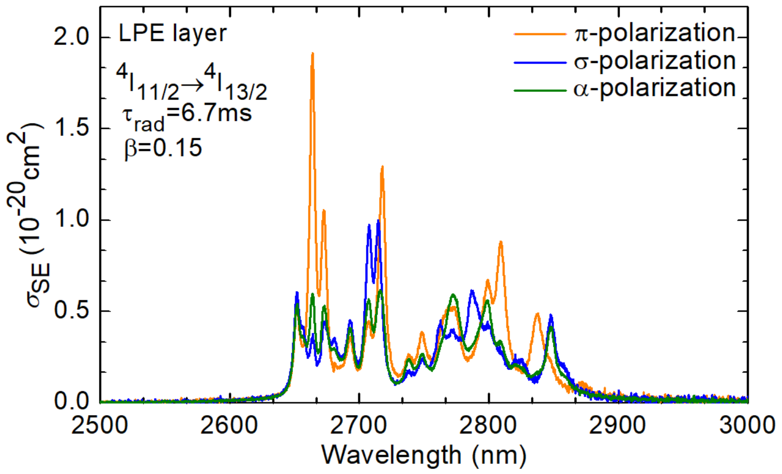

Figure III.20: Stimulated emission cross-section spectra of Er^{3+} ions from the Er:$LiYF_4$ epitaxial layer for the $^4I_{11/2} \rightarrow {}^4I_{13/2}$ transition.

Table III.4: Peak emission cross-sections for the $^4I_{11/2} \rightarrow {}^4I_{13/2}$ transition in Er^{3+}: epitaxial layer for π- and σ- polarizations compared to literature data [Kno92, Lab00, Die96].

Polar.	***λ*, nm**	***σ*SE, 10^{-20} cm^2**		***Δλ*, nm**
		This work	Literature	
π (***E*** ∥ ***c***, ***k*** ⊥ ***c***)	2663.2	1.91	2.1 [Kno92], 2.23 [Lab00], 3.8 [Die96]	5.2
	2673.0	1.06		6.9
	2717.6	1.30	1.41 [Lab00], 1.75 [Kno92],	6.8
	2809.4	0.88	1.8[Die96], 0.9[Lab00], 1.25 [Die96]	11.1
	2838.0	0.49		14.5
σ (***E*** ⊥ ***c***, ***k*** ⊥ ***c***)	2707.6	0.97		7.9
	2714.6	1.0	0.9 [Lab00]	7.9
	2786.5	0.62		26.1
	2848.2	0.48	0.3 [Lab00]	10.3

The maximum σ_{SE} is 1.91×10^{-20} cm^2 at 2663.2 nm for π-polarization and 1.0×10^{-20} cm^2 at 2714.6 nm for σ-polarization. It should be noted that the obtained values of the SE cross sections are somewhat different from those given in the literature [Kno92, Lab00, Die96]. The greatest contrasts are observed for the most intense SE cross-section peak at 2663.2 nm for π-polarization. Diening *et al.* reported the maximum value of 3.8×10^{-20} cm^2 at 2661 nm. The slightest variation in the cross-sections is observed with those given by Labbé *et al.* The intensity difference of the SE cross-sections can be attributed to several factors: deviation in the crystal orientation, contribution of water absorption in this spectral region, and differences in the selection rules of Stark sub-levels for MD and ED transitions.

1.3.4 Luminescence dynamics and ETU parameters

The luminescence lifetimes, τ_{lum} of different multiplets of Er^{3+} ions (from $^4I_{13/2}$ to $^4S_{3/2}$) were systematically studied. They are listed in Table III.5. For comparison, the lifetimes of Er^{3+} ions in the 1 at.% Er:$LiYF_4$ crystal reported by Rubin *et al.* [Rub86] are also given. Figure III.21 shows the luminescence decay curves for the levels involved in the ~2.8 µm laser transition, $\tau_{\mathrm{lum}}(^4I_{11/2})$ = 3.43 ms and $\tau_{\mathrm{lum}}(^4I_{13/2})$ = 7.51 ms. As shown in the Table III.5, the highly Er^{3+}-doped $LiYF_4$ epitaxial layer characterizes by more favorable ratio of upper-to-lower-level lifetimes thanks to efficient ETU1 transfer (Figure III.22). Upon Er^{3+} doping, the lifetime of the terminal laser level is considerably reduced, while the emitting level remains roughly constant.

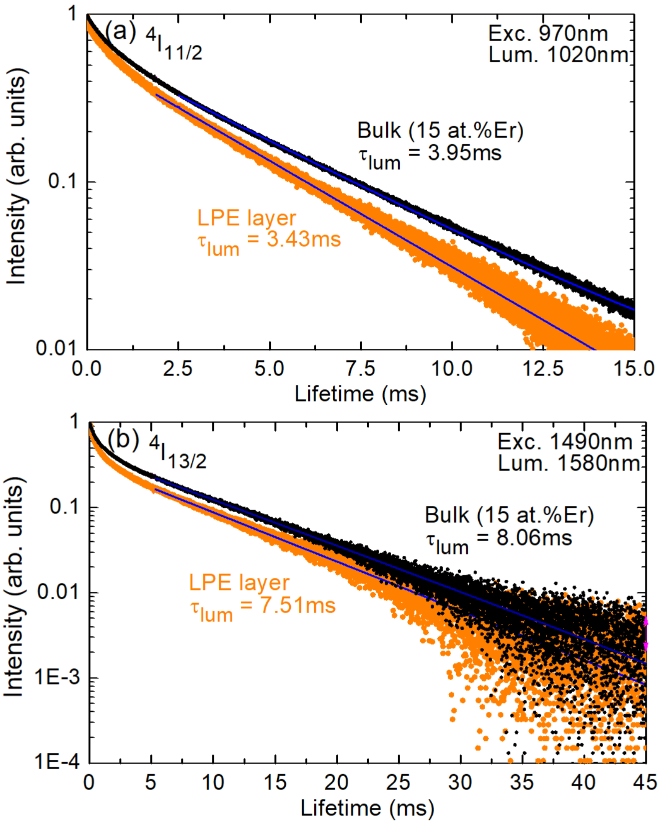

Figure III.21: Luminescence decay curves for emission from the (a) $^4I_{11/2}$ and (b) $^4I_{13/2}$ states of Er^{3+} ions in the 10.8 at.% Er^{3+}:$LiYF_4$ epitaxial layer, λ_{exc} = 970 nm and 1490 nm.

When single-exponential fits do not properly describe a luminescence decay curve, it is expected that interionic processes are taking place such as the ETU and cross-relaxation. The energy level scheme with energy transfer mechanisms is shown in Figure III.22. In order to simulate the relationship between energy transfer rates and luminescence decay, a few models have been proposed, namely the Burshtein [Bur72] or Inokuti-Hirayama (IH) [Ino65] model (ω=0) due to a dipole-dipole interaction when the total donor decay $\tau > \tau_A$ is calculated using Equation (III.3):

$$I_1(t) = I_0\left\{\exp(-\frac{t}{\tau_D} - \omega t - \gamma\sqrt{t}) - (\exp(\frac{t}{\tau_A})\right\} \tag{III.3}$$

Here, τ_A is the total lifetime of the acceptor exited state and τ_D is the intrinsic lifetime of the donor excited ion, γ is the energy transfer constant ($s^{-1/2}$) between donor and acceptor and ω gives the donor to acceptor energy transfer constant including donor excitation migration.

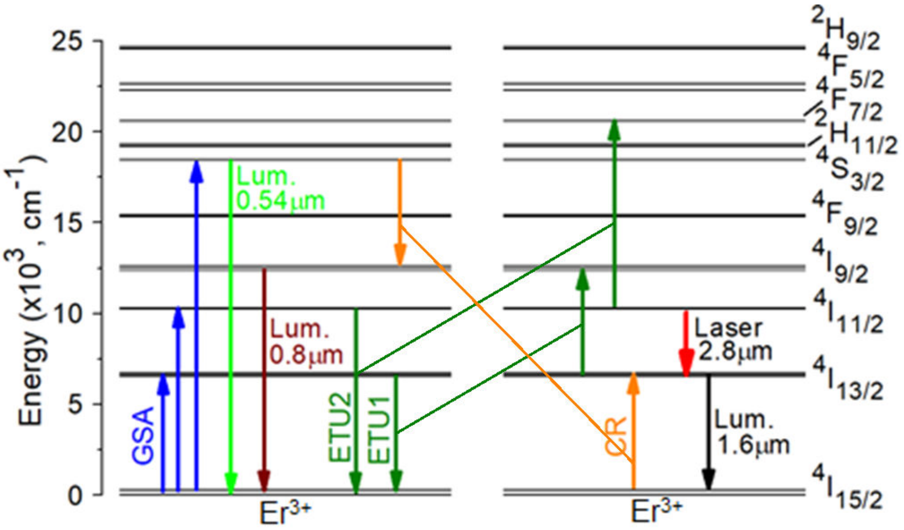

Figure III.22: Energy level scheme obtained from LT spectroscopy of Er^{3+} ions in $LiYF_4$ epitaxial layer (this work) and energy transfer mechanisms occurring in the system: (1) $^4I_{13/2} + {}^4I_{13/2} \rightarrow {}^4I_{9/2}$ (ETU1), (2) $^4I_{11/2} + {}^4I_{11/2} \rightarrow {}^4I_{F7/2} - h\omega \rightarrow {}^4S_{3/2}$ (ETU2) and, (3) $^4S_{3/2} + {}^4I_{15/2} \rightarrow {}^4I_{9/2} + {}^4I_{13/2}$ (CR).

Table III.5: Summary of the measured luminescence lifetimes, τ_{lum} for main Er^{3+} multiplets obtained from the lifetime measurements for LPE layer (10.8 at.% Er^{3+}) and bulk (15 at.% Er^{3+}) and comparison with lifetimes reported in the work [Kno92].

Multiplet	**τ_{lum}, ms**		
	Layer 10.8 at.% Er^{3+}:$LiYF_4$	Bulk 15at.% Er:$LiYF_4$	Bulk 1at.%Er:$LiYF_4$ [Kno92]
$^4I_{13/2}$	7.51	8.06	10
$^4I_{11/2}$	3.43	3.95	2.9
$^4I_{9/2}$	0.007	0.003	0.007
$^4F_{9/2}$	0.058	0.074	0.055
$^4S_{3/2}$	0.018	0.010	0.4

Figure III.23(a) shows the ETU1 luminescence of the $^4I_{9/2}$ level measured at $\lambda_{\mathrm{lum}} = 816$ nm and excitation at $\lambda_{\mathrm{exc}} = 1490$ nm. Using IH model, the best fit was performed with energy transfer parameters: $\gamma_{\mathrm{ETU1}} = 109$ $s^{-1/2}$, $\omega = 0$ s^{-1}, and $\tau_D = 7.51$ms. The rise time (τ_A) is amounted to be 7 μs corresponds luminescence lifetime of $^4I_{9/2}$ level. Using obtained ET parameters, we calculated the total donor lifetime τ by following Equation (III.4):

$$\tau = \int_0^{\infty} \exp\left(-\frac{t}{\tau_D} - \omega t - \gamma\sqrt{t}\right) dt \qquad \text{(III.4)}$$

Thus, the ETU1 rate constant in s^{-1} is calculated as $W_{11} = \tau^{-1} - \tau_1^{-1}$ and amounts to $W_{11} = 6360$ s^{-1} (where $\tau = 154$ μs and τ_1 is the $^4I_{13/2}$ level lifetime equal to 7.51 ms).

The parameters for ETU2 were calculated in the same manner as for ETU1. As shown in Figure 3.23(b), the ETU2 luminescence of the $^4S_{3/2}$ state at 556 nm was measured under excitation at 970 nm. The best-fitting parameters were $\gamma_{\mathrm{ETU2}} = 63$ $s^{-1/2}$, $\omega = 0$ s^{-1}, and $\tau_D = 4.5$ ms. The ETU2 rate constant is $W_{22} = 1992$ s^{-1} using $\tau = 438$ μs, and τ_3 is the $^4I_{11/2}$ level lifetime equal to 3.43 ms.

To calculate the CR rate constant, we observed luminescence from $^4S_{3/2}$ excited state measured at 556 nm, as shown in Figure III.23(c). Using the Burstein model, namely the first term in equation IH describing donor decay, the best fitting parameters were determined as $\gamma = 115$ $s^{-1/2}$, $\omega = 4.1\times10^4$ s^{-1}, and $\tau_D = 400$ μs. Thus, the CR rate constant W_{CR} was calculated as $W_{\mathrm{CR}} = \tau_{\mathrm{int}}^{-1} - \tau_D^{-1} = 5.4\times10^4$ s^{-1}.

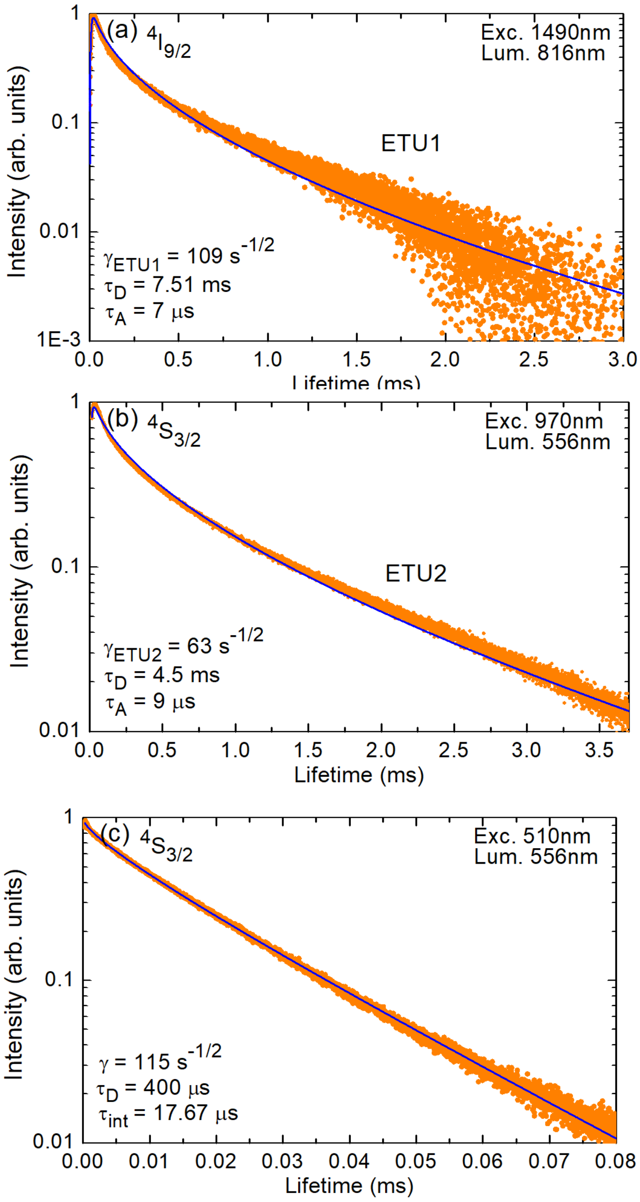

Figure III.23: Luminescence dynamics of Er^{3+} ions in the 10.8 at.% Er^{3+}:$LiYF_4$ epitaxial layer: (a) ETU1 luminescence of the $^4I_{9/2}$ excited state measured at 816 nm, , λ_{exc} = 1490 nm; (b) ETU2 luminescence of the $^4S_{3/2}$ excited state measured at 556 nm, λ_{exc} = 970 nm; (c) Luminescence decay of the $^4S_{3/2}$ state measured at 556 nm, λ_{exc} = 510 nm.

The experimentally obtained ET rate parameters are listed in Table III.6.

Table III.6: Experimental energy transfer rate parameters given in (s^{-1}) and in (cm^{3}s^{-1}) taking into account erbium concentration, $N_{Er} = 14.96 \times 10^{20}$ cm^{-3}.

	ETU1	**ETU2**	**CR**
This work	W_{11} (s^{-1})	W_{22} (s^{-1})	W_{CR} (s^{-1})
	6360	1992	5.4×10^4
	W_{11} (cm^3 s^{-1})	W_{22} (cm^3 s^{-1})	W_{CR} (cm^3 s^{-1})
	4.25×10^{-18}	1.33×10^{-18}	3.61×10^{-17}

1.4 Mid-infrared planar Er:LiYF$_4$ waveguide: Waveguiding experiment

The passive waveguiding properties of the polished Er:LiYF$_4$/LiYF$_4$ epitaxy were confirmed using a setup depicted in Figure III.25(a). As a laser source, we have used a continuous-wave Ti:Sapphire laser emitting a nearly diffraction limited ($M^2 \approx 1$) linearly polarized output. The laser wavelength was tuned to 925 nm (out of Er^{3+} absorption) and the laser polarization was set to be horizontal (σ). The laser radiation was coupled into the 40 μm thick layer using an aspherical lens with a focal length f = 40 mm. The guided mode at the output facet of the epitaxy was reimaged using a short focal length (f = 15 mm) CaF$_2$ lens and a CCD camera. The mode had a horizontal stripe profile characteristic for planar WGs (as there is no mode confinement in the plane of the layer), Figure III.25(b).

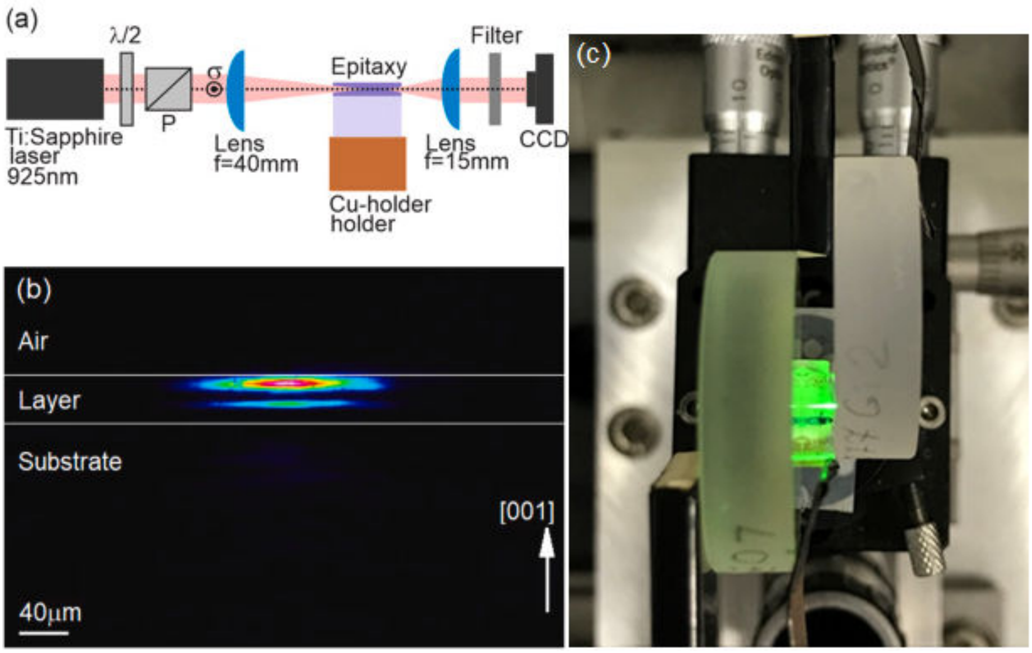

Figure III.24: Passive waveguiding experiment for the Er:LiYF$_4$/LiYF$_4$ epitaxy (layer thickness: t = 40 μm), λ = 925 nm, light polarization: σ (horizontal): (a) experimental setup; (b) near-field profile of the guided mode at the output facet of the epitaxy, *white lines* – layer/air and layer/substrate interfaces drawn as guides for eyes. (c) photograph of the WG in the laser cavity showing green upconversion luminescence from Er^{3+} ions.

2 Erbium-doped CaF_2 epitaxial layers

The as-grown Er^{3+}:CaF_2 / CaF_2 epitaxy is shown in Figure III.25. It can be seen that the epitaxial layer is crack-free and translucent. Meniscus formation is caused by the remaining LiF solvent, which crystallizes onto the substrate at the surface of the molten bath.

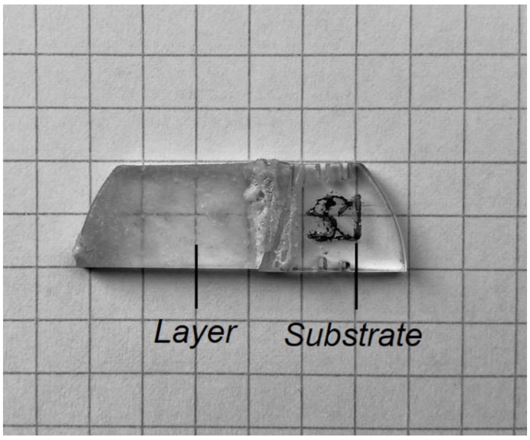

Figure III.25: Photograph of the as-grown Er:CaF_2 /CaF_2 epitaxy grown at 740°C during 42 min using (100)-oriented CaF_2 substrate.

2.1 Material characterization of the Er:CaF_2 epitaxy

The sample described in this sub-section was produced at a growth temperature of 738.5 °C and dipping duration of 70 min in the molten bath.

2.1.1 Powder XRD study of the Er:CaF_2 layer structure

To evaluate the phase purity of the as-grown Er:CaF_2 layer we carried out a powder X-ray diffraction (XRD) analysis of the material crystallized on the layer surface and the layer itself. The Figure III.26 presents XRD pattern of the Er^{3+}:CaF_2 milled polycrystalline matter of epitaxial layer.

The analysis of the X-ray patterns shows, as expected, that the studied substance has a multiphase nature. It consists of cubic CaF_2 structure with lattice constant a = 5.463 Å, LiF with cubic structure, a = 4.027 Å and tetragonal phase like $LiYF_4$. Crystallization of LiF on the top surface of the layer is expected because of the chosen initial composition, in which an excess of solvent (LiF) was present. As for the $LiYF_4$-type phase, it is highly probable that crystals of the $LiErF_4$ composition form in small amounts on the surface of the layer mixing in the polycrystalline phase with the remaining solvent due to ErF_3 doping.

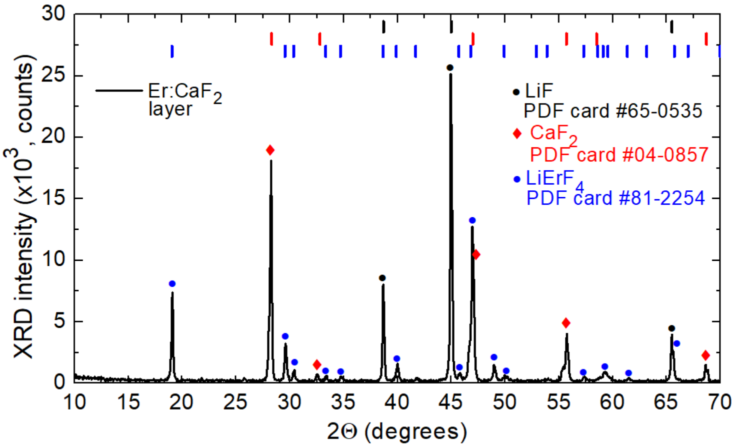

Figure III.26: Powder X-ray diffraction (XRD) pattern of the Er:CaF₂ epitaxial layer. *Red vertical lines* – theoretical peaks for CaF₂ (PDF #04-0857), *black* – theoretical peaks for LiF (PDF #65-0535), *blue* – theoretical peaks for LiYF₄ (PDF #81-2254).

2.1.2 Study of the Er:CaF₂ layer morphology

The surface morphology of the as-grown Er^{3+}:CaF₂ films was observed using a confocal scanning laser microscope (LSM 710, Carl Zeiss) equipped with ×20 and objective, a blue GaN laser (405 nm) at ITMO University. Figure III.27 shows the results of this observation. First, a transmission mode observation of the polished end-facet of the film is shown in Figure III.28(a), revealing a layer with the thickness, $t = 20 \pm 2$µm with a clear and uniform layer / substrate interface without apparent inclusions.

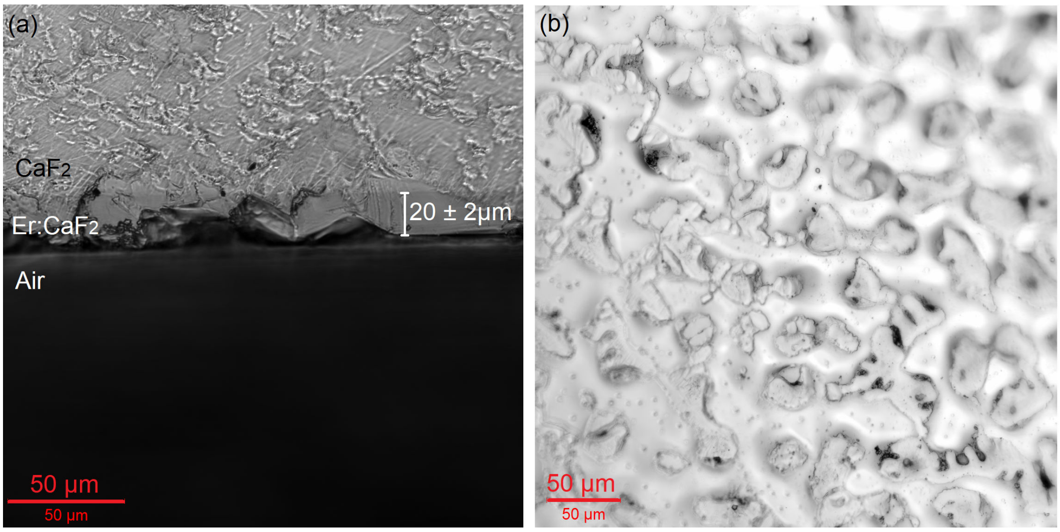

Figure III.27: Transmission mode observation of an LPE grown Er^{3+}:CaF₂ layer using a confocal scanning laser microscope with ×20 magnification: (a) polished end-facet; (b) layer top surface.

The Er^{3+}:CaF_2 epitaxial layer exhibit a smooth surface which looks like as a hilly-valley landscape on the micrometer scale as shown in Figure III.27(b). This can be partly explained by thermodynamic considerations, namely the surface energy of a curved surface is less than that of a perfectly flat one. As a result, the growth front takes on a more stable configuration at the atomic level during the LPE growth. The growth mechanisms involved in this crystallization process could be also correlated to the specific surface topography of the epitaxies. Additionally, surface topography of the as-grown Er^{3+}:CaF_2 layer was characterized by confocal microscopy. Figure III.28(a) shows a color top view of a three-dimensional topography of the clean part of the film surface free from residual solvent crystallization due to the thermal gradient in the molten bath. A 2D transverse profile along the A-B segment was extracted from it, as shown in Figure III.29(b). Thus, the RMS roughness is measured as less than 100 nm and the pear-valley (PV) is about 400nm.

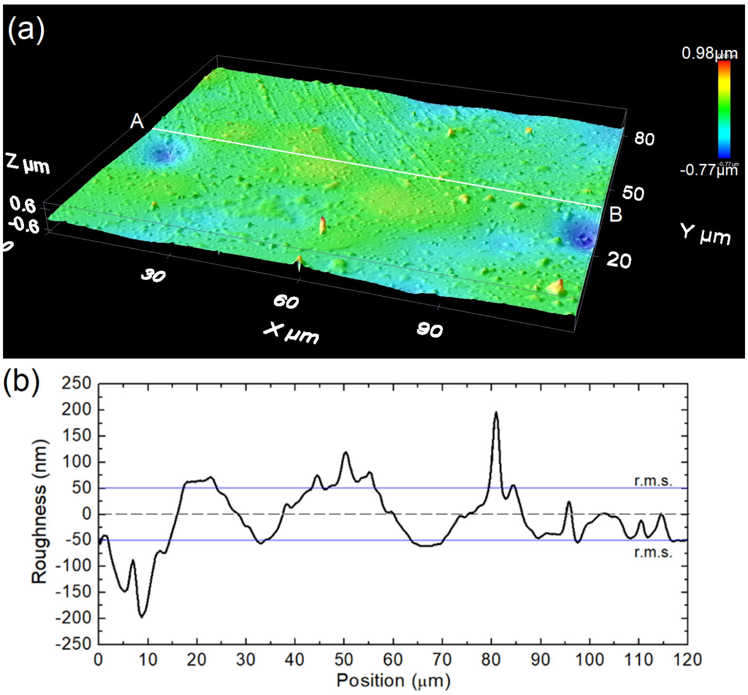

Figure III.28: (a) 2D topography map for the as-grown Er^{3+}:CaF_2 LPE layer; (b) Surface profile plot: *blue lines* indicate the range of root-mean-square (RMS) deviation of the roughness, A - B is the analyzed direction.

Figure III.29 shows an SEM image of the grown top surface of the film, revealing the crazing of the layer. It results in a rectangular-shaped pattern with characteristic dimensions of hundreds of µm. Several factors probably influence crazing phenomenon: (i) film thickness (less likely for films several nanometers thick), (ii) Er^{3+} doping level (more likely in heavily doped layers due to lattice distortion and lattice parameter mismatch with the substrate), and (iii) difference in thermal expansion coefficients between the layer and the substrate. Similar patterns were observed in CaF_2 films grown by molecular beam epitaxy (MBE) on (100) oriented InP substrates and (111) oriented Si substrates [Sin85, Sch85], where this phenomenon was explained by a change in lattice parameter mismatch during growth and at room temperature. In the case of homoepitaxy (our case), the lattice mismatch is relatively weak (estimated as $\Delta a/a_{\mathrm{subst}} = 0.12\%$), so other factors, such as the thermal expansion coefficient, may play a significant role, which we discuss in the next Sub-section.

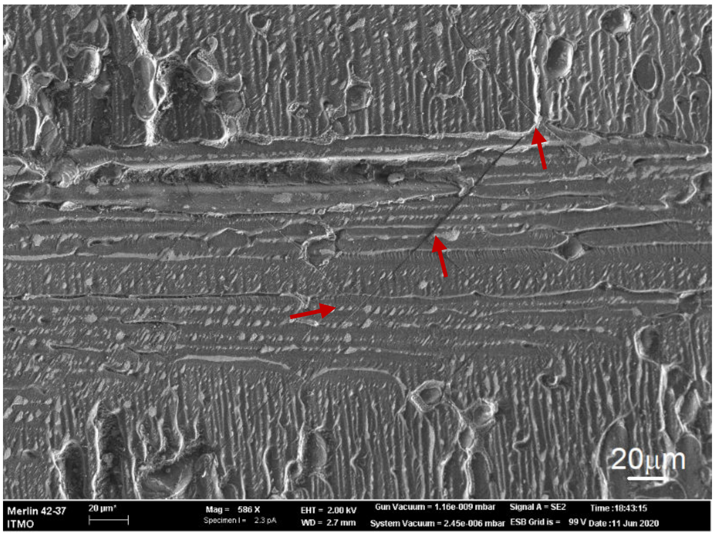

Figure III.29: (a) 2D topography map for the as-grown Er^{3+}:CaF_2 LPE film; (b) Surface profile plot: *blue lines* indicate the range of root-mean-square (RMS) deviation of the roughness, A - B is the analyzed direction.

2.1.3 Thermal expansion of the Er:CaF_2 crystal

To understand the origins of the crazing effect in the Er:CaF_2 epitaxial layers we measured the thermal dependence of the unit cell parameter of the 5at.% Er CaF_2 crystal from the room temperature to 500 °C using the X-ray diffraction technique, as shown in Figure III.31(a). This experiment have been performed by Rosa Maria Solé at University of Rovira i Virgili (Tarragona, Spain).

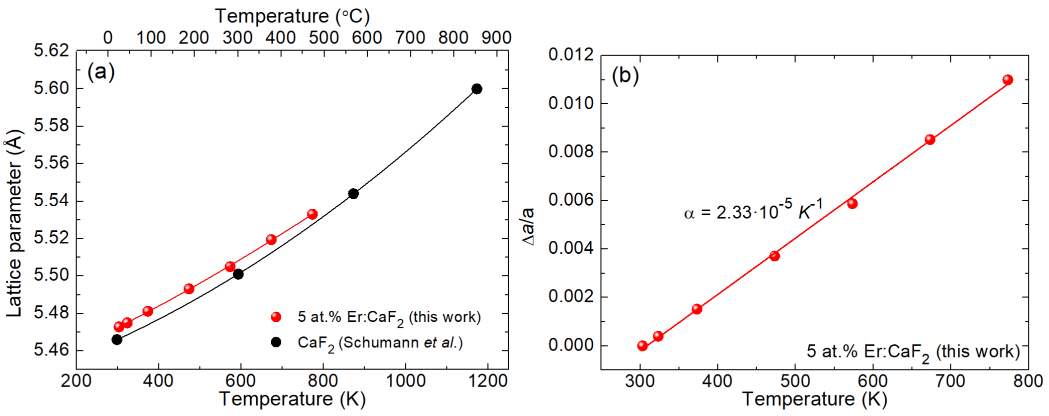

Figure III.30: (a) Lattice parameter *a* of the 5at.% Er:CaF$_2$ crystal as a function of temperature (*red*) and for comparison, the same dependence for undoped CaF$_2$ crystal from [Sch84] is given (*black*); (b) Dependence of thermal expansion, *Δa/a vs.* temperature, the linear thermal expansion coefficient (α) is determined as a slope of the linear fit.

When it refers to the coefficient of thermal expansion, it reflects the change in linear dimensions of an object when the temperature rises. The linear expansion coefficient is calculated as:

$$\alpha = \frac{1}{l_0}\frac{dl}{dT} \tag{III.6}$$

Where l_0 is a linear dimension of the object and dl/dT is the rate of change of that linear dimension per unit change in temperature. In our case, the linear thermal expansion coefficient of the 5at.% Er:CaF$_2$ bulk crystal was determined to be 2.33×10^{-5}K^{-1}. It is the slope of the linear fit in the graph *Δa/a vs.* temperature in Figure III.31(b). We can consider this value for the 5at.% Er:CaF$_2$ crystal to be an acceptable approximation for the linear thermal expansion coefficient of epitaxial layer of CaF$_2$ with 4.5at.% Er^{3+} doping. This value of linear thermal expansion coefficient is higher than that provided for undoped CaF$_2$ substrates at room temperature by Crystran, the substrate supplier, which is about 1.88×10^{-5} K^{-1}. Consequently, the discrepancy in the coefficient of thermal expansion at room temperature between the film and the substrate after cooling is 24% which is significant. However, it is biased to consider only the thermal expansion coefficient given at room temperature to describe the thermal expansion evolution of the films compared to that of their substrate at high temperatures, especially during the cooling stage. Therefore, Figure III.32 shows the variation in the linear thermal expansion coefficient versus temperature for Er^{3+}-doped (this work) and undoped CaF$_2$ crystals reported in the literature by Schumann *et al.* [Sch84].

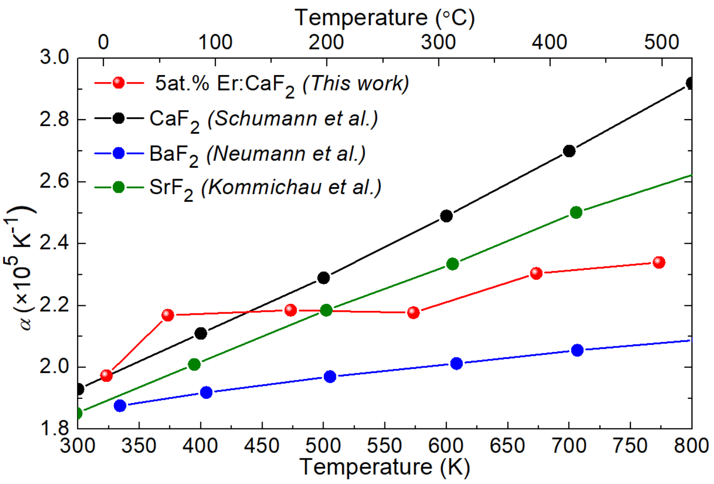

Figure III.31: Variation of linear thermal expansion coefficient, α (× 10^5 K^{-1}) for the Er:CaF$_2$ crystal with temperature in comparison with that of for undoped CaF$_2$, BaF$_2$ and SrF$_2$ crystal given in [Sch84, Neu86, Kom86].

The graph shows that undoped CaF$_2$ crystals have a faster increase in the coefficient of linear thermal expansion when heated. According to Schumann *et al.* [Sch84], this increase ranges from 1.97 to 2.86 × 10^5 K^{-1} for temperature range of 50- 500°C, which means that thermal expansion of the CaF$_2$ substrate is larger and increases faster than that of the Er:CaF$_2$ epitaxial film and let us note that at high temperatures, a potential deviation can reach 18.5%. This can introduces stress and local defects leading to a cracking of the films during cooling. Table III.7 provides the α values for undoped CaF$_2$ in the temperature range of 50-500°C and shows the deviation between these values and those for 5at.% Er:CaF$_2$.

Table III.7: Variation of linear thermal expansion coefficient of Er:CaF$_2$, undoped CaF$_2$ with temperature in the range of 50 – 500 °C.

Temperature, °C	**α × 10^5, K^{-1}**	
	Er:CaF$_2$ *(this work)*	**CaF$_2$ [Sch84]**
50	1.97	1.97
100	2.17	2.06
200	2.19	2.25
300	2.18	2.44
400	2.30	2.64
500	2.33	2.86

How can we overcome the problem of different thermal expansion coefficients between the film and the substrate and thus improve the quality of the epitaxies? The only solution to this challenge is to choose a substrate material with a lower coefficient of thermal expansion as well as a slower change in this parameter under heating. In this case, the isotypes of CaF$_2$, namely SrF$_2$ and BaF$_2$, could be suitable candidates for use as substrates. As shown in Figure III.32, comparing the thermal expansion coefficients of BaF_2 and CaF_2 at high temperatures in the range of 300-800 K, it can be seen that $\alpha(CaF_2)$ is consistently higher than $\alpha(BaF_2)$ at temperatures above 300 K. In addition, the rate of increase in the coefficient of thermal expansion with temperature was higher for CaF_2 than for BaF_2 [Neu86]. Furthermore, the use of BaF_2 substrates can lead to a significant lattice mismatch of up to 12%, given the larger Ba^{2+} ion radius compared with that of the Ca^{2+} ion. Therefore, the use of SrF_2 substrates could improve the film quality by reducing the contribution of the thermal expansion coefficient and the lattice mismatch between the layer and substrate. Because $\alpha(SrF_2)< \alpha(CaF_2)$ at high temperatures and simultaneously, these values are closer to the typical values for $Er:CaF_2$, and the expected lattice mismatch is estimated to be approximately 5.6%. It should be noted that the crystal lattice mismatch also changes with temperature. This was clearly demonstrated in the work described in [Kom86]. Herein, the CaF_2 layers were grown on InP substrates, and despite heteroepitaxial growth, the lattice mismatch at the considered growth temperatures was of the order of 0.0%. However, when these films are cooled, the difference in lattice constants between the film material and the substrate inevitably leads to cracking of the grown layer.

2.1 Spectroscopy of Er^{3+} ions in CaF_2 epitaxial layers

2.2.1 Absorption

For the absorption studies, a 4.5at.% $Er^{3+}:CaF_2$ epitaxy and 4.5at.% $Er^{3+}:CaF_2$ bulk crystal for comparison. The substrate was covered by the layer on one side (layer thickness: $t = 28\pm5$ µm).

The RT absorption spectrum of $Er^{3+}:CaF_2$ epitaxy shown in Figure III.33(a) displays broad and smooth bands (a “glassy-like” behavior) of Er^{3+} ion transitions from the ground state ($^4I_{15/2}$) to the excited states ($^4I_{13/2}$ to $^4G_{9/2}$). This is due to the doping mechanism of CaF_2, where Er^{3+} ions replace Ca^{2+} cations, and an interstitial fluorine anion (F^-) is needed to balance the charge.

The absorption bands shape of the 4.5 at.% $Er:CaF_2$ film differs from that of bulk crystal with similar Er^{3+} concentration as shown in Figure III.34(b,c). The difference in the shape of the spectrum may be due to (i) a tendency of “slow” cluster formation in $Er^{3+}:CaF_2$ epitaxial film which have been already observed previously in CaF_2 LPE- and MBE-grown film doped with RE ions [Osi71, Bau91, Dar94, and Loi21] and (ii) different types of formed clusters, possible presence of still significant portions of isolated ions at these doping levels and structural imperfections in thin layers affecting the local crystal field. As found by Bausa *et al.*, lower growth temperatures affect the predominant formation of clusters involving several Nd^{3+}–F^- pairs in the case of Nd-doped CaF_2 films obtained by epitaxial growth as compared to bulk crystal growth at melting temperatures [Bau91]; (iii) the presence of oxygen-assisted sites in the film that can modify the shape of the spectrum. We have already encountered this problem before with LPE-grown CaF_2 films doped with Yb^{3+} and Tm^{3+} ions [Loi19, Loi21].

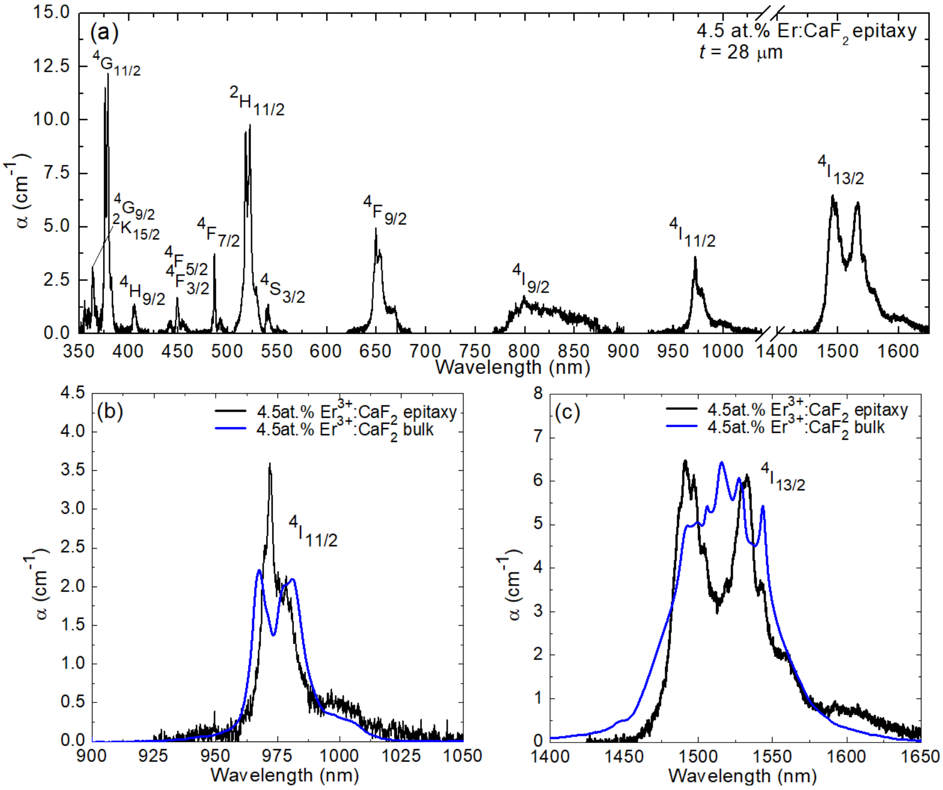

Figure III.32: RT absorption of Er^{3+}:CaF_2 epitaxy: (a) An overview absorption spectrum in the visible and near IR spectral range for 4.5at.% Er^{3+}:CaF_2 film *(black)*; (b,c) Absorption spectra for: (b) $^4I_{15/2} \rightarrow {}^4I_{11/2}$, (c) $^4I_{15/2} \rightarrow {}^4I_{13/2}$ transitions compared with the absorption spectra for a 4.5 at.% of Er^{3+}:CaF_2 single-crystal *(blue)*.

2.2.2 Low-temperature spectroscopy

To date, low-temperature absorption and luminescence spectra have been intensively studied to determine the Er^{3+} centers present in CaF_2 crystals [Tal75, and Moo81] and MBE-grown thin films [Dar94] for different Er^{3+} doping concentrations. However, Er^{3+} sites in CaF_2 thin films formed during LPE growth have not been studied previously. Therefore, in the following section, we will try to shed some light on the different Er^{3+} sites formed in the CaF_2 crystalline layers produced by liquid-phase epitaxy.

- **Site analysis: isolated ions *vs.* clusters**

Er^{3+}:CaF_2 is a highly complex crystal because of the presence of multiple sites for Er^{3+} doping. The distribution of these sites is influenced by several factors, including the interaction energies between Er^{3+}-F_i^- pairs, number of equivalent positions for F_i^-, and temperature history of the crystal. One of the identified sites for the Er^{3+} dopant is an A site or C_{4v} site with F_i^- at (100) position. This site has tetragonal symmetry and is characterized by a strong interaction between the Er^{3+} ion and the fluoride interstitial ion. Another site is a B site or C_{3v} site with F_i^- in the [111] direction, which has trigonal symmetry and is characterized by a weaker interaction between the Er^{3+} ion and the fluoride interstitial ion. In addition to these sites, there is also a cubic site (O_h) where the Er^{3+} ion experiences negligible perturbation from the fluoride interstitial ion. The distribution of these sites changes with the concentration, with fewer available lattice sites for distant compensation at higher concentrations. This leads to an increase in dipolar interactions, which, in turn, leads to the clustering of Er^{3+}-F_i^- pairs (C, D(1), D(2) sites). Table III.8 summarizes the types of crystallographic sites in Er^{3+}:CaF_2 with their formulas according to notation given by Tallant *et al.* [Tal75].

In the case of the Er^{3+}:CaF_2 thin films grown by LPE, the site assignment is not trivial because of the complexity of the optical spectra of Er^{3+} ions in general, as well as the temperature regime of epitaxial growth (830 °C), which differs significantly from the growth of bulk crystals (1450 °C). Daran *et al.* showed that growth temperature can modulate the relative proportion of different active centers for Er^{3+} in CaF_2. In case of MBE growth, it was found that isolated Er^{3+} centers are favored at growth temperature range of 500-520°C, whereas increasing or decreasing the temperature leads to an increase in the intensity of the emission associated with the aggregate centers [Dar94]. In addition to the sites listed above, the epitaxial films may contain multiple trigonal sites, so-called oxygen-assisted sites which appear due to the presence of oxygen traces during the growth.

Table III.8: Crystallographic sites in Er^{3+}:CaF_2.

Site notation		**Symmetry**	**Formula**
Isolated ions	LL	Cubic, O_h	$Er_{Ca}\cdot(F_i'$ distrant$)$
	A	Tetragonal, C_{4v}	$(Er_{Ca}\cdot F_i)^x$ (F_i'in (100) position)
	B	Trigonal, C_{3v}	$(Er_{Ca}\cdot F_i)^x$ (F_i'in (111) position)
Clusters	C	Trigonal, C_{3v}	$(2Er_{Ca}\cdot nF_i)$
	D1		$(mEr_{Ca}\cdot nF_i)$
	D2		$(mEr_{Ca}\cdot nF_i)$, $m > 2$
Oxygen-assisted	G1	Trigonal, C_{3v}	$(Er_{Ca}\cdot O_F)^x$
	G2		$(Er_{Ca}\cdot 2O_F\cdot V_F)^x$
	G3		$(Er_{Ca}\cdot 3O_F\cdot 2V_F)^x$
	G4		$(Er_{Ca}\cdot 4O_F\cdot 3V_F)^x$

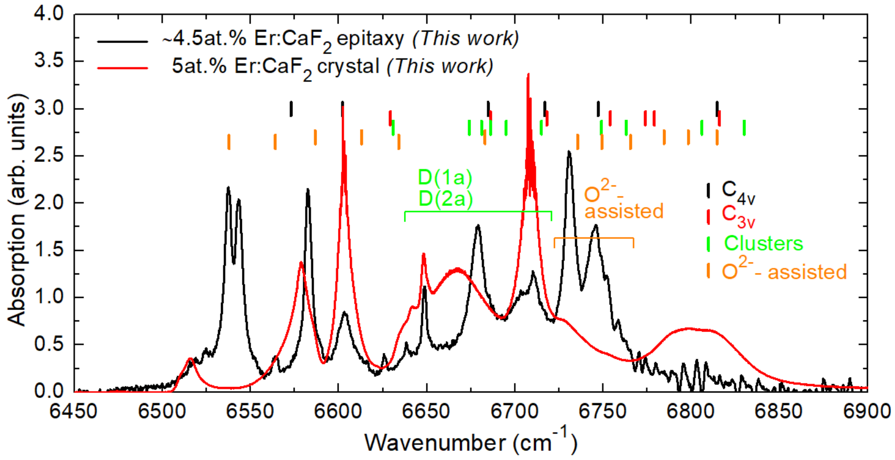

Figure III.33: LT (12 K) absorption spectra of Er^{3+} ions in CaF_2 epitaxial layer *(black)* and bulk crystal *(red)* for the $^4I_{15/2} \rightarrow {}^4I_{13/2}$ transition revealing the crystal-field splitting of $^4I_{13/2}$ multiple, *vertical dashes* –positions of electronic transitions for Er^{3+} ions in clusters and oxygen-assisted sites in CaF_2 given in literature [Tal75].

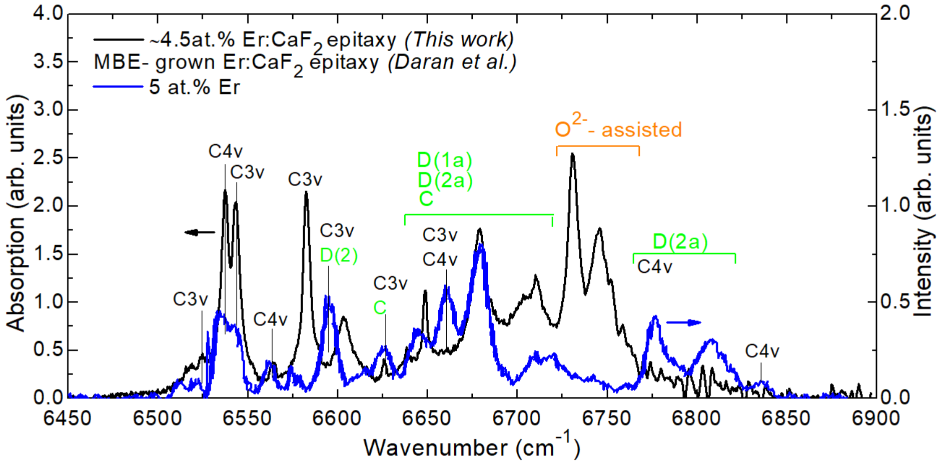

Figure III.34: LT (12 K) absorption spectrum of Er^{3+} ions in LPE-grown CaF_2 epitaxial layer *(black)* for the $^4I_{15/2} \rightarrow {}^4I_{13/2}$ transition; LT luminescence spectra of MBE- grown 5at% Er^{3+}:CaF_2 epitaxial films *(blue)* for the $^4S_{3/2} \rightarrow {}^4I_{13/2}$ transition reported by Daran *et al.* [Dar93].

Firstly, to identify more accurately the transitions related to clusters we have measured low-temperature absorption spectra of the investigated epitaxial film and the 5at.% Er:CaF_2 bulk crystal. This crystal was chosen for comparison because at this doping concentration in bulk crystals a complete transition from isolated ions to clusters is occurred [Pet08]. As shown in Figure III.34, in the LT absorption spectrum of the 4.5 at. % Er:CaF_2 epitaxial films we observe bands referred to the absorption of Er^{3+} ions in clusters, namely in the range 6630-6720 cm^{-1}. We observe also the tendency of "slow" cluster formation as it was shown in previous work about RE^{3+}:CaF_2 films grown by MBE. Daran *et al.* found that the fraction of ions in C4v sites decreases rapidly with increasing Er^{3+} doping level, with almost no isolated ions present at around 6 mol% Er^{3+} doping [Dar94]. Whereas in the 5at. % Er:CaF_2 bulk crystals, the isolated ion clusters are completely absent, as shown in Figure III.34. The clustering effect in CaF_2 crystals is already present when the Er^{3+} concentration is on the order of 1at. % [Dar94]. In addition to the sites assigned to clusters, the epitaxies also contained the oxygen-assisted sites in the range of 6720-6770 cm^{-1}. This is due to the possible slight contamination of the molten bath with residual moisture and/or traces of oxygen in the growth chamber, even though special care was taken to achieve a good secondary vacuum before starting to melt the precursors. In the molten state, fluorides are highly sensitive to oxygen contamination.

The remaining transitions were identified as isolated ion sites, namely trigonal, C_{3v}, and tetragonal C_{4v}. The assignment given for 5 at. % Er:CaF_2 films grown by molecular beam epitaxy was used as a reference [Dar93]. As mentioned above, films are characterized by “slow” cluster formation; therefore, against the background of broadening spectra, we still observe structured bands attributed to the sites of isolated ions, as it shown in Figure III.35.

2.2.3 Mid-IR luminescence spectra and lifetimes

The spectra of the mid-IR luminescence from the Er^{3+}:CaF_2 epitaxial layers are shown in Figure III.36 (λ_{exc} =800 nm, excitation to the $^4I_{9/2}$ state). The emission band is broad and smooth and it spans from 2500 to 3000 nm.

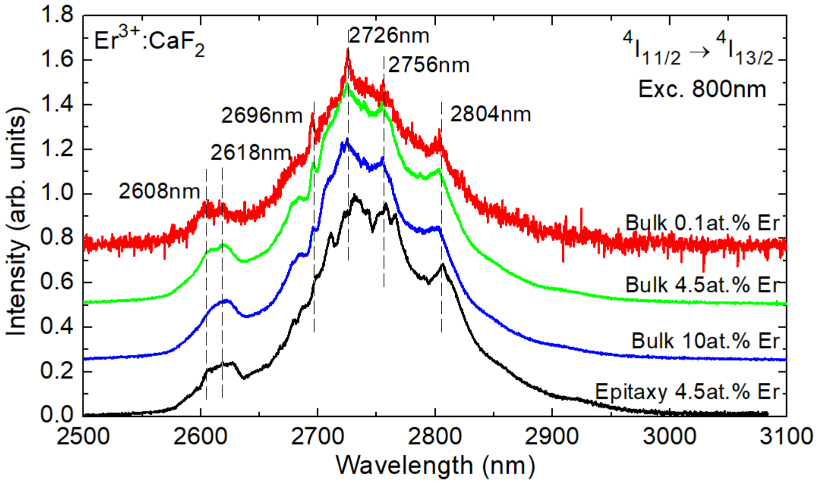

Figure III.35: Luminescence spectra of Er^{3+} ions in the LPE grown ~4.5 at Er^{3+}:CaF_2 layers and in the bulk CaF_2 crystals with Er^{3+} concentrations of 0.1, 4.5, 10at. % for the $^4I_{11/2} \rightarrow$ $^4I_{13/2}$, λ_{exc} = 800nm.

To compare and simplify the interpretation, we plotted the luminescence spectra of different bulk Er^{3+}:CaF_2 crystals with Er^{3+} doping levels varying from 0.1 to 10.%. The results shown in Figure III.36 show that the crystal with the lowest Er^{3+} doping, containing isolated ions, has a series of distinct emission peaks centered at 2608, 2618, 2696, 2729, 2756, and 2804 nm. Some of them are still present and clearly distinguishable in the luminescence spectrum of epitaxy against spectral broadening owing to clustering. The full spectral width at half-maximum (FWHM) for the low-doped crystal is 98 nm. The crystal with the highest Er^{3+} doping, which exhibits strong clustering, shows a wider spectrum (FWHM = 118 nm), indicating a change in the crystal field. The emission bands shape of the epitaxy is very similar to that of the highly doped bulk Er^{3+}:CaF_2 crystal, with residual evidence of the contribution of isolated centers in the form of structured bands.

The RT luminescence decay curves for the epitaxial Er^{3+}:CaF_2 layers are shown in Figure III.37, corresponding to emissions from the $^4I_{11/2}$ and $^4I_{13/2}$ states. Because the layer was quite thin in the order of a few tens of microns, the reabsorption effect can be neglected. This was confirmed by applying the pinhole method in the previous study for ~6at.% Tm-doped CaF_2 film, during which no noticeable change in τ_{lum} with pinhole diameter was detected [Loi21].

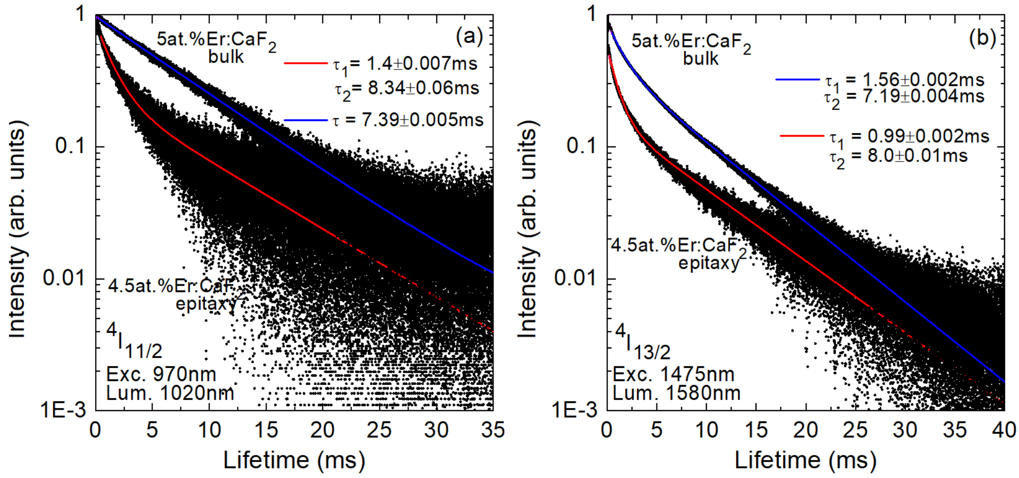

Figure III.36: Luminescence decay curves for emission from the (a) $^4I_{11/2}$ and (b) $^4I_{13/2}$ states of Er^{3+} ions in the 4.5 at.% Er^{3+}:CaF_2 epitaxial layer, λ_{exc} = 970 nm and 1475 nm.

The luminescence decay from the $^4I_{11/2}$ state for the 4.5at.% Er:CaF_2 epitaxy is clearly non-single-exponential, as shown in Figure III.37(a). By applying a biexponential fit (red curve), we obtained τ_{lum1} = 1.4 ± 0.007 ms and τ_{lum2} = 8.34 ± 0.06 ms. This is consistent with the idea of the multi-site nature of this epitaxy sample. The "slow" component is likely attributed to the cluster sites in the epitaxy, this fact can be confirmed by comparison with the decay curve for the bulk 5at.% Er:CaF_2 crystal, where only cluster sites are presented and whose decay curve is described by a single-exponential fit (blue curve) and $\tau_{lum} = 7.39 \pm 0.005$ ms. The "fast" component is assigned to the isolated ions.

The decay curves from the $^4I_{13/2}$ state for the epitaxial $Er:CaF_2$ layer and the bulk 5at.% $Er:CaF_2$ crystal are shown in Figure III.37(b). In both cases, the decay kinetics have a shape characteristic for systems with strong energy transfer. Here, it is the energy transfer upconversion ($^4I_{13/2}$, $^4I_{13/2}$) → ($^4I_{15/2}$, $^4I_{9/2}$), thereby populating the $^4I_{9/2}$ level, followed by fast non-radiative multi-phonon relaxation to $^4I_{11/2}$. For the epitaxy, the "fast" part of the decay curve represents the energy-transfer upconversion, $\tau_1 = 0.99 \pm 0.002$ ms, and the "slow" part corresponds to the intrinsic lifetime of the $^4I_{13/2}$ state, $\tau_2 = 8.0 \pm 0.01$ ms. For the 5at.% $Er:CaF_2$ crystal, the same values of "fast" and "slow" components are calculated, $\tau_1 = 1.56 \pm 0.002$ ms and $\tau_2 = 7.19 \pm 0.004$ ms, respectively.

3 Conclusions Chapter III

To conclude, in this Chapter we summarize the results on the homoepitaxial liquid phase epitaxy growth of Er^{3+}-doped fluoride single-crystalline layers based on $LiYF_4$ and CaF_2. In particular, for Er^{3+}:$LiYF_4$/$LiYF_4$ epitaxies we focused on heavily doped compositions which are essential for getting laser emission at 2.8 μm.

Er^{3+}:$LiYF_4$ epitaxial layers:

(i) Singly Er^{3+} doped and Er^{3+},Gd^{3+} codoped $LiYF_4$ epitaxial layers are of high optical quality are successfully grown by liquid phase epitaxy using LiF as a solvent and a starting composition 73 LiF – 27 REF_3 (mol%) providing the reduced growth temperatures about 746 °C (as compared to compositions being closer to the peritectic one). The growth rates were about 0.8-1.6±0.5 μm/min resulting in layer thickness of 30-90 μm. The layers are single-crystalline and well-oriented (the growth direction along the [001] crystallographic axis). The epitaxy preserved the tetragonal structure (sp.gr. $I4_1/a$) and exhibited relatively low lattice mismatch with respect to the substrate. They showed clear and clean layer / substrate interfaces, a uniform thickness over the substrate without cracks, as well as a homogeneous distribution of Er^{3+} ions.

(ii) We identified the important role of apparent supercooling control affecting the layer growth behavior. When working at a supercooling of 0.5 - 1 °C, the formation of cracks and polycrystalline areas in the layer, as well as excessive solvent deposition on its surface are avoided. A promising approach is the "healing" of the substrate surface by a short hold slightly above the liquidus temperature of the flux with a subsequent layer growth under small supercooling.

(iii)The grown epitaxial layers have strongly polarized mid-infrared luminescence around 2.8 μm according to $^4I_{11/2} \rightarrow {}^4I_{13/2}$ transition and maximum stimulated emission cross-section is 1.91×10^{-20} cm^2 at 2663.2 nm for π-polarization. They exhibited also very favorable ratio of upper-to-lower laser level lifetimes of 3.43 / 7.51 ms, as well as efficient energy transfer upconversion from the terminal laser level, $^4I_{13/2}$, which is relevant for efficient laser operation at 2.8 μm. The waveguiding properties of these layers are demonstrated. Thus, Er^{3+}:$LiYF_4$ epitaxial films are promising for the development of mid-IR waveguide lasers.

Er^{3+}:CaF_2 epitaxial layers:

(i) Er^{3+}-doped CaF_2 were homoepitaxially grown on CaF_2 substrate by liquid phase epitaxy using LiF as a solvent in the range of growth temperatures of 738.5 - 741 °C, layer thicknesses were in the range 20-90 μm depending on the growth duration.

(ii) The main problem for laser applications of the elaborated Er^{3+}:CaF_2 epitaxies is significant crazing effect. This defect appears in Er:CaF_2 films for two reasons: a lattice constant mismatch and a difference in the thermal expansion coefficient between the layer material and the substrate. It has been shown that under our homoepitaxial growth conditions the contribution of the lattice mismatch is negligible and is only $\Delta a/a_{\mathrm{subst}} = 0.12\%$. Whereas the difference in the coefficient of thermal expansion between the Er:CaF_2 layer and CaF_2 substrate at high temperatures (approximately 500°C) reaches 18.5% which is significant and breach the integrity of epilayer. This deviation could be minimized by an appropriate choice of substrate material with lattice parameters close to those of Er:CaF_2 films at high temperatures, namely by using CaF_2 isotypes as substrates. The most suitable candidate in our opinion is strontium fluoride, which has the closest lattice parameters and thermal expansion coefficient to those for the Er^{3+}-doped CaF_2 layer. Nevertheless, in such case, we would have a heteroepitaxy conditions, which, in general, is more difficult to control and not intuitive in the first approximation.

(iii)The perspective of development of the Er:CaF_2 epitaxial layers requires solve of complex physical-chemical problem to reduce the effect of crazing and at the same time to increase the Er^{3+} doping concentration in the layers to ensure that all the ions entered rare-earth clusters which is essential for mid-infrared laser applications.

Chapter IV

Mid-infrared lasers based on erbium-doped fluorite-type crystals

1 Structural & spectroscopic characterization of cubic fluorite-type crystals

1.1 Alkaline earth metal fluoride MF_2 (M = Ca, Sr, Ba and their mixture)

This section presents the results of a study of the spectroscopic characteristics of a group of fluorite-type crystals doped with 5 at.% Er^{3+}. The crystals studied were CaF_2, SrF_2, BaF_2, $(Ca,Sr)F_2$ and $(Ba,Sr)F_2$. As it was already discussed in Chapter II, these crystals were grown using the traditional Bridgman technique. The binary solid-solutions compositions found in the CaF_2 - SrF_2 – BaF_2 system have lower melting points than their parent compounds, which facilitates the growth of crystals with superior optical quality [Naf71, Kli08].

Certain characteristics of Er^{3+}:MF_2 fluorite-type crystals, namely the nominal Er^{3+} doping concentration (at. %), ion density, N_{Er} (10^{20} at/cm^3) and segregation coefficients, K_{Er} are summarized in Table IV.1.

Table IV.1: Summary of studied Er^{3+}:MF_2 (M = Ca, Sr, Ba and their mixture) crystals.

Crystal MF_2	**Er^{3+} doping, at.% (nominal concentration)**	**N_{Er}, 10^{20}at/cm^3**	**K_{Er}**
CaF_2	4.5 5	11.03 12.06	0.99
SrF_2	5	9.96	0.98
BaF_2		7.48	0.89
$(Ba,Sr)F_2$		9.09	0.98
$(Ca,Sr)F_2$		10.86	0.99

1.1.1 Effect of the matrix composition on the Raman spectra

We studied the vibronic properties of Er^{3+}-doped CaF_2 BaF_2, SrF_2, $(Ca,Sr)F_2$ and $(Ba,Sr)F_2$ crystals by Raman spectroscopy, see Figure IV.1(a). The excitation wavelength, λ_{exc} was 457 nm. This wavelength was chosen in order to avoid the overlapping with UC luminescence from the $^4S_{3/2}$ level. The factor group analysis predicts the following irreducible representations for the optical and acoustical modes at the Γ-point ($k = 0$): $\Gamma_{total} = 1T_{2g} + 2F_u$, of which 1 mode ($F_g$) is Raman active and 2 modes (F_u) are IR-active [Bez97].

For all the crystals, only one peak is found in the spectra being characteristic of the cubic fluorite structure (T_{2g} symmetry) [Gee66]. In order M = Ca → Sr → Ba, the phonon energy decreases from 321 to 242 cm^{-1}. Richman *et al.* reported the phonon energies for undoped parent compounds, they are listed in Table IV.2. We observe that their frequencies are slightly higher. This tendency can be explained by the fact that our crystals involve Er^{3+} ions and owing this relatively heavy “impurity” would be expected to lower the frequency of vibrations [Ric64].

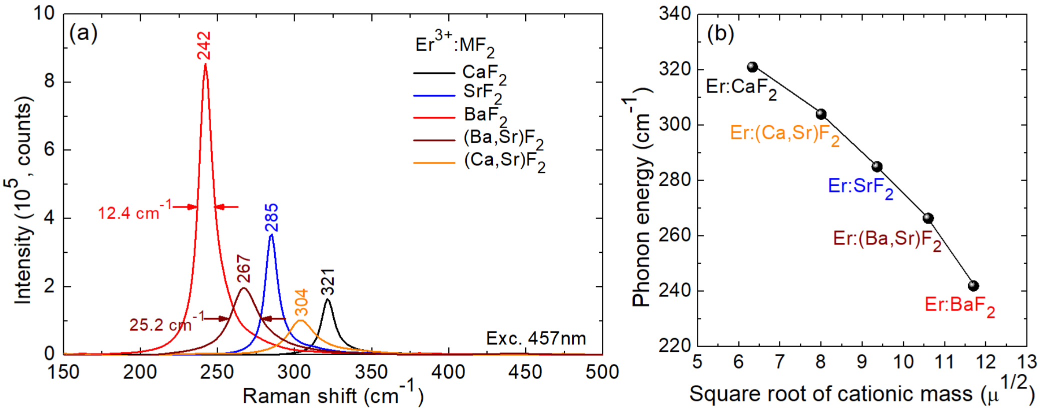

Figure IV.1: (a) Raman spectra of Er^{3+}:BaF_2, Er^{3+}:SrF_2, Er^{3+}:CaF_2, Er^{3+}:(Ca,Sr)F_2 and Er^{3+}:(Ba,Sr)F_2 crystals, λ_{exc} = 457 nm, *numbers* – phonon frequencies; (b) Phonon energy of the host matrix as a function from square root of cationic mass.

The phonon energy of Er^{3+}:BaF_2 (242 cm^{-1}) is smallest among that of other crystal the Raman peak intensity is higher for Er^{3+}:BaF_2. Reminding that the phonon energy is generally proportional to the square root of the inverse of cationic mass ($E \sim 1/\sqrt{M}$) [Uba08] and that of Ba^{2+} cation is heavier than Ca^{2+} and Sr^{2+}, respectively. This trend is illustrated in Figure IV.1(b).

Table IV.2: Summary of phonon energies ($h\omega$) and bandwidths (FWHM) for different MF_2 crystals.

Host crystal	**$h\omega$, cm^{-1}**		**FWHM, cm^{-1}**
	This work	**Literature**	
BaF_2	242	319 [Ric64]	12.4
CaF_2	321	456 [Ric64]	9.6
SrF_2	285	319 [Ric64]	10.5
(Ca,Sr)F_2	304	-	23.5
(Ba,Sr)F_2	267	-	25.2

The phonon energies and bandwidths (FWHM) characteristic for all studied crystals are listed in Table IV.2. For the “mixed” crystal, the Raman peak takes an intermediate position between those for the parent compounds, it is notably broadened and reduced in intensity (FWHM: 25.2 cm^{-1}, compare with 12.4 cm^{-1} for Er^{3+}:BaF_2). The Raman spectroscopy results suggest that the substitution of Sr^{2+} with Ba^{2+} or Ca^{2+} in (Ca/Ba,Sr)F_2 crystals leads to a decrease in phonon energy and an increase in Raman peak intensity. The broadening and reduction in intensity of the Raman peak in the “mixed” crystals indicate the formation of a solid-solution with no distinct crystalline domains.

1.1.2 Optical absorption: spectral behavior depending on the fluoride composition

The absorption measurements were performed at room temperature in near-infrared spectral range for two pump transitions at ~ 0.80 µm and ~ 0.97 µm suitable for pumping by commercial laser diodes.

The absorption cross-sections, σ_{abs}, for the $^4I_{15/2} \rightarrow {}^4I_{9/2}$ pump transition are plotted in Figure IV.2(a). The most intensive peak $\sigma_{abs} = 0.21\times10^{-20}$ cm^2 at 801.1 nm is observed for Er^{3+}:(Ba,Sr)F$_2$ crystal and its absorption bandwidth (FWHM) is 9.3nm. Parent crystals, in turn, have less intense absorption cross-sections that their “mixed” counterparts, equal of 0.09, 0.13 and 0.18 ×10^{-20} cm^2 for Er^{3+}:CaF$_2$, Er^{3+}:SrF$_2$ and Er^{3+}:BaF$_2$, respectively. At the same time, they exhibit broader spectra. Additionally, we observe the slight red shift in wavelength of peak absorption for “mixed” compounds in comparison with parent ones.

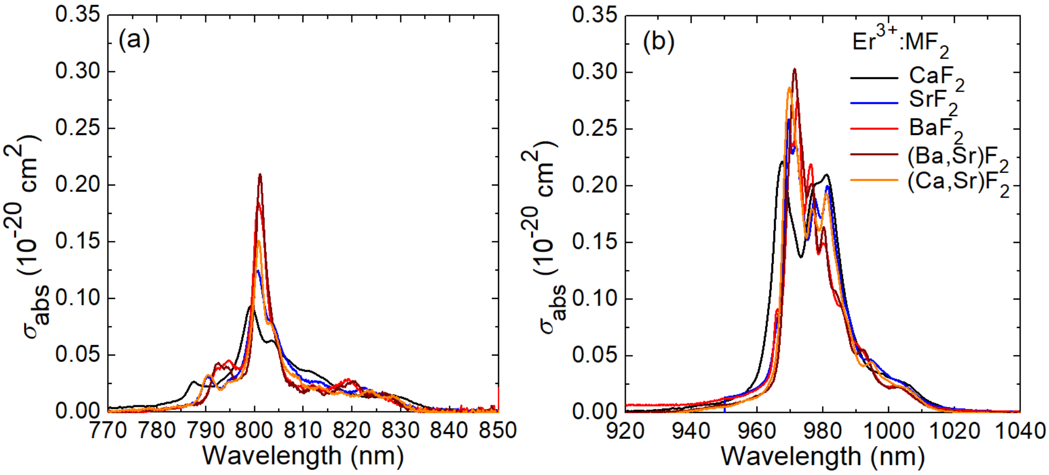

Figure IV.2: Absorption cross-sections, σ_{abs}, for the: (a) $^4I_{15/2} \rightarrow {}^4I_{9/2}$; (b) $^4I_{15/2} \rightarrow {}^4I_{11/2}$ transitions of Er^{3+}:BaF$_2$, Er^{3+}:SrF$_2$, Er^{3+}:CaF$_2$, Er^{3+}:(Ca,Sr)F$_2$ and Er^{3+}:(Ba, Sr)F$_2$ crystals.

For the $^4I_{15/2} \rightarrow {}^4I_{11/2}$ pump transition, in Figure IV.2(b), the maximum σ_{abs} is observed for both “mixed” compounds calculated to be 0.29 and 0.30 10^{-20} cm^2 for the Er^{3+}:(Ca,Sr)F$_2$ and Er^{3+}:(Ba,Sr)F$_2$, respectively. These crystals also exhibit a less structured and narrower absorption spectra as compared to parent ones. Table IV.3 summarizes the peak σ_{abs}, their corresponding wavelengths and bandwidths (FWHM) for both pump transitions.

A close look at the absorption spectra of “mixed” crystals indicate that there is a great similarity between those of (Er^{3+}:(Ca,Sr)F$_2$ and Er^{3+}:SrF$_2$) and (Er^{3+}:(Sr,Ba)F$_2$ and Er^{3+}:BaF$_2$) ones, suggesting that the dopant ions in such solid-solution compounds tend to reside in clusters with a local surrounding predominantly composed of one of the two host-forming cations (namely, the heavier / larger one – Sr^{2+} or Ba^{2+}, respectively). This suggests that Er^{3+} clusters have a tendency to site in the heavier-cation environment within the solid-solution $(M1_{1-x}M2_x)F_2$ crystals. A similar behavior was observed previously for clusters of Nd^{3+}/Lu^{3+} ions in "mixed" $(Sr,Ba)F_2$ crystals [Nor17].

Table IV.3: Summary of absorption cross-sections, σ_{abs}, for the $^4I_{15/2} \rightarrow {}^4I_{9/2}$ and $^4I_{15/2} \rightarrow {}^4I_{11/2}$ transitions.

Host crystal	**Transitions**					
	$^4I_{15/2} \rightarrow {}^4I_{9/2}$,(0.80μm)			**$^4I_{15/2} \rightarrow {}^4I_{11/2}$ (0.97μm)**		
	λ, nm	**σ_{abs} , 10^{-20} cm^2**	**FWHM, nm**	**λ, nm**	**σ_{abs}, 10^{-20} cm^2**	**FWHM, nm**
BaF_2	800.9	0.18	3.8	972.2	0.28	10.2
CaF_2	799.2	0.09	10.5	967.6	0.22	22.2
SrF_2	800.7	0.13	6.6	969.5	0.26	16.8
$(Ca,Sr)F_2$	800.9	0.15	4.2	969.7	0.29	15.7
$(Ba,Sr)F_2$	801.1	0.21	3.0	971.4	0.30	9.8

1.1.3 Judd-Ofelt analysis

The measured absorption spectra of Er^{3+} ions in the five studied MF_2 crystals were used to calculate the transition probabilities by means of the standard Judd-Ofelt (J-O) theory [Jud62, Ofe62]. The reduced squared matrix elements $U^{(k)}$ (k = 2, 4, 6) were calculated using the free-ion parameters from [Tan94]. The magnetic dipole (MD) contributions to transition intensities (for $\Delta J = J - J' = 0, \pm 1$) were calculated within the Russell–Saunders approximation on wave functions of Er^{3+} under an assumption of a free-ion.

Table IV.4 summarized the experimental and calculated absorption oscillator strengths (f_{exp} and f_{calc}, respectively) for the three parent compounds, Er^{3+}:CaF_2, Er^{3+}:SrF_2 and Er^{3+}:BaF_2. There exists a direct relation between the absorption oscillator strength / integrated absorption cross-section and the radiative lifetime of the excited-state (the principle of reciprocity, referring to Einstein coefficients). For Er^{3+} transitions from the ground-state ($^4I_{15/2}$) to the two lower-lying excited-states ($^4I_{13/2}$ and $^4I_{11/2}$), the f_{calc} value decreases in the M = Ca → Sr → Ba series, so that an opposite tendency is expected for the radiative lifetimes of these two states. The root mean square (r.m.s.) deviation between the f_{exp} and f_{calc} values is relatively low for all the tested Er^{3+}:MF_2 crystals, lying in the range of 0.137 – 0.257. The J-O (intensity) parameters Ω_2, Ω_4, Ω_6 for Er^{3+} ions in MF_2 crystals are listed in Table IV.5.

The determined J-O parameters were used to calculate the probabilities of spontaneous radiative transitions of Er^{3+} ions. In Table IV.6 we listed the parameters relevant for mid-infrared laser operation, i.e., the radiative lifetimes τ_{rad} of the $^4I_{13/2}$ and $^4I_{11/2}$ states and the luminescence branching ratio $\beta_{JJ'}$ for the $^4I_{11/2} \rightarrow {}^4I_{13/2}$ transition. In the M = Ca → Sr → Ba series, the τ_{rad} values for the considered excited-states tend to increase from 7.09 / 6.53 ms (Er^{3+}:CaF_2) to 7.57 / 6.99 ms (Er^{3+}:SrF_2) and further to 7.52 / 7.11 ms (Er^{3+}:BaF_2). The considered $\beta_{JJ'}$ value is also higher for Sr^{2+} and Ba^{2+}-containing crystals.

Table IV.4: Absorption oscillator strengths[a] for Er^{3+} ions in parent MF_2 (M = Ca, Sr, Ba) crystals. (published in Optical Material Express, 2023 [Nor23a])

Transition	**Er^{3+}:CaF_2**		**Er^{3+}:SrF_2**		**Er^{3+}:BaF_2**	
$^4I_{15/2} \rightarrow {}^{2S+1}L_J$	**f_{exp}, ×10^{-6}**	**f_{calc}, J-O ×10^{-6}**	**f_{exp}, ×10^{-6}**	**f_{calc}, J-O ×10^{-6}**	**f_{exp}, ×10^{-6}**	**f_{calc}, J-O ×10^{-6}**
$^4I_{13/2}$	2.496	$1.643^{ED}+0.448^{MD}$	2.129	$1.510^{ED}+0.448^{MD}$	0.220	$1.404^{ED}+0.461^{MD}$
$^4I_{11/2}$	0.714	0.693^{ED}	0.643	0.631^{ED}	0.598	0.592^{ED}
$^4I_{9/2}$	0.333	0.229^{ED}	0.328	0.283^{ED}	0.343	0.333^{ED}
$^4F_{9/2}$	2.264	2.139^{ED}	2.217	2.283^{ED}	2.265	2.406^{ED}
$^4S_{3/2} + {}^2H_{11/2}$	3.531	3.366^{ED}	3.422	3.544^{ED}	4.387	4.760^{ED}
$^4F_{7/2}$	2.141	2.454^{ED}	2.396	2.342^{ED}	2.205	2.236^{ED}
$^4F_{5/2} + {}^2F_{3/2}$	1.266	1.300^{ED}	1.114	1.173^{ED}	0.962	1.056^{ED}
$^2G_{9/2}$	0.898	0.970^{ED}	0.637	0.902^{ED}	0.603	0.840^{ED}
$^4G_{11/2} + {}^2K_{15/2} + {}^4G_{9/2} + {}^2G_{7/2}$	7.888	$7.917^{ED}+0.053^{MD}$	8.585	$8.474^{ED}+0.053^{MD}$	11.400	$11.168^{ED}+0.055^{MD}$
r.m.s. dev.		0.217		0.137		0.234

[a] f_{exp} and f_{calc} - experimental and calculated absorption oscillator strengths, respectively, ED – electric dipole, MD – magnetic dipole.

Table IV.5: Judd-Ofelt Parameters of Er^{3+} ions in MF_2 crystals. (published in Optical Material Express, 2023 [Nor23a])

Host crystal	**Ω_2, 10^{-20} cm^2**	**Ω_4, 10^{-20} cm^2**	**Ω_6, 10^{-20} cm^2**
CaF_2	1.436	1.364	1.892
$(Ca,Sr)F_2$	1.244	1.483	1.720
SrF_2	1.477	1.701	1.701
$(Ba,Sr)F_2$	1.519	1.836	1.529
BaF_2	2.397	1.964	1.487

Table IV.6: Selected Probabilities[a] of Spontaneous Radiative Transitions of Er^{3+} in MF_2 crystals. (published in Optical Material Express, 2023 [Nor23a])

Host crystal	**$\tau_{rad}(^4I_{13/2})$, ms**	**$\tau_{rad}(^4I_{11/2})$, ms**	**$\beta_{JJ'}(^4I_{11/2} \rightarrow {}^4I_{13/2})$, %**
CaF_2	7.09	6.53	14.9
$(Ca,Sr)F_2$	7.64	7.06	15.8
SrF_2	7.57	6.99	16.0
$(Ba,Sr)F_2$	7.90	7.56	16.5
BaF_2	7.52	7.11	16.1

[a] τ_{rad} – radiative lifetime, $\beta_{JJ'}$ – luminescence branching ratio.

1.1.4 Stimulated emission cross-sections for $^4I_{11/2}\rightarrow{}^4I_{13/2}$ transition

The stimulated-emission (SE) cross-sections, σ_{SE}, for the $^4I_{11/2} \rightarrow {}^4I_{13/2}$ transition in $Er^{3+}:MF_2$ crystals is discussed in this section. The Füchtbauer–Ladenburg formula was used to calculate the SE cross-sections, and the luminescence spectra were corrected for structured water vapor absorption.

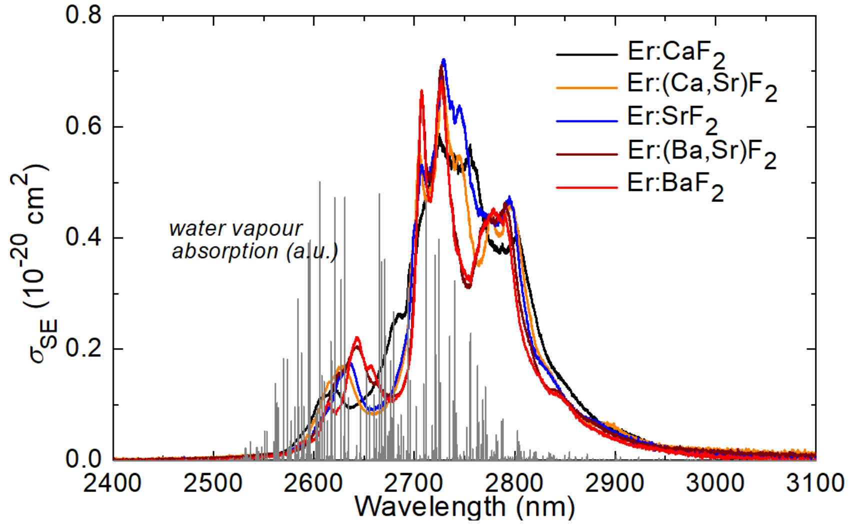

Figure IV.3: Stimulated emission (SE) cross-sections, σ_{SE}, for the $^4I_{11/2} \rightarrow {}^4I_{13/2}$ transition of $Er^{3+}:BaF_2$, $Er^{3+}:SrF_2$, $Er^{3+}:CaF_2$, $Er^{3+}:(Ca,Sr)F_2$ and $Er^{3+}:(Ba,Sr)F_2$ crystals, corrected for the structured water vapor absorption in air (in *grey*, according to HITRAN database).

The SE cross-section spectra for Er^{3+} ions in MF_2 crystals are shown in Figure IV.3. For all crystals, the spectra span from 2500 to 3050 nm and the main emission peak appear around 2.72 µm. They were found to be smooth and inhomogeneously broaden, which is attributed to the strong tendency for ion clustering at the studied doping levels. The spectra become more structured in the M = Ca → Sr → Ba series. Also for the solid-solution compounds, a great similarity between the emission spectra of (Er^{3+}:(Ca,Sr)F_2 and Er^{3+}:SrF_2) and (Er^{3+}:(Ba,Sr)F_2 and Er^{3+}:BaF_2) crystals is observed.

The highest SE cross-section is observed for Er^{3+}:SrF_2, $\sigma_{SE} = 0.72\times10^{-20}$ cm^2 at 2729 nm and at longer wavelengths, two other intense and broad peaks appear ($\sigma_{SE} = 0.64\times10^{-20}$ cm^2 at 2745 nm and 0.47×10^{-20} cm^2 at 2794 nm). The "mixed" compositions are also characterized by the intense σ_{SE}, amounted to be 0.71×10^{-20} cm^2 at 2726.8 nm and 0.69×10^{-20} cm^2 at 2727.7 nm for the Er^{3+}:(Ba,Sr)F_2 and Er^{3+}:(Ca,Sr)F_2, respectively. Table IV.7 summarizes the wavelengths, maximum SE cross-sections, and bandwidths for the studied Er^{3+}:MF_2 crystals.

Table IV.7: Summary of wavelengths, λ (nm), maximum SE cross-sections, σ_{SE} (10^{-20} cm^2) and bandwidths, FWHM (nm) for different Er^{3+}:MF_2 crystals.

Host crystal	**λ, nm**	**σ_{SE}, 10^{-20} cm^2**	**FWHM, nm**
BaF_2	2726.8	0.68	98
CaF_2	2725.3	0.59	124
SrF_2	2728.7	0.72	105
(Ca,Sr)F_2	2727.7	0.69	109
(Ba,Sr)F_2	2726.8	0.71	100

1.1.5 Luminescence lifetimes of $^4I_{11/2}$ and $^4I_{13/2}$ levels

The mean luminescence lifetimes $<\tau_{lum}>$ of the $^4I_{11/2}$ and $^4I_{13/2}$ Er^{3+} states were measured using finely powdered samples to avoid the effect of radiation trapping effect. The measured decay curves are shown in Figure IV.4. The mean luminescence lifetimes was calculated as $<\tau_{lum}> = \int I(t)t\mathrm{d}t/\int I(t)\mathrm{d}t$.

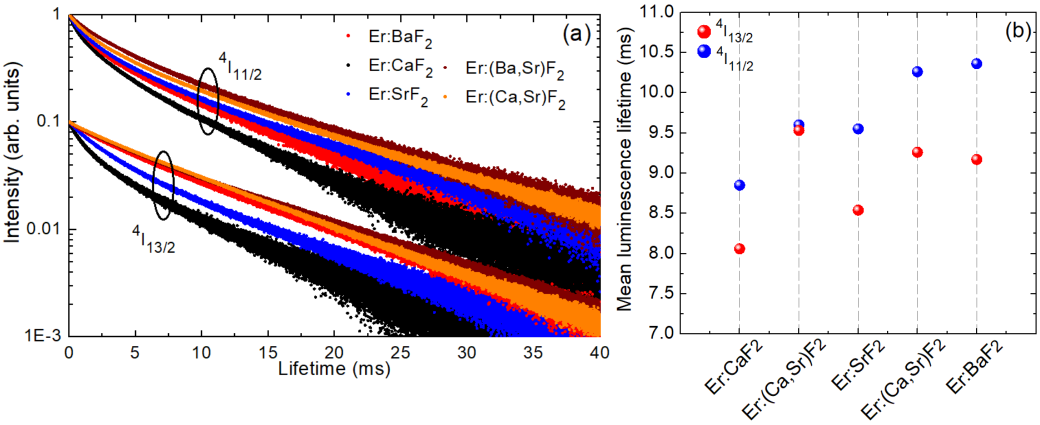

Figure IV.4: (a) Luminescence decay curves for Er^{3+} ions in CaF_2 *(black)*, SrF_2 *(blue)*, BaF_2 *(red)*, (Ca, Sr)F_2 *(orange)*, (Ba, Sr)F_2 *(dark red)*: from the $^4I_{13/2}$ state, $\lambda_{exc} = 1475$ nm, $\lambda_{lum} = 1572$ nm; and from the $^4I_{11/2}$ state, $\lambda_{exc} = 970$ nm, $\lambda_{lum} = 1020$ nm; (b) mean luminescence lifetimes $<\tau_{lum}>$ as a function of the host composition.

The summary of the <τ_{lum}> values for the five studied $Er^{3+}:MF_2$ crystals is given in Table IV.8. With increasing the average radius / atomic mass of the M^{2+} host-forming cations (in the M = Ca → Sr → Ba series), and, accordingly, decreasing the phonon energy of the host matrix, both the $^4I_{13/2}$ and $^4I_{11/2}$ luminescence lifetimes tend to increase, from 8.06 / 8.85 ms ($Er^{3+}:CaF_2$) to 8.54 / 9.55 ms ($Er^{3+}:SrF_2$) and further to 9.17 / 10.36 ms ($Er^{3+}:BaF_2$). This behavior agrees with that for the calculated radiative lifetimes of these manifolds. The ratio of the upper-to-lower laser level lifetimes is favorable for all the studied crystals being weakly dependent on the host matrix composition. The long luminescence lifetime of the upper laser level for the mid-infrared transition ($^4I_{11/2}$) is a prerequisite for a low-threshold behavior. However, it is worth noting that for all crystals, both lifetimes are still exceeding the radiation ones calculated using J-O theory (Table IV.6), which can be explained by residual reabsorption effect within Er^{3+} clusters.

Table IV.8: Mean luminescence decay lifetimes, <τ_{lum}> and radiative lifetimes, τ_{rad} of the $^4I_{11/2}$ and $^4I_{13/2}$ Er^{3+} manifolds in MF_2 crystals.

Host crystal	**<τ_{lum}> (ms)**		**τ_{rad} (ms)**	
	$^4I_{11/2}$	**$^4I_{13/2}$**	**$^4I_{11/2}$**	**$^4I_{13/2}$**
CaF_2	8.85	8.06	6.53	7.09
SrF_2	9.55	8.54	7.06	7.64
BaF_2	10.26	9.17	7.11	7.57
$(Ca,Sr)F_2$	9.60	9.53	6.99	7.64
$(Ba,Sr)F_2$	10.36	9.26	7.55	7.90

We carried out a thorough examination of the luminescence decay curves for nine crystals of $Er^{3+}:CaF_2$, each with varying Er^{3+} doping ranging from 0.05 to 10at. %, in order to study the impact of Er^{3+} concentration on the lifetime ratio of the upper-to-lower laser level. For the crystals with low doping levels (0.05 to 1at. %), the decay curves were clearly single-exponential, and therefore the lifetimes were extracted by fitting these curves. When the luminescence decay curves were not single-exponential, as was the case for higher-doped samples (<1at.%), the lifetime constants were obtained by calculating the mean lifetime, <τ_{lum}>. The results are shown in Figure IV.5.

The following findings can be drawn from the concentration dependence shown in Figure IV.5:

(i) For low-doped crystals (0.05 – 1.0at.%), a significant elongation of the lifetimes of both $^4I_{11/2}$ and $^4I_{13/2}$ levels is observed compared with the radiative ones given in Table IV.8. This is probably because of the effect of reabsorption in crystals of 5-8 mm thick used for measurements to improve the luminescence signal. A similar tendency has been observed for low-doped Er^{3+}:CaF_2 crystals and transparent ceramics in previous papers [Lab18b, Liu19b].

(ii) Both the $^4I_{11/2}$ and $^4I_{13/2}$ levels are weakly affected by the nonradiative multiphoton relaxation. For the Er^{3+} concentration range of 4.5 to 9.0 at.%, the luminescence lifetimes remain fairly close to that of the radiative ones (Table IV.8).

(iii)Er^{3+}:CaF_2 crystals with an Er^{3+} concentration greater than 4.5at.% reach a favorable lifetime ratio of the upper and lower laser levels due to the effective upconversion of energy transfer depleting lower laser level and refilling upper one, ($^4I_{13/2}$, $^4I_{13/2}$) → ($^4I_{15/2}$, $^4I_{9/2}$).

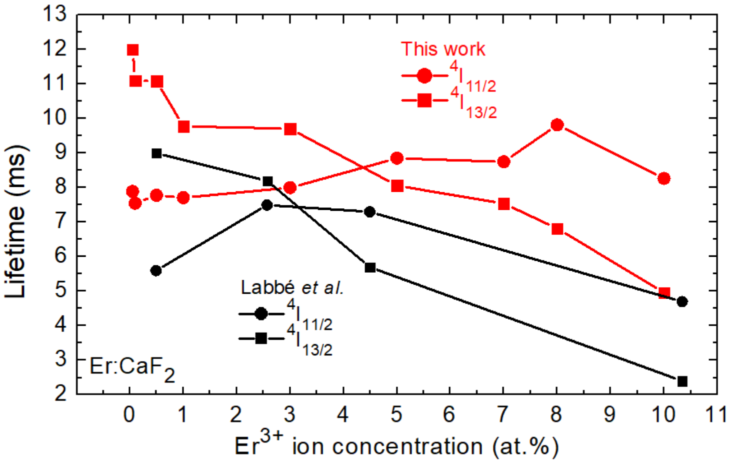

Figure IV.5: Measured luminescence lifetimes for the $^4I_{11/2}$ and $^4I_{13/2}$ levels as a function of the Er^{3+} doping concentration in CaF_2 *(red)*, as well as the lifetimes for the same levels *(black)* given in [Lab18b], plotted for comparison. The *circles* show the lifetime of the $^4I_{11/2}$ state, the *squares* are for the $^4I_{13/2}$ state.

1.1.6 Low-temperature spectroscopy

Figures IV.6 and IV.7 display the LT absorption and emission spectra, respectively, comparing the spectrum of a "mixed" compound with those of its parent crystals. The LT absorption spectra were plotted versus the phonon energy giving access to the splitting of the $^4I_{13/2}$ and $^4I_{11/2}$ excited-states, while the LT emission spectra were plotted *vs.* (E_{ZPL} – photon energy), where E_{ZPL} represents the zero-phonon line energy, allowing access to the splitting of the ground-state $^4I_{15/2}$. Table IV.9 summarizes experimentally obtained Stark components for the $^4I_{15/2}$, $^4I_{13/2}$ and $^4I_{11/2}$ Er^{3+} multiplets of studied MF_2 crystals.

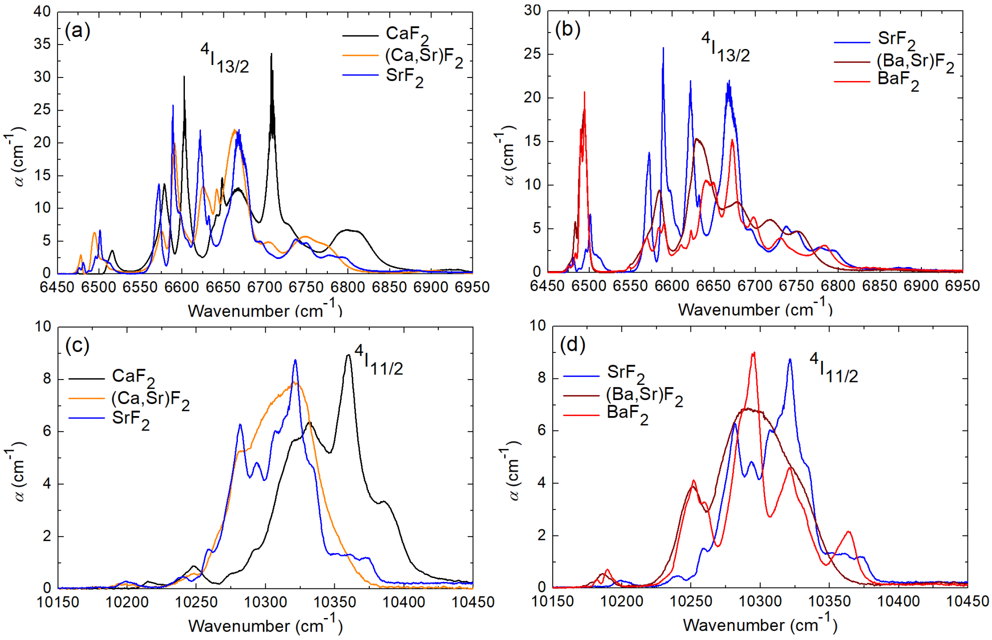

Figure IV.6: (a-d) LT (12 K) absorption spectra of Er^{3+} ions in fluorite-type crystals: (a,b) the $^4I_{15/2} \rightarrow {}^4I_{13/2}$ transition; (c,d) $^4I_{15/2} \rightarrow {}^4I_{11/2}$ transition. α_{abs} – absorption coefficient.

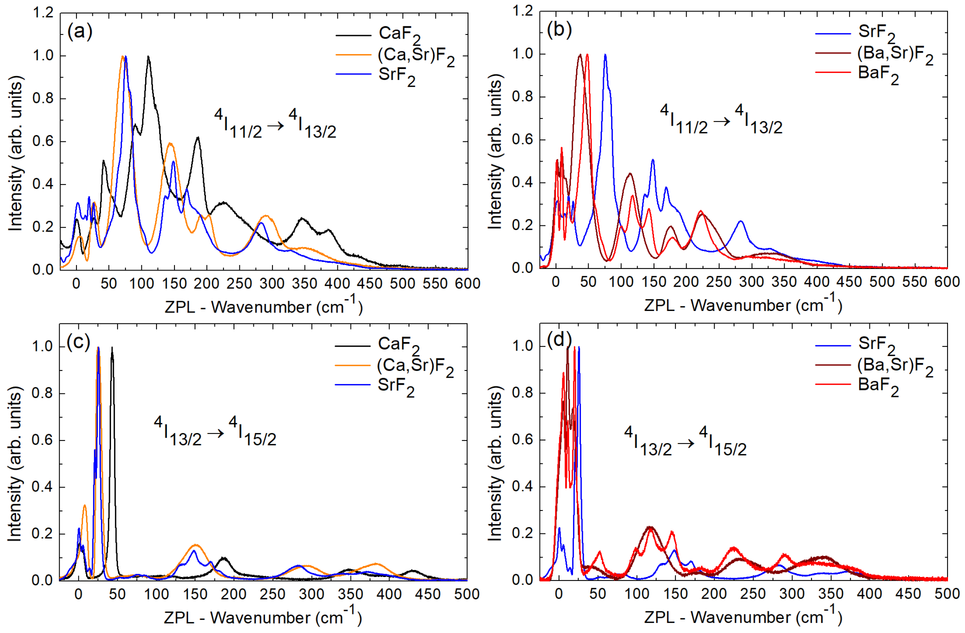

Figure IV.7: (a-d) LT (12 K) luminescence spectra of Er^{3+} ions in fluorite-type crystals: (a,b) the $^4I_{11/2} \rightarrow {}^4I_{15/2}$ transition; (c,d) $^4I_{13/2} \rightarrow {}^4I_{15/2}$ transition. ZPL – zero-phonon-line energy.

By examining the spectra, several conclusions can be drawn:

(i) At 12 K, the absorption and emission spectra of Er^{3+} ions in the MF_2 crystals showed broad bands, indicating significant inhomogeneous spectral broadening caused by the clustering of rare-earth ions. As one moves from calcium (Ca) to strontium (Sr) and barium (Ba), the spectra become more ordered, indicating a decrease in the diversity of cluster geometry.

(ii) The spectra of fluorite-type crystals with a combination of different host cations showed broader features than those of the corresponding parent compounds. This broadening can be explained by the presence of two different cations in the crystal structure. The spectra of these mixed crystals resemble those of the parent compounds with heavier cations. For example, $(Ca,Sr)F_2$ and SrF_2 have spectra similar to those of $(Ba,Sr)F_2$ and BaF_2.

(iii)The total splitting of Er^{3+} multiplets in clusters within MF_2 crystals decreased as one moved from calcium (Ca) to strontium (Sr) and barium (Ba) in the series. In addition, the barycenter energies of these multiplets gradually underwent a redshift. This phenomenon can be explained by an increase in the crystal field strength for smaller sites, characterized by smaller distances between the dopant ion and the surrounding M-F and M-M atoms. This increase in the crystalline field strength is the result of stronger lattice distortion. Indeed, the lattice constant increases in the series from CaF_2 (5.45 Å) to SrF_2 (5.80 Å) and BaF_2 (6.20 Å). Figure IV.8

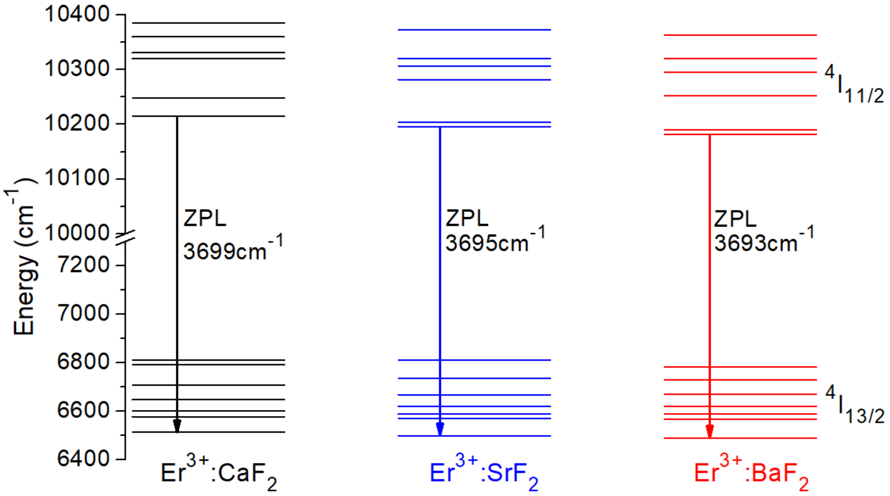

Figure IV.8: Stark splitting of the $^4I_{11/2}$, and $^4I_{13/2}$ multiplets of Er^{3+} ions in CaF_2, SrF_2, and BaF_2, *numbers* – Stark energies in cm^{-1}, ZPL – zero-phonon line.

Based on the LT absorption and emission spectra, the crystal-field splitting of the $^4I_{15/2}$, $^4I_{13/2}$ and $^4I_{11/2}$ multiplets of Er^{3+} ions forming clusters in three parent MF_2 crystals (M = Ca, Sr, Ba), was determined, Table IV.9. In the previous studies on site-selective spectroscopy of Er^{3+} ions in CaF_2 crystals grown under oxygen-free atmosphere, multiple possible sites were identified [Fen73, Tal75, Moo81]. At very low doping levels (<0.05 at.%), the Er^{3+} ions are mostly isolated and are distributed over tetragonal (A, C_{4v}), trigonal (B, C_{3v}) and cubic (O_h) sites, depending on the relative position of the charge-compensating interstitial fluorine anion (F_i^-), namely at the (100) positions, at the (111) positions or sufficiently far from the dopant ion to exert negligible perturbation, respectively [Fen73]. For higher doping levels of >0.1 at.%, the dopant ions form clusters of several types (assigned as C-sites, being close to dimers with a distorted C_{3v} symmetry, and D(1) and D(2) sites corresponding to larger agglomerates of Er^{3+} - F_i^- pairs).

For the studied heavily doped $Er^{3+}:MF_2$ crystals, we were not able to confirm the existence of two significantly different groups of ion clusters (D(1) and D(2)), as the LT emission spectra were almost independent on the excitation wavelength. Moreover, the bands in the LT spectra of ~5 at.% Er^{3+}-doped crystals (assigned to a single type of cluster D sites) experienced an additional broadening and spectral shifts as compared to those in 0.1 at.% Er^{3+}-doped crystals (assigned to D(1) and D(2) sites). Thus, we assumed that almost all the Er^{3+} ions form large-scale agglomerates (D) with close spectroscopic properties. Previously, it was suggested that for all the heavily doped MF_2 crystals (M = Ca, Sr, Ba) and their solid-solutions, such agglomerates most likely correspond to hexameric Y_6F_{37} superstructure units, which are nearly identical in volume and shape to the Ca_2F_{32} building blocks of the fluorite lattice and, consequently, they can be easily incorporated into this lattice while accommodating the excess F_i^- anions [Kaz02,Nik05]. The local crystal-field symmetry for the dopant ions in Y_6F_{37} clusters is tetragonal (C_{4v}) [Kaz02].

Table IV.9: Crystal-field splitting of selected Er^{3+} multiplets in MF_2. (published in Optical Material Express, 2023 [Nor23a])

Crystal	Er^{3+} $^{2S+1}L_J$	Sub-level / Energy (cm^{-1})							
		1	2	3	4	5	6	7	8
CaF$_2$	$^4I_{15/2}$	0	42	90	110	186	228	346	387
	$^4I_{13/2}$	6516	6579	6602	6648	6708	6793	6812	
	$^4I_{11/2}$	10215	10248	10320	10331	10360	10386		
SrF$_2$	$^4I_{15/2}$	0	25	63	75	148	187	283	330
	$^4I_{13/2}$	6501	6572	6589	6622	6669	6737	6796	
	$^4I_{11/2}$	10196	10204	10282	10307	10321	10373		
BaF$_2$	$^4I_{15/2}$	0	18	34	48	117	142	222	293
	$^4I_{13/2}$	6489	6569	6590	6622	6672	6730	6784	
	$^4I_{11/2}$	10182	10190	10252	10295	10321	10363		

1.2 Double yttrium sodium fluoride ($Na_5Y_9F_{32}$) crystal

The set of $Na_5Y_9F_{32}$ single-crystals doped with 0.2 – 10 at.% Er^{3+} were grown by the Czochralski (Cz) method using the composition 36%NaF – 64%(Y,Er)F_3 (mol.%). The summary of grown crystals and performed studies are listed in Table IV.10.

Table IV.10: Summary of grown Er^{3+}:$Na_5Y_9F_{32}$ single-crystals and performed studies.

Er^{3+} doping, at.% (in the crystal)	**Performed studies**				
	DTA	**XRD + Ritvield**	**Raman spectroscopy**	**RT &LT spectroscopy**	**Lifetime dymanics**
0.22			+		+
1.16					+
2					+
5.59	+	+		+	+
9.63					+

1.2.1 Investigation of the structural specificity

- **Differential Thermal Analysis (DTA)**

To understand the phase transformation occurring in the system 36% NaF – 64% YF_3 we performed the differential thermal analysis for the 5.59 at.% Er^{3+}:$Na_5Y_9F_{32}$ crystal.

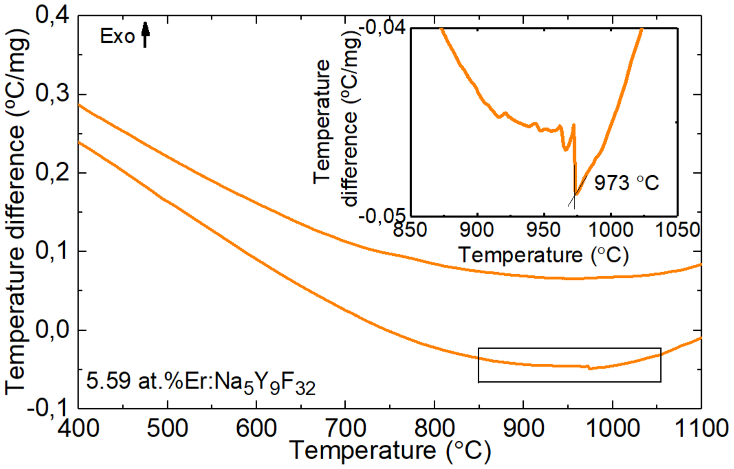

Figure IV.9: Differential thermal analysis curves for the 5.59 at.% Er^{3+}:$Na_5Y_9F_{32}$ crystal, *insert* - close view revealing phase transformation.

Figure IV.9 shows the obtained DTA curves. A unique exothermal peak on the cooling curve (T_{on} = 973°C) implies the crystallization of the fluorite-type $Na_5Y_9F_{32}$

($5NaF \cdot 9YF_3$) solid-solution phase from the melt confirmed by XRD analysis described later. This phase transformation is taking please in the range of temperatures of 921 - 973°C. Indeed, according to Thoma *et al.* the temperature of this transition (melt ↔ fluorite cubic $5NaF \cdot 9YF_3$) is 975°C. Fedorov *et al.* postulated a similar temperature range as well [Fed79].

- **Crystal structure**

The measured XRD pattern for the 5.59 at.% Er^{3+}:Na$_5$Y$_9$F$_{32}$ crystal is shown in Figure IV.10. No other peaks except those belonging to the cubic phase (Na$_{0.39}$Y$_{0.61}$F$_{2.22}$, ICSD card #01-071-5986) were found.

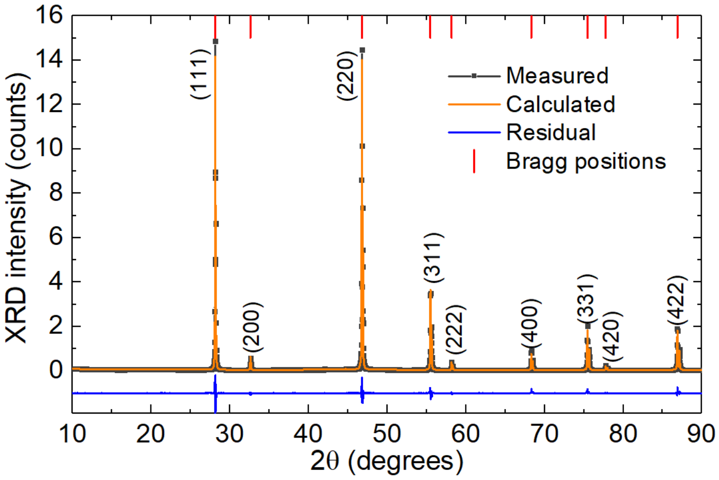

Figure IV.10: XRD pattern of a 5.59 at.% Er^{3+}:Na$_5$Y$_9$F$_{32}$ crystal, *blue peaks* – theoretical reflections for undoped Na$_{0.39}$Y$_{0.61}$F$_{2.22}$ (PDF card #01-071-5986), *numbers* – Miller's indices (*hkl*).

The crystal structure of Er^{3+}:Na$_5$Y$_9$F$_{32}$ was refined by the Rietveld method using the Topas software, Figure IV.10. This investigation was performed in collaboration with University of Rovira i Virgili (Tarragona, Spain) by Sami Slimi.

Er^{3+}:Na$_5$Y$_9$F$_{32}$ belongs to the cubic class (sp. gr. O^5_h - Fm-3m, No. 225) is isostructural with CaF$_2$. It presents the modified structure of CaF$_2$, in which about 40% of the Ca^{2+} cations is replaced by Na$^+$ cations and 60% by Y^{3+}cations. Owing to the requirement of charge neutrality, there was an excess of 10% F$^-$ anions. These excess F$^-$ ions occupy interstitial positions. In addition, owing to the requirement of local charge compensation, the remaining F$^-$ ions are expected to be displaced from their normal positions [Cho89b]. The calculated lattice constant a = 5.4881(2) Å, which is slightly lower than the ones of an undoped Na$_{0.41}$Y$_{0.59}$F$_{2.18}$ crystal (a = 5.503Å) [Pon87]. Since the ionic radius of Er^{3+} (R_{Er} = 1.14 Å) is smaller than that of Y^{3+} (R_Y = 1.16 Å,) [Kam13], the presence of Er^{3+} ions reasonably lead to slight lattice shrinkage. The calculated volume of the unit-cell V = 165.299(3) Å^3 is slightly less than that of Na$_{0.41}$Y$_{0.59}$F$_{2.18}$ as well (V = 165.65Å^3), which is attributed to the substitution of the larger Y^{3+} ions by the smaller Er^{3+}. The calculated density $\rho_{\text{calc}} = 4.67$ g/cm^3. Table IV.11 lists the refined atomic parameters of the 5.59%Er^{3+}:$Na_5Y_9F_{32}$ crystal.

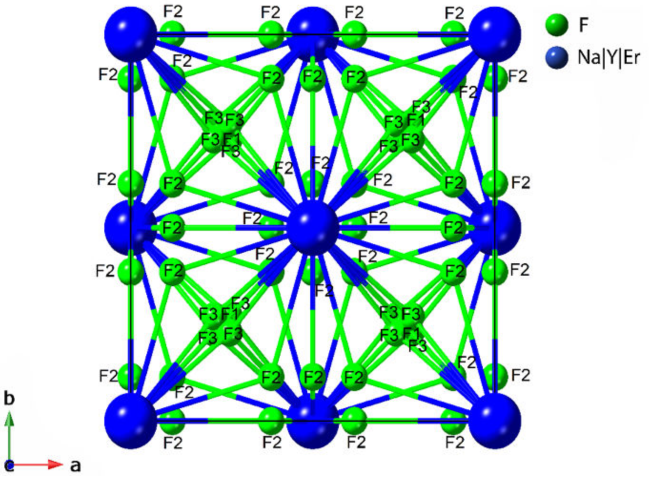

Figure IV.11: Structure of the Er^{3+}:$Na_5Y_9F_{32}$ crystal built based on a refined pattern that indicates the different positions (F1, F2, F3) of F^- anion.

In the studied Er^{3+}:$Na_5Y_9F_{32}$ structure, positions 4*a* in the corners and centers of the cube faces are occupied by Na^+, Y^{3+} and Er^{3+}cations (occupancy factor for 0.41 for Na^+, 0.54 for Y^{3+} and 0.05 for Er^{3+}ions, respectively). The local symmetry of the surrounding of the Y^{3+} ions (and thus also Er^{3+} ones) is C_{4v} [Tka01]. As for the positions occupied by F^- ions, there are three non-equivalent positions for fluorine anions: F1 - principal position 8*c* (¼, ¼, ¼) with O.F of 0.922; F2 - additional position 48*i* (1/2, y, y; y = 0.1142(2)) with O.F of 0.035; and F3 - interstitial positions 32*j* (x, x, x; x = 0.2710(3)), O.F is 0.047(7). Latter ones show the displacement of atoms F from the principle position 8*c* along the axes of symmetry of the third order [Pon87]. Figure IV.11 shows the refined structure of $Na_5Y_9F_{32}$ indicating different positions of F^- anion. In Table IV.12, we listed the interatomic distances.

Previous studies indicate that in $Na_{0.5-x}Y_{0.5+x}F_{2+2x}$ solid-solutions with x = 0 - 0.14, cuboctahedral clusters Y_6F_{36-38} are formed and enter as the main structural unit into clusters of $M_8Y_6F_{68-69}$ type [Sor92, Sor02]. The structure of non-stoichiometric fluorite-type $Na_{0,5-x}Y_{0,5+x}F_{2+2x}$ solid-solution crystal can be represented as composed of randomly arranged Y_6F_{37} clusters with interstitial fluorine (F^-) ions located at their periphery.

Table IV.11: Atomic coordinates, sites, occupancy factors (O.F) and isotropic displacement parameters Biso (Å^2) for the 5.59%Er^{3+}:$Na_5Y_9F_{32}$ crystal.

Atoms	x/a	y/b	z/c	O.F	B_{iso}	Sites
Na	0	0	0	0.41	0.0215(7)	4*a*
Y	0	0	0	0.54	0.0215(7)	4*a*
Er	0	0	0	0.05	0.0215(7)	4*a*
F1	1/4	1/4	1/4	0.922(1)	0.0531(9)	8*c*
F2	1/2	0.1142(2)	0.1142(2)	0.035(6)	2.984	48*i*
F3	0.2710(3)	0.2710(3)	0.2710(3)	0.047(7)	0	32*j*

Table IV.12: Interatomic distances for the different bond combinations.

Bond	Interatomic distance (Å)
Na/Y-F1	2.376(4)
Na/Y-F2	2.208
Na/Y-F’2	2.883(7)
Na/Y-F3	2.317(4)
Na/Y-F’3	2.576(3)
Na/Y-Na/Y	5.488
Na/Y-Na/Y	3.881

1.2.2 Raman spectroscopy

The Raman spectrum of the undoped $Na_5Y_9F_{32}$ crystal exhibits several broad poorly resolved bands with the maxima at 130, 229, 350, 404, 470 and 516 cm^{-1}, Figure IV.12. The most intense band is found at 404 cm^{-1}. For the 0.22 at.% Er^{3+}-doped crystal, the Raman bands overlap with the Er^{3+} luminescence. Despite this, a similar set of Raman-active modes is observed. The low phonon energy behavior of the $Na_5Y_9F_{32}$ host matrix is advantageous for Er^{3+} doping with the goal of observing mid-IR emission. For comparison, CaF_2 has single-mode Raman spectrum and a slightly lower the phonon energy of 322 cm^{-1} [Bas22c]. The Raman spectrum of $Na_{0.5-x}Y_{0.5+x}F_{2+2x}$ has been presented previously in single work [Tka04a]. Therein, the Raman spectrum of undoped NYF crystal contains a broad band with a peak at ~420 cm^{-1} spanning up to 600 cm^{-1}. Probably such a broadband behavior of Raman spectrum is associated with a strong disordering of the crystals with $Na_{0.5-x}Y_{0.5+x}F_{2+2x}$ composition.

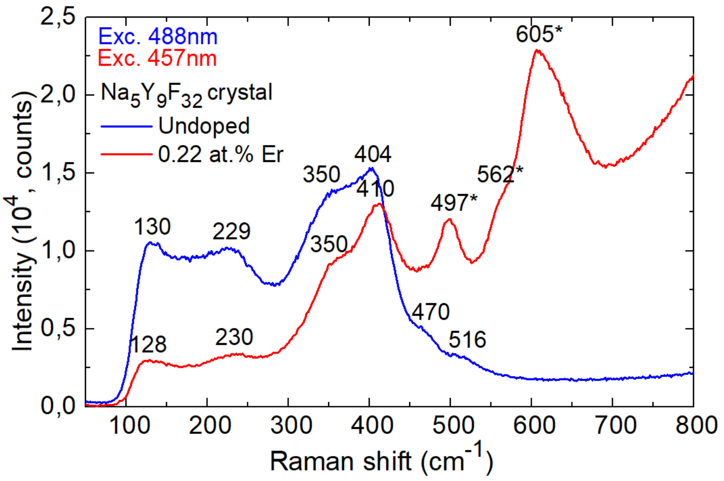

Figure IV.12: Unpolarized Raman spectra of undoped *(blue)* and 0.22 at.% Er^{3+}-doped *(red)* Na$_5$Y$_9$F$_{32}$ crystals, *numbers* denote the Raman frequencies in cm^{-1}.

1.2.3 Optical absorption and Judd-Ofelt analysis

• Room-temperature absorption

The absorption bands are related to transitions of Er^{3+} ions from the ground state, $^4I_{15/2}$, to excited-states ranging from $^4I_{13/2}$ up to $^2G_{7/2}$ shown in Figure IV.13(a). Here, the assignment is after Carnall *et al.* [Car62].

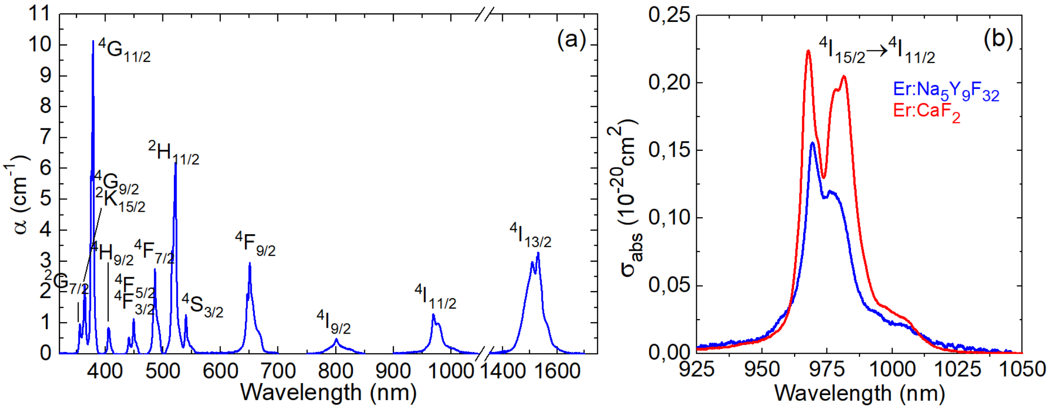

Figure IV.13: (a) An overview absorption spectrum of a 5.59 at.% Er^{3+}:Na$_5$Y$_9$F$_{32}$ crystal; (b) absorption cross-section spectra for the $^4I_{15/2} \rightarrow {}^4I_{11/2}$ transition of Er^{3+} ions in the Na$_5$Y$_9$F$_{32}$ and CaF$_2$ cubic crystals.

For the $^4I_{15/2} \rightarrow {}^4I_{11/2}$ transition which is typically used for pumping of Er^{3+}-doped materials, e.g., by using commercial InGaAs laser diodes, the peak absorption cross-section ($\sigma_{abs} = \alpha_{abs}/N_{Er}$, where $N_{Er} = 8.23\times10^{20}$ cm^{-3}) is 0.16×10^{-20} cm^2 at 969.3 nm corresponding to a large absorption bandwidth (full width at half maximum, FWHM) of ~18 nm, as shown in Figure IV.13(b). As compared to another cubic crystal exhibiting a “glassy-like” spectroscopic behavior, Er^{3+}:CaF_2 ($\sigma_{abs} = 0.23\times10^{-20}$ cm^2 at 967.8 nm, FWHM = 10 nm), Er^{3+}:$Na_5Y_9F_{32}$ provides lower absorption cross-sections while less structured absorption band. The broadband absorption properties of Er^{3+}:$Na_5Y_9F_{32}$ are of practical importance for diode pumping.

• Judd-Ofelt analysis

The transition intensities of Er^{3+} ions in $Na_5Y_9F_{32}$ were determined based in the framework of the standard Judd-Ofelt (J-O) theory based on the measured absorption spectrum [Jud62, Ofe62]. These calculations were performed by our colleagues from Vitebsk State Technological University, Vitebsk, Belarus. The results of the analysis are presented in Table IV.13.

Transition $^4I_{15/2} \rightarrow {}^{2S+1}L_J$	**<*E*>, cm^{-1}**	***Γ*, cm^{-1}*nm**	***f*$_{exp}$, 10^{-6}**	***f*$^{\Sigma}_{calc}$, 10^{-6} J-O**
$^4I_{13/2}$	6526	276.09	1.653	$0.903^{ED}+0.456^{MD}$
$^4I_{11/2}$	10168	33.155	0.477	0.416^{ED}
$^4I_{9/2}$	12462	14.438	0.306	0.117^{ED}
$^4F_{9/2}$	15280	49.246	1.581	1.129^{ED}
$^4S_{3/2}+{}^2H_{11/2}$	8821	68.896	3.459	3.546^{ED}
$^4F_{7/2}$	20558	23.328	1.348	1.322^{ED}
$^4F_{5/2}+{}^4F_{3/2}$	22240	9.058	0.621	0.705^{ED}
$^2G_{9/2}$	24606	5.234	0.435	0.522^{ED}
$^2G_{11/2}+{}^2K_{15/2}+{}^2G_{9/2}+{}^2G_{7/2}$	27178	73.462	7.205	$7.798^{ED}+0.054^{MD}$
r.m.s. dev.				0.450

The obtained intensity parameters are $\Omega_2 = 2.314$, $\Omega_4 = 0.673$ and $\Omega_6 = 1.002$ [10^{-20} cm^2]. Using these parameters, the probabilities of spontaneous radiative transitions $A^{\Sigma}_{calc}(JJ')$, the luminescence branching ratios $\beta(JJ')$ and the radiative lifetimes of the excited-states τ_{rad} were then calculated, Table IV.14. For the upper laser manifold ($^4I_{11/2}$), the radiative lifetime is as long as 9.99 ms and the luminescence branching ratio corresponding to emission in the mid-IR, $\beta(^4I_{11/2} \rightarrow {}^4I_{13/2})$ is relatively high, 17.6%.

Table IV.13: Emission probabilities for Er^{3+} ions in $Na_5Y_9F_{32}$ calculated within the J-O approximation.

Transition $^{2S+1}L_J \rightarrow {}^{2S+1}L_{J'}$		**$<\lambda_{em}>$, nm**	**$\beta(JJ')$**	**$A^{\Sigma}_{calc}(JJ')$, s^{-1}**	**A_{tot}, s^{-1}**	**τ_{rad}, ms**
$^4I_{13/2}$→	$^4I_{15/2}$	1532.3	1.000	63.22^{ED} $+31.98^{MD}$	95.20	10.50
$^4I_{11/2}$→	$^4I_{13/2}$	2745.7	0.176	$10.48^{ED}+7.12^{MD}$	100.05	9.99
	$^4I_{15/2}$	983.5	0.824	82.45^{ED}		
$^4I_{9/2}$ →	$^4I_{11/2}$	4359.2	0.022	$0.52^{ED}+1.13^{MD}$	73.42	13.62
	$^4I_{13/2}$	1684.6	0.408	29.92^{ED}		
	$^4I_{15/2}$	802.4	0.570	41.85^{ED}		
$^4F_{9/2}$ →	$^4I_{9/2}$	3548.6	0.005	$1.32^{ED}+2.05^{MD}$	684.01	1.46
	$^4I_{11/2}$	1956.2	0.064	$39.04^{ED}+5.13^{MD}$		
	$^4I_{13/2}$	1142.3	0.043	29.18^{ED}		
	$^4I_{15/2}$	654.4	0.888	607.29^{ED}		
$^4S_{3/2}$+	$^4F_{9/2}$	2824.1	0.003	$9.40^{ED}+0.14^{MD}$	3502.43	0.29
$^2H_{11/2}$→	$^4I_{9/2}$	1572.6	0.021	$73.97^{ED}+0.59^{MD}$		
	$^4I_{11/2}$	1155.7	0.015	$47.20^{ED}+7.23^{MD}$		
	$^4I_{13/2}$	813.3	0.115	344.13^{ED}		
	$^4I_{15/2}$	531.3	0.846	$+57.48^{MD}$ 2962.29^{ED}		
$^4F_{7/2}$ →	$^4S_{3/2}+{}^2H_{11/2}$	5757.0	0.000	0.38^{ED}	1958.63	0.51
	$^4F_{9/2}$	1894.6	0.006	$2.44^{ED}+10.23^{MD}$		
	$^4I_{9/2}$	1235.2	0.042	$71.83^{ED}+9.10^{MD}$		
	$^4I_{11/2}$	962.5	0.049	96.17^{ED}		
	$^4I_{13/2}$	712.6	0.082	160.1^{ED}		
	$^4I_{15/2}$	486.4	0.821	1608.35^{ED}		

1.2.4 Low-temperature spectroscopy

The expected inhomogeneous broadening of spectral bands of Er^{3+} ions in the disordered 5.59 at.% Er^{3+}:$Na_5Y_9F_{32}$ is revealed at low temperature. The LT (12 K) absorption and luminescence spectra used to determine the crystal-field splitting of Er^{3+} multiplets involved in the near- and mid-IR emissions (from $^4I_{15/2}$ to $^4I_{11/2}$) are shown in Figure IV.14(a,b). According to Dieke's earlier work [Var62], we used empirical notations for these sub-levels, namely Z_i (i = 1...8), Y_j (j = 1...7) and A_k (k = 1...6) for multiplets $^4I_{15/2}$, $^4I_{13/2}$ and $^4I_{11/2}$, respectively [Kis64]. To facilitate the assignment of electronic transitions, we used crystal field data for Er^{3+} ions in $Na_5Y_9F_{32}$ proposed by Tkachuk *et al* [Tka04a].

We have determined the experimental Stark energies for almost all Er^{3+} multiplets involved into laser transition at 2.8 µm, Table IV.14. We also confirmed by comparison with LT spectra measured for 0.22 at.% Er^{3+}: $Na_5Y_9F_{32}$ (low doped crystal), the presence of only one RE^{3+} site, namely the tetragonal site C_{4v}.

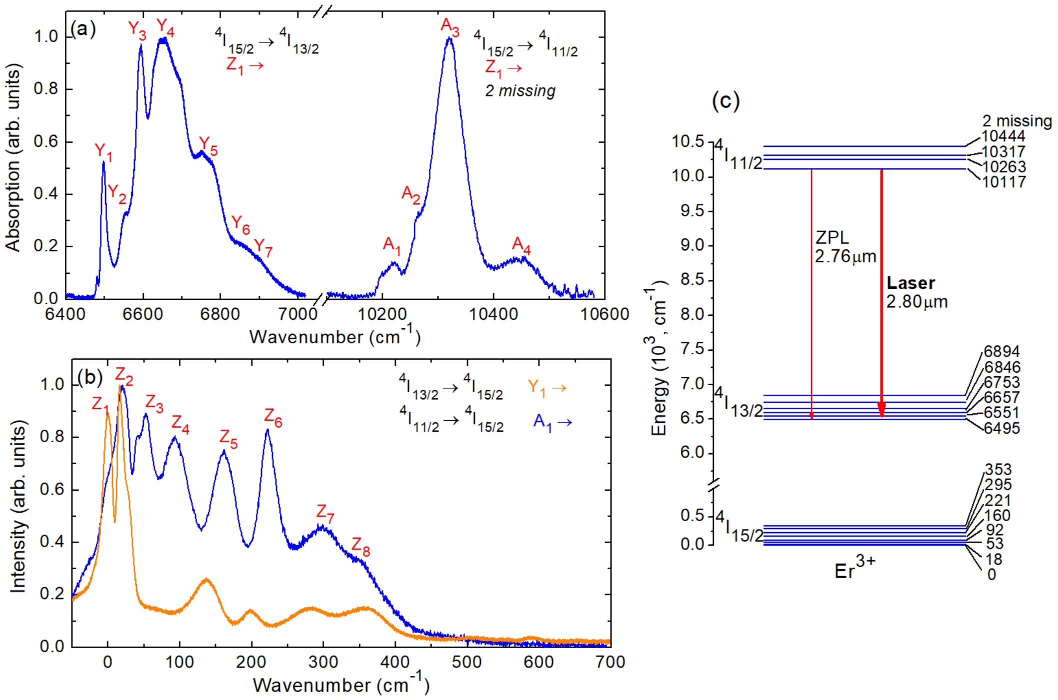

Figure IV.14: LT (12 K) spectroscopy of Er^{3+} ions in C_{4v} sites in $Na_5Y_9F_{32}$ crystal: (a) absorption spectra for the $^4I_{15/2} \rightarrow {}^4I_{13/2}$ and $^4I_{15/2} \rightarrow {}^4I_{11/2}$ transitions; (b) emission spectra for the $^4I_{11/2} \rightarrow {}^4I_{15/2}$ and $^4I_{13/2} \rightarrow {}^4I_{15/2}$ transitions. Z_i (i = 1...8), Y_j (j = 1...7) and A_k (k = 1...4) number the Stark sub-levels of the $^4I_{15/2}$, $^4I_{13/2}$ and $^4I_{11/2}$ multiplets, respectively; (c) Crystal-field splitting of the $^4I_{11/2}$, $^4I_{13/2}$ and $^4I_{15/2}$ multiplets of Er^{3+} ions in $Na_5Y_9F_{32}$, *numbers* – Stark energies in cm^{-1}, ZPL – zero-phonon line, *bold red arrow* – laser transition.

Table IV.14: Crystal-field splitting of the $^4I_{11/2}$, $^4I_{13/2}$ and $^4I_{15/2}$ multiplets of Er^{3+} ions in C_{4v} sites in $Na_5Y_9F_{32}$.

Manifold	**Notation**	**Stark components (cm^{-1})**
$^4I_{15/2}$	Z	0, 18, 53, 92, 160, 221, 295, 353
$^4I_{13/2}$	Y	6495, 6551, 6594, 6657, 6753, 6846, 6894
$^4I_{11/2}$	A	10117, 10263, 10317, 10444, *2 missing*

1.2.5 Mid-infrared luminescence spectra

The stimulated-emission (SE) cross-sections, σ_{SE}, for the $^4I_{11/2} \rightarrow {}^4I_{13/2}$ transition of Er^{3+} ions in the $Na_5Y_9F_{32}$ crystal were calculated using the Füchtbauer–Ladenburg (F-L). For this calculation, we have used the following parameters: $<n> = 1.470$, $\tau_{rad} = 9.99$ ms and $\beta(JJ') = 17.6\%$, according to the Judd-Ofelt analysis, taken from Table IV.13.

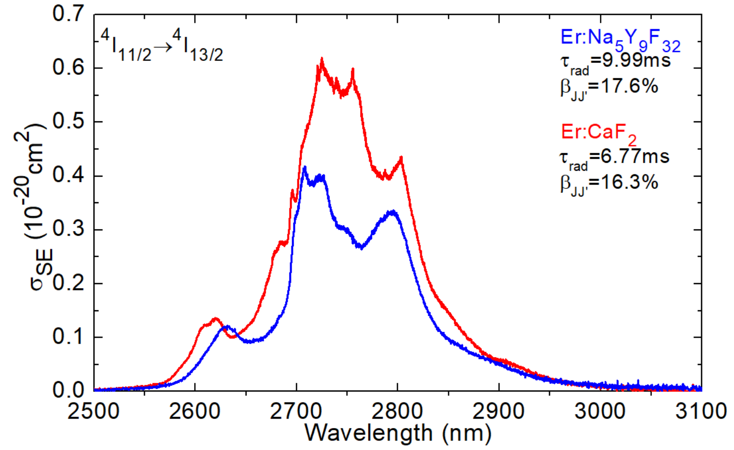

Figure IV.15: Stimulated-emission (SE) cross-sections, σ_{SE}, for the $^4I_{11/2} \rightarrow {}^4I_{13/2}$ transition of Er^{3+} ions in the $Na_5Y_9F_{32}$ and CaF_2 cubic crystals.

The calculated σ_{SE} spectrum for the Er^{3+}:$Na_5Y_9F_{32}$ crystal is shown in Figure IV.15. This material exhibits a broad and smooth emission band (a “glassy”-like behavior) spanning from 2.55 to 3.05 µm with a maximum $\sigma_{SE} = 0.42\times10^{-20}$ cm^2 at 2708 nm and another intense peak at a longer wavelength, 2795 nm ($\sigma_{SE} = 0.33\times10^{-20}$ cm^2). For comparison, in the same figure, we show the σ_{SE} spectrum for the Er^{3+}:CaF_2 crystal. Its maximum of SE cross-section is 0.62×10^{-20} cm^2 at 2724 nm. The spectra of both crystals are similar in shape. Due to the longer radiative lifetime of the $^4I_{11/2}$ Er^{3+} state in $Na_5Y_9F_{32}$, the absolute values of SE cross-sections for this material are lower than those for Er^{3+}:CaF_2 (τ_{rad} = 6.77 ms [Lab18b]).

1.2.6 Luminescence lifetimes: effect of the Er^{3+} doping

The decay curves of luminescence from the $^4I_{11/2}$ and $^4I_{13/2}$ states of Er^{3+} ions in the set of Er^{3+}:$Na_5Y_9F_{32}$ crystals measured under resonant excitation are shown in Figure IV.16 plotted in a semi-log scale. The luminescence decay was studied using finely powdered crystal samples to reduce the effect of radiation trapping (reabsorption). For the 5.59 at.% Er^{3+}:$Na_5Y_9F_{32}$ crystal, the luminescence decay times τ_{lum} amount to 7.72 ms ($^4I_{11/2}$) and 6.69 ms ($^4I_{13/2}$), representing a favorable ratio for mid-IR laser operation. As for the 5 at.% Er^{3+}:CaF_2 crystal, it has rather close luminescence lifetimes of 7.43 and 6.93 ms for the $^4I_{11/2}$ and $^4I_{13/2}$ multiplet, respectively.

Table IV.15 summarizes the τ_{lum} values as a function of the Er^{3+} doping concentration. At a very low doping level (0.22 at. % Er^{3+}), the lifetime of the lowest excited-state, $^4I_{13/2}$, is close to the radiative value determined using the J-O theory. For the next excited state, $^4I_{11/2}$, the τ_{lum} values is relatively close to the radiative lifetime indicating a weak non-radiative relaxation in agreement with the low phonon energy behavior of the host matrix. The multiphonon non-radiative relaxation (MNR) can be determine:

$$\frac{1}{\tau_{lum}} = \frac{1}{\tau_{rad}} + W_{NR} \tag{IV.1}$$

where W_{NR} is a probability of multiphonon non-radiative relaxation expressed in [s^{-1}]. Using abovementioned equation, we estimated the value for the $^4I_{11/2} \rightarrow {}^4I_{13/2}$ laser transition as 29.4 s^{-1} for 5.59 at.% Er^{3+}:$Na_5Y_9F_{32}$ crystal.

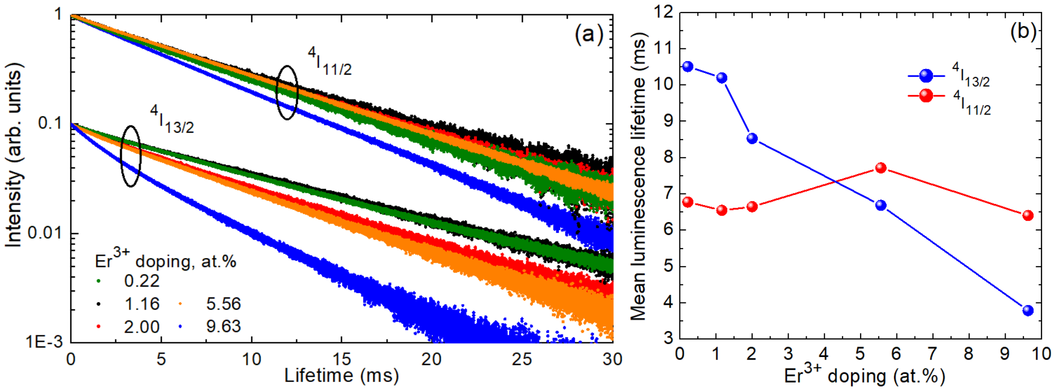

Figure IV.16: (a) Luminescence decay curves for Er^{3+} ions in Er^{3+}:$Na_5Y_9F_{32}$ crystals (0.2 – 10 at.% Er^{3+}) from the $^4I_{11/2}$ state, λ_{exc} = 970 nm, λ_{lum} = 1015 nm; and the $^4I_{13/2}$ state, λ_{exc} = 1480 nm, λ_{lum} = 1535 nm; (b) mean luminescence lifetimes $<\tau_{lum}>$ as a function of the Er^{3+} doping concentration.

As shown in Figure IV.16(b), upon Er^{3+} doping, the $^4I_{13/2}$ lifetime decreases significantly (from 10.51 to 3.79 ms for 0.22at. % Er^{3+} and 9.63 at.% Er^{3+}, respectively) while the $^4I_{11/2}$ one remains nearly constant. Indeed, MNR from the $^4I_{13/2}$ state increases strongly from W_{NR} = 0 s^{-1} (pure radiative transition) for 0.22at.% Er^{3+} to 168.6 s^{-1} for 9.63 at. % Er^{3+} thanks to ETU1 depleting this level. This highlights the potential of highly Er^{3+}-doped $Na_5Y_9F_{32}$ crystals for laser operation in the mid-IR. Considering the deteriorated optical quality of 9.63 at.% Er^{3+}-doped crystals, the doping levels about 4 – 7 at.% appear to be promising for laser experiments.

Table IV.15: Luminescence decay lifetimes, τ_{lum} of the $^4I_{11/2}$ and $^4I_{13/2}$ Er^{3+} manifolds in $Na_5Y_9F_{32}$ as a function of doping level.

Er content, at.%	**0.22**	**1.16**	**2**	**5.59**	**9.63**
$\tau_{lum}(^4I_{11/2})$, ms	6.78	6.55	6.65	7.72	6.41
$\tau_{lum}(^4I_{13/2})$, ms	10.51	10.20	8.53	6.69	3.79

1.3 Potassium yttrium fluoride (KY_3F_{10}) crystal: an overview of optical spectroscopy

As it was mentioned in Chapter II, the spectroscopy of $Er^{3+}:KY_3F_{10}$ has been already extensively studied in the literature [Lab18a]. Despite that, we will consider in this section, the essential spectroscopic properties of highly-doped Er^{3+}: KY_3F_{10} crystal relevant for understanding of laser behavior.

At first, we studied the spectral-kinetic properties relevant for the mid-IR laser. The stimulated-emission (SE) cross-sections, σ_{SE}, for the $^4I_{11/2} \rightarrow {}^4I_{13/2}$ transition were calculated by the Fuchtbauer–Ladenburg equation using the radiative lifetime τ_{rad} of 6.14 ms and the luminescence branching ratio $\beta_{JJ'}$ of 15.8% taken from previous work [Su18], Figure IV.17(a). The maximum σ_{SE} is 1.77×10^{-20} cm^2 at 2730 nm, corresponding to the zero-phonon line (ZPL) transition.

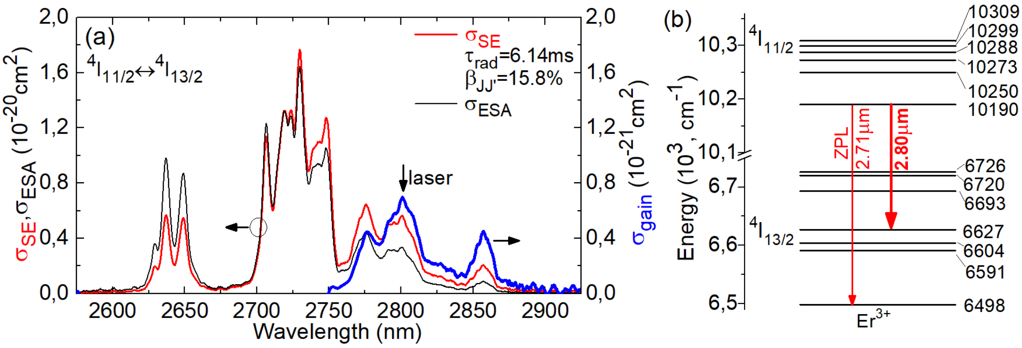

Figure IV.17: (a) Emission properties of $Er^{3+}:KY_3F_{10}$: (a) stimulated-emission (SE, *red*), σ_{SE}, excited-state absorption (ESA, *black*), σ_{ESA}, and gain (*blue*), σ_{gain}, cross-sections for the $^4I_{11/2} \leftrightarrow {}^4I_{13/2}$ transitions, the *arrow* indicates the laser wavelength, the inversion ratio $\beta = 0.45$; (b) Crystal-field splitting of the $^4I_{11/2}$ and $^4I_{13/2}$ multiplets of Er^{3+} ions in C_{4v} sites in KY_3F_{10}, *numbers* – Stark energies in cm^{-1}, *ZPL* – zero-phonon line, *bold red arrow* – laser transition.

The ESA cross-section, σ_{ESA}, spectrum was calculated by means of the reciprocity method using the crystal-field splitting for Er^{3+} in KY_3F_{10} [Su18], Figure 4.17(a,b) The maximum σ_{ESA} of 1.64×10^{-20} cm^2 corresponds to the zero-phonon-line (ZPL) transition at 2730 nm, i.e., the transition between the lowest Stark sub-levels of the two multiplets. The population of the terminal laser level ($^4I_{13/2}$) can be relatively high due to its long lifetime, so that the ESA from this level can be significant. Thus, the gain cross-sections, $\sigma_{gain} = \beta\sigma_{SE} - (1 - \beta)\sigma_{ESA}$, are calculated to conclude about the laser wavelength. Here, β is the inversion ratio, $\beta = N_3/(N_2 + N_3)$, N_3 and N_2 are the $^4I_{11/2}$ and $^4I_{13/2}$ state populations, respectively. According to the previous gain studies, β in highly-doped $Er^{3+}:KY_3F_{10}$ can be about ~0.45 [Su18]. The gain spectrum, Figure IV.17(a), presents a local maximum at 2800 nm (in agreement with the laser wavelength) and a gain bandwidth (FWHM) of ~40 nm. The laser wavelength was assigned to an electronic transition between the Stark sub-levels with the energies 10190 cm^{-1} ($^4I_{11/2}$) and 6627 cm^{-1} ($^4I_{13/2}$), Figure IV.17(b).

The luminescence decay curves from the $^4I_{11/2}$ and $^4I_{13/2}$ states of Er^{3+} in KY_3F_{10} are shown in Figure IV.18(a,b), measured using powders to avoid the radiation trapping effect. For 1 at.% doping, the average luminescence lifetimes $<\tau_{lum}> = \int I(t)t\mathrm{d}t/\int I(t)\mathrm{d}t$ are 5.39 ms ($^4I_{11/2}$) and 9.75 ms ($^4I_{13/2}$). By increasing the doping level up to 15 at.%, more favorable ratio of the upper-state to lower-state lifetimes is achieved: 4.64 ms ($^4I_{11/2}$) and 5.55 ms ($^4I_{13/2}$).

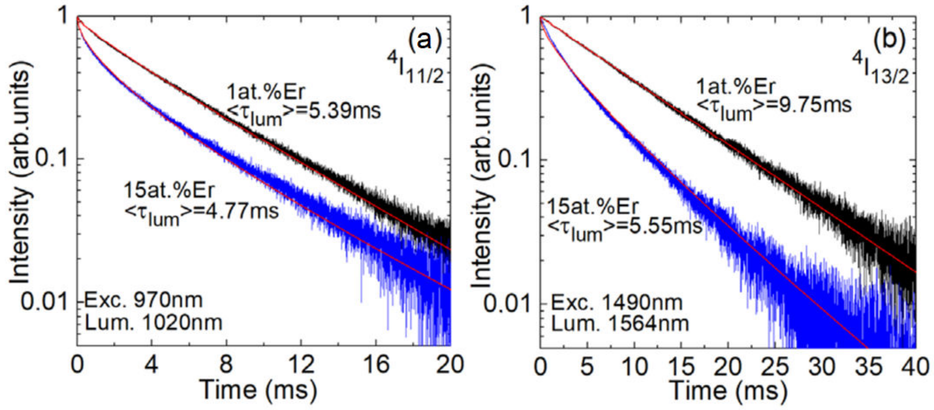

Figure IV.18: Luminescence decay curves from (a) the $^4I_{11/2}$ state and (b) the $^4I_{13/2}$ state for 1 and 15 at.% Er doping, $<\tau_{lum}>$ - mean luminescence lifetime.

1.4 Overview of the spectroscopic properties of studied cubic fluorite-type crystals

In summary, the spectroscopic properties of different cubic fluorite type crystals doped with Er^{3+} ions were investigated. Table IV.16 lists the following crystal properties: maximum phonon energy, $h\omega_{max}$, absorption cross-section, σ_{abs} at ~0.97 µm, stimulated emission cross-section, σ_{SE} at ~2.8 µm and lifetime, τ_{lum} of the $^4I_{11/2}$ and $^4I_{13/2}$ states.

All studied crystals exhibit extremely low phonon energies. The matrices MF_2 (M = Ca, Sr, Ba) have the lowest phonon energies. Within the series M = Ba → Sr → Ca, the phonon energy rises from 242 cm^{-1} (BaF_2) to 321 cm^{-1} (CaF_2). $Na_5Y_9F_{32}$ crystal has a slightly higher phonon energy of 404 cm^{-1}, while the crystal KY_3F_{10} has the highest value at 495 cm^{-1}. This low-phonon energy behaviour is a prerequisite for the almost vanishing multiphonon non-radiation pathway from both the $^4I_{11/2}$ and $^4I_{13/2}$ Er^{3+} manifolds.

The examined fluorite-type crystals have relatively intense and broad absorption peaks at ~0.97 µm, making them suitable for pumping by commercial InGaAs diodes. They exhibit strong mid-infrared emission around 2.8 µm with Er^{3+}:KY_3F_{10} having the largest stimulated emission cross-section of σ_{SE} of 1.77×10^{-20} cm^2 at 2730 nm, but limited spectral bandwidth (FWHM = 48 nm). Er^{3+}:MF_2 crystals, on the other hand, have broader emission spectra due to the clustering of Er^{3+} ions, with Er^{3+}:SrF_2 having the highest σ_{SE} of 0.72×10^{-20} cm^2 at 2729 nm and Er^{3+}:CaF_2 having the broadest spectrum (bandwidth, FWHM=124 nm). Er^{3+}:$Na_5Y_9F_{32}$ has the lowest σ_{SE} among the examined crystals and is equal to 0.42×10^{-20} cm^2 at 2708 nm. These findings have implications for the development of broadly tunable and mode-locked lasers in the mid-infrared range.

It was shown that a favorable ratio of the upper-to-lower laser level lifetimes in cubic fluorite-type crystals reaches at an Er^{3+} doping concentration of more than ~4.5at.%. For 5 at.% Er^{3+}:MF_2 crystals, the luminescence lifetimes of the $^4I_{13/2}$ / $^4I_{11/2}$ Er^{3+} manifolds increase, from 8.06 / 8.85 ms for Er^{3+}:CaF_2 to 9.17 / 10.36 ms Er^{3+}:BaF_2, respectively. For Er^{3+}: $Na_5Y_9F_{32}$ crystals, a favorable ratio of lifetimes of the $^4I_{13/2}$ / $^4I_{11/2}$ levels is calculated to be 6.69 / 7.72 ms and 3.79 / 6.41 for the 5.59 and 9.63 at.% Er^{3+} doping, respectively. Similar lifetimes of the$^4I_{13/2}$ / $^4I_{11/2}$ Er^{3+} levels were also observed for the 15 at.% Er:KY_3F_{10} crystal, which made it possible to achieve an effective population inversion between these levels.

Table IV.16: Summary of the spectroscopic properties of studied Er^{3+}-doped fluorite-type cubic crystals.

Crystal	**Doping, at.%**	$\hbar\omega_{max}$, **cm^{-1}**	σ_{abs}, **$10^{-20}cm^2$ ~0.97μm**	σ_{SE}, **$10^{-20}cm^2$**	$\tau_{lum}(^4I_{11/2})$, **ms**	$\tau_{lum}(^4I_{13/2})$, **ms**
CaF_2	5	321	0.22	0.59	8.85	8.06
SrF_2		285	0.26	0.72	9.55	8.54
BaF_2		242	0.28	0.68	10.26	9.17
$(Ca,Sr)F_2$		304	0.29	0.69	9.60	9.53
$(Ba,Sr)F_2$		267	0.30	0.71	10.36	9.29
$Na_5Y_9F_{32}$	0.22	404	0.16	0.42	6.78	10.51
	1.16				6.55	10.20
	2				6.65	8.53
	5.59				7.72	6.69
	9.63				6.41	3.79
KY_3F_{10}	15	495 [Mor91]	0.57	1.77	4.64	5.55

2 Fluoride bulk lasers at 2.8 µm

2.1 Laser set-up

The scheme of the mid-infrared laser set-up used for the experiments with the fluorite-type crystals shown in Figure IV.19**.** The laser crystals were mounted on a Cu-holder using a silver paint for better heat removal, it was passively cooled. The crystal was placed at normal incidence in a nearly hemispherical cavity formed by a flat pump mirror (PM) coated for high transmission in the two pump ranges ($T >$ 97% at 0.93 – 1.03 µm and $T >$ 80% at 0.78 – 0.84 µm), and for high reflectance (HR) at 2.6 – 3.0 µm, and a set of concave (radius of curvature, RoC = -100 mm) output couplers (OC) having a transmission T_{OC} of 0.33% - 4% at 2.7 – 2.9 µm.

For laser experiments with 4.5 at.% Er^{3+}:CaF_2 and 15 at.%Er^{3+}:KY_3F_{10} crystals, a single concave OC having a radius of curvature (RoC) of -75 mm and a transmission T_{OC} = 1.5% at ~2.8 µm. The geometrical cavity length was ~75 mm. The airgap between the crystal and the PM was less than 0.5 mm for all laser experiments.

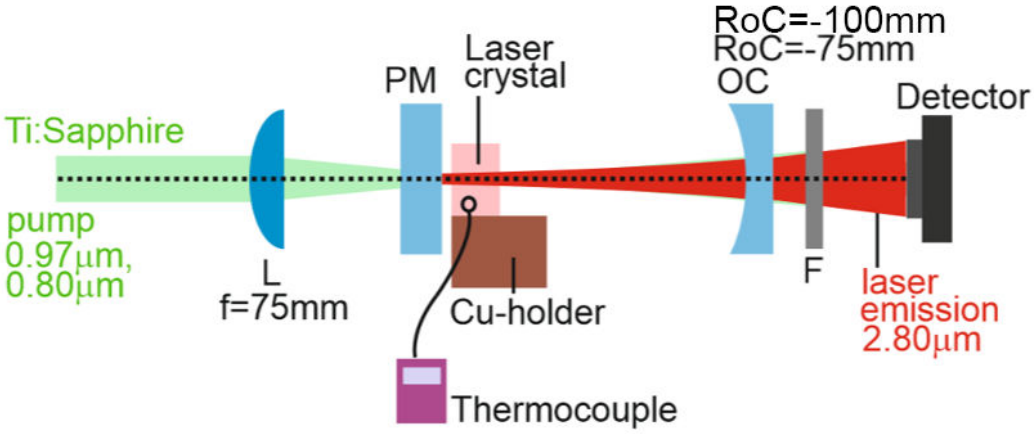

Figure IV.19: Scheme of the laser set-up: L - focusing lens, PM - pump mirror, OC - output coupler, F - long-pass filter.

A tunable CW Ti:Sapphire laser (model 3900S, Spectra Physics) with excellent beam quality ($M^2 \approx 1$) delivering up to 3.2 W at ~970 nm (the $^4I_{15/2} \rightarrow {}^4I_{11/2}$ Er^{3+} absorption peak). was used as a pump source. The measured pump spot radius at the 1/e^2 level w_P was 33±5 µm.

The non-absorbed (residual) pump was filtered out using a long-pass filter (LP1400, Spectrogon). The spectra of laser emission were measured using a ZrF_4 fiber (Thorlabs) and a laser spectrum analyzer (Bristol, 771 series). The spatial profile of the laser mode and the beam radii in the far-field were measured using a camera (Pyrocam IIIHR, Ophir-Spiricon). The M^2 parameter was evaluated using an ISO-standard procedure and the optical knife method for measuring the beam diameters.

A sensitive thermocouple (Type K, Ni-Cr + Ni-Al) was used in order to detect the crystal temperature change ΔT for further calculation of fractional heat loading of the 4.5 at.% $Er^{3+}:CaF_2$ crystal. The thermocouple was attached to the crystal edge using a small amount of silver paint.

2.2 Er:MF₂ lasers

2.2.1 Er:CaF₂ laser

Mid-infrared laser operation of $Er^{3+}:CaF_2$ was studied previously, in Table IV.17 there is a summary of the output characteristics. In this table, the results are grouped according to the pump source (a Ti:Sapphire laser or a laser diode). Labbe *et al.* used a highly doped crystal (10.3 at.% $Er^{3+}:CaF_2$) delivering 80mW at 2800 nm with a slope efficiency of 30% under Ti:Sapphire laser pumping [Lab02]. In [Lab02], three pumping schemes for $Er^{3+}:CaF_2$ lasers were proposed, namely pumping into the upper laser level $^4I_{11/2}$ (at ~0.97 μm), into the higher-lying multiplet $4I_{9/2}$ (at ~0.80 μm) and into the terminal laser level $4I_{13/2}$ (at ~1.54 μm). Further power scaling was demonstrated using a laser diode, Ma *et al.* achieved in 4 at.% $Er^{3+}:CaF_2$ crystal 304 mW of output power however with a deteriorated slope efficiency of 17.2% and a much higher laser threshold of 335mW mainly due to the poorer beam quality of the used pump source as compared to high-brightness laser pumping [Ma16a]. Zong *et al.* developed a diode-pumped laser using a low doped crystal (1.3 at.%. $Er^{3+}:CaF_2$) generating 2.2 W at 2744nm with a slope efficiency of 28.3% [Zon22].

Despite of the fact, that mid-infrared laser operation in $Er^{3+}:CaF_2$ was extensively studied previously, in this part of thesis, we aimed to study the further power scaling capabilities of 2.8 μm $Er^{3+}:CaF_2$ lasers with 4.5at.% and 5at.% Er^{3+} doping for two commonly used pumping schemes (pumping into the $^4I_{11/2}$ and $^4I_{9/2}$ states).

Table IV.17: Output performance of mid-Infrared $Er^{3+}:CaF_2$ lasers reported so far.

Pump	**Er doping, at.%**	**Material**	**λ_P, nm**	**P_{out}, mW**	**λ_L, nm**	**η, %**	**P_{th}, mW**	**Reference**
LD	1.3	Crystal	973	2200	2744	28.3	-	[Zon21]
	1.7	Crystal	980	2320	2726	21.2	500	[Zon22]
	4.0	Crystal	974	282	2790	13.9	~240	[Ma16a]
	4.0	Crystal	972	304	-	17.2	335	[Ma16b]
	4.0	Crystal	974	295	2794	16.7	724	[Li16]
	5	Crystal	980[b]	~370	2747	5	~5000	[Bas06]
	5.5	Ceramic	968	~4	2720	1.3	183	[Sul13]
TS	10.3	TS	968	80	2800	30	**23**	[Lab02]
	4.5	TS	967.6	**834**	2800	**31.6**	24	This work
	5	TS		**702**	2800	**37.9**	60	This work

[a] Pump: LD – laser diode, TS – Ti:sapphire laser, λ_P and λ_L – pump and laser wavelengths, respectively, P_{out} – output power, η – slope efficiency, P_{th} – laser threshold. [b] Transvers pumping

When pumping into the $^4I_{11/2}$ multiplet (λ_P = 967.6 nm), the Er^{3+}:CaF_2 laser generated a maximum CW output power of 834 mW at 2800 nm with a slope efficiency η of 31.6% (versus the absorbed pump power) and a threshold P_{th} of only 24 mW, Figure IV.20(a). This slope efficiency is only slightly below the Stokes limit, $\eta_{St,L} = \lambda_P/\lambda_L$ = 34.6%. The optical-to-optical efficiency η_{opt} with respect to the pump power incident on the crystal reached 23.2%.

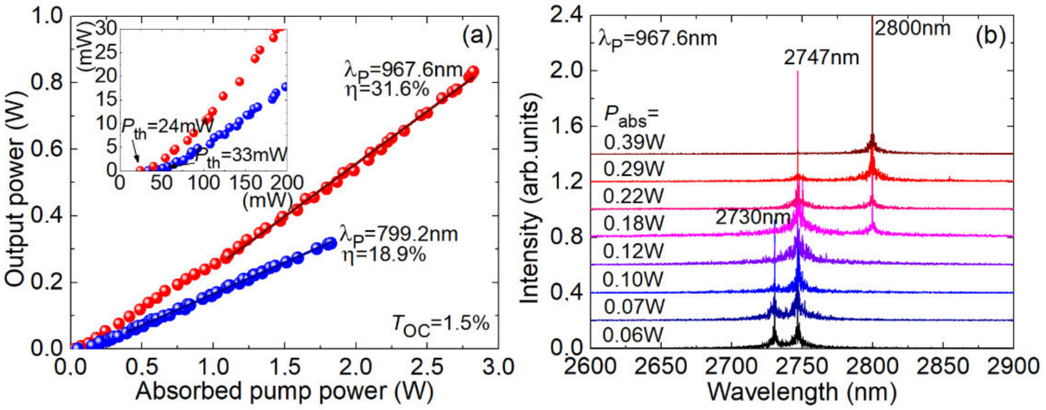

Figure IV.20: Output performance of 4.5at.% Er^{3+}:CaF_2 lasers: (a) input-output dependences, η – slope efficiency, *inset* – a close look at the laser thresholds; (b) typical spectra of laser emission for λ_P = 967.6 nm measured at different pump powers, T_{OC} = 1.5%. The laser emission is unpolarized.

When pumping into the $^4I_{9/2}$ state (λ_P = 799.2 nm), the maximum output power was lower, namely 318 mW at 2800 nm with reduced η = 18.9% and slightly higher P_{th} of 33 mW. The reduction of the slope efficiency is mainly due to an additional energy loss originating from the non-radiative relaxation between the $^4I_{9/2}$ and $^4I_{11/2}$ states. The input-output dependences for both pump wavelengths were linear well above the laser threshold and no thermal roll-over nor crystal fracture were observed in the studied range of pump powers. A slight nonlinearity of the output dependence was observed near the threshold, as shown at the inset of Figure IV.20(a). For both pump wavelengths, the emission wavelength experienced a red shift with increasing the pump power slightly above the laser threshold (from 2730 nm to 2747 nm and further to 2800 nm) and stabilized for high pump levels, as shown in Figure IV.20(b) for the particular case of λ_P = 967.6 nm.

To explain this spectral behavior, one need to consider several factors. First, briefly, the $^4I_{11/2} \rightarrow {}^4I_{13/2}$ laser transition is a quasi-four level one with no reabsorption. However, for Er^{3+} ions, there exist a strong resonant excited-state absorption (ESA) channel, $^4I_{13/2} \rightarrow {}^4I_{11/2}$, which may play a significant role considering a relatively high population of the metastable $^4I_{13/2}$ state. In Figure IV.21(a), we show the stimulated-emission (SE) cross-section, σ_{SE}, spectrum for the $^4I_{11/2} \rightarrow {}^4I_{13/2}$ transition, calculated using the Füchtbauer–Ladenburg (F-L) equation using a radiative lifetime τ_{rad} = 6.77 ms and a luminescence branching ratio $B(JJ')$ = 16.3% [Lab18b]. The maximum σ_{SE} =

0.61×10^{-20} cm^2 at 2730 nm. The broad and smooth profile SE cross-section spectrum is due to a strong ion clustering appearing for Er^{3+}:CaF_2 crystals for doping levels >0.5 at.% leading to a significant inhomogeneous spectral broadening. By reciprocity method (RM), the ESA cross-sections, σ_{ESA}, were calculated, Figure IV.21(a). The maximum $\sigma_{ESA} = 0.45\times10^{-20}$ cm^2 at 2730 nm.

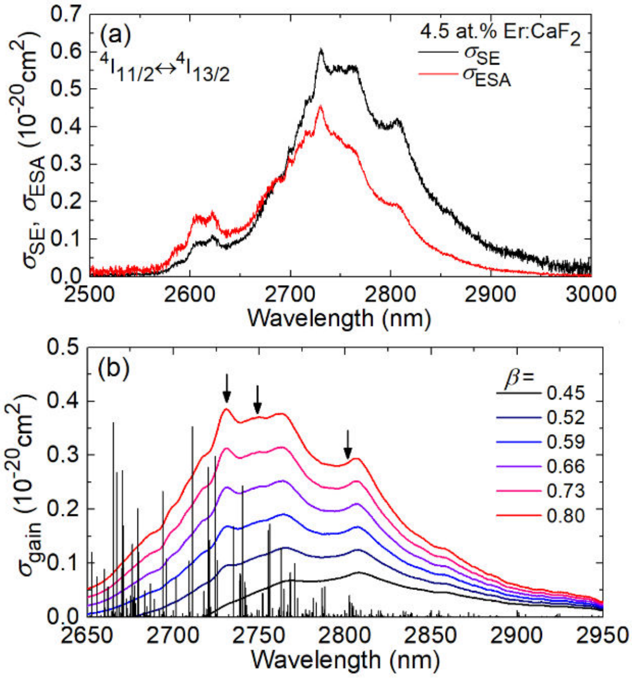

Figure IV.21: (a) Mid-infrared emission properties of Er^{3+} ions in the CaF_2 crystal: stimulated-emission (SE), σ_{SE}, and excited-state absorption (ESA), σ_{ESA}, cross-sections for the $^4I_{11/2} \leftrightarrow {}^4I_{13/2}$ transition (excluding water vapor absorption in the atmosphere); (b) gain cross-section spectra for different inversion ratios, β. *Vertical lines* – water vapor absorption in the atmosphere (according to HITRAN database), in arb. units.

Thus, by analogy to quasi-three-level lasers, the gain cross-sections, $\sigma_{gain} = \beta\sigma_{SE} - (1 - \beta)\sigma_{ESA}$, were calculated, where $\beta = N(^4I_{11/2})/(N(^4I_{11/2}) + N(^4I_{13/2}))$ is the inversion ratio and N are the manifold populations, as shown in Figure IV.21(b). With decreasing β, several local peaks appear in the gain spectra centered at 2.73, 2.75, 2.76 and 2.81 µm, depending on the inversion level. Not all these wavelengths can be generated because of the structured water vapor absorption in the atmosphere spectrally overlapping with the mid-IR Er^{3+} luminescence. The possible lines are indicated by arrows, and they agree well with the laser spectra. The decrease of β with the pump power causing the observed red-shift of the laser wavelength is probably due to the pump-dependent ETU refilling the upper laser level.

Thus, by analogy to quasi-three-level lasers, the gain cross-sections, $\sigma_{gain} = \beta\sigma_{SE} - (1 - \beta)\sigma_{ESA}$, were calculated, where $\beta = N(^4I_{11/2})/(N(^4I_{11/2}) + N(^4I_{13/2}))$ is the inversion ratio and N are the manifold populations, as shown in Figure IV.21(b).

With decreasing β, several local peaks appear in the gain spectra centered at 2.73, 2.75, 2.76 and 2.81 µm, depending on the inversion level. Not all these wavelengths can be generated because of the structured water vapor absorption in the atmosphere spectrally overlapping with the mid-IR Er^{3+} luminescence. The possible lines are indicated by arrows, and they agree well with the laser spectra. The decrease of β with the pump power causing the observed red-shift of the laser wavelength is probably due to the pump-dependent ETU refilling the upper laser level.

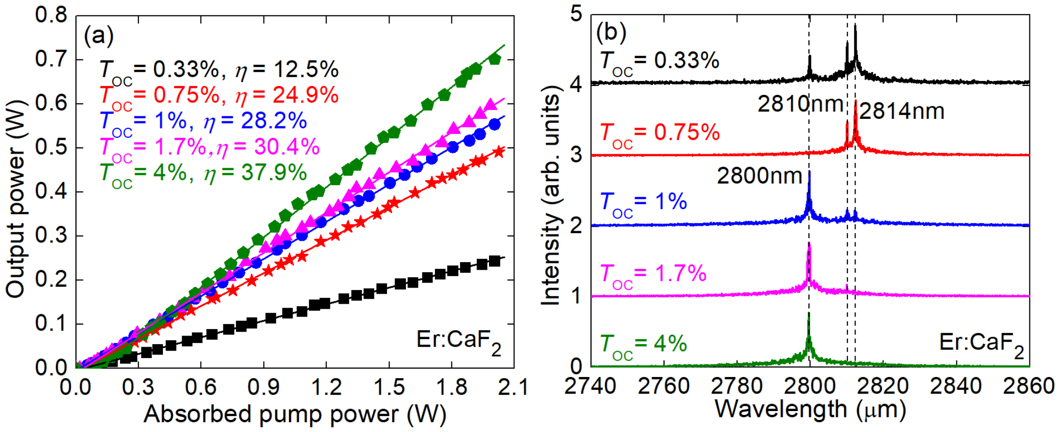

Figure IV.22: Output performance of 5 at.% Er^{3+}:CaF_2 lasers: (a) input-output dependences, λ_P = 967.6nm, η – slope efficiency; (b) typical laser spectra, P_{abs}~1.5 W.

The better laser performance was achieved using the 5at.% Er^{3+}:CaF_2 crystal. Laser generated an output power of 702 mW at 2800 nm with a slope efficiency, η of 37.9% (vs. the absorbed pump power) when using the output coupler with T_{OC} = 4%, as shown in Figure IV.22(a). The laser threshold gradually increased from 16 mW to 60 mW with increasing output coupling from T_{OC} = 0.33% to 4%. The measured pump absorption for 5at.% Er^{3+}:CaF_2 was weakly dependent on the output coupling and reached 81.9%. The optical-to-optical efficiency (vs. the pump power incident on the crystal) η_{opt} was 31.0%. The output dependences were linear within the studied range of pump powers, and further power scaling was limited by the available pump. The achieved laser slope efficiency exceeded the Stokes limit of 34.6%, indicating the role of the ETU process $^4I_{13/2} + {}^4I_{13/2} \rightarrow {}^4I_{9/2} + {}^4I_{15/2}$ in refilling the upper laser level and depopulating the intermediate $^4I_{13/2}$ state.

The typical emission spectra of the 5 at.% Er^{3+}:CaF_2 laser are shown in Figure IV.22(b), measured well above the laser threshold. The laser emission occurred at 2810 and 2814 nm for small output couplers (<1%) and at 2800 nm for higher transmission T_{OC}. These wavelengths correspond to the long-wave emission peak of Er^{3+} ions in CaF_2 and match the transparency ranges between the structured water vapor absorption lines, as shown in Figure IV.3. Note that due to strong resonant excited-state absorption from the terminal laser level with a non-negligible population, $^4I_{13/2} \rightarrow {}^4I_{11/2}$, the $^4I_{11/2} \rightarrow {}^4I_{13/2}$ Er^{3+} laser transition represents a quasi-three-level laser scheme with reabsorption, which explains the blue-shift of the laser spectra with increasing the output coupling.

For 4.5at.% Er^{3+}:CaF_2 crystal, we measured the laser excitation curves (the dependence of the output power on the pump wavelength for a fixed incident pump power P_{inc}) for both pump transitions, as shown in Figure IV.23. When pumping into the $^4I_{11/2}$ and $^4I_{9/2}$ manifolds, lasing was achieved for λ_P in the ranges of 944.9 – 1014.8 nm and 781.0 – 834.2 nm, respectively. For comparison, in Figure IV.23 we also show the corresponding absorption cross-section, σ_{abs}, spectra. The two sets of data agree well with each other, indicating that pumping into the absorption peak is desirable. For the $^4I_{15/2} \rightarrow {}^4I_{11/2}$ transition, $\sigma_{abs} = 1.85\times10^{-21}$ cm^2 at 967.6 nm and the absorption bandwidth (FWHM) is as broad as ~21 nm.

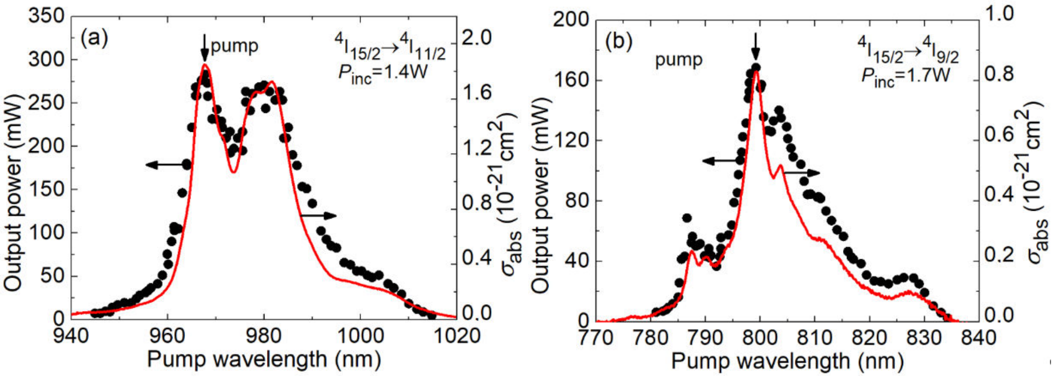

Figure IV.23: Laser excitation curves for the 4.5 at.% Er^{3+}:CaF_2 laser operating at ~2800 nm. The pump transitions are (a) $^4I_{15/2} \rightarrow {}^4I_{11/2}$ and (b) $^4I_{15/2} \rightarrow {}^4I_{9/2}$. *Symbols* – experimental data, *curves* - absorption cross-section, σ_{abs}, spectra.

The round-trip passive losses L in the 5at.% Er^{3+}:CaF_2 laser crystal using the Findlay-Clay analysis [Fin66], i.e., by plotting the laser threshold P_{th} as a function of ln(1/R_{OC}), where $R_{OC} = - T_{OC}$ is the output coupler reflectivity, as shown in Figure IV.24. This estimation uses a model of a quasi-four-level laser accounting for the reabsorption at the laser wavelength [Ser16] (originating from ESA, $^4I_{13/2} \rightarrow {}^4I_{11/2}$) The best-fit of experimental points yielded a round-trip passive loss L = 0.79 % corresponding to a loss coefficient $\delta = 0.006$ cm^{-1} for the 5at.% Er^{3+}:CaF_2 laser. The loss coefficient, δ is determined from the expression (IV.2):

$$L = 2\delta l \qquad \text{(IV.2)}$$

Where L is the round trip losses in unit fraction, l is a thickness of the laser element. The thickness of the 5 at.% Er:CaF_2 laser crystal was t = 6.82 mm.

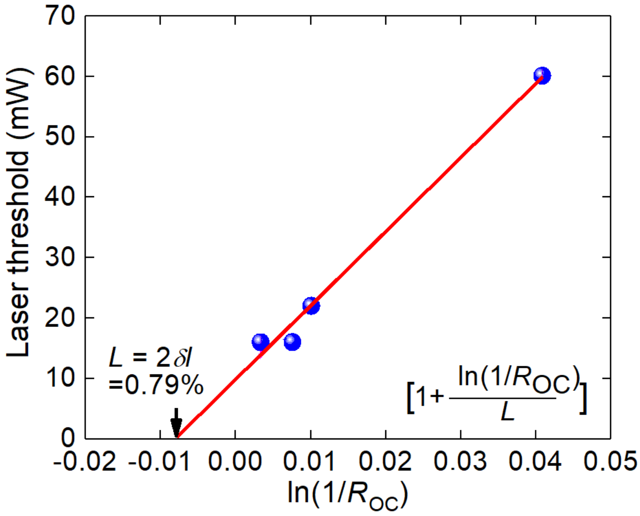

Figure IV.24: Findlay-Clay analysis for the determination of the round-trip passive loss, *L* for the 5 at.% Er^{3+}:CaF_2 laser operating at ~2800 nm.

2.2.2 Thermo-optic effects of Er:CaF_2 crystal

Crystals have a significant advantage over other materials, particularly glasses, in laser applications due to their periodic lattice structure, which provides higher thermal conductivity and efficient heat dissipation. This is very important, especially for materials used in high-power lasers.

The main source of heat generation is the non-radiative relaxation process from the pump level to the upper laser level and from the lower laser level to the ground state (i.e., the difference in energy between the pump photon and the laser radiation). Heat release also occurs in energy transfer processes involving absorption from the excited state, upconversion transitions, and cross-relaxation. The heat release centers in an active element matrix can be impurities, inhomogeneities, or defects [Loi12]. As already discussed in Chapter I, calcium fluoride (CaF_2) crystals have very high thermal conductivity values of the order of 9.7W·$m^{-1}K^{-1}$, which makes it a good candidate for applications requiring materials with good heat dissipation and thermal shock resistance. However, when CaF_2 is doped with RE^{3+}, the thermal conductivity drops dramatically [Pop08]. In the case of erbium lasers emitting at 2.8 µm, the expected contribution of thermal effects is significant because of multiple energy transfer conversion and cross-relaxation processes accompanying the non-radiative relaxation of Er^{3+} ions.

In order to explain the thermal distortions of the active component, we rely on a thermal lens model, which is essentially an ideal lens that produces the same impact on the radiation's wavefront as the distorted active medium caused by thermo-optics. A feature of a thermal lens is the proportional relationship between its optical power and pump power [Loi12]. In general, the expression for the optical power of the thermal lens of the solid-state laser active element under laser pumping is following:

$$D = \frac{\eta_h P_{abs}}{\pi w_p^2 \kappa}\left(dn/dT + P_{stress} + Q_{dist} \right) \quad \text{(IV.3)}$$

where *P*abs is the absorbed pump power, η_h is the fractional heat loading (i.e the part of P_{abs} dissipated in the active element as heat), ω_p is the pump mode radius in the active element, κ is the thermal conductivity, d*n*/d*T* is the value describing the contribution of the refractive-index temperature dependence in the absence of stress, P_{stress} is the photoelastic effect, and Q_{dist} is the contribution of the distortion of the active element end faces.

Thermal lensing is an important effect for solid-state laser engineering as it affects the cavity stability and the mode-matching efficiency leading to deterioration of the laser performance. So far, thermo-optic effects have never been studied for mid-infrared Er:CaF$_2$ lasers. In this work, we aimed to study thermo-optics (including the astigmatic thermal lensing and the fractional heat loading) of ~2.8 µm Er:CaF$_2$ lasers for two commonly used pump schemes (pumping into the $^4I_{11/2}$ and $^4I_{9/2}$ Er^{3+} states), for the first time, to the best of our knowledge.

- **Fractional heat loading**

The fractional heat loading, i.e., the fraction of an absorbed pump power transferred into heat is an important parameter for calculation of the optical power of the thermal lens, as well as for evaluation of the risk of thermal fracture. This parameter is defined as:

$$\eta_h = P_{\text{heat}}/P_{abs} \quad \text{(IV.4)}$$

In the present work, the fractional heat loading was measured by laser calorimetry (the gradient method). The principle of this gradient method is as follows. The change of the crystal temperature ΔT at its periphery was monitored as a function of time *t* when the pump was on ($0 < t < t_p$) and off ($t > t_p$, $t_p = 120$ s – pump pulse duration). The heating and the cooling curves were measured with a time step of 5 s and 10 s, respectively. By fitting the heating curve as an exponential rise, the heating rate $(dT/dt)_h$ was determined at the moment of $t \approx 0.8t_p$. By fitting the cooling curve with an exponential decay, the cooling rate $(dT/dt)_c$ was determined at the moment of equal temperature, Figure IV.25(a). Then, the fractional heat loading was calculated as:

$$\eta_h = \left[\sum m_i C_i / P_{abs} \right] \times \left[\left(dT/dt \right) h + \left(dT/dt \right) c \right] \quad \text{(IV.5)}$$

where m_i and C_i are the masses and the specific heats of the crystal ($m = 0.941$ g and $C = 0.858$ Jg^{-1}K^{-1}) and the Cu-holder ($m = 3.698$ g and $C = 0.385$ Jg^{-1}K^{-1}), respectively. Between the measurements, the laser crystal was left for ~10 min to return to the thermal equilibrium. Each measurement was repeated 3 times and the obtained η_h values were averaged.

When pumping into the $^4I_{11/2}$ state, $\eta_{h,L}$ = 52.0±2% and $\eta_{h,NL}$ = 71.7±3%. When pumping into the $^4I_{11/2}$ state, both values increase and approach each other, $\eta_{h,L}$ = 64.1±4% and $\eta_{h,NL}$ = 77.6±5%. The heat dissipation in $Er^{3+}:CaF_2$ originates from multiphonon non-radiative (NR) relaxation and non-radiative transitions related to energy migration to defects and impurities from the excited-states directly populated via pump absorption, as well as populated via ETU. For the $^4I_{15/2} \rightarrow {}^4I_{9/2}$ pumping scheme, the heat loading both under L and NL conditions is increased due to an additional NR relaxation channel between the closely located $^4I_{9/2}$ and $^4I_{11/2}$ states.

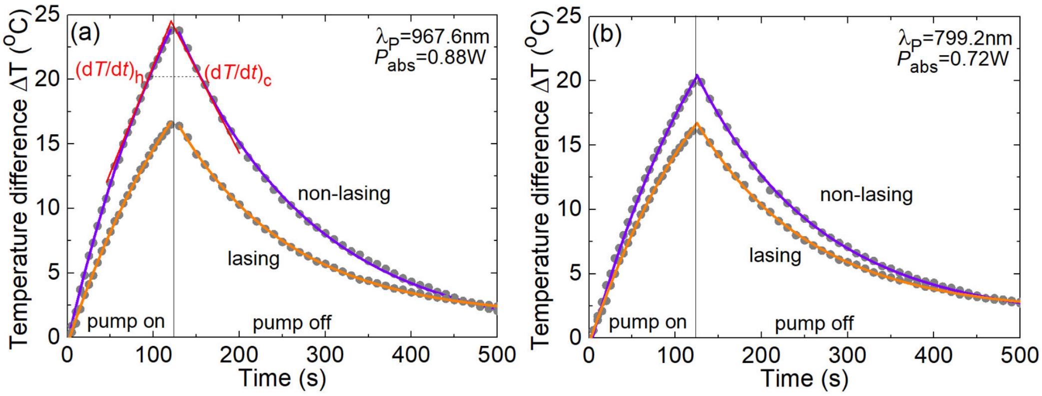

Figure IV.25: Evaluation of the fractional heat loading η_h in a 4.5 at.% $Er^{3+}:CaF_2$ laser crystal for lasing and non-lasing conditions. The pump wavelength λ_P is (a) 967.6 nm and (b) 799.2 nm. *Symbols* – experimental data, *curves* –exponential fits of rise and decay. *Vertical line* – the moment of switching off the pump (t_p), *dashed line* – temperature rise at $t = 0.8\ t_p$, *red lines* – heating and cooling slopes.

This experimental results agree well with the theoretical estimations by Pollnau [Pol03] for $Er^{3+}:LiYF_4$ crystals pumped into the $^4I_{11/2}$ Er^{3+} state (Figure IV.26) with doping levels optimized for high slope efficiency [Wys97], both qualitatively (the fractional heat loading is weaker under lasing conditions) and quantitatively.

Moreover, in work [Pol03], it is shown that in 3-µm Er lasers ETU processes, characteristic of population mechanisms, do not directly contribute to heat generation. However, they cause non-radiative decay through MNR processes, which leads to the dissipation of a significant amount of heat in the crystal. Under non-lasing conditions, this problem is exacerbated due to the higher population density at the upper laser level, which leads to additional ETU. As a consequence, the higher temperature and thermal lens power explain why crystal damage is frequent in this laser system compared to other similar lasers under equivalent pumping conditions.

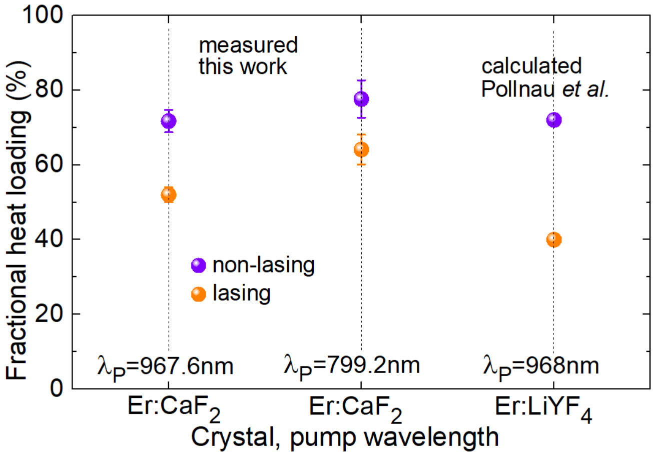

Figure IV.26: A summary of measured values of the fractional heat loading η_h for a 4.5 at.% Er^{3+}:CaF_2 laser crystal under lasing and non-lasing conditions. The calculated data for Er^{3+}:$LiYF_4$ are given for comparison [Pol03].

Let us discuss in detail the mechanisms of heat generation in Er^{3+}:CaF_2. First, the relevant energy-transfer processes have to be considered, as shown in Figure IV.27. These are two energy-transfer upconversion processes, ETU1 ($^4I_{13/2} + {}^4I_{13/2} \rightarrow {}^4I_{15/2} + {}^4I_{9/2}$) and ETU2 ($^4I_{11/2} + {}^4I_{11/2} \rightarrow {}^4I_{15/2} + {}^4F_{7/2}$), as well as a cross-relaxation process, CR ($^4S_{3/2} + {}^4I_{15/2} \rightarrow {}^4I_{9/2} + {}^4I_{13/2}$). Due to the strong ion clustering in Er:CaF_2 even at moderate doping levels, all the energy-transfer processes are expected to be more efficient than intrinsic decay from the long-living states, i.e., $^4I_{13/2}$, $^4I_{11/2}$ and thermally-coupled $^4S_{3/2}$+$^2H_{11/2}$ ones. Thus, the multiphonon NR relaxation from these states weakly contributes to heat generation. Still, for the levels quenched by fast NR relaxation, $^4I_{9/2}$, $^4F_{9/2}$ and $^4F_{7/2}$, its contribution to heat generation could be significant. As the $^4S_{3/2}$+$^2H_{11/2}$ states are mainly depleted by CR bypassing the $^4F_{9/2}$ state, the latter manifold has low population and does not contribute to heat release. Thus, two processes have to be considered: NR1 ($^4I_{9/2} \rightarrow {}^4I_{11/2}$) and NR2 ($^4F_{7/2} \rightarrow {}^4S_{3/2}$). Note that both of them are associated with an ETU process: NR1 follows ETU1 and NR2 follows ETU2. Under non-lasing conditions, the population of the $^4I_{11/2}$ level is not clamped by the threshold condition, and it greatly increases as compared to lasing conditions giving rise to an efficient ETU2 process followed by NR1, CR and NR2 processes. This explains higher η_h values observed under non-lasing conditions.

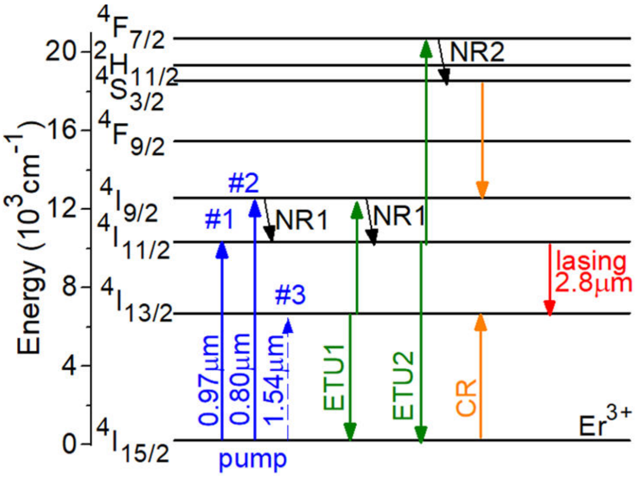

Figure IV.27: Energy-level scheme of Er^{3+} ions showing pump (*blue*) and laser (*red*) transitions, energy transfer upconversion (ETU, *green*), cross-relaxation (CR, *orange*) and non-radiative relaxation (NR, *black*) processes.

- **Thermal lensing**

The thermal lens in Er^{3+}:CaF_2 crystals was quantified under lasing conditions by measuring the divergence of the laser beam in the far-field (at ~9 cm from the OC) at different pump powers. The laser mode inside the cavity, as well as its propagation outside of the cavity were simulated using the ray transfer matrix formalism (ABCD) accounting for a thin ideal astigmatic thermal lens located in the center of the crystal, as well as the measured beam quality parameters $M^2_{x,y}$ of the laser radiation [Loi17]. An example evaluation of the beam quality factors $M^2_{x,y}$ for the Er^{3+}:CaF_2 laser pumped at λ_P = 967.6 nm is shown in Figure IV.29. It was performed according to the ISO-standard procedure. At an absorbed pump power P_{abs} of 0.75 W, they amounted to M^2_x = 1.35 and M^2_y = 1.88. At the inset of Figure IV.28, the typical profile of the laser mode in the far-field is shown. The mode shows only slight ellipticity.

According to the ellipticity of the laser beam, two meridional planes of the thermal lens were established, denoted as "*r*" and "*θ*". Here, we use the same notations for cubic crystals as in the state-of-the-art works of Koechner [Koe06] and Chenais *et al.* [Che06]. Note that these planes are not necessarily linked to the horizontal and vertical directions.

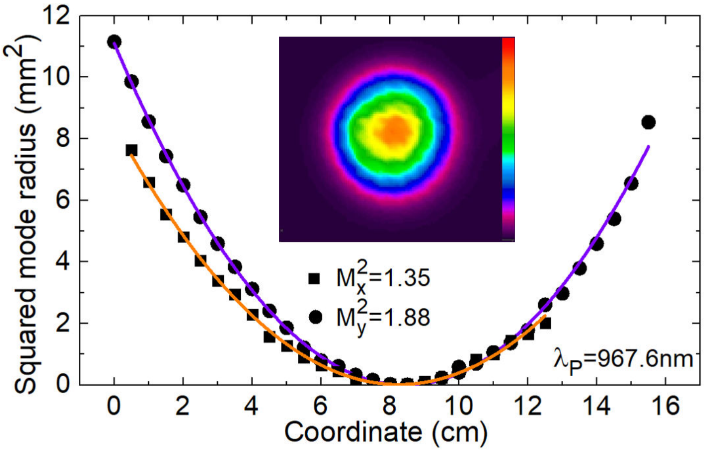

Figure IV.28: Evaluation of the beam quality factors $M^2_{x,y}$ for the 4.5at.% Er^{3+}:CaF_2 laser, *inset* – typical far-field profile of the laser mode, P_{abs} = 0.75 W, λ_P = 967.6 nm.

The beam radii of the laser mode measured as a function of the absorbed pump power for λ_P = 799.2 nm are shown in Figure IV.29. The laser mode expands with the pump power indicating an action of a negative (divergent) thermal lens. The beam ellipticity is weak. In the same graph, we show the simulated dependences (curves) accounting for a pump-dependent thermal lens.

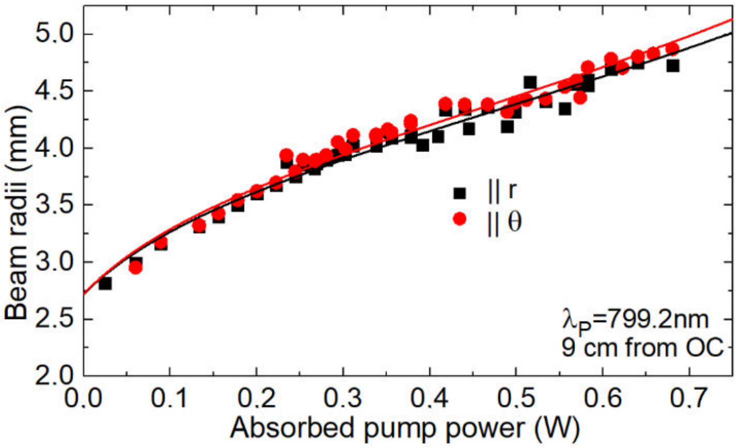

Figure IV.29: Measured radii of the output beam from the Er^{3+}:CaF_2 laser, λ_P = 799.2 nm, the distance from the OC is 9 cm, "*r*" and "*θ*" mark the semiaxes of the elliptical beam.

The results on the corresponding optical (refractive) power of the thermal lens *D* = 1/f for both pump transitions are shown in Figure IV.30. Due to different positions of the focus, pump beam quality and pump wavelengths, the pump beam radii averaged along the crystal <w_P> were slightly different for the two pump schemes. From the measurements performed by the optical knife method, they were determined to be <w_P> = 63±5 μm (λ_P = 967.6 nm) and 48±5 μm (λ_P = 799.2 nm).

Thus, for the sake of correct comparison, the optical power of the thermal lens was plotted versus the on-axis absorbed pump intensity for a Gaussian beam,

$$I_{abs} = {}^{2P_{abs}}\!\big/_{\pi < w_P >^2} \qquad \text{(IV.6)}$$

The thermal lens in $Er^{3+}:CaF_2$ is negative. Within the studied range of absorbed pump powers, the dependence of the optical power on I_{abs} can be reasonably good approximated with a linear law. Pollnau have simulated thermal lensing in $Er^{3+}:LiYF_4$ and predicted a non-linear variation of the dioptric power, especially at high pump levels, mainly due to a temperature dependence of material parameters [Pol03]. Such effects seem to be still weak for the studied lasers.

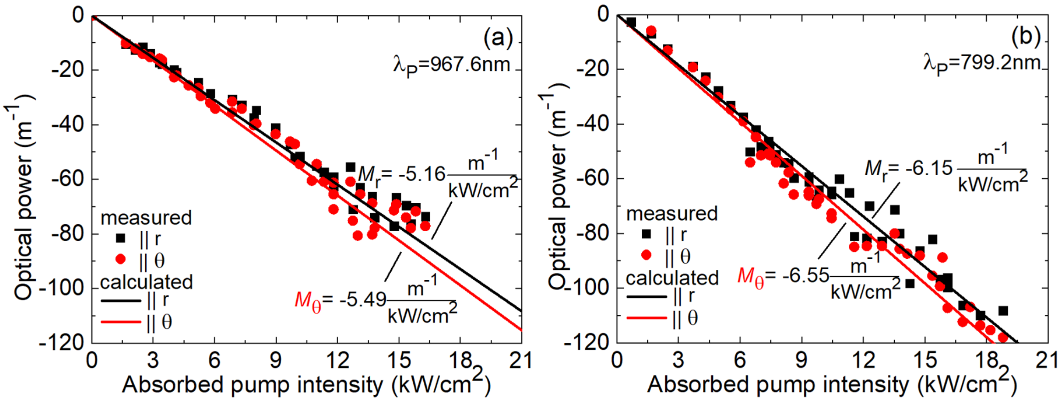

Figure IV.30: Thermal lensing in the $Er^{3+}:CaF_2$ laser crystal: optical power for principal meridional planes, *symbols* – experimental data, *lines* – calculation using Equation (IV.7), the calculated sensitivity factors (M) are indicated. The pump wavelength λ_P is (a) 967.6 nm and (b) 799.2 nm.

The slopes of these dependences are called the sensitivity factors showing the increase of the optical power due to a variation of the pump intensity by 1 kW/cm^2 [Loi09], were determined by Equation (IV.7):

$$M_{\mathrm{r}(\theta)} = {}^{dD_{r(\theta)}}\!\big/_{dI_{abs}} \qquad \text{(IV.7)}$$

For $\lambda_P = 967.6$ nm, we obtained $M_r = -4.84$ and $M_\theta = -5.15$ $[m^{-1}/(kW/cm^2)]$. The thermal lens is weakly astigmatic: the astigmatism degree, $S/M = |M_\theta - M_r|/|M_\theta|$, is only ~6%. For $\lambda_P = 799.2$ nm, the thermal lens becomes stronger owing to the stronger heat dissipation, $M_r = -6.15$ and $M_\theta = -6.49$ $[m^{-1}/(kW/cm^2)]$. For completeness, we also list the sensitivity factors of the thermal lens versus the absorbed pump power (note that they should not be directly compared due to the slightly different mean pump spot radii), $M_r = -77.7$ and $M_\theta = -82.7$ $[m^{-1}/W]$ ($\lambda_P = 967.6$ nm) and $M_r = -133.7$ and $M_\theta = -142.3$ $[m^{-1}/W]$ ($\lambda_P = 799.2$ nm).

At the maximum applied pump power, the focal length of the thermal lens ($f = 1/D$) is as short as −12... −13mm (λ_P = 967.6 nm) and −8... −9mm (λ_P = 799.2 nm).

The main reasons for such a strong lens are the following: (i) high fractional heat loading for Er^{3+} ions (e.g., as compared to Yb^{3+} ones [Che06]) and (ii) small pump spot size used in the present work together with a Gaussian profile of the pump beam (as compared to typical values for diode-pumped lasers). The latter is beneficial for the thermal lens measurements as it allowed us to observe stronger (and more easily detectable) effect of the thermal lens on the laser characteristics. Despite the observed relatively short focal lengths of the thermal lens, the laser cavity remained stable. The calculated stability limit of such a cavity expressed in the focal length of a divergent thermal lens is $f = -4$ mm.

The optical power of the thermal lens in a longitudinally pumped laser element made of a cubic crystal in the "plane stress" approximation is given by [Che06]:

$$D_{r(\theta)} = \frac{\eta_h P_{abs}}{\pi \langle w_P \rangle^2 \kappa} \left(dn/dT + 2n^3 \alpha C_{r(\theta)} + (1+\nu)(n-1)\alpha \right) \tag{IV.8}$$

where κ is the thermal conductivity, n is the refractive index and dn/dT is the thermo-optic coefficient, α is the coefficient of thermal expansion, ν is the Poisson ratio and $C_{r(\theta)}$ are the so-called photoelastic constants [Koe06]. The three terms in parentheses correspond to three main effects contributing to the thermal lens formation: (i) Temperature dependence of the refractive index under zero strains, $\varepsilon = 0$ (expressed by the dn/dT term); (ii) The photo-elastic effect (expressed by the photo-elastic term, $P_{PE,r(\theta)}$); (iii) Macroscopic bulging of crystal end faces (expressed by the end-bulging term, Q_{dist}), respectively. The whole expression in parentheses is called the "generalized" thermo-optic coefficient and determines as:

$$\chi_{r(\theta)} = dn/dT + P_{PE,r(\theta)} + Q_{dist} \tag{IV.9}$$

Equation (IV.8) considers the case of a Gaussian spatial profile of the pump beam. The $C_{r(\theta)}$ values for an optically isotropic material are given by [Che06]:

$$C_r = \frac{-(1+\nu)(9p_{11} + 15p_{12})}{48} \tag{IV.10a}$$

$$C_\theta = \frac{-(1+\nu)(7p_{11} + 17p_{12} - 8p_{44})}{48} \tag{IV.10b}$$

where p_{ij} are the elasto-optical coefficients. The set of material parameters involved in the thermal lens simulation is provided in Table IV.18 [Mal63, Dru11].

Note that the expression for the end-bulging term, $Q_{dist} = (1+\nu)(n-1)\alpha$ (this term is shown in Equation IV.8), is strictly valid for an infinitely thin crystal [Che06] (or at least in the case when the heat loading is strongly localized near the input crystal face due to a strong pump absorption). Cousins showed that for a laser element (rod) with a length / diameter ratio of about 1.5, this expression overestimates the actual bulging by about 1/3 [Cou92]. Thus, it should be taken as an upper limit estimation of end bulging and stronger negative thermal lens is expected in long uniformly pumped $Er^{3+}:CaF_2$ crystals.

Table IV.18: Material parameters of $Er^{3+}:CaF_2$ involved in thermal lens calculation. (published in Optics Express 2022 [Bas22c])

Parameter	**Value [Mal63, Dru11]**	**Parameter**	**Value [Dru11]**
n	1.419	p_{11}	0.038
dn/dT [10^{-6} K^{-1}]	-8.5×10^{-6} K^{-1}	p_{12}	0.266
α [10^{-6} K^{-1}]	18.9×10^{-6} K^{-1}	p_{44}	0.0254
v	0.21	C_r	-0.109
K [Wm^{-1} K^{-1}]	5.4 $Wm^{-1}K^{-1}$	C_θ	-0.116

Table IV.19: Calculated thermal lens parameters of $Er^{3+}:CaF_2$ crystal.

Parameter	**Value (calc.)**
$P_{PE,r}$ [10^{-6} K^{-1}]	-11.76
$P_{PE,\theta}$ [10^{-6} K^{-1}]	-12.48
Q_{dist} [10^{-6} K^{-1}]	9.58
χ_r	-10.71
χ_θ	-11.40

The determined parameters of the thermal lens in $Er^{3+}:CaF_2$ crystals listed in Table (IV.19) are relevant for the design of power-scalable mid-infrared lasers based on this gain material, including diode-pumped ones. In this case, the parameters of the thermal lens can be easily recalculated from our data by considering the changed pump spot size. The knowledge of the thermal lens of a laser element is crucial for determining the stability of a designed laser cavity, as well as matching of the pump and laser modes in the laser element with increasing the pump power.

2.2.3 Other Er:MF$_2$ lasers

- **Er:BaF$_2$ and Er:(Ba,Sr)F$_2$ lasers**

In this part of work, we aimed to demonstrate for the first time the mid-infrared laser operation at ~ 2.8 um in Er^{3+}-doped Ba-containing fluorite-type crystals, namely Er:BaF$_2$ and Er:(Sr,Ba)F$_2$. As it was discussed above, their mid-infrared emission properties are particularly encouraging due to the lowest phonon energies resulting in almost negligible non-radiative relaxation from upper laser level, $^4I_{11/2}$.

The output characteristics for Er:BaF$_2$ crystal are shown in Figure IV.31(a). The Er^{3+}:BaF$_2$ laser generated a maximum output power of 350 mW at 2792 nm with a slope efficiency η of 17.2% (*vs.* the absorbed pump power) and a laser threshold P_{th} of 26 mW (for T_{OC} = 1.7%). With decreasing output coupling from 4% to 0.33%, P_{th} gradually decreased from 93 mW to 17 mW. Such a low-threshold behaviour is assigned to the long luminescence lifetime of the upper laser level ($^4I_{11/2}$).

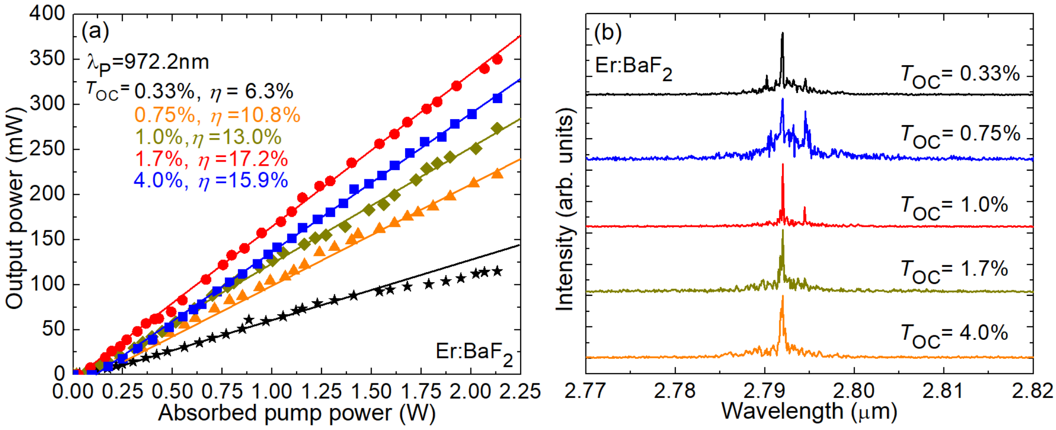

Figure IV.31: Mid-infrared Er^{3+}:BaF$_2$ laser: (a) input-output dependences, λ_P = 972.2nm, η - slope efficiency; (b) laser emission spectra depending on T_{OC} measured well above the laser threshold.

Improved mid-infrared laser performance was achieved using “mixed” crystals with better optical quality. The Er:(Sr,Ba)F$_2$ laser generated a maximum output of 519 mW at 2792 and 2794 nm, with a higher slope efficiency of 25.0% and a similar laser threshold of 27 mW (for T_{OC} = 1.7%), as shown in Figure IV.32(a). The laser emission was unpolarized. The typical spectra of laser emission measured well above the laser threshold are shown in Figure IV.32(b). They are weakly dependent on the output coupling.

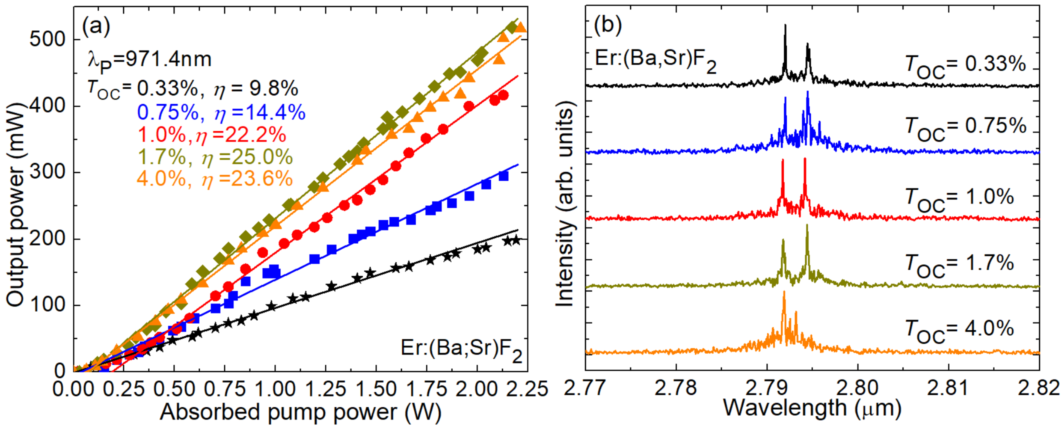

Figure IV.32: Mid-infrared Er^{3+}:BaF$_2$ laser: (a) input-output dependences, λ_P = 972.2nm, η - slope efficiency; (b) laser emission spectra depending on T_{OC} measured well above the laser threshold.

The laser emission spectra of both studied crystals were found to be dependent on the level of pump absorption near the laser threshold. In the case of Er:(Sr,Ba)F$_2$, Figure IV.33 shows that at low absorbed pump powers (<70 mW), the laser generated at 2729 nm. As the absorbed pump power increased, other laser lines at 2792 nm and 2794 nm appeared, with the latter becoming dominant. The quasi-three-level laser scheme was observed due to the existence of a resonant ESA channel $^4I_{13/2} \rightarrow {}^4I_{11/2}$ and a long luminescence lifetime of the terminal laser level. The laser spectra were also affected by the structured water vapor absorption in air.

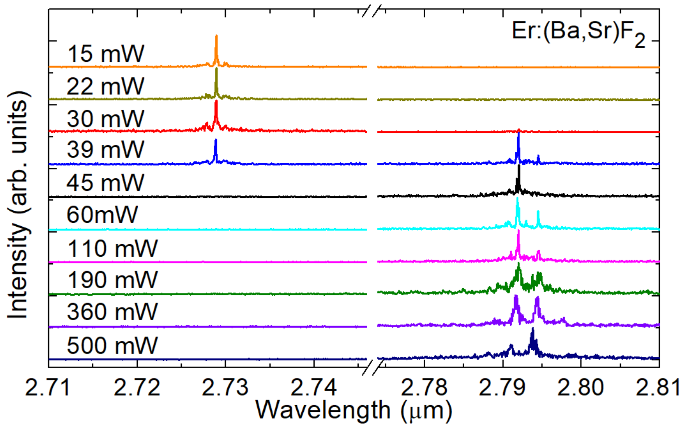

Figure IV.33: Dependence of the laser emission spectra of Er^{3+}:(Ba,Sr)F$_2$ on the absorbed pump power, T_{OC} = 1.7%.

The evaluation of the beam propagation factor for the Er:(Sr,Ba)F$_2$ laser is shown in Figure IV.34(b). At the maximum pump power, the measured M^2 = 1.08 confirms the laser operation at the fundamental transverse mode. Inset shows the far-field beam profile of the Er:(Sr,Ba)F_2 laser. There is slight asymmetry and the 1D intensity profiles are well fitted with a Gaussian function.

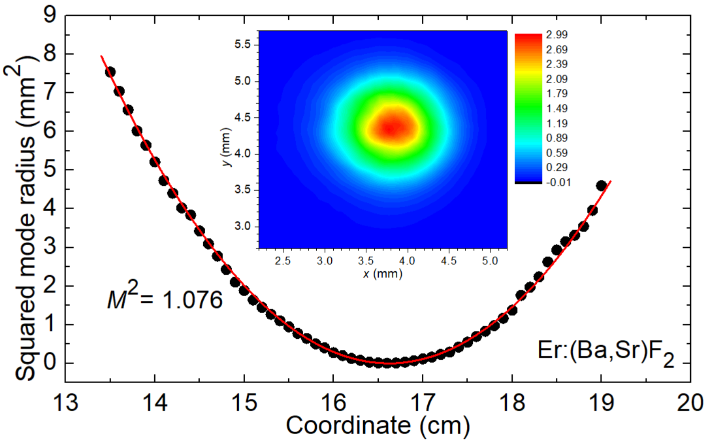

Figure IV.34: Evaluation of the beam quality factor M^2 for the Er^{3+}:(Ba,Sr)F_2 laser, *inset* – typical far-field profile of the laser mode, T_{OC} = 1.7%, P_{abs} = 2.2 W.

The round-trip passive losses L in both laser crystals using the Findlay-Clay analysis, as shown in Figure IV.35. The best-fit of experimental points yielded a round-trip passive loss L = 1.5% corresponding to a loss coefficient δ = 0.112 cm^{-1} for the Er^{3+}:BaF_2 laser, Figure IV.35(a), and L = 1.25% and δ = 0.009 cm^{-1} for the Er^{3+}:(Ba,Sr)F_2 laser, Figure IV.35(b) , respectively.

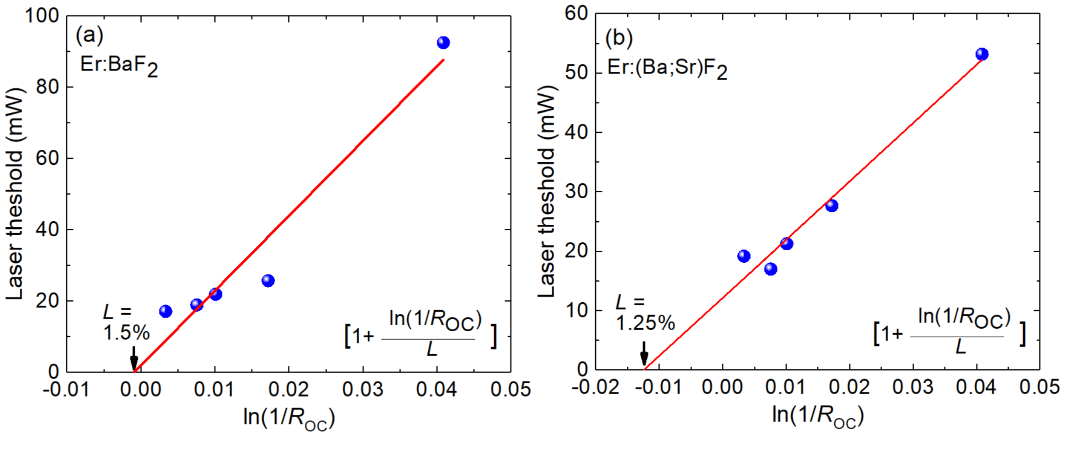

Figure IV.35: Round-trip losses L estimation for the (a) Er^{3+}:BaF_2 and (b) Er^{3+}:(Ba,Sr)F_2 lasers using the Findlay - Clay method.

- **Er:SrF_2 and Er:$(Ca,Sr)F_2$ lasers**

To date, $Er^{3+}:SrF_2$ [Ma16b] and $Er^{3+}:(Ca,Sr)F_2$ [Zha18, Liu19a] crystals have been studied for mid-infrared lasers. In 2016, a dual-wavelength continuous wave laser was realized in Er^{3+}: SrF_2 crystals pumped by a laser diode by Ma *et al.* [Ma16b] with a slope efficiency of 22% and a maximum output power of 483 mW. Subsequently, the use of "mixed" counterparts made it possible to achieve slope efficiencies exceeding the Stokes limit. Liu *et al.* demonstrated CW laser operation in "mixed" Er-doped CaF_2-SrF_2 with a maximum output power of 712 mW and a slope efficiency of 41.4%, which is the highest efficiency achieved with a laser diode pumped fluorite-type crystals [Zha18].

Although we were unable to outperform the results obtained in [Zha18], we set out to compare the laser characteristics at 2.8 μm of strontium-containing crystals and other fluorite-type counterparts. Figure IV.36 shows the output performance and laser spectra of five studied $Er^{3+}:MF_2$ crystals with the same output coupling (T_{OC} = 1.7%). The slope efficiency gradually decreased in the sequence $Er^{3+}:CaF_2$ → $Er^{3+}:SrF_2$ and Sr-containing crystals → $Er^{3+}:BaF_2$, while the laser threshold was in the range of 17 – 28 mW for all the crystals, being only slightly higher for Ba-containing ones. The laser emission occurred at 2792 – 2800 nm, except of $Er^{3+}:SrF_2$ for which the laser operated at shorter wavelengths, 2730 and 2747 nm.

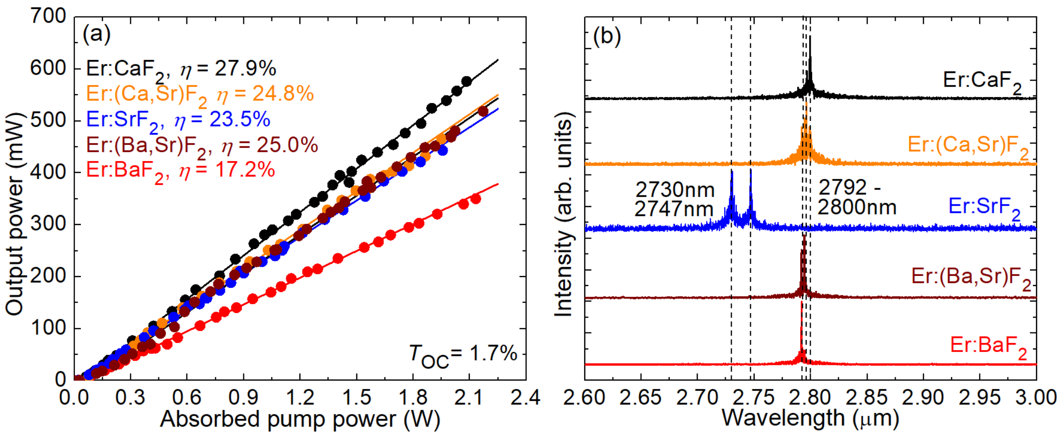

Figure IV.36: Mid-infrared $Er^{3+}:MF_2$ lasers: (a) a comparison of output characteristics and (b) typical laser spectra for T_{OC} = 1.7%.

2.3 Er:$Na_5Y_9F_{32}$ laser

For laser experiments, the 5.59at.% $Er^{3+}:Na_5Y_9F_{32}$ crystal of 1.85-mm thickness was implemented into hemispherical cavity shown in Figure IV.19 (Sub-section 2.1).

The input-output power characteristics of 5.59at.% $Er^{3+}:Na_5Y_9F_{32}$ laser are shown in Figure 4.37(a). The $Er^{3+}:Na_5Y_9F_{32}$ laser generated a maximum output power of 57 mW at 2800 nm with a slope efficiency η of 20.2% (related to the absorbed pump power) and a threshold P_{th} of only 24 mW. These characteristics were measured for an output coupler with a transmission, T_{OC} of 1.7%. As T_{OC} decreases, there is a degradation in laser performance, including a decrease in slope efficiency from 20.2% (T_{OC} = 1.7%) to 5.1% (T_{OC} = 0.33%). The maximum slope efficiency is well below the Stokes limit, $\eta_{St,L} = \lambda_P/\lambda_L = 34.6\%$. The decrease in the slope efficiency is mainly due to the weak absorption in the Er^{3+}:$Na_5Y_9F_{32}$ crystal, which is twice as low as in the Er:CaF_2 crystal. Tkachuk *et al.* have already previously reported laser emission at 2.8 µm obtained in the Er^{3+}:NYF ($Na_{0.4}Y_{0.6}F_{2.2}$) crystal with a composition similar to ours. They reached an output power of about 72 mW with a slope efficiency of ~4% [Tka04b].

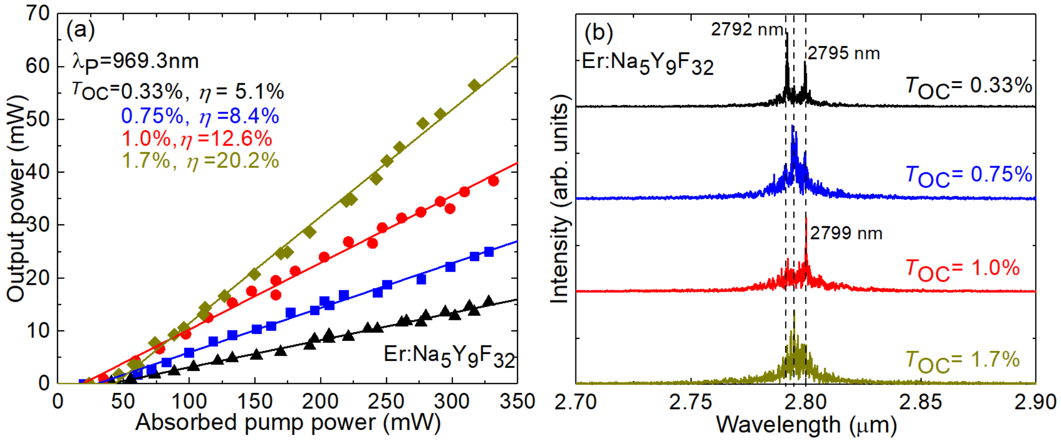

Figure IV.37: Mid-infrared Er^{3+}:MF_2 lasers: (a) a comparison of output characteristics and (b) typical laser spectra for T_{OC} = 1.7%.

The laser emission spectra are shown in Figure IV.37(b). For T_{OC}= 0.33% - 1.7%, the laser operated at 2791-2799 nm in agreement with the long-wavelength maximum of the $^4I_{11/2} \rightarrow {}^4I_{13/2}$ emission band of Er^{3+} ions in $Na_5Y_9F_{32}$. The spectra are weakly dependent on the transmission of OCs. Such laser wavelength behavior can be explained by the structured absorption of water vapor in the atmosphere overlapping with main peak of SE cross-section for the $^4I_{11/2} \rightarrow {}^4I_{13/2}$ at 2708 nm, which may contribute additional losses.

The passive losses in the laser element were estimated using the Findlay-Clay analysis, i.e., in the same way as for Er:MF_2 crystals in previous section. The best-fit of experimental points yielded a round-trip passive loss L = 4.91% corresponding to a loss coefficient δ = 1.33 cm^{-1} at ~2.8 µm. Such significant losses in the laser can be associated with the quality of the crystal.

2.3 Er:KY$_3$F$_{10}$ laser

For laser experiments, a cylindrical element (diameter: 5.0 mm, thickness: 2.2 mm) was cut from 15 at.% Er^{3+}:KY$_3$F$_{10}$. We studied two pumping schemes into ^{4}I$_{11/2}$ multiplet at 970.6 nm (selected the most intense absorption peak) and at 980.4 nm; and into ^{4}I$_{9/2}$ multiplet at 801.3 nm.

At first, for direct pumping into the ^{4}I$_{11/2}$ multiplet, in the quasi-CW regime with a duty cycle of 1:4, the laser generated a maximum peak output power of 255 mW at 2.80 µm with a slope efficiency η of 10.9% (versus the absorbed pump power) and a laser threshold P_{th} of 58 mW, as shown in Figure IV.38(a). The optical-to-optical efficiency η_{opt} was 9.7% (vs. the pump power incident in the crystal P_{inc}). Further attempt power scaling was limited by the available pump and no thermal roll-over nor crystal fracture were observed until the maximum P_{inc} of 2.60 W. When reducing the duty cycle in the quasi-CW regime (down to 1:3 and 1:2) and further switching to the true CW operation, a thermal roll-over was observed. The CW output power reached 57 mW.

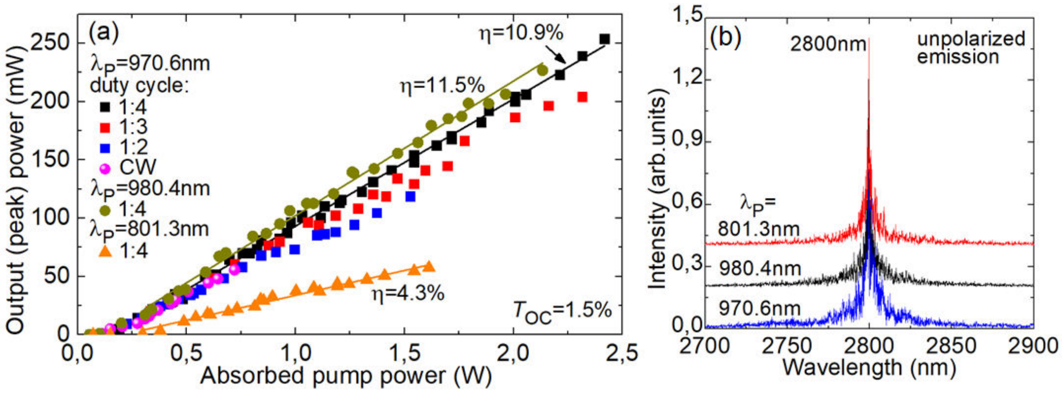

Figure IV.38: Mid-infrared Er^{3+}:KY$_3$F$_{10}$ laser: (a) input-output dependences, η – slope efficiency, λ_{P} – pump wavelength, T_{OC} = 1.5%; (b) typical emission spectra of the Er^{3+}:KY$_3$F$_{10}$ laser.

For the ^{4}I$_{15/2}$ → ^{4}I$_{11/2}$ pump transition, the laser excitation curve (the dependence of the output power on the pump wavelength λ_{P} at fixed P_{inc}) was measured, as shown in Figure IV.40(a). It was compared with the corresponding GSA cross-section, σ_{abs}, spectrum. It was possible to achieve lasing for λ_{P} in the range of 967 – 1004 nm. The highest output power corresponded to the most intense absorption peak with $\sigma_{\mathrm{abs}} = 0.57\times10^{-20}$ cm^2 at 970.6 nm and a small bandwidth (full width at half maximum, FWHM) of 1.0 nm. Much broader peak is observed at longer wavelengths, with $\sigma_{\mathrm{abs}} = 0.33\times10^{-20}$ cm^2 at 980.4 nm and FWHM = 4.1 nm. Pumping into this peak provided slightly better laser efficiency: the laser generated 228 mW at 2.80 µm with η = 11.5% and P_{th} = 55 mW (in the quasi-CW regime with a duty cycle of 1:4), as shown in Figure IV.38(a). This was probably due to the more uniform pump distribution in the crystal. The peak at 980.4 nm looks suitable for the use of InGaAs diode lasers as pump sources as it is expected to provide weaker sensitivity to the temperature drift of the pump wavelength, Figure IV.40(a).

The typical spectra of laser emission are shown in Figure IV.38(b). They are nearly independent on λ_P; the laser wavelength is centered at 2800 nm. It is longer than the main peak in the SE cross-section spectrum at 2730 nm, Figure IV.17(a). The reason for that is the efficient excited-state absorption (ESA) process from the terminal laser level, namely $^4I_{13/2} \rightarrow {}^4I_{11/2}$. The ESA spectrum is shown in Figure IV.17(a). The Er^{3+}:KY_3F_{10} laser operated in the fundamental transverse mode with a nearly circular profile, Figure IV.39(b).

Typical oscilloscope traces of the pump (at 970.6 nm) and laser (at 2800 nm) radiation for the Er^{3+}:KY_3F_{10} laser are shown in Figure IV.39(a). After switching on the pump, relaxation oscillations are observed within ~1 ms followed by a stable CW output. Without a chopper, true CW operation occurs. The weak slow intensity instabilities for the laser radiation originate from the pump instabilities.

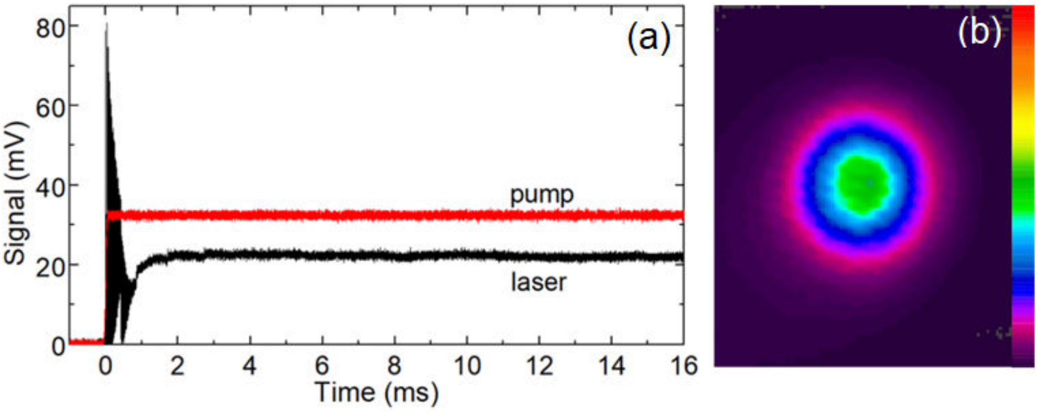

Figure IV.39: (a) Oscilloscope traces of the pump (0.97 μm) and laser (2.8 μm) radiation from the Er^{3+}:KY_3F_{10} laser; (b) far-field mode profile, duty cycle 1:4, P_{abs} ~1.0 W, λ_P = 970.6 nm.

Another possible pump transition, which was studied is the $^4I_{15/2} \rightarrow {}^4I_{9/2}$ one and it is interesting for the use of AlGaAs diode lasers. The $^4I_{9/2}$ state of Er^{3+} ions in KY_3F_{10} is short-living (lifetime: ~5 μs) and the ions relax fast to the lower-lying $^4I_{11/2}$ upper laser level via multi-phonon non-radiative (NR) relaxation. By pumping into the most intense absorption peak at 801.3 nm, the laser generated 58 mW at 2.80 μm with smaller η = 4.3% and higher P_{th} = 71 mW (as compared to pumping into the $^4I_{11/2}$ state) in the quasi-CW regime with a duty cycle of 1:4. The deterioration of the laser performance originates mainly from the lower Stokes efficiency and stronger heat loading for this pump scheme. The laser excitation curve for pumping into the $^4I_{9/2}$ state was also measured, Figure IV.40(b). The laser operation was achieved in much narrower range of λ_P, 796 - 805 nm. The main absorption peak of Er^{3+} ions is also relatively narrow with $\sigma_{abs} = 0.29\times10^{-20}$ cm^2 at 801.3 nm and FWHM = 1.6 nm.

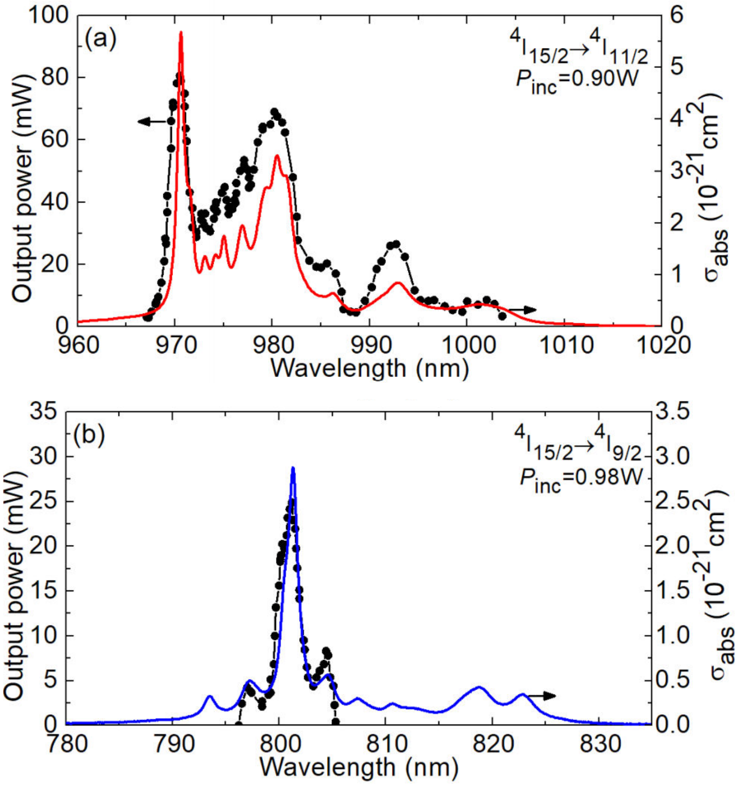

Figure IV.40: Laser excitation curves for the mid-infrared $Er^{3+}:KY_3F_{10}$ laser for pumping: (a) into the $^4I_{11/2}$ state, (b) into the $^4I_{9/2}$ state. The absorption cross-section, σ_{abs}, spectra are shown for comparison.

2.4 Overview of laser performances of studied cubic fluorite-type crystals

All studied crystals were tested in the same laser configuration, namely hemispherical cavity formed by a flat pump mirror and a set of output couplers (OC) having a transmission T_{OC} of 0.33% - 4% at 2.7 – 2.9 µm.

The most impressive results were achieved for the 5 at.% $Er^{3+}:MF_2$ crystals. The best output laser characteristics have been achieved in 5 at.% $Er^{3+}:CaF_2$ laser generating 702 mW of output power with slope efficiency of 37.9% well above the Stokes efficiency limit of 34.6% indicating the impact of the ETU process $^4I_{13/2} + {}^4I_{13/2} \rightarrow {}^4I_{9/2} + {}^4I_{15/2}$, refilling the upper laser level and depopulating the intermediate $^4I_{13/2}$ state. For 4.5 at.% CaF_2, the output power was even higher 0.84 W at 2.8 µm owing to a high optical quality of the crystal and a moderate doping level.

As newcomer materials for mid-infrared laser operation, Ba-containing crystals have demonstrated promising laser performance at 2.8 µm. $Er^{3+}:(Ba,Sr)F_2$ laser generated 519 mW with a slope efficiency of 25%, surpassing the laser characteristics of its “parent” counterpart Er^{3+}:BaF_2, which generated a maximum output power of 350 with a slope efficiency of 17.2%. Further power scaling are expected when using crystals with optimized Er^{3+} doping levels to balance crystal quality, thermal properties, pump absorption, and ETU efficiency.

The first laser operation of the highly Er^{3+}- doped KY_3F_{10} crystal in the mid-IR spectral range. The quasi-CW Er^{3+}:KY_3F_{10} laser generated up to 255 mW at 2.8µm with a slope efficiency up to 11.5% and a laser threshold down to 55 mW. The power scaling in the CW regime was limited by thermal effects in the passively cooled crystal. The improvement of the laser efficiency seems possible by optimizing the Er^{3+} concentration between 7 – 15 at.%.

Table IV.20: Summary of the laser characteristics of studied Er^{3+} - doped fluoride crystals.

Crystal	**Doping, at.%**	**λ_P, nm**	**P_{out}, mW**	**η vs. P_{abs}, %**	**λ_L, nm**	**P_{th}, mW**
CaF_2	4.5	967.6	834	31.6	2800	24
		799.2	318	18.9	2800	33
	5.0	967.6	702	37.9	2800	60
SrF_2	5.0	969.5	443	23.5	2747	20
BaF_2		972.2	350	17.2	2792	26
$(Ca,Sr)F_2$		969.7	466	24.8	2796	17
$(Ba,Sr)F_2$		971.4	519	25	2794	28
$Na_5Y_9F_{32}$	5.59	969.3	57	20.2	2792	24
KY_3F_{10}	15.0	801.3	58	4.3	2800	78
		970.6	255	10.9		58
		980.4	228	11.5		55

3 Conclusions Chapter IV

To conclude, we have systematically studied the spectroscopic properties, the mid-infrared laser performances of several cubic Er^{3+}-doped fluorite-type single-crystals including fluorite-type ones Er^{3+}:MF_2 (where M = Ca, Sr., Ba and their mixture: Ca/Sr, Ba/Sr), Er^{3+}:$Na_5Y_9F_{32}$ and Er^{3+}:KY_3F_{10}. All these materials feature low phonon energies inherent to fluoride materials leading to long lifetime of the upper laser level ($^4I_{11/2}$), a favourable $^4I_{11/2}$ to $^4I_{13/2}$ lifetime ratio. Moreover, they benefit from smooth and broad emission spectra around 2.8 µm related to the $^4I_{11/2} \rightarrow {}^4I_{13/2}$ transition.

(i) Thermo-optical properties of the well-known mid-infrared laser material, Er^{3+}:CaF_2 crystals were studied with the goal of assessing its potential for power scalable operations. Two pump transitions were compared, namely pumping into the $^4I_{9/2}$ and $^4I_{11/2}$ states. Direct excitation into the upper laser level provides higher slope efficiency, lower fractional heat loading under lasing conditions and consequently a weaker thermal lens. The latter is found to be negative (divergent) for the Er:CaF_2 crystal due to the negative thermo-optic coefficient, as well as a large and negative contribution of the photo-elastic effect. The mechanisms of heat generation such as energy transer upconversion non radiative path in Er:CaF_2 are discussed. A significant improvment of the output power of the mid-infrared Er:CaF_2 laser is achieved: the output power reached 0.84 W at 2800 nm with a slope efficiency of 31.6%, being only slightly lower than the Stokes limit.

(ii) Based on a detailed comparative spectroscopic study of 5 at.% Er^{3+}:MF_2 fluorite-type crystals, the following conclusions are derived. In the M = Ca → Sr → Ba series, the absorption and mid-infrared emission spectra gradually become narrower and more structured, which is linked to the decreasing complexity of Er^{3+} clusters and the luminescence lifetimes of the $^4I_{13/2}$ / $^4I_{11/2}$ Er^{3+} manifolds increase, from 8.06 / 8.85 ms for Er^{3+}:CaF_2, to 9.17 / 10.36 ms for Er^{3+}:BaF_2. The Er^{3+} ions in "mixed" crystals tend to stay in a local environment predominantly composed of the larger / heavier M^{2+} cations, leading to a great similarity between the spectra of Er^{3+}:SrF_2 and Er^{3+}:$(Ca,Sr)F_2$, Er^{3+}:BaF_2 and Er^{3+}:$(Sr,Ba)F_2$. At LT, the spectra of Er^{3+} ions in solid-solution crystals exhibit a notable inhomogeneous broadening. For the doping level of 5 at.% Er^{3+} in MF_2 crystals, the LT spectroscopy reveals the existence of a single class of Er^{3+} clusters with rather close absorption / emission properties (D centers), contrary to crystals with lower doping ratios subject to ion clustering of various nature (D(1) and D(2)).

(iii) We have demonstrated the first laser operation on the $^4I_{11/2} \rightarrow {}^4I_{13/2}$ transition in continuous-wave regime of several Er^{3+}-doped fluoride crystals including BaF_2, $(Ba,Sr)F_2$, $Na_5Y_9F_{32}$ and KY_3F_{10} crystals in the mid-infrared spectral range around 2.8 µm. In particular, Er:$(Ba,Sr)F_2$ laser generated 0.52W with a slope efficiency of 25%. Further power scaling of Er^{3+}-doped MF_2 type crystals is expected under the diode-pumping by commercial multimode high-power InGaAs laser diods emitting around 960nm.

(iv) Among the studied cubic fluorite-type crystals, Er:CaF_2 and its isotypes appear as the most promising, due to a combination of very good thermal properties, smooth and broad absorption spectra, inhomogeneously broaden emission spectra around 2.8 µm and long luminescence lifetimes. Although in our experiments, Er:CaF_2 crystals have demonstrated the best laser performances, we believe that low phonon energy fluorite-type crystals such as BaF_2 and its solid-solutions could be promising because of the longer luminescence lifetimes leading potential low threshold behaviour. While for the moment, the main technological challenge consists of improving the optical quality of these materials, by an optimization of their growth parameters. Apart from the 2.8 µm laser transition, Er:BaF_2 is very appearent for the emission at 3.5 µm originating from $^4F_{9/2} \rightarrow {}^4I_{9/2}$ transition. So far, laser action at 3.5 µm in Er^{3+}-doped BaF_2 has not been demonstrated yet.

(v) Another interesting direction is the implementation of the terminal laser level pumping aroung 1.54 µm, by using commercially available high-power and high-brightness Er doped fiber lasers. The laser action at 2.8 µm in that case is expected due to the positive effect of the energy transfer upconversion populating the upper laser level and depleting the lower laser level.

Chapter V

Erbium-doped transparent “mixed” sesquioxide ceramics

The Chapter V is devoted to compositionally "mixed" sesquioxide system $(R1)_2O_3$ – $(R2)_2O_3$ – $(R3)_2O_3$ (R = Y, Lu, Sc) doped with Er^{3+} ions. Sich solid-solution compositions are interesting for tailoring the spectroscopic properties of RE^{3+} ions under the various crystal-field strengths associated with the randomly distributed host –forming cations resulting in strong inhomogeneous spectral broadening, which is attractive, e.g., for broadly tunable and especially mode-locked lasers. As previously discussed, one of the best solutions to fabricate such complex materials is transparent ceramic technology. Transparent "mixed" sesquioxide ceramics doped with various RE^{3+} ions such as Yb^{3+} [Jin21], Tm^{3+} [Jin17], Ho^{3+} [Jin18] are known. Recently, the use of Tm^{3+}-doped "mixed" $(Lu,Sc)_2O_3$ and $(Lu,Y)_2O_3$ ceramic employed in mode-locked lasers lead to generation of ultrafast (sub-100 fs) pulses at the wavelength of ~2 μm [Wan18, Zha20]. This stimulates further research on "mixed" A_2O_3 ceramics with different compositions doped with Er^{3+}ions.

Thus, in this Chapter, we demonstrate the results of structural and spectroscopic investigations, as well as laser experiments in CW regime to explore the potential of Er^{3+}-doped sesquioxide solid-solution ceramics for ultrafast laser applications.

1 Laser-quality scandium-containing transparent sesquioxide ceramics (structure & spectroscopy)

1.1 Er:$(Lu,Sc)_2O_3$ ceramics

Transparent “mixed” 7 at.% Er:$(Lu,Sc)_2O_3$ sesquioxide ceramic of high optical quality was produced by our colleagues at the Institute of Chemical Materials, Chinese Academy of Engineering Physics, China. Ceramic sample was fabricated by hot isostatic pressing of commercial sesquioxide powders at 1750 °C / 200 MPa in argon atmosphere. A photograph of studied ceramic elements is shown in Figure V.1. The ceramic was transparent with rose coloration due to the Er^{3+} doping.

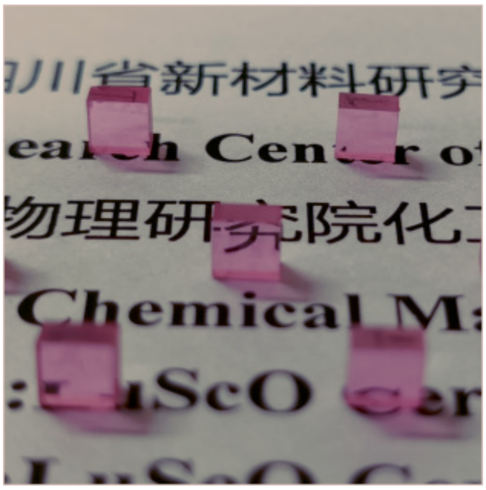

Figure V.1: Photograph of annealed and polished Er:$(Lu,Sc)_2O_3$ ceramic elements.

1.1.1 Structural study

The phase purity of the ceramic was studied by XRD, Figure V.2. In the measured XRD pattern, only one phase was identified, namely, the cubic (sp. gr. $Ia\bar{3}$ - T7h, No. 206) sesquioxide phase with the so-called *C*-type or bixbyite-type structure [Guz14] (bixbyite is a manganese iron oxide mineral with chemical formula $(Mn,Fe)_2O_3$). The diffraction peaks for the ceramic are located between those for undoped Lu_2O_3 (ICDD card #76–0162) and Sc_2O_3 (ICDD card # 84–1880). Accordingly, the lattice constant of the ceramic a = 10.198 Å, occupies an intermediate position between those of Lu_2O_3 (a = 10.391 Å) and Sc_2O_3 (a = 9.857 Å) [Kra15]. Note that a cubic stoichiometric Er_2O_3 phase also exists (a = 10.55 Å) [Guo07].

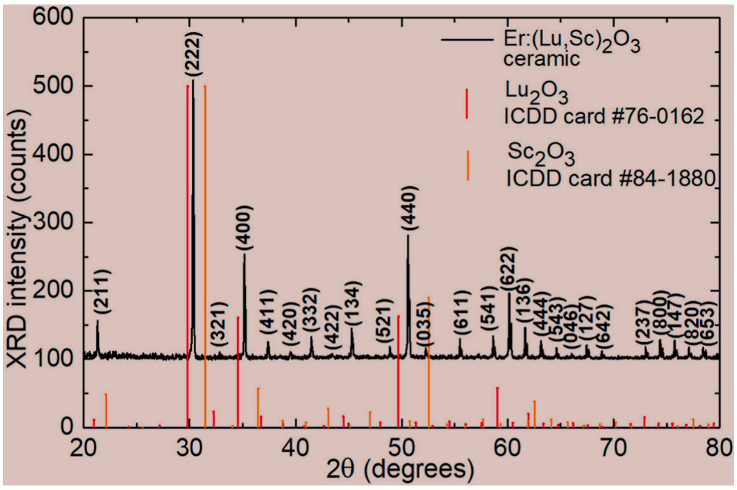

Figure V.2: X-ray powder diffraction pattern of Er:(Lu,Sc)$_2$O$_3$ ceramic, *red* and *orange* peaks – theoretical patterns for Lu$_2$O$_3$ (ICDD card #76–0162) and Sc$_2$O$_3$ (ICDD card #84–1880), respectively, *numbers* – Miller's indices (*hkl*).

In the bixbyite structure, there are two rare-earth sites with the local symmetries of C_2 and C_{3i} [Cha82]. Both correspond to VI-fold coordination by oxygen (O^{2-}). In the sesquioxide unit-cell, there is a total of 32 cationic positions: 24 (3/4) correspond to the C_2 sites and 8 (1/4) - to the C_{3i} ones. The dopant ions (Er^{3+}, in our case) are expected to replace the host-forming trivalent cations in both sites. Indeed, there exists spectroscopic evidence of the presence of dopant Er^{3+} ions in both C_2 and C_{3i} sites in sesquioxides [Ter11]. However, it is difficult to predict the actual distribution of the dopant ions over these sites. There exist theoretical studies on this topic [Bla08, Zha21, Sta07 and And03]. The main conclusion is that the preference in occupying the two available sites is determined by the difference of ionic radii of the involved cations. This process is expected to be particularly complex in “mixed” materials due to the difference of ionic radii of the host-forming cations (Lu^{3+} (0.861 Å) and Sc^{3+} (0.745 Å) [Sha79], in our case), and the dopant ions (Er^{3+} (0.890 Å) [Sha79], in our case). The differences in the second coordination sphere of Er^{3+} ions will induce the inhomogeneous broadening of their spectral bands.

A typical SEM image of the polished surface of the Er:(Lu,Sc)$_2$O$_3$ ceramic is shown in Figure V.3(a). It reveals a close-packed microstructure with clean grain boundaries and a lack of secondary phases and inclusions. The dark points in the SEM image represent the residual sub-μm sized pores inside the grains. The main challenge for the synthesis of “mixed” sesquioxide ceramics is the complete pore removal. The area of the ceramic disk with the highest pore content was intentionally selected for SEM observations. In contrast, for laser experiments, the elements were cut from the area presenting the lowest pore content. An environmental SEM image of a fracture surface of ceramic is presented in Figure V.3(b). It becomes evident that the intragranular fracture mechanism dominates for the ceramic. The grain size distribution is shown at the inset of Figure V.3(b). The mean grain size is 5.7 µm.

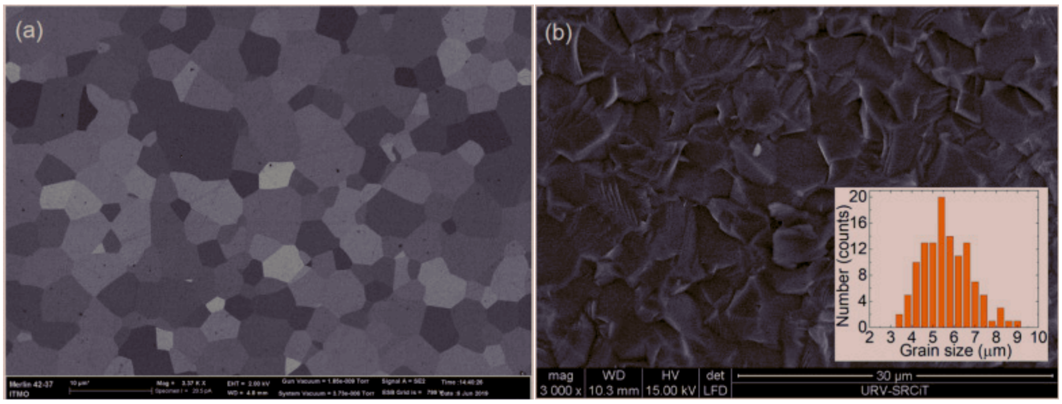

Figure V.3: SEM of Er:$(Lu,Sc)_2O_3$ ceramic: (a) SEM images of the polished surface; (b) environmental SEM image of the fracture surface. *Inset* in (b) – grain size distribution.

1.1.2 Optical absorption and mid-infrared luminescence

- **Transmission & Absorption**

The transmission spectrum of the polished ceramic sample (thickness: $t = 1.0$ mm) is shown in FigureV.4. The spectrum is dominated by absorption bands of the Er^{3+} ion. The UV absorption edge is at 0.25 µm. At a wavelength of 1.2 µm (out of Er^{3+} absorption), the measured transmission, $T = 79.1$ % is close to the theoretical value determined by Fresnel losses and accounting for multiple reflections, $T_0= 2n/(n^2+1)$, namely 82.0 % (calculated assuming a linear variation of the reflective index in the $Lu_2O_3 – Sc_2O_3$ substitutional solid solution [Zel13] yielding a value of $n = 1.916$). A reduction of the measured transmission with respect to the theoretical value is assigned to the presence of residual pores, cf. Figure V.3(a).

The absorption spectra are shown in Figure V.4. The electronic configuration of Er^{3+} is $[Xe]4f^{11}$. The observed absorption bands are due to transitions of Er^{3+} ions from the ground-state ($^4I_{15/2}$) to various excited-states indicated in Figure V.4 and ranging from $^4I_{13/2}$ up to $(^2H,^2G)_{9/2}$ (in the increased energy order). Here, the assignment is given after [Car68]. The absorption cross-sections were calculated as $\sigma_{abs} = \alpha_{abs}/N_{Er}$, where N_{Er} is the Er^{3+} ion density (20.0×10^{20} cm^{-3}). It should be pointed out, that the spectroscopic properties of cubic sesquioxides are mainly determined by dopant ions residing in C_2 sites. For the C_{3i} sites, the electric dipole (ED) transitions are forbidden due to the local inversion symmetry and only magnetic dipole (MD) transitions (with $\Delta J = J – J' = 0, \pm 1$, except of $0 \leftrightarrow 0'$) are allowed. There exists an approach to calculate σ_{abs} for sesquioxides assuming (3/4) of the dopant ions are residing in the C_2 sites. As explained above, this approach is not correct for a “mixed” material, in addition, for certain Er^{3+} transitions, the MD contribution may be significant. Thus, we consider σabs as "effective" cross-section.

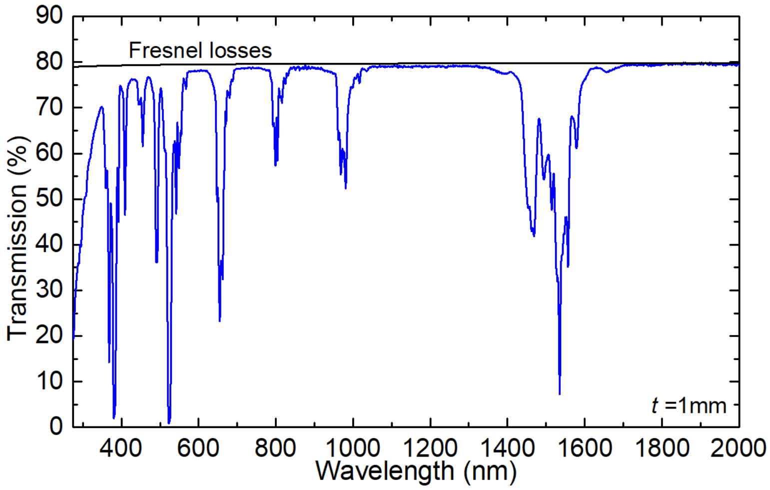

Figure V.4: Transmission spectrum of a laser-grade-polished Er:$(Lu,Sc)_2O_3$ ceramic disk (thickness, t = 1.0 mm), *black curve* – theoretical transmission determined by the Fresnel losses.

For the $^4I_{15/2} \rightarrow {}^4I_{13/2}$ transition (which corresponds to in-band pumping for 1.6 µm lasers and terminal level pumping for ~2.8 µm lasers), the maximum σabs is 1.76×10^{-20} cm^2 at 1535 nm and the absorption bandwidth is 3.8 nm (full width at half maximum, FWHM). For the $^4I_{15/2} \rightarrow {}^4I_{11/2}$ one (upper laser level pumping for ~2.8 µm lasers), σ_{abs} is 0.24×10^{-20} cm^2 at 980.6 nm.

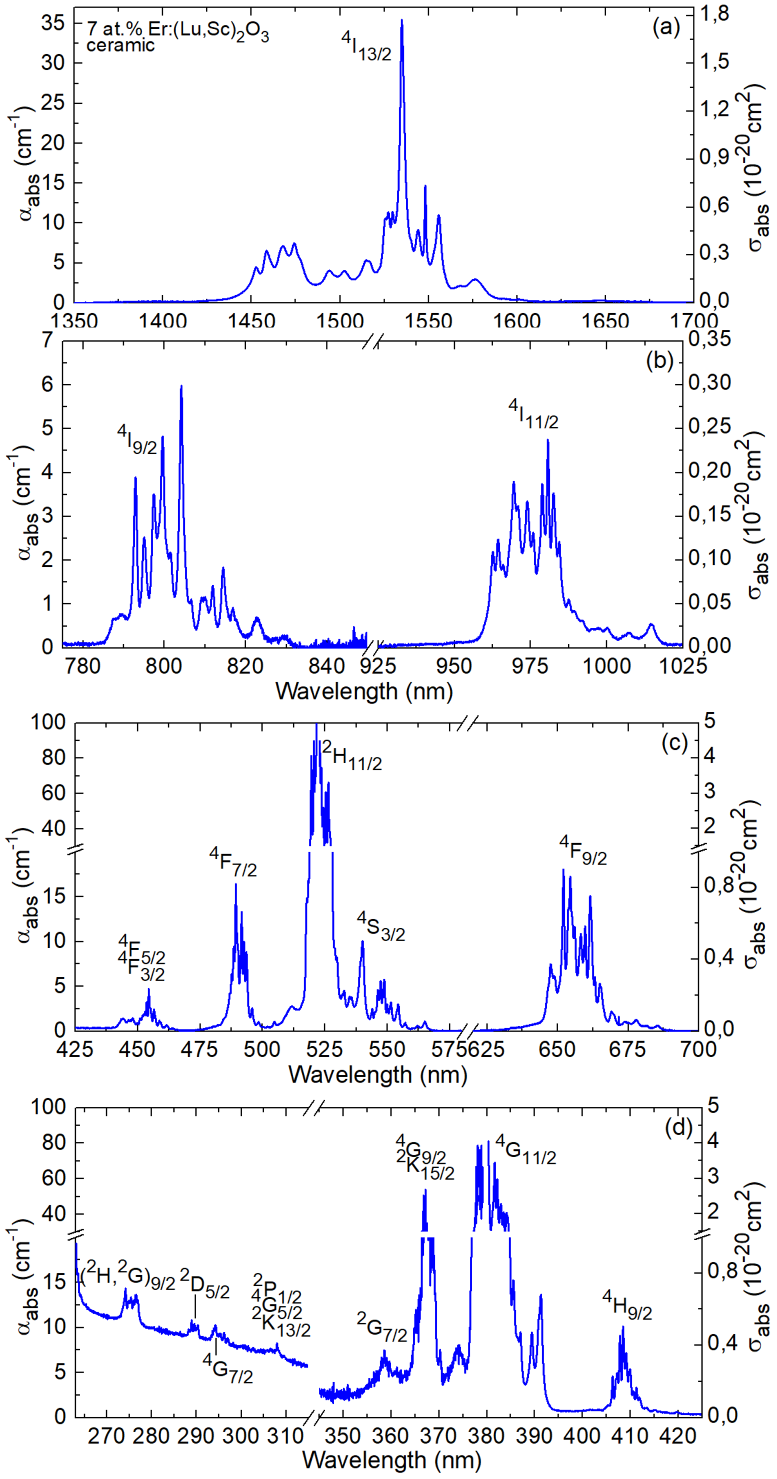

Figure V.5: (a-d) RT absorption spectra of 7 at.% Er:(Lu,Sc)$_2$O$_3$ ceramic (α_{abs} – absorption coefficient, $\sigma_{abs} = \alpha_{abs}/N_{Er}$ – absorption cross-section).

- **Luminescence (spectra and lifetimes)**

In Figure V.6, we have compared the normalized emission spectra corresponding to the $^4I_{11/2} \rightarrow {}^4I_{13/2}$ transition for Er^{3+} ions in the studied compositionally "mixed" $(Lu,Sc)_2O_3$ ceramic, as well as parent single-crystalline sesquioxides, Lu_2O_3 and Sc_2O_3. For the "mixed" ceramic, the luminescence spectrum is less structured and smoother and broader as compared to those for parent compounds, representing the effect of inhomogeneous spectral line broadening. Indeed, for the most intense emission peak, the emission bandwidths (FWHM) are 5.0 nm (at 2716.7 nm, for $Er:Lu_2O_3$) and 4.8 nm (at 2715.7 nm, for $Er:Sc_2O_3$), compare with ~26 nm (at ~2718 nm, for $Er:(Lu,Sc)_2O_3$).

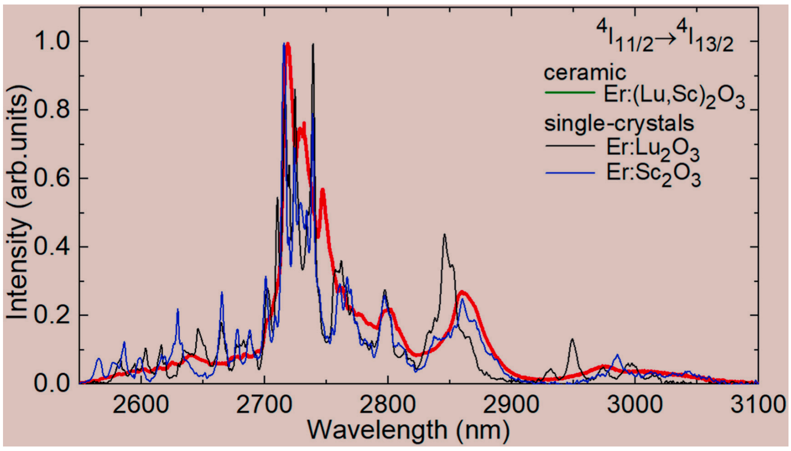

Figure V.6: A comparison of normalized mid-infrared emission spectra of Er^{3+} ions in compositionally "mixed" $(Lu,Sc)_2O_3$ ceramic and parent single-crystalline sesquioxides, Lu_2O_3 and Sc_2O_3 at RT.

The RT luminescence decay curves from the $^4I_{13/2}$ and $^4I_{11/2}$ states of Er^{3+} ions in 7 at.% $Er:(Lu,Sc)_2O_3$ ceramics, plotted in a semi-log scale are shown in Figure V.7. They were measured under resonant excitation using powdered samples to reduce the effect of radiation trapping. For both decay curves, first, we calculated the average decay time, which amounted to 4.89 ms ($^4I_{13/2}$) and 1.07 ms ($^4I_{11/2}$).

In FigureV.8, we provide a comparison of the previously reported lifetimes of the $^4I_{13/2}$ and $^4I_{11/2}$ states of Er^{3+} ions in parent Lu_2O_3 and Sc_2O_3 sesquioxides [Tis91, For00, Ghe08, Li12, Ter11, San10 and Qia11] with those determined in the present work for the "mixed" $(Lu,Sc)_2O_3$ ceramic. For $Er:Lu_2O_3$, the lifetime of the $^4I_{13/2}$ state at low Er^{3+} doping levels (the intrinsic one) is in the range of 10.5–11.4 ms and it decreases fast with doping. The intrinsic lifetime of the $^4I_{11/2}$ state is in the range of 1.75–1.95 ms and it shows much weaker dependence on the Er^{3+} doping concentration. For Er: Sc_2O_3, the intrinsic lifetimes of both considered states are much shorter than for its lutetia counterpart, namely 6.8–5.6 ms ($^4I_{13/2}$) and 0.31–0.34 ms ($^4I_{11/2}$). The lifetimes for the "mixed" $Er:(Lu,Sc)_2O_3$ ceramic studied in the present work agree well with the previously reported ones for single-crystals of $Er{:}Lu_2O_3$ with comparable doping levels [Li12].

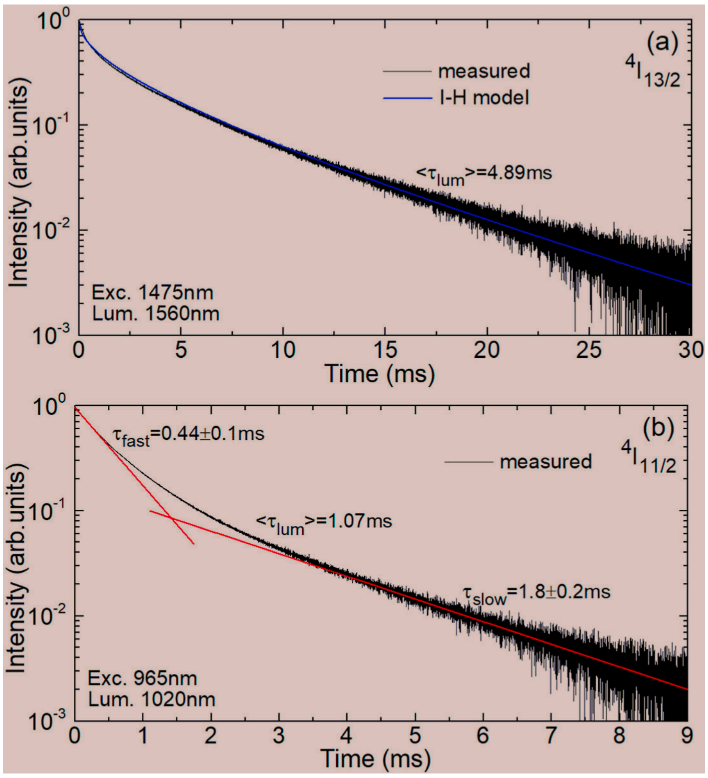

Figure V.7: RT luminescence decay curves for 7 at.% $Er{:}(Lu,Sc)_2O_3$ ceramic: (a) decay from the $^4I_{13/2}$ state, λ_{exc} = 1475 nm, λ_{lum} = 1560 nm; (b) decay from the $^4I_{11/2}$ state, λ_{exc} = 965 nm, λ_{lum} = 1020 nm. *Blue curve* in (a) - Inokuti-Hirayama (I–H) model fit, $<\tau_{lum}>$– mean luminescence lifetime.

The decay curve from the $^4I_{13/2}$ state was fitted using the Inokuti-Hirayama (I-H) model accounting for the energy transfer processes in the absence of migration [Ino65]:

$$I(t)=I_0\exp\left(-(t/\tau_0)-\alpha(t/\tau_0)^{3/s}\right), \tag{V.2}$$

where, I(t) is the emission intensity after pulsed excitation, τ_0 is the lifetime of an isolated donor (D) or the so-called intrinsic lifetime, the parameter s stands for the mechanism of the ion interaction (s = 6 for dipole-dipole (D-D) and s = 8 for dipole-quadrupole (D-Q) processes) and α is a constant describing the probability of energy-transfer:

$$\alpha = \frac{4\pi}{3}\Gamma\left(1-\frac{3}{s}\right)N_{Er}R_C^3 \tag{V.3}$$

where Γ is the gamma-function and R_C is the critical distance of transfer (the donor – acceptor separation for which the rate of energy transfer is equal to the rate of intrinsic decay of the donor). For the decay from the $^4I_{13/2}$ state, assuming $\tau_0 \sim 10$ ms, according to Figure V.8(a), the best-fit parameters are $s = 6.74 \pm 0.1$ (predominantly D-D interaction) and $\alpha = 2.00 \pm 0.07$. Thus, the critical distance RC amounts to 5.30 Å. It should be compared with the average $Er^{3+} – Er^{3+}$ distance for the studied material, $R = (4\pi N_{Er}/3)^{-1/3} = 4.92$ Å. Thus, the energy migration between Er^{3+} ions is very efficient for the 7 at.% Er^{3+} doped ceramic.

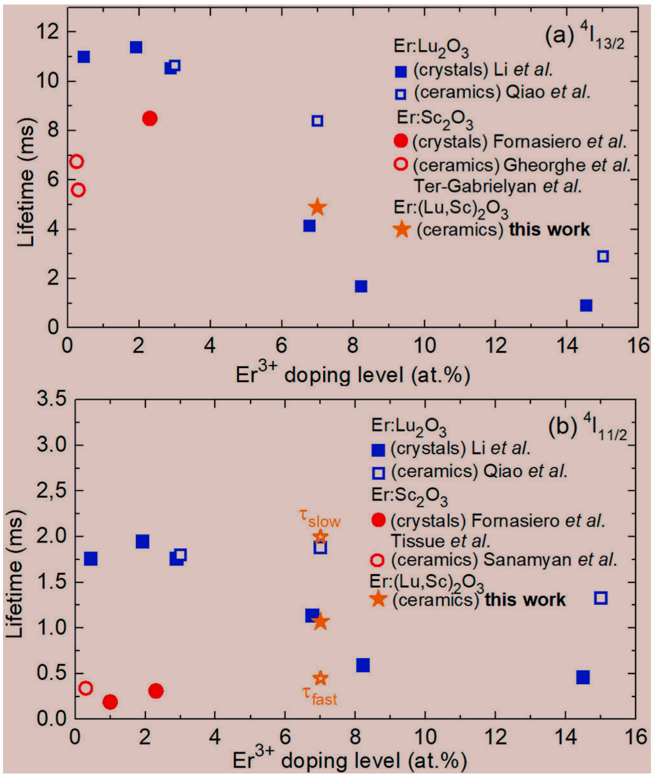

Figure V.8: Concentration dependence of luminescence lifetimes of the (a) $^4I_{13/2}$ and (b) $^4I_{11/2}$ Er^{3+} states in parent Lu_2O_3 and Sc_2O_3 sesquioxides given in literature, as well as the "mixed" $(Lu,Sc)_2O_3$ ceramic (*this work*).

The attempt to use the I–H model for fitting the luminescence decay curve from the $^4I_{11/2}$ state failed. The shape of this decay curve deviated from that expected for luminescence decay of a single type of ions in the presence of energy migration. Indeed, it revealed the signatures of two nearly single exponential "fast" and "slow" components with characteristic lifetimes $\tau_{fast} = 0.44\pm0.1$ ms and $\tau_{slow} = 1.8\pm0.2$ ms, which suggested the presence of two distinct ion classes. The Er^{3+} ions in the ceramic may reside in C_2 and C_{3i} sites. However, the $^4I_{11/2} \rightarrow {}^4I_{15/2}$ transition is of purely ED nature, and it cannot reveal the possible spectroscopic signatures of the C_{3i} sites. The appearance of different ion classes in polycrystalline ceramics is not surprising. The granular structure of ceramics determines variation of compositional and crystallographic properties at the level of each particular grain. One can suggest two possible mechanisms of formation of two spectroscopically distinct ion classes in "mixed" ceramics. The first one is the possible segregation of dopant ions at the grain boundaries where the interaction between the ions themselves and with defect and impurity centers is greatly promoted. The segregation was observed using high-resolution transmission electron microscopy in sesquioxide ceramics [Epi12]. However, the authors of [Epi12] concluded that it is relatively weak for small cations located in the end of the lanthanide series (as in the case of Er^{3+} replacing Lu^{3+}). Thus, this effect is expected to be hardly visible at the level of macroscopic spectroscopic properties. Second, as pointed out above, one may expect a predominant substitution of Lu^{3+} by Er^{3+} leading to depletion of these host-forming cations in other regions. Thus, locally, two types of centers differing by the second coordination sphere composed mainly by Lu^{3+} or Sc^{3+} can be formed.

It was found that among the sesquioxide materials doped with Er^{3+} ions, particularly for Er:Sc_2O_3, the intrinsic luminescence lifetime of the $^4I_{11/2}$ state is notably shortened (0.31–0.34 ms) as compared to its Er: Lu_2O_3 counterpart (1.75–1.95 ms), see Figure V.8(b). This matches our observations. The difference of the $^4I_{11/2}$ intrinsic lifetimes for Sc_2O_3 and Lu_2O_3 and, furthermore, for Sc and Lu enriched regions in ceramic may be explained by different rates of multi-phonon relaxation resulting from different phonon spectra of Sc_2O_3 and Lu_2O_3 (local phonons, in the case of ceramic). This effect is probably less pronounced for the decay from $^4I_{13/2}$ due to much weaker non-radiative relaxation from this state.

The obvious disagreement between the lifetimes of the $^4I_{13/2}$ state for Er^{3+} ions in cubic sesquioxides determined by different methods, namely (i) the intrinsic (luminescence) lifetime (measured directly at low Er^{3+} doping levels), (ii) the radiative lifetime determined using the theory of transition intensities (i.e., the J-O formalism) and (iii) the radiative lifetime estimated from the comparison of the stimulated emission cross-sections calculated by the F-L and RM approaches, is challenging to be clarified at the moment. We believe that the main reason for this is the unknown contribution of MD allowed transitions for Er^{3+} ions residing in C_{3i} sites. Further work is required in this direction to establish the relative occupancies for the C_2 and C_{3i} sites in Er^{3+}-doped parent and "mixed" sesquioxides, as well as to determine the transition probabilities for Er^{3+} ions in C_{3i} sites (e.g., by site-selective spectroscopy of the $^4I_{13/2} \leftrightarrow {}^4I_{15/2}$ transitions at LT). In contrast, the radiative lifetime of the $^4I_{11/2}$ state of Er^{3+} ions calculated using the J-O theory and its modifications which is relevant for the mid-IR laser operation seems to be much less affected by the above-described controversy.

1.1.3 Low-temperature spectroscopy

The expected inhomogeneous broadening of spectral bands of Er^{3+} ions in the "mixed" ceramic is revealed at low temperature. The LT (12 K) absorption and luminescence spectra used to determine the crystalfield splitting of Er^{3+} multiplets involved in the near- and mid-IR emissions (from $^4I_{15/2}$ to $^4I_{11/2}$) are shown in Figure V.9. For Er^{3+} ions in C_2 sites, each $^{2S+1}L_J$ multiplet splits into J+1/2 non-degenerated Stark sub-levels (considering non-integer J). Following the early work by Varsanyi and Dieke [Var62], we will use empirical notations for these sub-levels, namely Z_i ($i = 1 \ldots 8$), Y_j ($j = 1 \ldots 7$) and A_k ($k = 1 \ldots 6$) for the $^4I_{15/2}$, $^4I_{13/2}$ and $^4I_{11/2}$ multiplets, respectively [Kis64].

Two transitions in absorption were studied, namely $^4I_{15/2} \rightarrow {}^4I_{13/2}$ and $^4I_{15/2} \rightarrow {}^4I_{11/2}$, as shown in Figure V.9(a and b). At LT, the thermal populations of Stark sub-levels of the ground-state are almost negligible, so that the observed transitions in absorption occur from the lowest sublevel (Z_1), namely $Z_1 \rightarrow Y_j$ and $Z_1 \rightarrow A_k$, respectively. To simplify the assignment of electronic transitions, the horizontal scale for LT absorption spectra corresponds to wavenumbers $\tilde{\upsilon}$. To reveal the crystal-field splitting of the ground-state, two transitions in emission were studied at LT, namely $^4I_{13/2} \rightarrow {}^4I_{15/2}$ and $^4I_{11/2} \rightarrow {}^4I_{15/2}$. At LT, transitions in emission are expected to occur only from the lowest Stark sub-level of the emitting state, i.e., $Y_1 \rightarrow Z_i$ and $A_1 \rightarrow Z_i$, respectively. Both spectra in emission reveals the splitting of the same terminating level. To simplify their assignment, the horizontal scale for LT emission spectra was determined as ($E_{ZPL} - \tilde{\upsilon}$), Figure V.9(c). In this way, it corresponds directly to the Stark energies of the ground-state.

During the assignment of electronic transitions, we used the crystal field data for Er^{3+} ions in Sc_2O_3 derived by Lupei *et al.* [Lup08] (shown by vertical dashes in Figure V.9). The bands related to electronic transitions of Er^{3+} ions in C_2 sites in the $(Lu,Sc)_2O_3$ ceramic experience a significant inhomogeneous broadening, as compared to Er^{3+}-doped "parent" sesquioxides [Kis64, Lup08].

We have determined experimentally the Stark energies for all Er^{3+} multiplets ranging from $^4I_{15/2}$ up to $^4G_{11/2}$ (except of few missing levels), Table V.1. The corresponding energy-level scheme is shown in Figure V.10(a) together with the processes relevant for ~2.8 μm laser operation. A close look on the crystal-field splitting of the $^4I_{11/2}$ and $^4I_{13/2}$ multiplets is given in Figure V.10(b). As pointed out above, the spectroscopic signatures of Er^{3+} ions in C_{3i} sites can be found for the MD $^4I_{15/2} \rightarrow {}^4I_{13/2}$ transition. In the present work, the intense and narrow peak at 6539 cm^{-1} is unambiguously assigned to C_{3i} sites in agreement with the findings of Gruber et al. for $Er:Y_2O_3$ [Gru85]. Other possible peaks are hardly resolved because of the broad bands due to the C_2 site absorption.

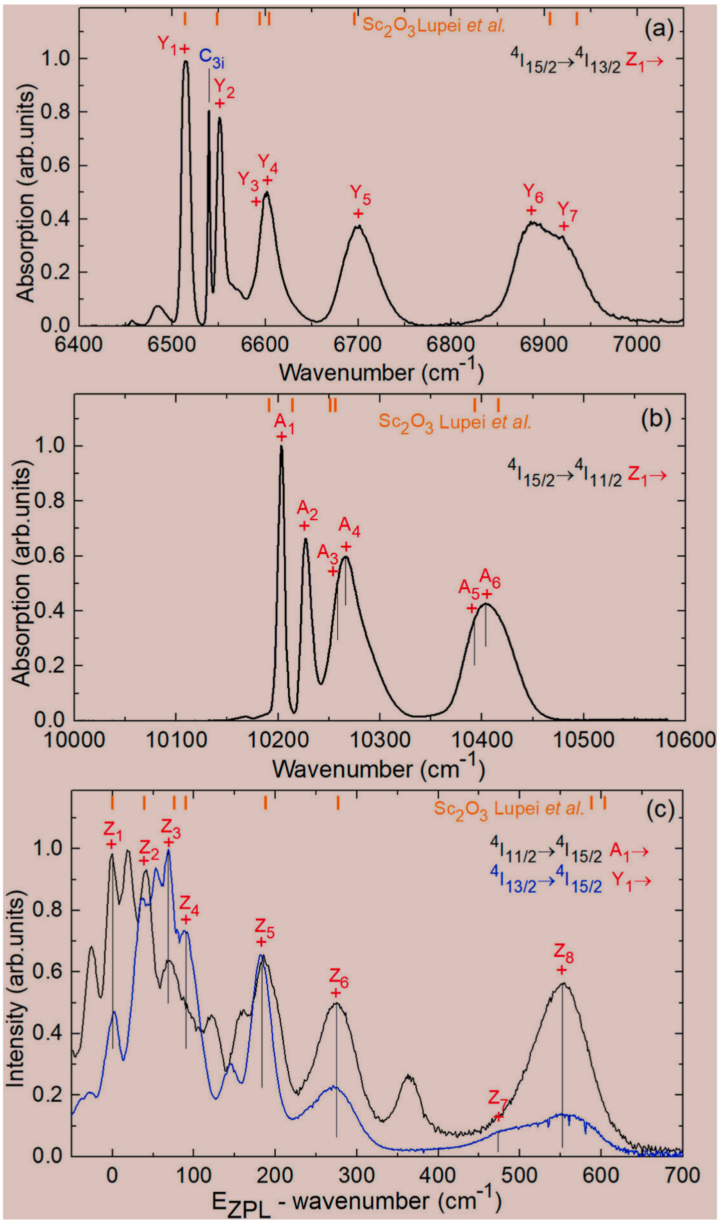

Figure V.9: LT (12 K) spectroscopy of Er^{3+} ions in $(Lu,Sc)_2O_3$ ceramic: (a,b) absorption spectra: (a) the $^4I_{15/2} \rightarrow {}^4I_{13/2}$ transition, (b) the $^4I_{15/2} \rightarrow {}^4I_{11/2}$ transition; (c) emission spectra for the $^4I_{11/2} \rightarrow {}^4I_{15/2}$ and $^4I_{13/2} \rightarrow {}^4I_{15/2}$ transitions. Z_i (i = 1...8), Y_j (j = 1...7) and A_k (k = 1...6) number the Stark sub-levels of the $^4I_{15/2}$, $^4I_{13/2}$ and $^4I_{11/2}$ multiplets, respectively, for C_2 sites. C_{3i} in (a) – lines assigned to MD transitions for C_{3i} sites. *Orange dashes* – crystal-field splitting for Er^{3+} in C_2 sites in Sc_2O_3 [Lup08].

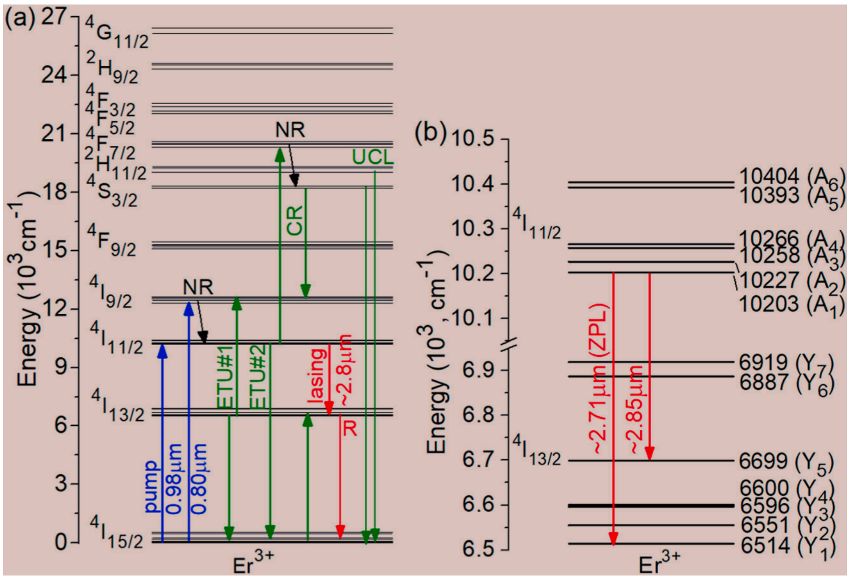

Figure V.10: Scheme of energy-levels of Er^{3+} ions in C_2 sites in $(Lu,Sc)_2O_3$ ceramic: (a) general scheme: *blue and red arrows* – pump and laser transitions, respectively, ETU – energy-transfer upconversion, CR – cross-relaxation, R and NR – radiative and non-radiative transitions, respectively, UCL – upconversion luminescence; (b) splitting of the $^4I_{11/2}$ and $^4I_{13/2}$ multiplets, *arrows* – observed laser lines.

Table V.1: Crystal-field splitting for Er^{3+} ions in C_2 sites in $(Lu,Sc)_2O_3$ ceramic. The empirical notations of the multiplets are after [Kis64].

Manifold	Notation	Stark components (cm^{-1})
$^4I_{15/2}$	Z	0, 41, 68, 90, 184, 275, 473, 552
$^4I_{13/2}$	Y	6514, 6551, 6596, 6600, 6699, 6887, 6919
$^4I_{11/2}$	A	10203, 10227, 10258, 10266, 10393, 10404
$^4I_{9/2}$	B	12303, 12439, 12523, 12600, 12630
$^4F_{9/2}$	D	15109, 15191, 15292, 15330, 15467
$^4S_{3/2}$	E	18201, 18309
$^2H_{11/2}$	F	19049, 19233,19307 (*3 missing*)
$^4F_{7/2}$	G	20322, 20467, 20496, 20607
$^4F_{5/2}$	H	22050, 22179 (*1 missing*)
$^4F_{3/2}$	I	22398, 22589
$^2H_{9/2}$	K	24337, 24554, 24614 (*2 missing*)
$^4G_{11/2}$	L	26137, 26448 (*4 missing*)

1.1.4 Calculation of stimulated emission cross-sections for $^4I_{11/2} \rightarrow {}^4I_{13/2}$ and $^4I_{13/2} \rightarrow {}^4I_{15/2}$ Er transitions

Two transitions in emission, $^4I_{13/2} \rightarrow {}^4I_{15/2}$ (at ~1.6 μm) and $^4I_{11/2} \rightarrow {}^4I_{13/2}$ (at ~2.8 μm) were analyzed. For both, the stimulated-emission (SE) cross-sections, σ_{SE}, were calculated using the Füchtbauer–Ladenburg (F-L) formula:

$$\sigma_{\mathrm{SE}}(\lambda) = \frac{\lambda^5}{8\pi < n >^2 \tau_{\mathrm{rad}} c} \frac{B(JJ')W'(\lambda)}{\int \lambda W'(\lambda) \mathrm{d}\lambda}, \tag{V.1}$$

where, λ is the light wavelength, $<n>$ is the refractive index of the ceramic corresponding to the mean luminescence wavelength $<\lambda_{\mathrm{lum}}>$, τ_{rad} is the radiative lifetime of the emitting state ($^4I_{13/2}$ or $^4I_{11/2}$) and $B(JJ')$ is the luminescence branching ratio of the considered transition, c is the speed of light and $W'(\lambda)$ is the luminescence spectrum accounting for the apparatus function of the set-up.

It is known that the SE cross-section spectrum calculated by the F-L formula can be inaccurate due to the possible reabsorption at the emission wavelengths. For the $^4I_{13/2} \rightarrow {}^4I_{15/2}$ transition, the reabsorption is expected to be particularly strong in the studied highly doped ceramic. Thus, a complementary approach was also used, i.e., the reciprocity method (RM) [Pay92]:

$$\sigma_{\mathrm{SE}}(\lambda) = \sigma_{\mathrm{abs}}(\lambda) \frac{Z_1}{Z_2} \exp\left(-\frac{(hc/\lambda) - E_{\mathrm{ZPL}}}{kT} \right), \tag{V.2a}$$

$$Z_m = \sum_k g_k^m \exp(-E_k^m / kT). \tag{V.2b}$$

Here, h is the Planck constant, k is the Boltzmann constant, T is the temperature (RT), E_{ZPL} is the energy corresponding to the so-called zero-phonon-line (ZPL) transition occurring between the lowest Stark sub-levels of the involved multiplets, Z_m are the so-called partition functions of the lower (m = 1) and upper (m = 2) manifolds, and $g_{mk} = 1$ is the degeneracy of the Stark sub-level with a number k and energy Emk measured from the lowest sub-level of each multiplet. The data on the crystal-field splitting for Er^{3+} obtained in the present work were used (Section 1.1.3).

For the $^4I_{13/2} \rightarrow {}^4I_{15/2}$ transition, the simultaneous use of the F-L equation and RM gives a good agreement only at the wavelengths above 1.6 μm (where the reabsorption is weak) for the $\tau_{\mathrm{rad}}(^4I_{13/2})$ values of 8.0 ± 0.5 ms which reasonably agrees with the J-O analysis (its results published in paper [Bas22a], in this thesis they are not presented). In this spectral range, the use of the F-L formula is preferable as the spectrum calculated by the RM is too noisy due to the exponential term in Equation (V.2a). At shorter wavelengths, the use of the F-L formula clearly underestimates the σ_{SE} values because of the strong reabsorption in highly doped ceramic. Thus, for constructing the final σ_{SE} spectrum, both complimentary approaches should be used. The maximum σ_{SE} is 1.43×10^{-20} cm^2 at 1535 nm (corresponding to ZPL at RT) and at longer wavelengths where the laser operation is expected, σ_{SE} is lower, namely 0.14×10^{-20} cm^2 at 1658 nm, as shown in Figure V.11(a).

For the $^4I_{11/2} \rightarrow {}^4I_{13/2}$ transition, the SE cross-sections determined using the F-L equation are 1.49×10^{-20} cm^2 at 2718 nm (ZPL) and 0.40×10^{-20} cm^2 at 2859 nm, Figure V.11(b). The corresponding emission bandwidths (FWHM) are 25 nm and 44 nm, respectively. Using the reciprocity method, we have also calculated the spectrum of excited-state absorption (ESA) corresponding to the $^4I_{13/2} \rightarrow {}^4I_{11/2}$ transition, Figure V.11(b).

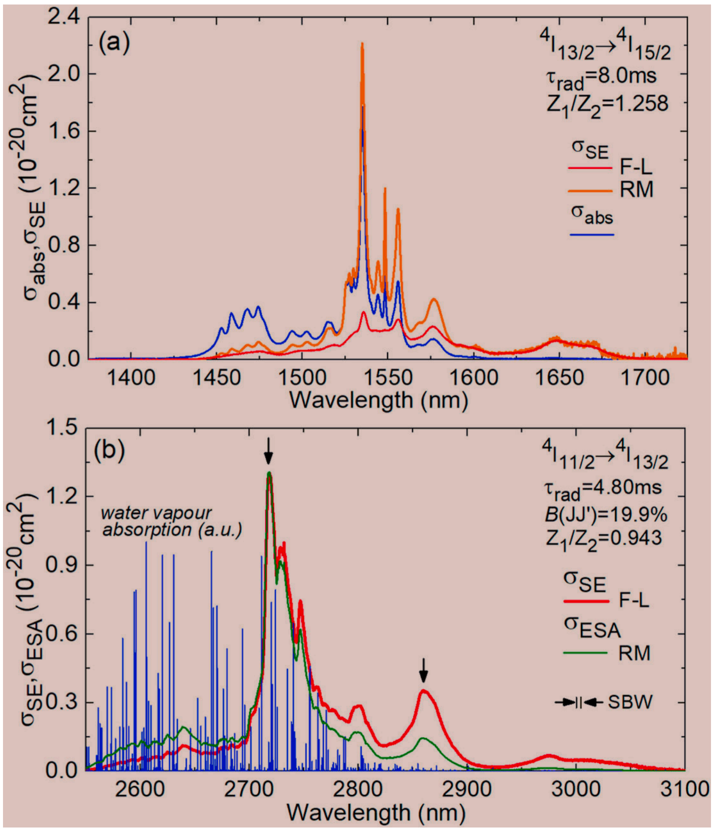

Figure V.11: RT stimulated-emission cross-sections, σ_{SE}, for Er^{3+} ions in $(Lu,Sc)_2O_3$ ceramic: (a) the $^4I_{13/2} \rightarrow {}^4I_{15/2}$ transition and (b) the $^4I_{11/2} \rightarrow {}^4I_{13/2}$ transition. F-L - Füchtbauer–Ladenburg equation, RM – reciprocity method. *Blue spectrum* in (b) – water vapor absorption in the atmosphere (from Hitran database). In (a), the σ_{abs} spectrum is given for comparison. In (b), the σ_{ESA} spectrum ($^4I_{13/2} \rightarrow {}^4I_{11/2}$) is calculated. *Arrows* indicate the observed laser lines.

1.2 Er:$(Y,Sc)_2O_3$ ceramics

A series of ~7 at.% Er:$(Y,Sc)_2O_3$ ceramics (cf. Figure V.12 for exact compositions) was obtained from the Institute of Electrophysics, RAS, Ekaterinburg, Russia (IE RAS). Ceramic samples were fabricated by vacuum sintering at 1750 °C for 5 h using laser-ablated nanoparticles [Loi21a] and 2 wt% ZrO_2 as a grain growth inhibitor. The ceramics were then annealed in air at 1400 °C for 2 h. The obtained ceramic disks (Φ11 mm) were polished to laser-grade quality, resulting in a thickness (*t*) of ~2 mm. The ceramics rose in color owing to Er3+ doping, as shown in Figure V.12.

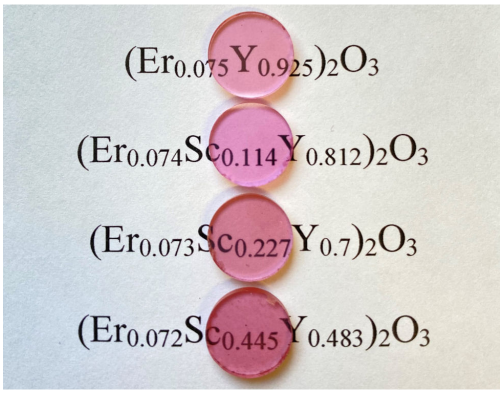

Figure V.12: A photograph of laser-grade polished ceramic disks.

1.2.1 Structural characterization

Figure V.13(a) shows the XRD patterns of the transparent Er:$(Sc_xY_{1-x})_2O_3$ ceramics, where various Sc contents were used. The observed diffraction peaks correspond well to a single-phase sesquioxide solid-solution with a cubic bixbyite structure (C-type, sp. gr. $Ia\bar{3}$), closely resembling the cubic Y_2O_3 phase in terms of peak positions and relative intensities (ICSD pattern No. 01-086-1326), as shown in Figure V.13(b). There is no evidence of secondary phases related to the presence of ZrO_2 as a sintering additive.

As the Sc content increases, the diffraction peaks shift towards larger diffraction angles, as depicted in Figure V.13(c,d), particularly emphasizing the most intense (222) reflection of the cubic sesquioxide structure. This shift confirms the formation of a solid-solution between yttria (Y_2O_3, a = 10.604 Å) and scandia (Sc_2O_3, a = 9.845 Å). The lattice parameter of the ceramics was further examined using a full-profile analysis of the XRD patterns through the Rietveld method. The results indicated that the lattice parameter decreases linearly with the increase in Sc content, consistent with Vegard's law. For samples containing 0, 11.4 at.%, 22.7 at.%, and 44.5 at.% Sc^{3+}, the respective lattice parameters were determined as 10.5947 Å, 10.5067 Å, 10.4211 Å, and 10.2421 Å.

The ionic radii of Sc^{3+} and Y^{3+} ions, in the VI-fold oxygen coordination, are 0.745 Å and 0.9 Å, respectively [Sha76]. As a result, when Sc^{3+} cations replace Y^{3+} at their respective sites, the crystal structure undergoes significant distortion, and compressive strains develop randomly throughout the lattice. Notably, there are not additional diffraction peaks corresponding to potential impurity phases, indicating that Sc_2O_3, Er_2O_3, and ZrO_2 completely dissolve in the Y_2O_3 matrix.

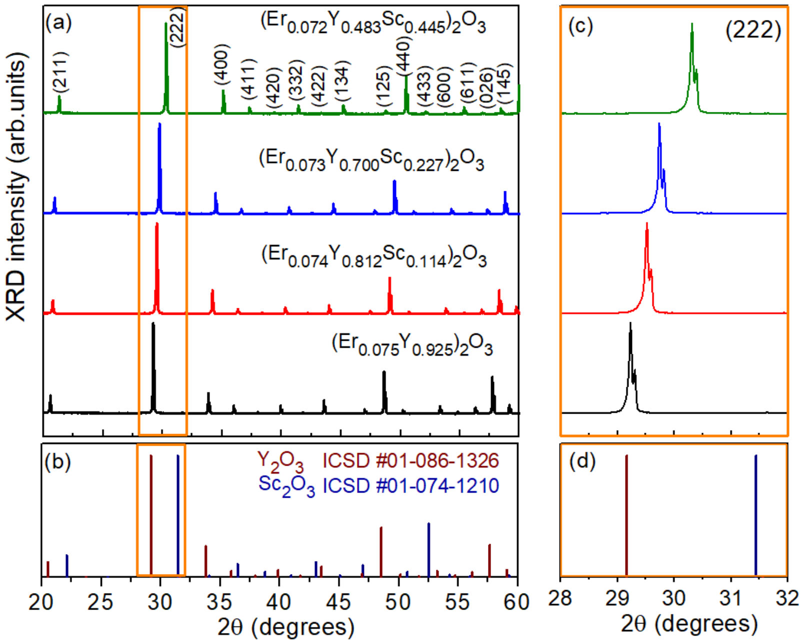

Figure V.13: (a) X-ray diffraction (XRD) patterns of the as-sintered $Er:(Sc_xY_{1-x})_2O_3$ ceramics, *numbers* – Miller's indices (*hkl*); (b) theoretical XRD patterns of Y_2O_3 (ICSD card No. 01-086-1326) and Sc_2O_3 (ICSD card No. 01-074-1210); (c) a close look on the (222) reflection of the sesquioxide phase; (d) the corresponding theoretical reflections of Y_2O_3 and Sc_2O_3.

Figure V.14 shows the surface morphology of the $Er:(Sc_xY_{1-x})_2O_3$ ceramics after polishing and thermal etching. These sintered samples consisted of close-packed crystallites with polyhedral shapes separated by well-defined grain boundaries. The average grain size increased from 9.6 µm for $Er:Y_2O_3$ ceramic to 21.6 µm, 23.5 µm, and 24.7 µm for ceramics containing 11.4 mol%, 22.7 mol%, and 44.5 mol% of Sc_2O_3, respectively. Throughout the depth of the ceramics, spherical pores with a characteristic size of 2-5 µm were relatively homogeneously distributed, as shown in the insets of Figure V.14. The average content of these pores is measured as 3.2 ppm, 4.2 ppm, 31.4 ppm, and 33.8 ppm for ceramics with 0.0 mol%, 11.4 mol%, 22.7 mol%, and 44.5 mol% of Sc_2O_3, respectively.

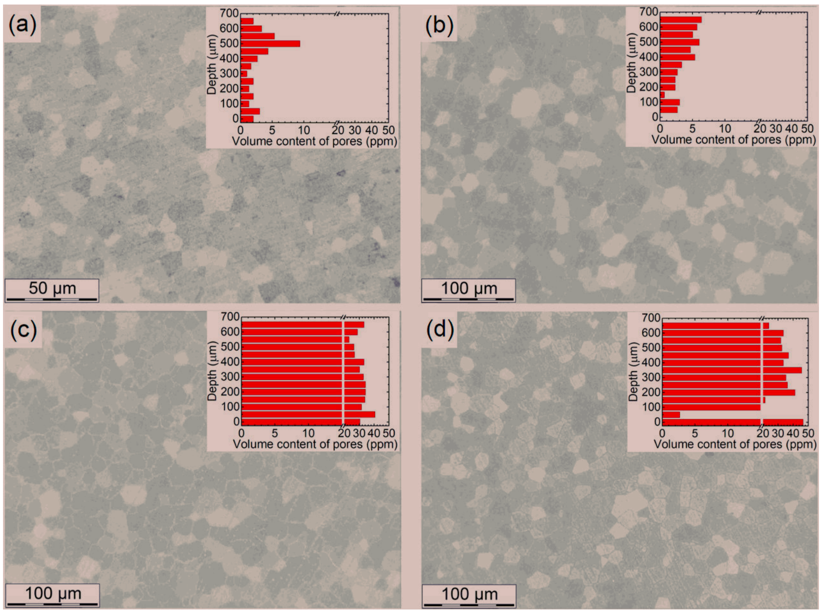

Figure V.14: Optical microscopy images of polished and thermally etched surface of ceramic disks: (a) $(Er_{0.075}Y_{0.925})_2O_3$; (b) $(Er_{0.074}Sc_{0.114}Y_{0.812})_2O_3$; (c) $(Er_{0.073}Sc_{0.227}Y_{0.7})_2O_3$; (d) $(Er_{0.072}Sc_{0.445}Y_{0.483})_2O_3$. *Insets* – the distributions of scattering centers across the depth of ceramics.

1.2.2 Investigation of thermal properties

The thermal conductivity of ceramics has been determined by our colleagues from IE RAS institute. The thermal conductivity (κ) of the $Er:(Sc_xY_{1-x})_2O_3$ ceramic samples was determined using the following equation:

$$\kappa = \alpha C_p \rho \tag{V.3}$$

where α is the thermal diffusivity, C_p is the specific heat and ρ is the density evaluated from the XRD analysis. The former two parameters were measured in the temperature range of 25–300 °C by the laser flash method using a LFA 467 HyperFlash system (NETZSCH, Germany). The values of thermal diffusivity and specific heat capacity of the synthesized $Er:(Sc_xY_{1-x})_2O_3$ ceramics at room temperature measured by the laser flash method along with the calculated thermal conductivities are listed in Table V.2. With increasing the Sc content in the ceramics from 0 to 44.5 at.%, the room temperature thermal conductivity gradually decreases from 6.14 to 3.66 $Wm^{-1}K^{-1}$, as expected for solid-solution compositions.

Considering the presence of ~1.7 mol% ZrO_2 in the fabricated ceramics, the thermal conductivity of 6.14 ± 0.31 $Wm^{-1}K^{-1}$ for the $(Er_{0.075}Y_{0.925})_2O_3$ ceramic sample is comparable with the previously reported values of 7.05 $Wm^{-1}K^{-1}$ for a $(Yb_{0.08}Y_{0.92})_2O_3$ single-crystal and 6.39 $Wm^{-1}K^{-1}$ for a $(Yb_{0.08}Y_{0.89}Zr_{0.03})_2O_3$ ceramic, respectively [Mun06, Hou11]. Since the atomic mass and the ionic radius of Er^{3+} are close to those of Yb^{3+}, a similar level of disorder and effect on the thermal properties could be expected upon partial substitution of Y^{3+} cations by Er^{3+} or Yb^{3+} ones in the Y_2O_3 host matrix. In addition, the measured value of 3.66±0.18 $Wm^{-1}K^{-1}$ for the $(Er_{0.072}Sc_{0.445}Y_{0.483})_2O_3$ ceramic is only slightly lower than that previously reported for a single-crystal with a relatively close composition $(Er_{0.07}Sc_{0.50}Y_{0.43})_2O_3$, $\kappa = 4.1$ $Wm^{-1}K^{-1}$ [Kra21], indicating only slightly higher concentration of lattice defects in the sintered ceramics.

Table V.2: Thermal properties of $Er:(Sc_xY_{1-x})_2O_3$ transparent ceramics with various Sc contents at room temperature.

Sc content, at.%	**Thermal diffusivity, mm²/s**	**Specific heat capacity, $Jg^{-1}K^{-1}$**	**Density, g/cm³**	**Thermal conductivity, $Wm^{-1}K^{-1}$**
0.0	3.023	0.383	5.307	6.14
11.4	2.362	0.391	5.208	4.81
22.7	1.982	0.412	5.100	4.16
44.5	1.680	0.445	4.895	3.66

1.2.3 Raman spectroscopy

The Raman spectra of the $Er:(Sc_xY_{1-x})_2O_3$ transparent ceramics are shown in Figure V.15. They were measured for $\lambda_{exc} = 457$ nm to avoid overlap with the Er^{3+} luminescence. The measured spectra are characteristic for cubic sesquioxides.

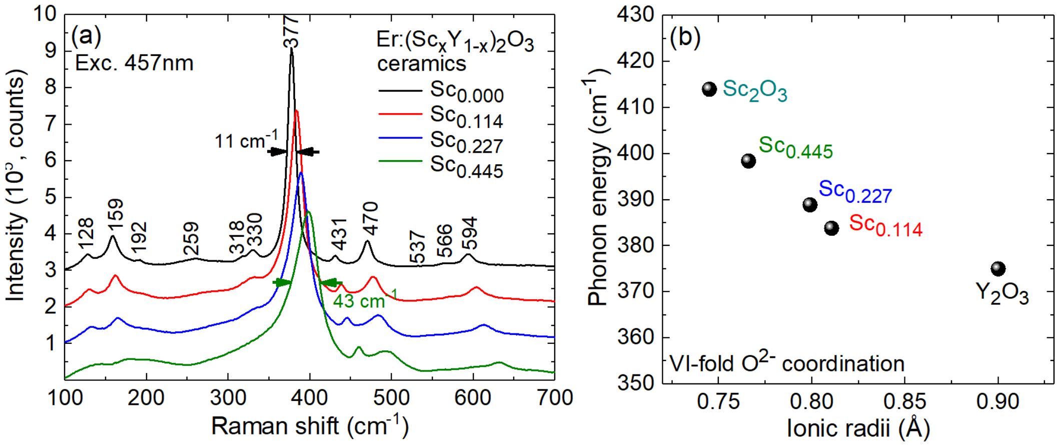

Figure V.15: Raman spectra of $Er:(Sc_xY_{1-x})_2O_3$ ceramics, *numbers* – peak Raman frequencies, $\lambda_{exc} = 457$ nm; (b) phonon energy vs. the ionic radius of the host-forming cations (VI-fold oxygen coordination). Data for Sc_2O_3 is given for comparison.

For the $(Er_{0.075}Y_{0.925})_2O_3$ ceramic, a total of 12 modes are observed: ~128, 159, 192, 259, 318, 330, 378, 431, 470, 537, 566 and 594 cm^{-1}. The most intense mode at 377.5 cm^{-1}) is assigned to $A_g + F_g$ vibrations. With increasing the Sc^{3+} content in the ceramics, the Raman spectra notably broaden, and the positions of the prominent Raman peaks shift to larger energies. E.g., for the ceramics with 0 at.%

Sc^{3+}, 11.4 at.% Sc^{3+}, 22.7 at.% Sc^{3+} and 44.5 at.% Sc^{3+}, the most intense Raman peak is observed at 377.5, 383.8, 388.9 and 398.4 cm^{-1}, respectively and its width broadens (full width at half maximum, FWHM: from 11 to 43 cm^{-1}). This behavior well agrees with the phonon spectra of the parent compounds showing the most intense peaks at 376 cm^{-1} (Y_2O_3) and 419 cm^{-1} (Sc_2O_3) and indicated a formation of a solid-solution rather than a mixture of two separate cubic sesquioxide phases. A similar behavior for certain “mixed” polycrystalline sesquioxides was observed previously [Pan00]. The dependence of the dominant Raman peak energy with the average ionic radius of the host-forming in ceramics is shown in Figure V.15(b).

1.2.4 Optical absorption

The in-line transmission spectra of the annealed Er:$(Sc_xY_{1-x})_2O_3$ ceramics with a thickness of 1.8 mm are shown in Figure V.16. The spectra exhibit absorption band characteristic for Er^{3+} ions. The ceramic with a parent composition Er:Y_2O_3 possesses the highest transmission T of 83.1 ± 1% at the wavelength of 1100 nm (out of Er^{3+} absorption). The theoretical transmission T_0 of pure Y_2O_3 and Sc_2O_3 ceramics can be calculated using the refractive index data reported by Kaminskii *et al.* [Kam03, Tak07] and a modified Fresnel equation accounting for multiple light reflections at the sample interfaces. Consequently, the theoretical value was estimated to be 82.7% for Y_2O_3 and 81.0% for Sc_2O_3 at 1100 nm and the transmission measured for Sc^{3+}-doped ceramics reaches these limits except of the sample $(Er_{0.072}Sc_{0.445}Y_{0.483})_2O_3$ for which T is only 79.2%.

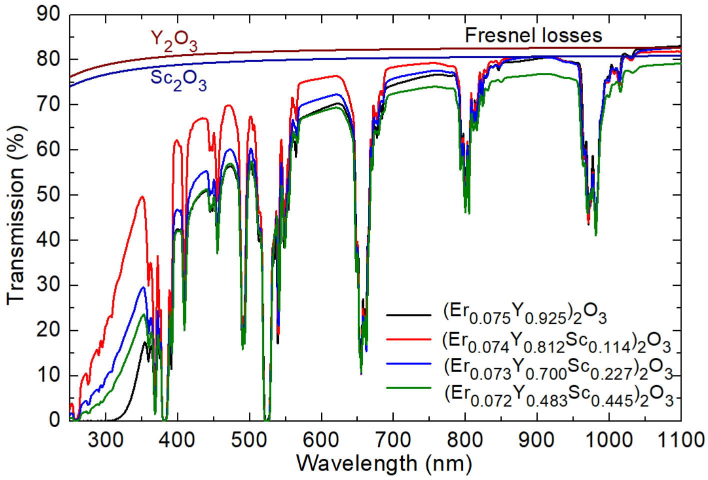

Figure V.16: Transmission spectra of the fabricated Er:$(Sc_xY_{1-x})_2O_3$ transparent ceramics (t ~ 2.0 mm).

We suppose that the drop-off in transmission in the visible and UV spectral ranges is due to a combination of light scattering by pores and absorption by uncontrolled impurities. Yttrium and scandium sesquioxides are known to possess a broad transparency range from 0.23 μm to about 8 μm. From the transmission data presented in Figure V.16, one can notice a strong absorption near 250 nm, which could be attributed to accidental iron impurities [Kre09] introduced by raw materials and cross contamination of nanopowders.

The absorption spectra of ceramics corresponding to the $^4I_{15/2} \rightarrow {}^4I_{11/2}$ Er^{3+} transition are shown in Figure V.17. The spectra broadened with increasing the content of Sc^{3+} ions. For the $(Er_{0.073}Sc_{0.227}Y_{0.700})_2O_3$ ceramic (N_{Er} = 2.02×10^{21} at/cm^3), the maximum absorption cross-section σ_{abs} was 0.26×10^{-20} cm^2 at 981.1 nm and the absorption bandwidth (FWHM) was 1.4 nm as shown in Figure V.17(b).

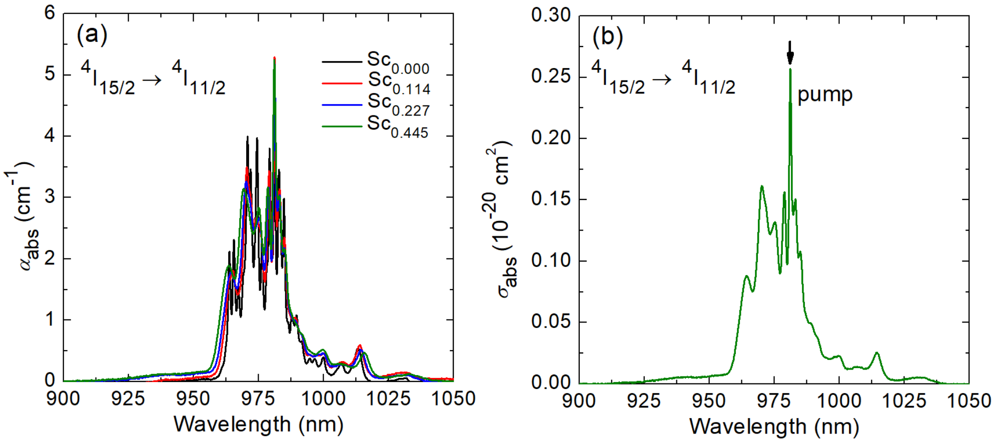

Figure V.17: (a) Absorption spectra of the $Er:(Sc_xY_{1-x})_2O_3$ transparent ceramics for the $^4I_{15/2} \rightarrow {}^4I_{11/2}$ transition; (b) Absorption cross-sections, σ_{abs}, for the $^4I_{15/2} \rightarrow {}^4I_{11/2}$ transition.

1.2.5 Mid-infrared luminescence (spectra and decay)

The spectra of MIR luminescence of Er^{3+} ions in the $Er:(Sc_xY_{1-x})_2O_3$ ceramics (water vapor absorption excluded) are shown in Figure V.17(a). The spectra are broad spanning from 2.55 to 3.1 μm; the luminescence is assigned to the $^4I_{11/2} \rightarrow {}^4I_{13/2}$ Er^{3+} transition. With increasing the Sc^{3+} content in the ceramics, the spectra are notably broadened. For the $(Er_{0.075}Y_{0.925})_2O_3$ ceramic, the spectrum contains several narrow intense peaks at 2710, 2717, 2725 and 2740 nm and a broad less intense band at 2842 nm (FWHM = 22 nm) usually used for achieving laser operation due to the weaker overlap with the structured water vapor absorption in the air. For the $(Er_{0.072}Sc_{0.445}Y_{0.483})_2O_3$ ceramic, the spectrum contains a broad structured band with a maximum at 2716 nm and another less intense band centered at 2848 nm with increased FWHM of 34 nm. Figure V.17(b) focuses on the spectral range of 2820–2910 nm indicating a continuous red-shift of the long-wavelength Er^{3+} emission band with increasing the Sc^{3+} content in the ceramic. It agrees well with the increase of the crystal field strength between Y_2O_3 and Sc_2O_3.

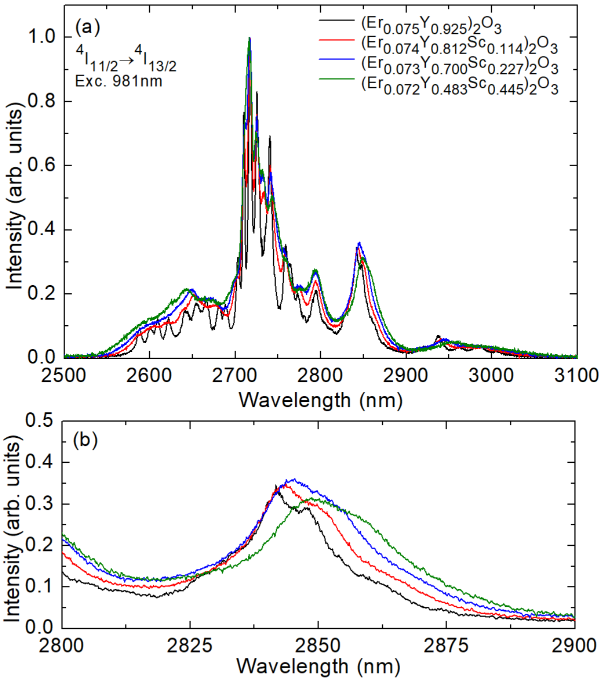

Figure V.18: MIR luminescence spectra of Er^{3+} ions in the $Er:(Sc_xY_{1-x})_2O_3$ transparent ceramics, (a) full spectra, (b) a close look at the 2800–2900 nm range, λ_{exc} = 981 nm.

Figure V.19(a) compares the luminescence decay curves for the Er^{3+} states $^4I_{11/2}$ and $^4I_{13/2}$ in $(Sc_xY_{1-x})_2O_3$ at room temperature (RT). They were measured under resonant excitation using finely powdered ceramic samples to exclude the reabsorption effects. The decay curves exhibit a shape characteristic for decay in the presence of an energy transfer (non single-exponential decay). Thus, the mean luminescence lifetimes for these states were calculated as $<\tau_{lum}> = \int tI(t)dt/\int I(t)dt$. They are shown in Figure V.19(b).

For the parent sesquioxides, the intrinsic luminescence lifetimes τ_{lum} of the $^4I_{11/2}$ and $^4I_{13/2}$ states given in [Uva23] are 2.58 ms / 7.08 ms for $Er:Y_2O_3$ and 0.36 / 6.28 ms $Er:Sc_2O_3$. For the $Er:Y_2O_3$ ($Sc_{0.000}$) ceramics with 7 at.% Er^{3+}, the luminescence lifetimes for both multipletes are sligtly shortened due to concentration-quenching and amouted to 2.13 ms / 5.46 ms for the $^4I_{11/2}$ / $^4I_{13/2}$ states. Note, that for the $^4I_{11/2}$ states the luminescence lifetime remains nearly constant indicating the contribution of concentration dependent energy-transfer upconversion process: $^4I_{13/2} + ^4I_{13/2} \rightarrow ^4I_{15/2} + ^4I_{11/2}$. This leads to a more favorable proportion between the relatively constant lifetime of $^4I_{11/2}$ and the quenched $^4I_{13/2}$ state. For both multiplets, the mean luminescence lifetimes tended to decrease with increasing Sc^{3+} content in the ceramics. Considering the difference in the phonon energy of the ceramics (higher phonon energy for Sc-containing compounds), as presented in Figure V.15, as well as the relatively close probabilities of radiative transitions for the parent compounds ($Er:Y_2O_3$ and $Er:Sc_2O_3$) given in [Uva23], this difference can be explained by the effect of nonradiative multiphonon relaxation.

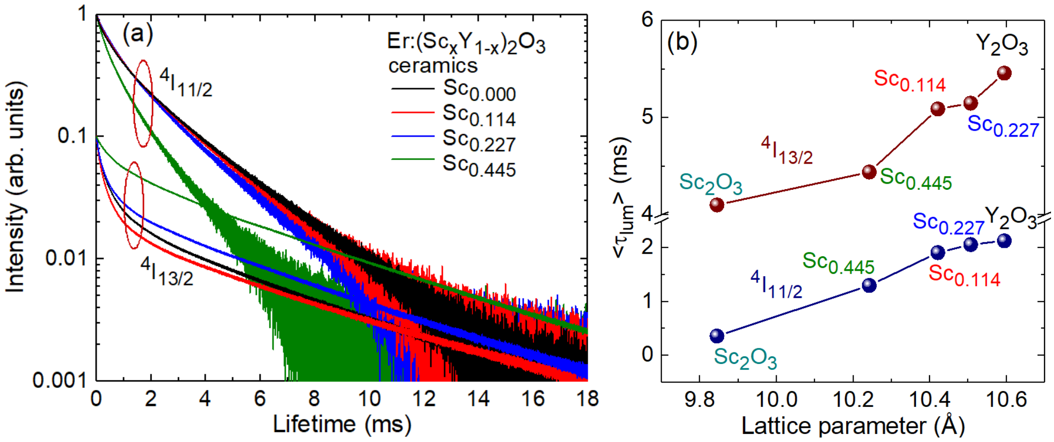

Figure V.19: (a) Luminescence decay curves for Er^{3+} ions in the $(Sc_xY_{1-x})_2O_3$ ceramics for the $^4I_{11/2}$ state, λ_{exc} = 965 nm, λ_{lum} = 1020 nm; and $^4I_{13/2}$ state, λ_{exc} = 1460 nm, λ_{lum} = 1560 nm; (b) $<\tau_{lum}>$ plotted as a function of lattice parameter of the $Er:(Sc_xY_{1-x})_2O_3$ ceramics. Solid lines are guides for the eye that have no physical meaning.

2 Laser-quality lanthanum-containing transparent sesquioxide ceramics (structure & spectroscopy)

The transparent sesquioxide ceramics of high optical quality with two compositions: $(Er_{0.07}La_{0.10}Y_{0.83})_2O_3$ and $(Er_{0.07}La_{0.05}Y_{0.25}Lu_{0.63})_2O_3$ were obtained by our collegues at G.G. Devyatykh Institute of Chemistry of High-Purity Substances of the RAS, Nizhniy Novgorod, Russia. Both ceramic samples were obtained by vacuum sintering at 1750 / 1780 °C for 3 hours. La_2O_3 acted as a sintering additive and induce the additional disorder of the sesquioxide lattice. The powder preparation was performed according to the self-propagating high-temperature synthesis (SHS) glycine-nitrate method described in detail in previous works [Per18, Bal21].

2.1 Microstructural characterization

• Powder XRD study

Both ceramics $Er,La:Y_2O_3$ and $Er,La:(Y,Lu)_2O_3$ were studied by X-ray powder diffraction (XRD) to confirm their phase purity. As it has been earlier shown that after sintering and/or the subsequent annealing in air of ceramics in some cases on boundaries of ceramic grains the secondary phases enriched by lanthanum can be formed [Bal20]. This phase, in turn, can play the role of additional scattering centers; therefore, it is essential to eliminate its presence.

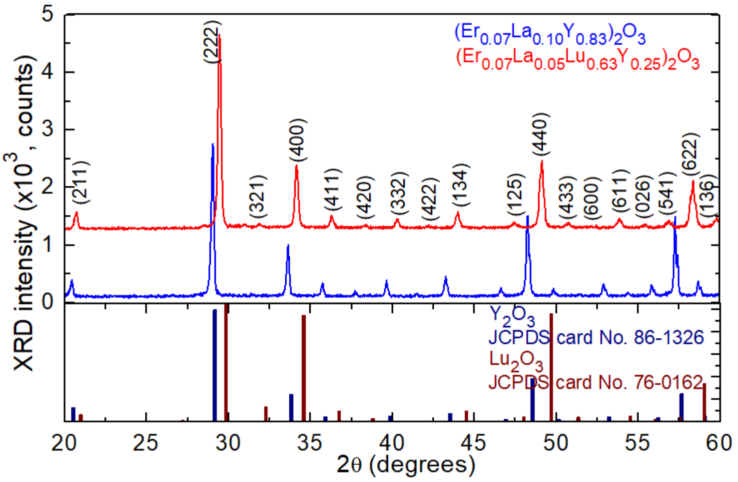

Figure V.20: X-ray powder diffraction (XRD) pattern of the $Er,La:Y_2O_3$ (*blue*) and $Er,La:(Y,Lu)_2O_3$ (*red*) ceramics, *bars* – theoretical reflections for Y_2O_3 (JCPDS card No. 86-1326) and Lu_2O_3 (JCPDS card No. 76-0162), *numbers* – Miller’s indices (*hkl*).

The Er,La:Y_2O_3 ceramic was found to be a single-phase material with a cubic, bixbyite-type structure (space group Ia3, lattice constant: $a = 10.6664(3)$ Å, density: $\rho_{calc} = 5.4011(4)$ g/cm^3). This was confirmed by an X-ray powder diffraction (XRD) study in Figure V.2. The relative intensities of diffraction peaks matched the theoretical values for yttria (Y_2O_3, JCPDS card No. 86-1326). However, the positions of the peaks were shifted towards smaller angles due to the presence of larger cations La^{3+} with ionic radius of 1.032 Å compared to Y^{3+} (0.90 Å) and Er^{3+} (0.89 Å) for VI-fold oxygen coordination. In the case of the Er,La:$(Y,Lu)_2O_3$ ceramic, its diffraction peaks fell between those of undoped Lu_2O_3 (ICDD card #76-0162) and Y_2O_3, indicating the presence of a solid-solution composition. The lattice parameter of the ceramic ($a = 10.473 \pm 0.008$ Å) occupied an intermediate position between Lu_2O_3 ($a = 10.391$ Å) and Y_2O_3 ($a = 10.602$ Å) [Kra15].

- **SEM observations**

The microstructures of the ceramics were studied using Scanning Electron Microscopy. Figure V.21 shows the SEM images of the fracture surfaces of the Er,La:Y_2O_3, and Er,La:$(Y,Lu)_2O_3$ ceramics. The images reveal a closely packed microstructure without discernible secondary phases at the grain boundaries. The average grain sizes were approximately 17 and 15 µm for Er,La:Y_2O_3 and Er,La:$(Y,Lu)_2O_3$, respectively. The grain size distribution exhibited a relatively broad spread for both ceramics, as shown in the bottom part of Figure V.21. Notably, intense grain growth is a characteristic feature of La-doped yttria [Iva14, Zha20a]. Additionally, the growth of larger grains, reaching 2-3 times the average size, can be expalined by the presence of rigid agglomerates in the SHS powders. To further enhance the optical quality of ceramics, it is essential to remove such agglomerates, which can be achieved through methods such as sedimentation.

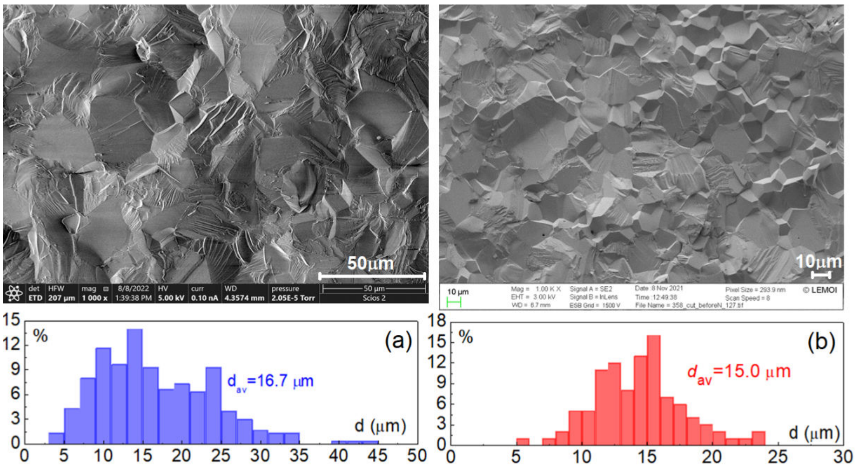

Figure V.21: SEM images of the ceramic fracture surfaces: (a) Er,La:Y_2O_3 and (b) Er,La:$(Y,Lu)_2O_3$. Corresponding grain disstributions are shown in bottom part for (a) in *blue* and (b) in *red*.

Despite the rapid grain growth during sintering, there is no pore-grain boundary separation with the formation of intragranular porosity. Any residual sub-micrometer pores are primarily situated along the grain boundaries and in triple junctions, and they do not appear to cluster together. This observation suggests that there is room for improving the quality of ceramics by employing a longer soaking time at the sintering temperature. By that, any remaining sub-micrometer pores can potentially be minimized, enhancing the overall quality and performance of the ceramic.

2.2 Raman spectroscopy

For cubic (C-type) sesquioxides with a body-centered structure, the factor group analysis predicts the following irreducible representations for the optical (Γ_{op}) and acoustical modes (Γ_{ac}) at the Γ-point ($\boldsymbol{k} = 0$):

$$\Gamma_{op} = 4A_g + 4E_g + 14F_g + 5A_{2u} + 5E_u + 16F_u,$$

$$\Gamma_{ac} = F_u$$

where 22 modes (A_g, E_g and F_g) are Raman-active, 16 modes (F_u) are IR-active and the rest are silent [Lav01, Tod13].

The Raman spectrum of the Er,La:Y_2O_3 ceramic shown in Figure V.22, is typical for cubic bixbite-type sesquioxides. The most intense peak appears at 370 cm^{-1} (the A_g + F_g modes), and it is broadened and red-shifted with respect to that for a Er:Y_2O_3 ceramic (377 cm^{-1}) indicating a formation of a substitutional solid-solution in presence of a minor amount of lantana.

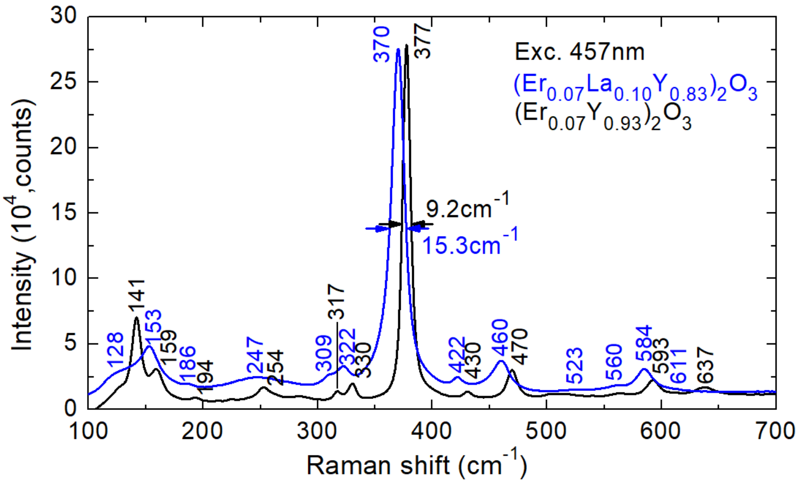

Figure V.22: Raman spectrum of the Er,La:Y_2O_3 ceramic (*blue*). Raman spectrum of the parent compound Er:Y_2O_3 (*black*) given for comparison, λ_{exc} = 457 nm.

2.3 Transmission & Absorption

As discussed in Chapter II (Section 2.3), the as-sintered ceramics were annealed in air to remove the oxygen vacancies. The effect of air-annealing on optical transmission is shown in Figure V.23. The in-line transmission spectra of the as-sintered and annealed ceramic disks of Er,La:$(Y,Lu)_2O_3$ (thickness: $t = 1.36$ mm) in the range 200 – 1100 nm are demonstated. The as-sintered sample is characterized by rapidly decreasing transmission in the visible region due to the oxygen vacancies formed during ceramic synthesis under oxygen-deficient conditions at high sintering temperatures and oil vacuum. Annealing under oxygen-rich conditions improves the transparency of the ceramic. The UV absorption edge of the annealed ceramic was observed at 234 nm ($E_g = 5.3$ eV). At a wavelength of 1.05 µm (out of Er^{3+} absorption), the measured transmission $T = 78.9\%$ is close to the theoretical limit determined by the Fresnel losses and accounts for multiple reflections, $T_0 = 2n/(n^2 + 1) = 81.5\%$ (calculated assuming a linear variation of the reflective index in the $Lu_2O_3 – Y_2O_3$ solid solution [Zel13], yielding an estimated value of the refractive index n = 1.937).

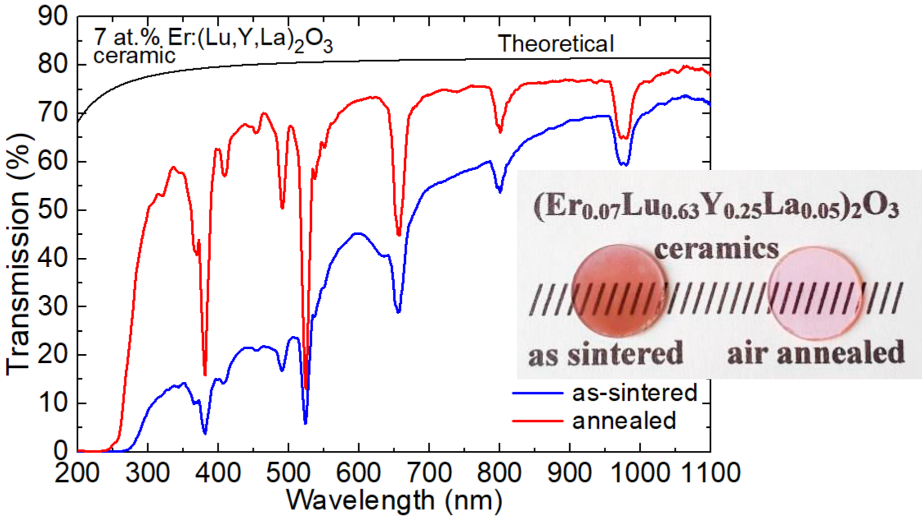

Figure V.23: Transmission spectra of the as-sintered (*blue*) and air annealed (*red*) Er,La:$(Y,Lu)_2O_3$ ceramic disks, *black curve* – theoretical transmission determined by the Fresnel losses. Thickness of the ceramic disk: $t = 1.36$ mm. *Insert* – a photograph of the as-sintered and air annealed sample.

Ground state absorption specrta into $^4I_{11/2}$ manifold were calculated from transmission spectra. This absorption band is suitable for pumping Er-lasers using commercially available InGaAs laser diodes emitting around 0.94–0.98 µm.

Figure V.24(a) shows absorption cross-sections, σ_{abs}, for the Er,La:Y_2O_3 ceramic. The peak absorption cross-section $\sigma_{abs} = \alpha_{abs}/N_{Er}$ (α_{abs} – absorption coefficient and $N_{Er} = 17.22\times10^{20}$ at/cm^3 is the Er^{3+} ion density in the ceramic) is

0.34×10^{-20} cm^2 at 981.3 nm and the corresponding absorption bandwidth (FWHM) is less than 1 nm and another broader peak is found at 971.1 nm ($\sigma_{abs} = 0.22\times10^{-20}$ cm^2). Compared to the absorption spectrum of parent $Er:Y_2O_3$ ceramic, the spectrum of $Er,La:Y_2O_3$ appears less structured due to La^{3+} codoping, which introduces additional inhomogeneous spectral broadening similar to other "mixed" sesquioxides ceramics.

Figure V.25(b) shows absorption cross-sections, σ_{abs}, for the $Er,La:(Y,Lu)_2O_3$ ceramic (Er^{3+} ion density, $N_{Er} = 19.6\times10^{20}$ at/cm^3). The absorption cross-section for the $^4I_{15/2} \rightarrow {}^4I_{11/2}$ transition for “mixed” ceramic is broadened as compared to both parent compounds Y_2O_3 and Lu_2O_3; The maximum σ_{abs} is 0.19×10^{-20} cm^2 at 970.5 nm corresponding to an absorption bandwidth $\Delta\lambda_{abs}$ (combining several peaks) of 16 nm, compared with $\sigma_{abs} = 0.22 \times 10^{-20}$ cm^2 at 970.9 nm with $\Delta\lambda_{abs}$ of ~3 nm for the $Er:Lu_2O_3$ ceramic.

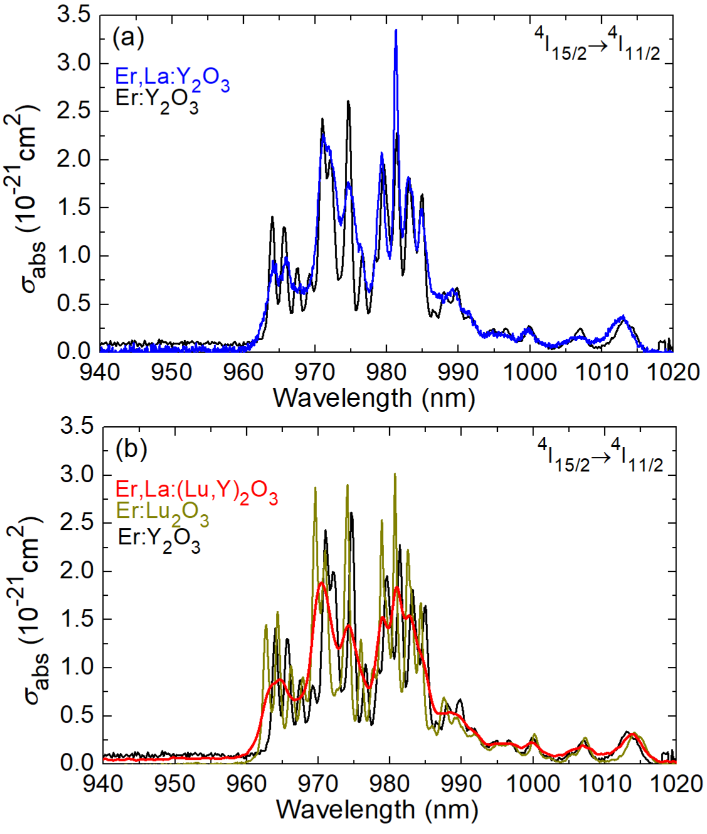

Figure V.24: Absorption cross-sections, σ_{abs}, for the $^4I_{15/2} \rightarrow {}^4I_{11/2}$ transition of Er^{3+} ions in the (a) $(Y,La)_2O_3$ and Y_2O_3 ceramics; (b) $(Lu,Y,La)_2O_3$, Y_2O_3 and Lu_2O_3 ceramics.

2.4 Mid-infrared emission (spectra & lifetimes)

The spectra of mid-IR luminescence of the annealed compositionally “mixed” $Er,La:(Lu,Y)_2O_3$ ceramic and the two parent ceramics, $Er:Lu_2O_3$ and $Er:Y_2O_3$, studied for comparison were measured using an optical spectrum analyzer (Yokogawa AQ6376) purged with N_2 gas to eliminate the structured water vapor absorption in the air and a zirconium fluoride (ZrF_4) fiber. As an excitation source, a Ti:Sapphire laser tuned to 970 nm was used. The normalized emission spectra of Er^{3+} ions in the $(Lu,Y,La)_2O_3$, Y_2O_3 and Lu_2O_3 ceramics are shown in Figure V.25.

The observed emission is related to the $^4I_{11/2} \rightarrow {}^4I_{13/2}$ transition. The spectra are very broad spanning from 2.58 to 3.05 μm. For the "mixed" ceramic, the spectrum exhibits less stuctured shape and a notable inhomogeneous line broadening as compared to those of the parent compounds. The spectral maximum is found at ~2717 nm. The laser operation with Er^{3+}-doped sesquioxides is usually achieved at longer wavelengths around 2.85 μm because of the weaker effect of the water vapor absorption in the air. A close look at the 2800–2900 nm range of emission spectra shown in Figure V.25(b). For the $Er,La:(Lu,Y)_2O_3$ ceramic, a broad peak is observed at 2843 nm, in between the positions for $Er:Lu_2O_3$ (2842 nm) and $Er:Y_2O_3$ (2846 nm). The emission bandwidth for this peak also exceeds those for the parent compounds supporting the assumption about the formation of a solid-solution.

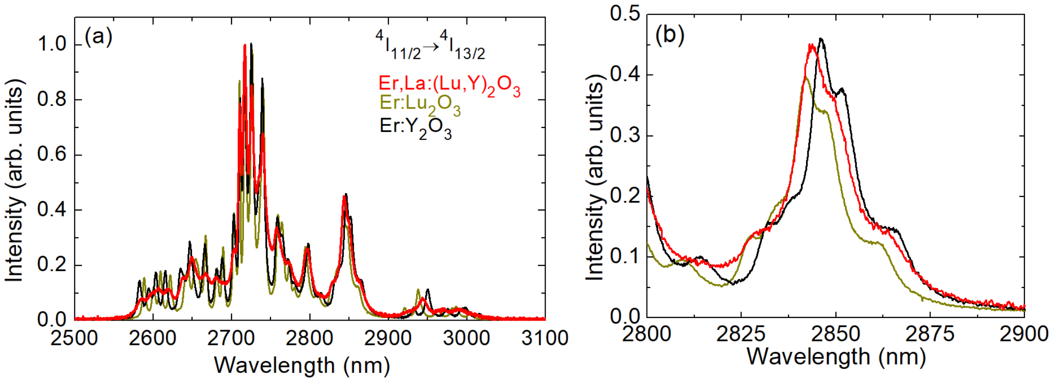

Figure V.25: Mid-IR emission spectra of Er^{3+} ions in the $(Lu,Y,La)_2O_3$, Y_2O_3 and Lu_2O_3 ceramics, (a) full spectra, (b) a close look at the 2800–2900 nm range, $\lambda_{exc} = 970$ nm.

For the $Er,La:Y_2O_3$ ceramic, we calculated the stimulated-emission (SE) cross-sections, σ_{SE}, of the $^4I_{11/2} \rightarrow {}^4I_{13/2}$ transition by the Füchtbauer-Ladenburg formula with the radiative lifetime of the emitting state ($\tau_{rad} = 5.39$ ms) and the luminescence branching ratio ($\beta_{JJ'} = 18.3\%$) for Er^{3+} ions in yttria calculated in [Uva23] using the standard Judd-Ofelt theory. The mid-infrared emission spectra of Er^{3+} ions are very broad spanning from 2.6 to 3.0 μm and the maximum σ_{SE} is 1.06×10^{-20} cm^2 at 2719 nm, as shown in FigureV.26. At longer wavelengths, where the laser operation is expected, σ_{SE} amounts to 0.45×10^{-20} cm^2 at 2849 nm.

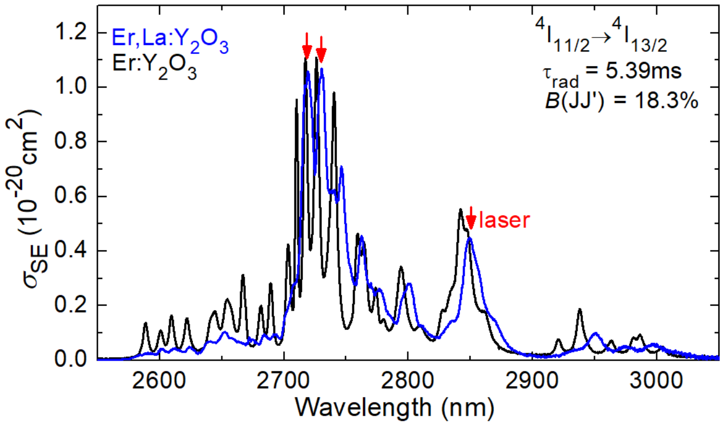

Figure V.26: Stimulated-emission (SE) cross-sections, σ_{SE}, for Er^{3+}ions in $(Y,La)_2O_3$ and Y_2O_3 ceramics for the $^4I_{11/2} \rightarrow ^4I_{13/2}$ transition.

The luminescence dynamics was studied using a ns optical parametric oscillator (Horizon, Continuum) employed as an excitation source, a 1/4 m monochomator, a fast InGaAs detector and an 8 GHz digital oscilloscope (DSA70804B, Tektronix). The luminescence decay curves from the upper ($^4I_{11/2}$) and lower ($^4I_{13/2}$) laser levels of Er^{3+} in the Er,La:Y_2O_3 and Er,La:$(Lu,Y)_2O_3$ ceramics were measured under resonant excitation, as shown in Figure V.27 and Figure V.28 plotted in a semi-log scale. The decay was studied using finely powdered ceramic samples to reduce the effect of radiation trapping (reabsorption). Mean luminescence lifetimes were calculated as $<\tau_{lum}> = \int tI(t)dt/\int I(t)dt$.

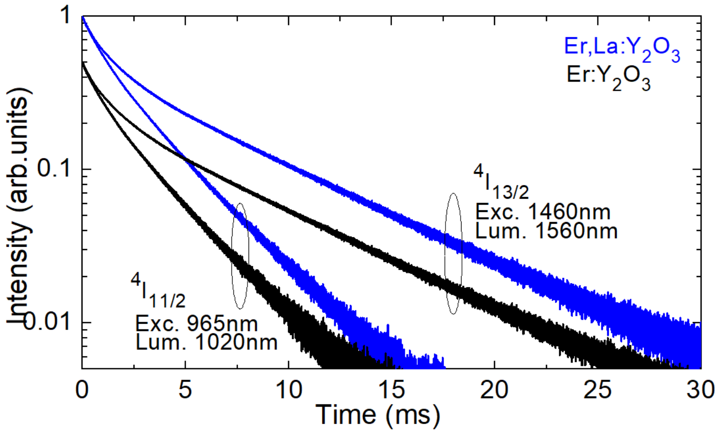

Figure V.27: Luminescence decay curves for Er,La:Y_2O_3 ceramic from the $^4I_{11/2}$ and $^4I_{13/2}$ Er^{3+} states under resonant excitation ($^4I_{11/2}$: λ_{exc} = 965 nm, λ_{lum} = 1020 nm; $^4I_{13/2}$: λ_{exc} = 1460 nm, λ_{lum} = 1560 nm). The decay curves for the parent ceramic, Er:Y_2O_3, is given for comparison.

For the Er,La:Y_2O_3 ceramic, the mean luminescence lifetimes $<\tau_{lum}>$ are 2.73 ms and 5.91 ms, respectively, representing a favorable ratio for mid-infrared laser operation. For comparison, we also determined the corresponding luminescence lifetimes for the Er:Y_2O_3 ceramic, $<\tau_{lum}>$ = 2.74 ms and 5.88 ms, respectively, indicating a minor effect of La^{3+}.

For the Er,La:$(Lu,Y)_2O_3$ ceramic, mean luminescence lifetimes amounted to 1.99 ms ($^4I_{11/2}$) and 3.35 ms ($^4I_{13/2}$), as shown in Figure V.28(a,b). For $^4I_{13/2}$ state, the decay curve is clearly not single-exponential owing to strong contribution of the energy-transfer upconversion (ETU) process $^4I_{13/2} + {}^4I_{13/2} \rightarrow {}^4I_{15/2} + {}^4I_{11/2}$ at this doping level (7at.%). This phenomenon is responsible for improved ratio of the nearly constant $^4I_{11/2}$ lifetime and the quenched $^4I_{13/2}$ is favorable for 2.8 µm lasers based on the transition between these multiplets. Measured luminescence lifetimes of the $^4I_{11/2}$ and $^4I_{13/2}$ Er^{3+} states in ceramics are listed in Table V.3.

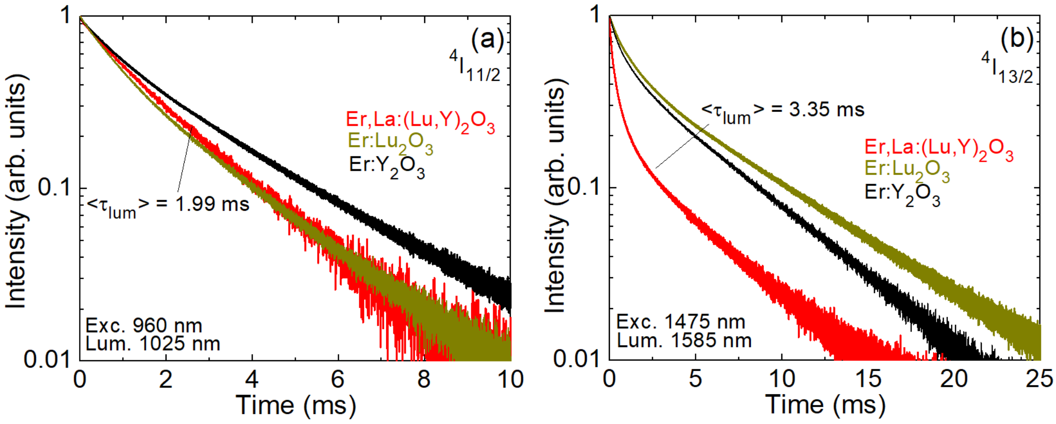

Figure V.28:Luminescence decay curves for Er^{3+} ions in the $(Lu,Y,La)_2O_3$ ceramic: (a) $^4I_{11/2}$ state, λ_{exc} = 960 nm, λ_{lum} = 1025 nm; (b) $^4I_{13/2}$ state, λ_{exc} = 1475 nm, λ_{lum} = 1585 nm, $<\tau_{lum}>$ - mean luminescence lifetime. The decay curves for the parent ceramics, Er:Lu_2O_3 and Er:Y_2O_3, are given for comparison.

Table V.3: Measured luminescence lifetimes of the $^4I_{11/2}$ and $^4I_{13/2}$ Er^{3+} states in the $(Y,La)_2O_3$, $(Lu,Y,La)_2O_3$ and two parent, Y_2O_3 and Lu_2O_3 ceramics.

Ceramics (7 at.% Er)	$<\tau_{lum}>$, ms	
	$^4I_{11/2}$	$^4I_{13/2}$
Er,La:Y_2O_3	2.73	5.91
Er,La:$(Lu,Y)_2O_3$	1.99	3.35
Er:Y_2O_3	2.74	5.88
Er:Lu_2O_3	2.10	4.91

3 Sesquioxide ceramic lasers at 2.8 µm

3.1 Ceramic laser set-up

The scheme of the mid-infrared laser set-up used for the experiments with the sesquioxide ceramics shown in Figure V.29**.** A simple linear hemispherical laser cavity was formed by a flat pump mirror (PM) coated for high transmission (HT) at 0.92 – 1.06 µm and high reflection (HR) at 2.6 – 3.0 µm, and a set of concave output couplers (OCs) having a radius of curvature (RoC) of -100 mm and a transmission at the laser wavelength T_{OC} in the range 0.33% - 4.0%. The ceramic element was placed close to the PM with an airgap of ~0.5 mm. The ceramic laser element polished from both sides to laser-grade quality and remained uncoated was mounted on a passively-cooled Cu-holder using a silver paste for better heat removal. The total cavity length was about 100 mm.

As a pump source, we used a continuous-wave (CW) Ti:Sapphire laser (3900S, Spectra Physics) tuned to the absorption peak.

The residual (non-absorbed) pump power was filtered out using a long-pass filter (LP1400, Spectrogon). The laser spectra were measured using an optical spectrum analyzer (AQ6376, Yokogawa).

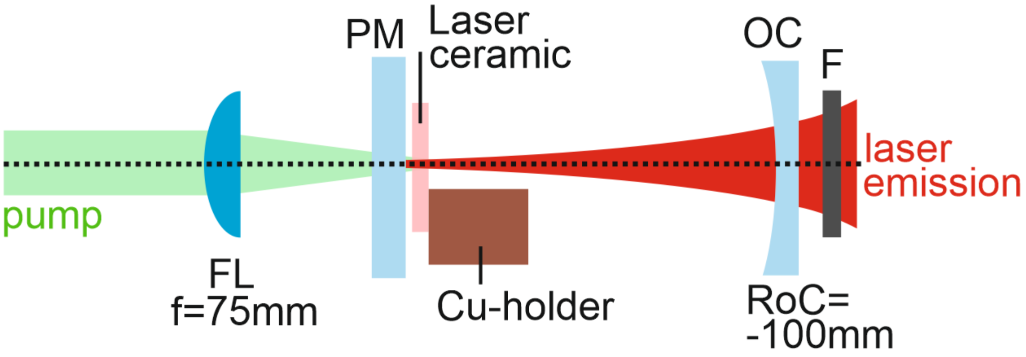

Figure V.29: Ceramic laser set-up: FL – focusing lens, PM – pump mirror, OC – output coupler, F- filter.

The spectra of laser emission were detected using a Fourier transform laser spectrum analyzer (771 series, Bristol). The laser mode was captured using a pyroelectric camera (Pyrocam IIIHR, Ophir-Spiricon).

3.2 Er:(Lu,Sc)$_2$O$_3$ ceramic laser

Laser cavity shown in Figure V.29 was used for the experiments. A rectangular active element (thickness: 1.98 mm, aperture: 3.0 × 3.0 mm^2) was fabricated from the 7 at.% Er:(Lu,Sc)$_2$O$_3$ceramic. A CW Ti:Sapphire laser used as a pump source operated in the fundamental mode (TEM$_{00}$, $M^2 \approx 1$) and delivering up to 2.7 W at 804.4 nm and 2.15 W at 980.6 nm. The OC was partially reflective for the pump (i.e., the pumping was in double pass). The total pump absorption under lasing conditions $\eta_{abs,L}$ amounted to 60.2 % and 47.1 % for λ_P = 804.4 and 980.6 nm, respectively.

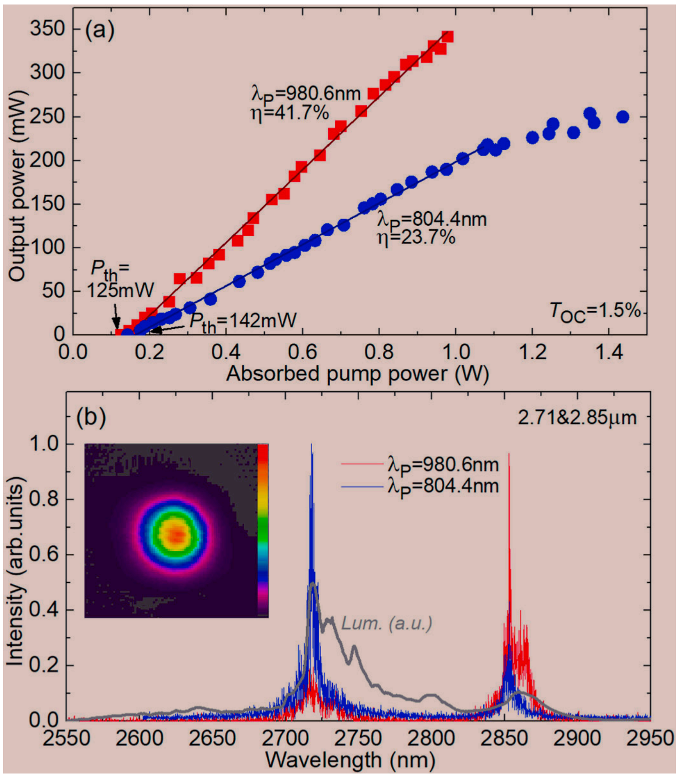

Figure V.30: (a) input-output power dependences for λ_P = 804.4 nm and 980.6 nm, η – slope efficiency; (b) typical laser emission spectra, *inset* – spatial profile of the laser mode in the far-field. T_{OC} = 1.5 %. The laser emission is unpolarized. For comparison the luminescence curve is implemented (*gray*).

Two pump schemes were studied, namely, pumping into the $^4I_{11/2}$ and $^4I_{9/2}$ Er^{3+} multiplets, Figure V.29. For optimum λ_P = 980.6 nm, the laser generated a maximum output power of 342 mW at ~2717 and 2853–2864 nm with a slope efficiency η of 41.7 % (with respect to the absorbed pump power) and a laser threshold P_{th} of 125 mW, Figure V.29(a). The optical-to-optical efficiency ηopt amounted to 16.5 % (versus the power incident on the ceramic). Power scaling was limited by the available pump. Almost no signs of thermal effects were observed in the input-output dependence. The η value exceeded the Stokes efficiency under lasing conditions, $\eta_{\mathrm{St,L}} = \lambda_{\mathrm{P}}/\lambda_{\mathrm{L}} \approx 34$ %, indicating an efficient ETU process (#1), Figure V.10(a), refilling the population of the upper laser manifold.

For pumping into the $^4I_{9/2}$ state (λ_{P} = 804.4 nm), the laser output reached 254 mW at ~2717 and 2853 nm with lower slope efficiency of 23.7 % and nearly the same threshold, 142 mW, Figure V.30(a). For absorbed pump powers exceeding 1.1 W, a thermal roll-over was observed. It is related to stronger heat loading for this pump scheme (in particular, the energy loss related to multiphonon non-radiative relaxation between the $^4I_{9/2}$ and $^4I_{11/2}$ states).

Typical spectra of laser emission are shown in Figure V.30(b). Lasing in two spectral regions, at ~2.71 and 2.85 μm, was observed. For the latter we consider two possible reasons. First, the main peak in the SE cross-section spectrum for the $^4I_{11/2} \rightarrow {}^4I_{13/2}$ transition overlaps with the structured water vapor absorption in the atmosphere, Figure V.30(b), which may introduce additional loss. Second, a resonant excited-state absorption (ESA) process, $^4I_{13/2} \rightarrow {}^4I_{11/2}$, which becomes efficient at high populations of the metastable $^4I_{13/2}$ state, forces the laser to operate at wavelengths longer than the ZPL (~2.71 μm). The observed relatively broad laser lines are due to the resolution limitation of the used spectrometer. The laser operated in the fundamental transverse mode, see the mode profile in the inset of Figure V.30(b)

For both studied pump schemes, the laser excitation curves (i.e., the dependence of the output power on the pump wavelength at a fixed incident pump power) were measured. They are shown in Figure V.31 together with the absorption cross-section spectra for the $^4I_{15/2} \rightarrow {}^4I_{11/2}$ and $^4I_{9/2}$ Er^{3+} transitions. The laser excitation curves follow the shape of the σ_{abs} spectra indicating that pumping into the most intense absorption peak is preferable for relatively short samples. CW laser operation was achieved for λ_{P} in the ranges of 957–1001 nm and 786–820 nm, limited by the weak pump absorption and coatings of the laser mirrors.

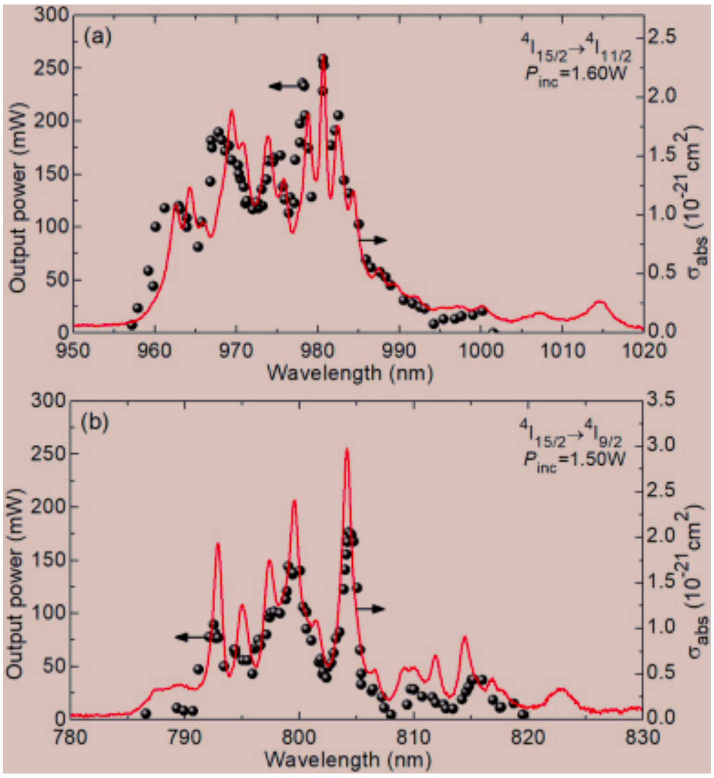

Figure V.31: Laser excitation curves for the Er:(Lu,Sc)$_2$O$_3$ ceramic laser (output power vs. the pump wavelength) measured at a fixed incident pump power Pinc: pumping into (a) the $^4I_{11/2}$ state and (b) the $^4I_{9/2}$ state. *Symbols* – laser output power, curves – σ_{abs} spectra.

3.3 Er:$(Y,Sc)_2O_3$ ceramic laser

Laser experiments were performed using the $(Er_{0.073}Sc_{0.227}Y_{0.700})_2O_3$ ceramic sample (t = 2.0 mm) mounted to the laser resonator shown in FigureV.29. The pump source was a Ti:Sapphire laser tuned to 981.1 nm (absorption peak), the measured single-pass pump absorption was 53.2%.

The ceramic laser was operated in the continuous-wave mode, generating a maximum output power of 312 mW at a wavelength of 2716 nm. The slope coefficient, η was 18.6%, (versus the absorbed pump power, fitting the input-output dependence well above the laser threshold of 128 mW) when using T_{OC} = 1.7%, as shown in Figure V.32(a). Note that no thermal roll-over was observed in the range of pump powers investigated, which could limit laser performance.

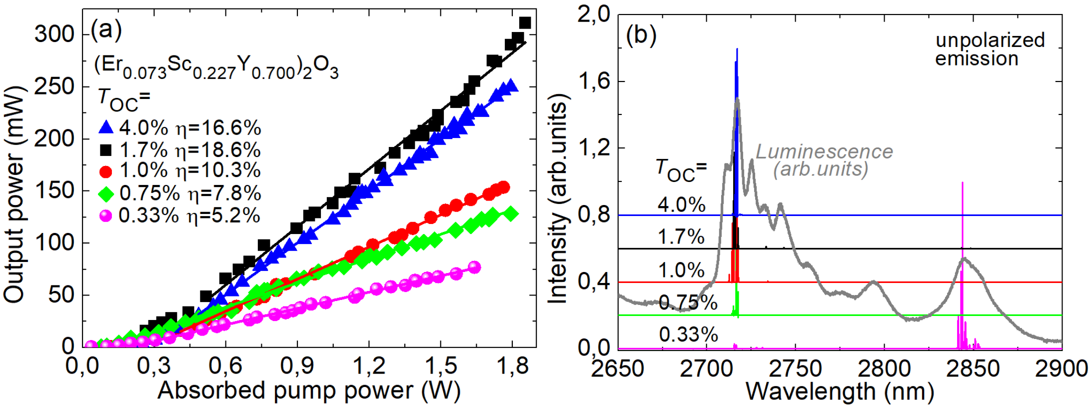

Figure V.32: MIR laser performance of the Er:$(Y,Sc)_2O_3$ ceramic: (a) input-output dependences, η – slope efficiency; (b) typical spectra of laser emission, unpolarized radiation, P_{abs} ~ 0.70 W,

The laser threshold gradually increased with output-coupling, it ranged from 37 mW for T_{OC} of 0.33% to 237 mW for T_{OC} of 4.0%. The laser emission was unpolarized, and the spectral analysis revealed that for T_{OC} values between 0.75% and 4.0%, the laser operated at wavelengths around 2714-2718 nm, in agreement with the maximum of the $^4I_{11/2} \rightarrow {}^4I_{13/2}$ emission band. In contrast, for a very low T_{OC} of 0.33%, the laser generated at longer wavelengths in the range of 2841-2853 nm. The laser spectra were weakly dependent on the pump power. The laser spectra were weakly dependent on the pump power. The laser operated in fundamental transverse mode ($M^2 < 1.2$).

The passive losses in the ceramic element were estimated using the Findlay-Clay analysis, i.e., by plotting the laser threshold P_{th} as a function of $\ln(1/R_{OC})$, where $R_{OC} = 1 - T_{OC}$ is the output coupler reflectivity, Figure V.33. The best-fit of experimental points yielded a round-trip passive loss L = 0.88% corresponding to a loss coefficient δ = 0.022 cm^{-1} at ~2.8 µm. This value gives an estimation for scattering losses in the ceramic related to its residual porosity.

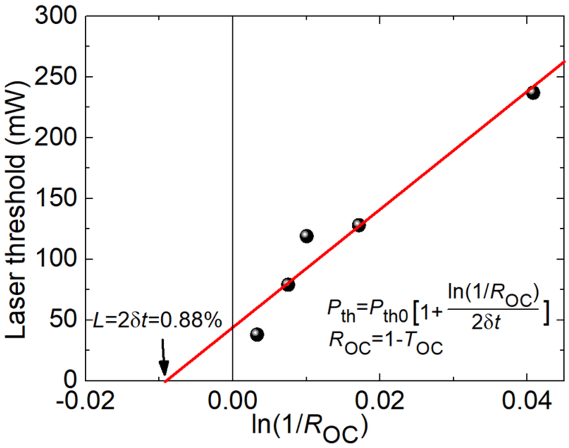

Figure V.33: Findlay-Clay analysis for the determination of the round-trip passive loss *L* in the Er:(Y,Sc)$_2$O$_3$ ceramic laser.

3.4 Er,La:Y_2O_3 ceramic laser

The $(Er_{0.07}La_{0.10}Y_{0.83})_2O_3$ ceramic (Φ12 mm, t = 0.93 mm) was polished from both sides to laser-grade quality and left uncoated. It was mounted to laser cavity shown in FigureV.29. A continuous-wave Ti:sapphire laser delivered up to 3.2 W at 981 nm with a diffraction-limited beam quality ($M^2 \approx 1$). The pumping was into the $^4I_{15/2} \rightarrow {}^4I_{11/2}$ absorption band of Er^{3+} ions. The pump beam was focused into the ceramic element through the PM using an AR-coated achromatic lens (focal length: f = 75 mm) resulting in a pump spot radius w_P of 33±5 µm (at the $1/e^2$ level). The measured single-pass pump absorption was 36.7%.

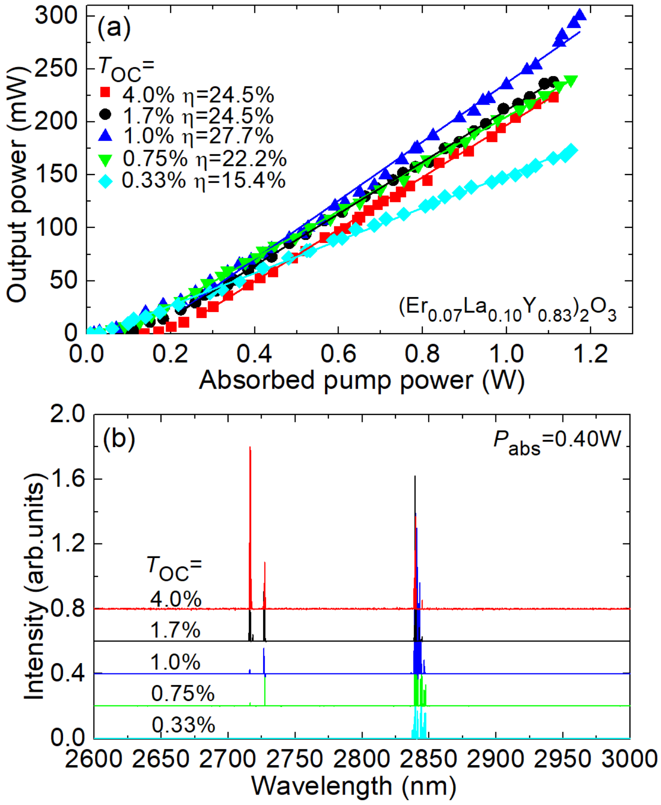

Figure V.34: Mid-infrared Er,La:Y_2O_3 ceramic laser: (a) input-output dependences, η – slope efficiency; (b) typical spectra of laser emission.

The mid-infrared Er,La:Y_2O_3 ceramic laser operating on the $^4I_{11/2} \rightarrow {}^4I_{13/2}$ transition generated a maximum output power of 300 mW at ~2840 nm with a slope efficiency η of 27.7% (with respect to the absorbed pump power). The laser threshold was remarkably low, only 17 mW for an output coupling (T_{OC}) of 1.0%, as shown in FgureV.34(a). The laser threshold gradually increased with output coupling, from 9 mW (T_{OC} = 0.33%) to 135 mW (T_{OC} = 4%). The input-output dependences were linear well above the laser threshold. Further power scaling was limited by the relatively low pump absorption in a thin ceramic sample and the available pump power. It is expected by applying commercially available InGaAs laser diodes emitting at ~980 nm as pump sources.

The typical spectra of laser emission are shown in Figure V.34(b). For small output coupling (T_{OC} ≤ 1%), the laser operated at ~2840 nm and for higher transmissions of the OC, the laser emission was observed both at ~2716 and 2840 nm. The laser emission was unpolarized. The Er,La:Y_2O_3 ceramic laser operated on the fundamental transverse mode (TEM_{00})

4 Conclusions Chapter V

In conclusion, we have studied compositionally “mixed” transparent sesquioxide ceramics doped with Er^{3+} ions, focusing on their mid-infrared emission properties and, in particular, their inhomogeneous spectral line broadening induced by a compositional disorder. Four binary systems were studied: lutetia-scandia (Lu_2O_3 – Sc_2O_3), lutetia – yttria (Lu_2O_3 – Y_2O_3), yttria – lantana (Y_2O_3 – La_2O_3), and yttria – scandia (Y_2O_3 – Sc_2O_3). Such “mixed” ceramics belonging to the family of rare-earth cubic sesquioxides (A_2O_3) appear very promising for applications in efficient solid-state lasers emitting around 2.8 μm due to noticeable spectral line broadening due to the high sensitivity of crystal-field strength to the ionic radius of the host-forming cation, A^{3+} (in our case, A^{3+} = Lu, Sc, Y or La). Such broadband emission spectra are of great interest for broadly tunable and femtosecond mode-locked lasers. The first laser action at 2.8 um was achieved for number of “mixed” sesquioxide ceramic compositions.

(i) For a lutetia-scandia, $(Lu,Sc)_2O_3$ single-phase transparent sesquioxide ceramic, it is shown that the compositional disorder of the host matrix promoted by the large difference in the ionic radii of the host-forming cations (Lu^{3+} and Sc^{3+}) leads to a significant inhomogeneous spectral line broadening of the absorption and emission bands, as revealed by low-temperature spectroscopy. At RT, the emission bandwidth of such ceramics exceeds 40 nm at ~2.86 μm. We reported the highly efficient laser operation of an $Er:(Lu,Sc)_2O_3$ ceramic laser at 2.85 μm with a slope efficiency of 41.7%, exceeding the Stokes efficiency. This indicates an efficient ETU process, $(^4I_{13/2}, {}^4I_{13/2}) \rightarrow (^4I_{9/2}, {}^4I_{15/2})$, refilling the population of the upper laser manifold, $^4I_{11/2}$, and depleting the intermediate metastable level $^4I_{13/2}$. This is due to the high optical quality of this ceramic featuring a close-packed microstructure (average grain size of 5.7 μm) and an optimized Er^{3+} doping level, leading to efficient energy transfer between the dopant ions, as evidence by the lifetime studies.

(ii) Furthermore, we systematically studied the effect of compositional mixing in yttria-scandia ceramics with increasing Sc content. In the sesquioxide material family, compounds based on Y and Sc correspond to the two extreme cases of the weakest and strongest crystal-field, that’s why studying such “mixed” material is of high interest for inducing string spectral line broadening. The addition of Sc^{3+} has a significant effect on the material properties of ceramics: (i) the lattice parameter shrinks according to the formation of a substitutional solid solution; (ii) the frequency of the most intense Raman mode increases and it is significantly broadened; (iii) the mean grain size increases; (iv) the transmission drops only for high Sc^{3+} doping levels ($x > 0.227$) owing to the larger number of pores, probably resulting from rapid grain growth; (v) the thermal conductivity of ceramics moderately decreases, still representing a reasonable value for potential laser applications; (vi) the mid-infrared emission spectra are progressively broadened, favoring broadly tunable laser operation.

The first laser action in the Er^{3+}-doped yttria-scandia laser ceramic was achieved with an output power of 312 mW at 2.72 µm with and slope efficiency of 18.6%.

(iii) For the first time, we studied lantanum-containing cubic sesquioxide laser ceramics doped with Er^{3+} ions, the role of La^{3+} ions consist of both as a sintering additive improving the process of Y_2O_3 ceramic fabrication, as well as inducing additional inhomogeneous spectral line broadening to the ceramics. Such ceramics preserve their cubic structure (C-type, sp. gr. $Ia\bar{3}$). The addition of La reduces the phonon energy of the yttria host, provides additional spectral broadening for the absorption and emission bands and leads to an increase in the luminescence lifetimes of Er^{3+} ions. The first laser action in the Er^{3+} -doped yttria-lantana sesquioxide ceramic is achieved with a noticeable low laser threshold of 9 mW and a slope efficiency up to 27.7%.

(iv) Based on the performed X-ray diffraction studies, Raman spectroscopy and low-temperature (12 K) spectroscopy of Er^{3+} ions in “mixed” sesquioxide ceramics, we proved that these materials represent compositional solid solutions in binary and ternary systems with the mixing of host-forming cations at the atomic level.

(v) Based on the study of multiple “mixed” sesquioxide ceramics doped with Er^{3+} ions, we have identified the Sc-containing ones, as the most promising for further laser developments, because they provide the strongest inhomogeneous spectral line broadening, which is favorable for diode-pumping (as broad absorption bands will be less sensitive to temperature drift of the laser diode wavelengths), broadly tunable and potentially fs mode-locked operations. Currently, laser experiments in the mode-locked regime are mainly limited by the absorption of structured water vapor in atmospheric air. Therefore, a well-controlled atmosphere, purged with nitrogen gas for examples, is required to achieve such laser characteristics.

General conclusions & Perspectives

The following results have been achieved in this PhD thesis:

(i) This research work demonstrates the successful growth of high-quality and high optical grade singly Er^{3+} doped and Er^{3+},Gd^{3+} codoped $LiYF_4$ epitaxial layers onto $LiYF_4$ orientated substrates using the liquid phase epitaxy growth method, by using LiF as a solvent and self-flux compound. Reduced growth temperatures (746 °C) compared to compositions closer to the peritectic one were achieved, resulting in single-crystalline and well-oriented epitaxial layers with a tetragonal structure and a low lattice mismatch regarding to their substrates, as well as a very low mosaicity. The layers exhibited clear interfaces, uniform thicknesses and a homogeneous distribution of Er^{3+} ions. The key factor identified in controlling layer growth behavior was the apparent supercooling, with a supercooling range of 0.5 - 1 °C preventing cracks, polycrystalline areas and an excessive crystallization of residual solvent onto the top surface of the layers. The "healing" approach, involving a short hold above the liquidus temperature and thus inducing a very slight dissolution of the substrate, have demonstrated that it improves the substrate surface quality and could lead to a better quality of the subsequent layer growth. Nevertheless, this approach modify slightly the flatness of the substrate surfaces, which could perturbate the subsequent waveguiding properties of a layer grown on such a substrate.

(ii) The epitaxial layers exhibit strongly polarized mid-infrared luminescence at 2.8 μm, indicating the potential for efficient laser operation. The maximum stimulated emission cross-section is found to be 1.91×10^{-20} cm^2 at 2663.2 nm for the π-polarization. The layers also demonstrate a favorable ratio of upper-to-lower laser level lifetimes and efficient energy transfer upconversion, making them suitable for mid-IR waveguide laser development.

(iii) Thermo-optical properties of Er^{3+}:CaF_2 crystals were studied to assess its potential for power scalable operation. Direct excitation into the upper laser level ($^4I_{11/2}$) showed higher efficiency and weaker thermal lens. The mid-infrared Er:CaF_2 laser achieved 0.84 W output power at 2800 nm with 31.6% slope efficiency, approaching the Stokes limit.

(iv) A comparative spectroscopic study of 5 at.% Er^{3+}:MF_2 fluorite-type crystals (M = Ca, Sr, Ba) have shown that the absorption and mid-infrared emission spectra become narrower and more structured, as we move from CaF_2 to SrF_2 and then to BaF_2. Luminescence lifetimes increase in the order $CaF_2 < SrF_2 < BaF_2$. Er^{3+} ions in "mixed" crystals tend to stay in a local environment dominated by larger M^{2+} cations, leading to similar spectra for certain combinations. At LT, Er^{3+} ions in solid-solution crystals exhibit inhomogeneous broadening. The study also revealed a single class of Er^{3+} clusters (D centers) for the 5 at.% Er^{3+} in MF_2 crystals, in contrast to lower doping ratios that show various ions clustering nature (D(1) and D(2)).

(v) Among the studied cubic fluorite-type crystals, Er:CaF_2 and its isotypes appear as the most promising, due to their good thermal properties, smooth and broad absorption spectra, inhomogeneously broadened emission spectra at 2.8 µm and long luminescence lifetimes. Although Er:CaF_2 showed the best laser performances in experiments, low phonon energy fluorite-type crystals such as BaF_2 and its solid-solutions hold strong potential for low laser threshold behavior with longer luminescence lifetimes.

(vi) The study found that among the various mixed sesquioxide ceramics doped with Er^{3+} ions, those containing Sc showed the most promising properties and performances for laser development. These ceramics exhibit strong inhomogeneous spectral line broadening owing to compositional disorder resulting from the size difference of Lu^{3+} and Sc^{3+} ions, making them ideal for diode pumping because of their broad absorption bands, which are less affected by the temperature drift of the laser diode wavelengths. For the Er:$(Lu,Sc)_2O_3$ ceramic, the emission bandwidth exceeded 40 nm at ~2.86 µm at room temperature. We demonstrated highly efficient laser operation at 2.85 µm using the Er:$(Lu,Sc)_2O_3$ ceramic with a slope efficiency of 41.7%, surpassing the Stokes efficiency. This indicates efficient energy transfer processes, refilling of the upper laser manifold ($^4I_{11/2}$) and depletion of the intermediate metastable level ($^4I_{13/2}$).

Future perspectives:

(i) Concerning the LPE growth of high optical grade single-crystalline layers, it is promising to study Er:LiYF$_4$ epitaxy with higher doping ratios, between 15 - 30 at. %, according to the previous studies in bulk Er:LiYF$_4$ crystals, which featured the record-high laser slope efficiency. These laser performances are not yet reached with other laser materials. At the same time, the epitaxial growth of such heavily doped epitaxies is clearly not trivial and requires a careful optimization of the lattice mismatch and of the growth conditions, as we expected certain changes in the phase diagram upon the introduction of such high Er doping levels. Regarding the epitaxial growth of Er:CaF$_2$ layers, although we have demonstrated the first results, significant efforts are still required to overcome the problem of crazing, which could be reduced by adjusting either the layer composition and/or the substrate material, to match the thermal expansion coefficients of the layer and the substrate. For this purpose, isotypes of CaF$_2$, such as SrF$_2$ or BaF$_2$, are considered to be used as substrates for further LPE growth runs of Er-doped CaF$_2$ epitaxial layers. In such a case, we would have heteroepitaxy conditions and a quaternary chemical system should be considered, which is more complex to manage.

(ii) In our work, we have also compared several fluorite-type cubic materials featuring relatively broad and smooth emission spectra around 2.8 μm. Considering the combination of high optical quality and laser efficiency as well as good thermal properties, we identified Er^{3+}-doped MF$_2$ -type crystals as the most promising candidates. Although Er:CaF$_2$ for the present moment offers the best optical quality and laser performances, low-phonon-energy compounds such as BaF$_2$ may also be very attractive because of their long luminescence lifetimes and low laser thresholds. Further laser development can be directed towards the realization of terminal pumping of the laser level in the region of 1.54 μm using commercially available high-power fiber Er lasers.

(iii) Er^{3+}-doped sesquioxide "mixed" ceramics are very promising for 2.8 μm lasers, and we identified Sc-containing compositions as the most interesting in terms of inhomogeneous spectral line broadening. Further experiments should focus on diode-pumping of such ceramics for pulse scalability.

(iv) The developed materials are characterized by inhomogeneously broadened emission bands in the region of 2.8 μm and for some materials such as Er:MF$_2$ crystals, these bands strongly look like those of Er-doped fluoride glasses, so that one can speak of glassy behavior. Furthermore, considering the success of Er:ZBLAN (glass) mode-locked fiber lasers for generating ultrashort pulses in the 2.8 μm region, it can be assumed that Er:MF$_2$-type crystals are also very promising for application in broadly tunable and especially mode-locked lasers generating ultrashort pulses in the mid-infrared spectral range, and the development of such lasers is only a starting point. For this purpose, there are two main limitations: first, the identification of potential saturable absorbers for such lasers, such as gallium antimonide (GaSb)-based semiconductor saturable absorption mirrors (SESAMs), which have begun to appear nowadays and the control of the atmosphere inside the laser cavity owing to the overlap of the emission spectra of Er^{3+} ions in such crystals with the structured absorption of water vapor in the atmosphere, which leads to a strong structuring of the laser spectra. The latter problem can be solved by purging the laser cavity with nitrogen gas for exemple. Indeed, as showed by our experiments, in purging the luminescence setup with nitrogen gas, we were able to almost completely eliminate the structure of the luminescence spectra caused by water vapor absorption. A similar positive effect can be expected from the development of lasers. Moreover, even for continuous-wave lasers operating under nitrogen atmosphere, an improvement in laser performance is expected owing to the suppression of absorption losses.

(v) Focusing on Er^{3+}-doped MF_2-type crystals is also promising for concentration-dependence studies. In fact, this work has just started in this thesis. A set of $Er:CaF_2$ single-crystals with doping ratios ranging between 0.01 – 10 at. % was grown and a strong drop of thermal properties of these crystals when going to doping levels above 5 at.% has been observed, while it is important to determine the equilibrium between their pump absorption in ion clusters from one hand and the drop of thermal conductivity from another hand. Regarding other MF_2-type compounds, the most critical issue is the improvement in the optical quality of these crystals, which can be potentially achieved by reducing the growing rates. Materials featuring low-phonon-energy behavior, such as $Er:BaF_2$ crystals, are also very interesting for laser emission even further in the mid-infrared at ~3.5 and ~4.5 µm, corresponding to the $^4F_{9/2} \rightarrow {}^4I_{9/2}$ and $^4I_{9/2} \rightarrow {}^4I_{11/2}$ transitions respectively, which have not been demonstrated yet. The potential of other low-phonon energy matrices, such as Er-doped sesquioxides for example, for these mid-IR emission remains to be evaluated.

List of Publications

Publications in scientific journals

1. **L. Basyrova**, P. Loiko, W. Jing, Y. Wang, H. Huang, E. Dunina, A. Kornienko, L. Fomicheva, B. Viana, U. Griebner, V. Petrov, M. Aguiló, F. Díaz, X. Mateos, and P. Camy, "Spectroscopy and efficient laser operation around 2.8µm of Er:(Lu,Sc)$_2$O$_3$ sesquioxide ceramics," *Journal of Luminescence*, 240, 118373 (2021).
2. **L. Basyrova**, P. Loiko, J. L. Doualan, A. Benayad, A. Braud, C. Labbé, and P. Camy, "Er: KY$_3$F$_{10}$ laser at 2.80µm," *Optics Letters* 46(22) 5739-5742 (2021).
3. **L. Basyrova**, P. Loiko, J. L. Doualan, A. Benayad, A. Braud, B. Viana, and P. Camy, "Thermal lensing, heat loading and power scaling of mid-infrared Er:CaF$_2$ lasers," *Optics Express* 30(5), 8092-8103 (2022).
4. **L. Basyrova**, G. Brasse, P. Loiko, C. Grygiel, R. M. Solé, M. Aguiló, F. Díaz, X. Mateos, A. Benayad, J.L. Doualan, and P. Camy, "Liquid phase epitaxy growth and structural characterization of highly-doped Er^{3+}: LiYF$_4$ thin films, " *Optical Materials,* 132, 112574 (2022)
5. S. Balabanov, P. Loiko, **L. Basyrova**, D. Permin, D. Kosyanov, T. Evstropov, S. Filofeev, A. Braud, and P. Camy, "Mid-infrared laser operation of (Er$_{0.07}$La$_{0.10}$Y$_{0.83}$)$_2$O$_3$ sesquioxide ceramic," *Laser Physics Letters*, 20 (4), 045801 (2023).
6. R. Maksimov, V. Shitov, V. Osipov, O. Samatov, D. Vakalov, F. Malyavin, **L. Basyrova**, P. Loiko, and P. Camy, "Fabrication, microstructure and mid-infrared luminescence of Er:(Sc$_x$Y$_{1-x}$)$_2$O$_3$ transparent ceramics," *Optical Materials*, 137, 113542 (2023).
7. S. Normani, **L. Basyrova**, P. Loiko, A. Benayad, A. Braud, A. Hideur, and P. Camy, "Mid-infrared laser operation of Er^{3+}-doped BaF$_2$ and (Sr,Ba)F$_2$ crystals," *Optics Letters,* 48(2), 431-434 (2023).
8. S. Normani, P. Loiko, **L. Basyrova**, A. Benayad, A. Braud, E. Dunina, L. Fomicheva, A. Kornienko, A. Hideur, and P. Camy, "Mid-infrared emission properties of erbium-doped fluorite-type crystals," *Optical Materials Express* 13, 1836-1851 (2023).

International conferences

1. **L.Basyrova**, G. Brasse, P. Loiko, A. Benayad, G. Daniil, J. Doualan, A. Braud, and P. Camy, "Liquid Phase Epitaxy Growth and Spectroscopy of Waveguiding Tm^{3+}:CaF_2 Thin Films, " in Advanced Solid State Lasers 2020 (ASSL 2020) conference, 13-16 October 2020, **Poster presentation** – **IPG Student Paper Award**.
2. **L. Basyrova**, P. Loiko, G. Brasse, A. Benayad, J. Doualan, A. Braud, and P. Camy, "Highly-Doped Er:$LiYF_4$ Waveguiding Epitaxial Films for ~2.7 µm Laser Sources," in CLEO 2021 conference, 09–14 May 2021, Oral presentation.
3. **L. Basyrova**, P. Loiko, W. Jing, Y. Wang, H. Huang, M. Aguiló, F. Díaz, E. Dunina, A. Kornienko, U. Griebner, V. Petrov, X. Mateos, B. Viana, Patrice Camy, "Efficient Laser Operation of Transparent “Mixed” 7 at.% Er:$(Lu,Sc)_2O_3$ Sesquioxide Ceramics near 2.8 µm," in CLEO/Europe-EQEC 2021, organized by EPS, 21-25 June 2021, Oral presentation.
4. **L. Basyrova**, P. Loiko, J.L. Doualan, A. Benayad, A. Braud, C. Labbé, and P. Camy, "Mid-Infrared Laser Operation of Er:KY_3F_{10} Crystal at 2.80 µm," ALT 2021, 6-10 September 2021, Oral presentation.
5. **L. Basyrova**, P. Loiko, J. Doualan, A. Benayad, A. Braud, B. Viana, and P. Camy," Power Scaling and Thermal Lensing in ~2.8 µm Er:CaF_2 Lasers: Effect of the Pump Wavelength," Laser Congress 2021 (ASSL), 3–7 October 2021, Oral presentation - **Laser Congress Student Paper Award Finalist.**
6. **L. Basyrova**, S. Balabanov, P. Loiko, D. Permin, D. Kosyanov, T. Evstropov, S.Filofeev, J.-L.Doualan, A. Braud, and P. Camy, "Synthesis and mid-infrared luminescence of “mixed” Er:$(Lu,Y,La)_2O_3$ transparent ceramics," SPIE Photonics Europe 2022 On Demand, 9–15 May 2022, Oral presentation.
7. **L. Basyrova**, P. Loiko, J.-L. Doualan, A. Benayad, G. Z. Elabedine, R. M. Solé, M. Aguiló, F. Díaz, Xavier Mateos, Elena Dunina, A. Kornienko, A. Braud, C. Labbé, P. Camy, "Growth and spectroscopy of Er^{3+}-doped $Na_5Y_9F_{32}$ ($5NaF·9YF_3$) crystal," SPIE Photonics Europe 2022 On Demand, 9–15 May 2022, Oral presentation.
8. **L. Basyrova**, P. Loiko, R. Maksimov, V. Shitov, J. Doualan, A. Braud, A. Hideur, B. Viana, and P. Camy, "Spectroscopy and Mid-Infrared Laser Operation of “Mixed” Sesquioxide Ceramics Er:$(Y,Sc)_2O_3$," CLEO 2022, 15–20 May 2022, Oral presentation.

9. **L. Basyrova**, P. Loiko, S. Balabanov, D. Permin, S. Filofeev, T. Evstropov, J.-L. Doualan, A. Braud, and P. Camy, "Mid-infrared laser operation of transparent ceramic $(Er_{0.07}La_{0.10}Y_{0.83})_2O_3$," Laser Optics 2022, 20-24 June 2022, Oral presentation.
10. **L. Basyrova**, P. Loiko, A. Benayad, G. Brasse, J.-L. Doualan, A. Braud, A. Hideur, and P. Camy, "Growth and mid-infrared emission properties of "mixed" fluorite-type $Er:(Ca,Sr)F_2$ and $Er:(Ba,Sr)F_2$ crystals," EOSAM 2022, 12-18 September 2022, Porto, Portugal, Oral presentation.

French national conferences

1. **L. Basyrova**, P. Loiko, G. Brasse, A. Benayad, J.-L. Doualan, A. Braud, and P. Camy, "Liquid Phase Epitaxy Growth and Spectroscopy of Er^{3+}-doped $LiYF_4$ Thin Films for ~2.7 μm Waveguide Lasers, " in Optique DIJON 2021 conference, organized by SFO, 5-9 July 2021, Dijon, France, upgraded to Oral presentation.
2. **L. Basyrova**, P. Loiko, A. Benayad, G. Brasse, J.-L. Doualan, A. Braud, A. Hideur and P. Camy, "Mid-infrared emission properties of $Er:MF_2$ (M = Ca, Sr, Ba) fluorite-type crystals: A comparative study," Optique NICE 2022, 24-8 July 2022, Nice, France, Oral presentation.

References

[Abe77] J.S. Abell, I.R. Harris, and B. Cockayne, "A study of the $LiYF_4$-$LiErF_4$ psuedo-binary system," *Journal of Materials Science*, 12, 670-674 (1977).

[Ale12] V.V Alexander, O.P. Kulkarni, M. Kumar, C. Xia, M.N. Islam, F.L. Terry Jr, M.J. Welsh, K. Ke, M.J. Freeman, M. Neelakandan, and A. Chan, "Modulation instability initiated high power all-fiber supercontinuum lasers and their applications," *Optical Fiber Technology*, 18(5), 349-374 (2012).

[All97] T.H. Allik, S. Chandra, D.M. Rines, P.G. Schunemann, J.A. Hutchinson, R. Utano, "Tunable 7–12-μm optical parametric oscillator using a Cr,Er:YSGG laser to pump CdSe and $ZnGeP_2$ crystals," *Optics Letters*, 22, 597–599 (1997).

[And03] K. Anduleit and G. Materlik, "A holographic approach to point defect structure determination in inorganic crystals: Er-doped Sc_2O_3. Acta Crystallographica Section A," *Foundations of Crystallography*, 59(2), 138-142 (2003).

[Amb00] P. F. Ambrico, A. Amodeo, P. Di Girolamo, and N. Spinelli, "Sensitivity analysis of differential absorption lidar measurements in the mid-infrared region," *Applied Optics*, 39, 6847-6865 (2000).

[Aul82] B. F. Aull and H. P. Jenssen, "Vibronic interactions in Nd:YAG resulting in nonreciprocity of absorption and stimulated emission cross sections," *IEEE Journal of Quantum Electronics*, 18(5), 925-930 (1982).

[Bak12] C. Baker, W. Kim, J. Sanghera, R. Goswami, G. Villalobos, B. Sadowski, and I. Aggarwal, "Flame spray synthesis of Lu_2O_3 nanoparticles," *Materials Letters*, 66(1) 132-134 (2012).

[Bag83] K.S Bagdasarov, V.I Zhekov, V.A. Lobachev, T.M Murina, and A.M. Prokhorov, "Steady-State Emission from a $Y_3Al_5O_{12}$: Er^{3+} Laser (λ= 2.94 μ, T= 300 K)," *Soviet Journal of Quantum Electronics*, 13(2), 262 (1983).

[Bal20] S. Balabanov, K. Demidova, S. Filofeev, M. Ivanov, D. Kuznetsov, J.Li, D. Permin, and E. Rostokina, "Influence of Lanthanum Concentration on Microstructure of $(Ho_{1-x}La_x)_2O_3$ Magneto-Optical Ceramics," *Physica status solidi (b)*, 257(8), 1900500 (2020).

[Bal21] S. Balabanov, D. Permin, T. Evstropov, P. Andreev, L. Basyrova, P. Camy, M. Baranov, X. Mateos, and P. Loiko, "Hot pressing of Yb:Y_2O_3 laser ceramics with LiF sintering aid," *Optical Materials*, 119:111349 (2021).

[Bar80] N.P. Barnes, D.J. Gettemy, "Temperature variation of the refractive indices of yttrium lithium fluoride," *Journal of the Optical Society of America*, 70 1244-1247 (1980).

[Bas06] T.T. Basiev, Y.V. Orlovskii, M.V. Polyachenkova, P.P. Fedorov, S.V. Kuznetsov, V.A. Konyushkin, V.V. Osiko, O.K. Alimov, and A.Y. Dergachev, "Continuously tunable cw lasing near 2.75 µm in diode-pumped $Er^{3+}:SrF_2$ and $Er^{3+}:CaF_2$ crystals," *Quantum Electronics*, 36(7), 591–594 (2006).

[Bas19] L. Basyrova, R. Maksimov, V. Shitov, M. Baranov, V. Mikhaylovsky, A. Khubetsov, O. Dymshits, X. Mateos, and P. Loiko, "Effect of SiO_2 addition on structural and optical properties of Yb: $Lu_3Al_5O_{12}$ transparent ceramics based on laser ablated nanopowders," *Journal of Alloys and Compounds*, 806, 717-725 (2019).

[Bas21a] L. Basyrova, P. Loiko, W. Jing, Y.C. Wang, H. Huang, E. Dunina, A. Kornienko, L. Fomicheva, B. Viana, U. Griebner, V. Petrov, M. Aguilo, F. Diaz, X. Mateos, and P. Camy, "Spectroscopy and efficient laser operation around 2.8 µm of $Er:(Lu,Sc)_2O_3$ sesquioxide ceramics," *Journal of Luminescence*, 240, 118373 (2021).

[Bas21b] L. Basyrova, P. Loiko, J.-L. Doualan, A. Benayad, A. Braud, C. Labbé, and P. Camy, "$Er:KY_3F_{10}$ laser at 2.80 µm," *Optics Letters*, 46, 5739-5742 (2021).

[Bas22a] L. Basyrova, P. Loiko, R. Maksimov, V. Shitov, J. Doualan, A. Braud, A. Hideur, B. Viana, and P. Camy, "Spectroscopy and Mid-Infrared Laser Operation of “Mixed” Sesquioxide Ceramics $Er:(Y,Sc)_2O_3$," Conference on Lasers and Electro-Optics, Technical Digest Series (Optica Publishing Group, 2022), paper SF1D.3.

[Bas22b] L. Basyrova, P. Loiko, S. Balabanov, D. Permin, S. Filofeev, T. Evstropov, J.L. Doualan, A. Braud, and P. Camy, "Mid-Infrared Laser Operation of Transparent Ceramic $(Er_{0.07}La_{0.10}Y_{0.83})_2O_3$," International Conference Laser Optics (ICLO), Saint Petersburg, Russian Federation, 1-1, (2022).

[Bas22c] L. Basyrova, P. Loiko, J.-L. Doualan, A. Benayad, A. Braud, B. Viana, and P. Camy, "Thermal lensing, heat loading and power scaling of mid-infrared $Er:CaF_2$ lasers," *Optics Express*, 30, 8092-8103 (2022).

[Bau91] L.E. Bausa, R. Legros and A. Muñoz-Yagüe, "Effect of Nd^{3+} concentration on the eission spectra of $CaF_2:Nd$ layers grown by molecular-beam epitaxy," *Journal of Applied Physics*, 70(8), 4485-4489 (1991).

[Bee52] Beer, "Bestimmung der Absorption des rothen Lichts in farbigen Flüssigkeiten," *Annalen der Physik*, 162, 78-88 (1852).

[Bel05] M. Beltram and B. Drnovsek-Olup, "New collagen synthesis in skin fibroblasts after Er:YAG laser skin resurfacing," *Lasers in surgery and medicine*, 17, 33 (2005).

[Ber11] E. H. Bernhardi, H. A. G. M. van Wolferen, K. Wörhoff, R. M. de Ridder and M. Pollnau, "Highly efficient, low-threshold monolithic distributed-Bragg-reflector channel waveguide laser in $Al_2O_3:Yb^{3+}$," *Optics Letters,* 36(5), 603–605 (2011).

[Bez97] D. F. Bezuidenhout, Handbook of optical constants of solids (Academic Press, 1997).

[Bla08] J. Blanusa, N. Jovic, T. Dzomic, B. Antic, A. Kremenovic, M. Mitric, and V. Spasojevic, "Magnetic susceptibility and ordering of Yb and Er in phosphors Yb, Er: Lu_2O_3," *Optical Materials*, 30(7), 1153-1156 (2008).

[Bol12] W. Bolanos, F. Starecki, A. Benayad, G. Brasse, V. M enard, J.-L. Doualan, A. Braud, R. Moncorg ́e and P. Camy, "Tm:$LiYF_4$ planar waveguide laser at 1.9 µm," *Optics Letters*, 37 (2012) 4032–4034, (2012).

[Bol13] W. Bolanos, F. Starecki, A. Braud, J.-L. Doualan, R. Moncorge and P. Camy, "2.8 W end- pumped $Yb^{3+}:LiYF_4$ waveguide laser," *Optics Letters*, 38 5377–5380 (2013).

[Bow90] S. Bowman, W. Rabinovich, A. Bowman, B. Feldman, and G. Rosenblatt, "3µm laser performance of Ho:$YAlO_3$ and Nd, Ho:$YAlO_3$," *IEEE Journal of Quantum Electronics*, 26, 403 (1990).

[Bra19] G. Brasse, P. Loiko, C. Grygiel, P. Leprince, A. Benayad, F. Lemarie, J.L. Doualan, A. Braud and P. Camy, "Liquid Phase Epitaxy growth of Tm^{3+}-doped CaF_2 thin-films based on LiF solvent," *Journal of Alloys and Compounds*, 803, 442-449 (2019).

[Bra21] G. Brasse, P. Loiko, C. Grygiel, A. Benayad, F. Lemarie, V. Zakharov, A. Veniaminov, J.L. Doualan, A. Braud, and P. Camy, "Liquid Phase Epitaxy growth, structure and spectroscopy of highly-doped 20 at.% $Yb^{3+}:LiYF_4$ thin films," *Journal of Luminescence*, 236, 118071 (2021).

[Bud00] P.A. Budni, L.A. Pometanz, M.L. Lemons, C.A. Miller, J.R. Mosto and E.P. Chicklis, "Efficient mid-infrared laser using 1.9-µm-pumped Ho:YAG and $ZnGeP_2$ optical parametric oscillators," *Journal of Optical Society of America*, 17, 723–8 (2000).

[Bur72] A.I. Burstein, "Hopping mechanism of energy transfer," *Journal of Experimental and Theoretical Physics* 35, 882–885 (1972).

[Can08] H. Cankaya, U. Demirbas, A.K. Erdamar, and A. Sennaroglu, "Absorption saturation analysis of Cr^{2+}:ZnSe and Fe^{2+}:ZnSe," *Journal of the Optical Society of America B*, 25(5), 794-800 (2008).

[Cap07] P. Capper and M.G. Mauk, "Liquid Phase Epitaxy of Electronic," *Optical and Optoelectronic Materials*, (2007).

[Cap17] P. Capper, "Bulk crystal growth: methods and materials," S*pringer Handbook of Electronic and Photonic Materials* (2017).

[Car62] W.T. Carnall, P.R. Fields and K. Rajnak, "Electronic energy levels in the trivalent lanthanide aquo ions. I. Pr^{3+}, Nd^{3+}, Pm^{3+}, Sm^{3+}, Dy^{3+}, Ho^{3+}, Er^{3+}, and Tm^{3+}," *Journal of Chemical Physics*, 49(10), 4424-4442 (1968).

[Car68] W.T. Carnall, P.R. Fields and K. Rajnak, "Electronic energy levels in the trivalent lanthanide aquo ions. I. Pr^{3+}, Nd^{3+}, Pm^{3+}, Sm^{3+}, Dy^{3+}, Ho^{3+}, Er^{3+}, and Tm^{3+}," *The Journal of chemical physics*, 49(10), 4424-4442 (1968).

[Cha82] N.C. Chang, J.B. Gruber, R.P. Leavitt and C.A. Morrison, "Optical spectra, energy levels, and crystal-field analysis of tripositive rare earth ions in Y_2O_3. I. Kramers ions in C 2 sites," *The Journal of Chemical Physics*, 76(8), 3877-3889 (1982).

[Che13] C.K. Chen, N.J. Chang, J.H. Ke, E. Fu, W.H. Lan, "Er: YAG laser application for removal of keratosis using topical anesthesia," *Journal of Dental Sciences*, 8(2):196-9 (2013).

[Che20] M. Chen, P. Loiko, J. M. Serres, S. Veronesi, M. Tonelli, M. Aguiló, F. Díaz, S. Y. Choi, J. E. Bae, F. Rotermund, S. Dai, Z. Chen, U. Griebner, V. Petrov and X. Mateos, "Fluorite-type Tm^{3+}:KY_3F_{10}: A promising crystal for watt-level lasers at ~1.9 µm," *Journal of Alloys and Compounds*, 813, 152176 (2020).

[Che99] D.-W. Chen, C.L. Fincher, T.S. Rose, F.L. Vernon and R. A. Fields, "Diode-pumped 1-W continuous-wave Er:YAG 3-µm laser," *Optics Letters*, 24, 385-387 (1999).

[Cho89a] H. Chou, P. Albers, A. Cassanho and H.P. Jenssen, "CW Tunable laser emission of Nd^{3+}: $Na_5Y_9F_{32}$," *MIT laboratory*, 22 (1989).

[Cho89b] H. Chou and H. P. Jenssen, "Upconversion processes in Er-activated solid state laser materials," in Tunable Solid State Lasers (OSA Proceedings Series, Vol. 5), M. L. Shand and H. P. Jenssen, Eds. Washington, DC: Optical Society of America, 167–174 (1989).

[Cre08] D. Creeden, P.A. Ketteridge, P.A. Budni, S.D. Setzler, Y.E. Young, J.C. McCarthy, K. Zawilski, P.G. Schunemann, T.M. Pollak, E.P. Chicklis, and M. Jiang, "Mid-infrared $ZnGeP_2$ parametric oscillator directly pumped by a pulsed 2 µm Tm-doped fiber laser," *Optics Letters* 33, 315-317 (2008).

[Cra15] S. Crawford, D. D. Hudson and S. D. Jackson, "High-Power Broadly Tunable 3-μm Fiber Laser for the Measurement of Optical Fiber Loss," *IEEE Photonics Journal*, 7(3), 1-9, (2015).

[Dam66] T.C. Damen, S.P.S. Porto, and B. Tell, "Raman effect in zinc oxide," *Physical Review,* 142, 570-574 (1966).

[Dar93] E. Daran, L.E. Bausa, A. Muñoz-Yagüe and C. Fontaine, "Er^{3+} doping of CaF_2 layers grown by molecular beam epitaxy," *Applied physics letters*, 62(21), 2616-2618 (1993).

[Dar94] E. Daran, R. Legros, A. Muñoz-Yagüe, C. Fontaine, and LE.Bausá, "Effect of growth temperature and doping concentration on the distribution of the emitting centers in CaF_2:Er molecular beam epitaxial layers," *Journal of Applied Physics*, 75(6), 2749-2752 (1994).

[Den18] B. Denker, V. Dorofeev, B. Galagan, Y. Korostelin, V. Kozlovsky, S. Motorin, and S. Sverchkov, "Short pulse formation in a 2.3 μm Tm-doped tellurite glass laser by an Fe^{2+}: ZnS saturable absorber," *Laser Physics Letters*, 15(10), 105801 (2018).

[Dep06] B. Depuydt, A. Theuwis and I.Romandic, "Germanium: From the first application of Czochralski crystal growth to large diameter dislocation-free wafers," *Materials Science in Semiconductor Processing*, 9(4-5) 437-443 (2006).

[Der00] A.Y. Dergachev, J.H. Flint, and P.F. Moulton, "1.8-W CW Er:YLF diode-pumped laser," in Conference on Lasers and Electro-Optics, S. Brueck, R. Fields, M. Fejer, and F. Leonberger, eds., OSA Technical Digest (Optical Society of America, 2000), paper CFA2.

[Der08] A. Dergachev, D. Armstrong, A. Smith, T. Drake and M. Dubois, "High-power, high-energy ZGP OPA pumped by a 2.05-um Ho: YLF MOPA system," In Nonlinear Frequency Generation and Conversion: Materials, Devices, and Applications VII (Vol. 6875, pp. 40-49). SPIE. (2008).

[Dev06] J. Devenson, D. Barate, O. Cathabard, R. Teissier and A.N. Baranov, "Very short wavelength (λ=3.1 - 3.3 μm) quantum cascade lasers," *Applied Physics Letters*, 89, 191115, (2006).

[Dia00] M. Diaf, A. Braud, C. Labbé, J.L. Doualan, S. Girard, J. Margerie, R. Moncorgé and M. Thuau, "Synthesis and spectroscopic studies of Tm^{3+}-doped KY_3F_{10} single crystals," *Canadian Journal of Physics*, 77(9), 693-697 (2000).

[Die96] A. Diening, T. Jensen and G. Huber, "Emission cross section measurements in the 3μm spectral range of Er: YLF," in *European Quantum Electronics Conference*. *Optica Publishing Group*, QWD10 (1996).

[Die98] A. Diening, E.A. Möbert, E. Heumann, G. Huber and B.H.T. Chai, "Diode-pumped cw lasing of Yb, Ho:KYF_4 in the 3 µm spectral range in comparison to Er:KYF_4," *Laser Physics*, 8, 214 (1998).

[Din22] M. Ding X. Li, F. Wang, D. Shen, J. Wang, D.Tang, and H. Zhu, "Power scaling of diode-pumped Er:Y_2O*3* ceramic laser at 2.7 µm," *Applied Physics Express*, 15(6), (2022).

[Din94] Bradley J. Dinerman, and Peter F. Moulton, "3-µm cw laser operations in erbium-doped YSGG, GGG, and YAG," *Optics Letters*, 19, 1143-1145 (1994).

[Dje97] N. Djeu, V.E. Hartwell, A.A. Kaminskii and A.V. Butashin, "Room temperature 3.4 µm Dy:$BaYb_2F_8$ laser," *Optics Letters*, 22, 997 (1997).

[Dor09] M.E. Doroshenko, H. Jelínkov´a, P. Koranda, J. ˇSulc, T.T. Basiev, V.V. Osiko, V.K. Komar, A.S. Gerasimenko, V.M. Puzikov, V.V. Badikov and D.V. Badikov, "Tunable mid-infrared laser properties of Cr^{2+}:ZnMgSe and Fe^{2+}:ZnSe crystals," *Laser Physics Letters*, 7 38–45 (2009).

[Dor16] A.E. Dormidonov, K.N. Firsov, E.M. Gavrishchuk, V.B. Ikonnikov, S.Yu. Kazantsev, I.G. Kononov, T.V. Kotereva, D.V. Savin and N.A. Timofeeva, "High-efficiency room-temperature ZnSe:Fe^{2+} laser with a high pulsed radiation energy," *Applied Physics B*, 122(8), 211 (2016). [CrossRef]

[Dou10] J. L. Doualan, P. Camy, A. Benayad, V. Ménard, R. Moncorgé, J. Boudeile, F. Druon, F. Balembois and P. Georges, "Yb^{3+} doped (Ca,Sr,Ba)F_2 for high power laser applications," *Laser Physics*, 20(2), 533–536 (2010).

[Dud10] J.M. Dudley and J.R. Taylor, eds., "Supercontinuum generation in optical fibers," *Cambridge University Press* (2010).

[Ehr17] G. Ehret, P. Bousquet, C. Pierangelo, M. Alpers, B. Millet, J.B. Abshire, H. Bovensmann, J.P. Burrows, F. Chevallier, P. Ciais, C. Crevoisier, A. Fix, P. Flamant, C. Frankenberg, F. Gibert, B. Heim, M. Heimann, S. Houweling, H.W. Hubberten, P. Jöckel, K. Law, A. Löw, J. Marshall, A. Agusti-Panareda, S. Payan, C. Prigent, P. Rairoux, T. Sachs, M. Scholze and M. Wirth, "MERLIN: A French-German Space Lidar Mission Dedicated to Atmospheric Methane," *Remote Sensing*, 9(10), 1052 (2017).

[Eld10] I. Elder, "Performance requirements for countermeasures lasers," Proc. SPIE 7836, Technologies for Optical Countermeasures VII, 783605 (2010).

[Epi12] T. Epicier, G. Boulon, W. Zhao, M. Guzik, B. Jiang, A. Ikesue and L. Esposito, "Spatial distribution of the Yb^{3+} rare earth ions in $Y_3Al_5O_{12}$ and Y_2O_3 optical ceramics as analyzed by TEM," *Journal of Materials Chemistry*, 22(35), 18221-18229 (2012).

[Eva12] J.W. Evans, P.A. Berry and K.L. Schepler, "840 mW continuous-wave Fe:ZnSe laser operating at 4140 nm," *Optics Letters*, 37(23), 5021–5023 (2012).

[Eva15] J.W. Evans, T. Sanamyan and P.A. Berrya, "A continuous-wave Fe:ZnSe laser pumped by an efficient Er:Y_2O_3 laser," *Proceedings of SPIE*, 9342, 93420F (2015).

[Fir15] K.N. Firsov, E.M. Gavrishchuk, V.B. Ikonnikov, S.Y. Kazantsev, I.G. Kononov, S.A. Rodin, D.V. Savin and N.A. Timofeeva, "High-energy room-temperature Fe^{2+}:ZnS laser," *Laser Physics Letters*. 13, 015001-1-7 (2015).

[Ike08] A. Ikesue and Y. Aung, "Ceramic laser materials," *Nature Photonics*, 2, 721–727 (2008).

[Jay89] C.K. Jayasankar, M.F. Reid, and F.S Richardson, "Comparative Crystal-Field Analyses of $4f^N$ Energy Levels in $LiYF_4$:Ln^{3+} Systems," *phys. stat. sol. (b)*, 155, 559-569 (1989).

[Jel15] H. Jelínková, M.E. Doroshenko, M. Jelínek, J. Šulc, M. Němec, V. Kubeček, Y.A. Zagoruiko, N.O. Kovalenko, A.S. Gerasimenko, V.M. Puzikov, and V.K. Komar, "Fe:ZnSe and Fe:ZnMgSe lasers pumped by Er:YSGG radiation," Proceedings of SPIE 9342, Solid State Lasers XXIV: Technology and Devices, 93421V, (2015).

[Fan16] M. Fan, T. Li, S. Zhao, G. Li, X. Gao, K. Yang, D. Li, and C. Kränkel, "Multilayer black phosphorus as saturable absorber for an Er:Lu_2O_3 laser at ∼3 μm," *Photonics Research*, 4, 181-186 (2016).

[Fan18] M. Fan, T. Li, J. Zhao, S. Zhao, G. Li, K. Yang, L. Su, H. Ma, and C. Kränkel, "Continuous wave and ReS_2 passively Q-switched Er : SrF_2 laser at ∼3 μm," *Optics Letters*, 43, 1726-1729 (2018).

[Fat16] B. Fatou, P. Saudemont, E. Leblanc, D. Vinatier, V. Mesdag, M. Wisztorski, C. Focsa, M. Salzet, M. Ziskind and I. Fournier, "In vivo Real-Time Mass Spectrometry for Guided Surgery Application," *Scientific Reports* (2016).

[Fat84] R.W. Fathauer and L.J. Schowalter, "Surface morphology of epitaxial CaF_2 films on Si substrates," *Applied Physics Letters*, 45, 519–521 (1984).

[Fed02] P.P. Fedorov, B.P. Sobolev, L.V. Medvedeva, and B.M. Reiterov, "Revised phase diagrams of LiF-RF_3 (R = La-Lu, Y) systems," in *Growth of Crystals*, 21 (Springer, Boston, MA), 141-154 (2002).

[Fed05] P.P. Fedorov, I.I. Buchinskaya, N.A. Ivanovskaya, V.V. Konovalova, S.V. Lavrishchev and B.P. Sobolev, "CaF_2-BaF_2 phase diagram," *Doklady Physical Chemistry*, 401(4-6), 53–55 (2005).

[Fed06] V.V. Fedorov, S.B. Mirov, A. Gallian, D.V. Badikov, M.P. Frolov, Y.V. Korostelin, V.I. Kozlovsky, A.I. Landman, Y.P. Podmar'kov, V.A. Akimov, and A.A. Voronov, "3.77-5.05-µm tunable solid-state lasers based on Fe^{2+}-doped ZnSe crystals operating at low and room temperatures," *IEEE Journal of Quantum Electronics*, 42(9), 907-917 (2006).

[Fed79] P. P. Fedorov, B. P. Sobolev, and S. F. Belov, "Fusibility diagram of the system NaF – YF_3 and the cross section $Na_{0.4}Y_{0.5}F_{2.2}$ YOF," *Izvestiya Akademii nauk SSSR, Neorganicheskiye materialy*, 15(5), 816-819 (1979).

[Fen73] J. B. Fenn, J. C. Wright, and F. K. Fong, "Optical study of ion-defect clustering in CaF_2:Er^{3+}," *Journal of Chemical Physics* 59(10), 5591-5599 (1973).

[Fer99] .B. Ferrand, B. Chambaz, and M. Couchaud, "Liquid phase epitaxy: A versatile technique for the development of miniature optical components in single crystal dielectric media," *Optical Materials*, 11(2–3), 101–114 (1999).

[Fin66] D. Findlay, and R.A. Clay, "The measurement of internal losses in 4-level lasers," *Physics Letters*, 20(3), 277-278 (1966).

[For00] L. Fornasiero, E. Mix, V. Peters, K. Petermann and G. Huber, "Czochralski growth and laser parameters of RE^{3+}-doped Y_2O_3 and Sc_2O_3," *Ceramics International*, 26(6), 589-592 (2000).

[For19] V. Fortin, F. Jobin, M. Larose, M. Bernier, and R. Vallée, "10-w-level monolithic dysprosium-doped fiber laser at 3.24 µm," *Optics Letters*, 44(3), 491–494 (2019).

[Fra09] K. Franjic, M.L. Cowan, D. Kraemer and R.J. Miller, "Laser selective cutting of biological tissues by impulsive heat deposition through ultrafast vibrational excitations," *Optics Express*, 17, 22937–22959 51 (2009).

[Hei13] A.M. Heidt, J.H.V. Price, C. Baskiotis, J.S. Feehan, Z. Li, S.U. Alam, and D.J. Richardson, "Mid-infrared ZBLAN fiber supercontinuum source using picosecond diode-pumping at 2 µm," *Optics express*, 21(20), 24281-24287, (2013).

[Gao21] Q. Gao, Y. Chen, Y. He, H. Yuan, J. Zhou, W. Yao, S. Liu, Y. Zhang, H. Zhang, and Y. Zhao, "Spectroscopy and 2.8 µm laser operation of Er^{3+}-doped (Lu, Y, Sc)-mixed garnet crystal," (2021).

[Gar93] E. Garcia and R.R. Ryan, "Structure of the laser host material $LiYF_4$," *Acta Crystallographica Section C: Crystal Structure Communications*, 2053-2054 (1993).

[Gau15] J.C. Gauthier, V. Fortin, S. Duval, R. Vallée, and M. Bernier, "In-amplifier mid-infrared supercontinuum generation," *Optics Letters*, 40, 5247-5250 (2015).

[Gau18] J.C. Gauthier, L.R. Robichaud, V. Fortin, R. Vallée, and M. Bernier, "Mid-infrared supercontinuum generation in fluoride fiber amplifiers: current status and future perspectives," *Applied Physics B*, 124, 122 (2018).

[Gee66] R. Gee, D.C. O'Shea, and H.Z. Cummins, "Raman scattering and fluorescence in calcium fluoride," *Solid State Communications*, 4, 43-46 (1966).

[Geo91] S. Georgescu, V. Lupei, A. Lupei, V.I. Zhekov, T.M. Murina and M.I. Studenikin, "Concentration effects on the up-conversion from the 4I13/2 level of Er^{3+} in YAG," *Optics Communications*, 81(3-4), 186-192 (1991).

[Ges10] D. Geskus, S. Aravazhi, C. Grivas, K. Wörhoff, and M. Pollnau, "Microstructured $KY(WO_4)_2$:Gd^{3+}, Lu^{3+}, Yb^{3+} channel waveguide laser," *Optics Express*, 18(9), 8853–8858 (2010).

[Ghe08] C. Gheorghe, S. Georgescu, V. Lupei, A. Lupei and A. Ikesue, "Absorption intensities and emission cross section of Er^{3+} in Sc_2O_3 transparent ceramics," *Journal of Applied Physics*, 103(8) (2008).

[Gil17] A.S. Gilbert, "Encyclopedia of Spectroscopy and Spectrometry. Elsevier," Amsterdam, NY, USA: 2017. Vibrational, Rotational and Raman Spectroscopy, Historical Perspective; 600–609

[Gra16] J. A. Grant-Jacob, S. J. Beecher, T. L. Parsonage, P. Hua, J. I. Mackenzie, D. P. Shepherd, and R. W. Eason, "An 11.5 W Yb:YAG planar waveguide laser fabricated via pulsed laser deposition," *Optics Material Express* 6(1), 91–96 (2016).

[Gru08] J.B. Gruber, K. L. Nash, D. K. Sardar, U. V. Valiev, N. Ter-Gabrielyan, and L. D. Merkle, "Modeling optical transitions of Er^{3+} ($^4f_{11}$) in C_2 and C_{3i} sites in polycrystalline Y_2O_3," *Journal of Applied Physics,* 104(2), 023101-023101 (2008).

[Gru85] J.B. Gruber, J.R. Quagliano, M.F. Reid, F.S. Richardson, M.F. Hills, V.D. Seltzer, S.B. Stevens, C.A. Morrison and T.H. Alik, "Energy levels and correlation crystal-field effects in Er^{3+}-doped garnets,” *Physical Review B*, 48, 15561-15573 (1993).

[Gui20] L. Guillemot, P. Loiko, R. Soulard, A. Braud, J.-L. Doualan, A. Hideur and P. Camy, "Close look on cubic Tm:KY_3F_{10} crystal for highly efficient lasing on the $^3H_4 \rightarrow {}^3H^5$ transition," *Optics Express* 28, 3451-3463 (2020).

[Gui21] L. Guillemot, "Etude de la transition 3H4 → 3H5 de l'ion Tm3+ pour une émission laser moyen infrarouge (entre 2 et 3µm)," (Doctoral dissertation, Université de Caen Normandie) (2021).

[Guo07] Q. Guo, Y. Zhao, C. Jiang, W.L. Mao, Z. Wang, J. Zhang and Y. Wang, "Pressure-induced cubic to monoclinic phase transformation in erbium sesquioxide Er_2O_3," *Inorganic chemistry*, 46(15), 6164-6169 (2017).

[Guz14] M. Guzik, J. Pejchal, A. Yoshikawa, A. Ito, T. Goto, M. Siczek, T. Lis and G. Boulon, "Structural investigations of Lu_2O_3 as single crystal and polycrystalline transparent ceramic," *Crystal growth & design*, 14(7), pp.3327-3334 (2014).

[Hen89] B. Henderson, G.F. Imbusch, "Optical Spectroscopy of Inorganic Solids," Oxford University Press, Oxford, (1989).

[Heu18] A.M. Heuer, P. von Brunn, G. Huber, and C. Kränkel, "Growth and mid-infrared continuous wave laser action of Er^{3+}:Sc_2O_3," 8th EPS-QEOD Europhoton Conference, poster 24.22 (2018).

[Hoh97] U. Hohenleutner, S. Hohenleutner, W. Bäumler and M. Landthaler, "Fast and effective skin ablation with an Er: YAG laser: determination of ablation rates and thermal damage zones," Lasers in Surgery and Medicine, 20(3), 242-7 (1997).

[Hou11] X. Hou, S. Zhou, T. Jia, H. Lin, H. Teng, "Structural, thermal and mechanical properties of transparent Yb:$(Y_{0.97}Zr_{0.03})_2O_3$ ceramic," *Journal of the European Ceramic Society*, 31(5), 733-738 (2011).

[Hou23] W. Hou, Y. Xue, Z. Qin, H. Tang, G. Xie, Q. Wang, X. Xu and J. Xu, "Efficient continuous wave and passively Q switched Er:$GdScO_3$ laser using Fe:ZnSe at 2.8 µm," *Optics Letters*, 48, 2118-2121 (2023).

[Hu19] Q. Hu, H. Nie, W. Mu, Y. Yin, J. Zhang, B. Zhang, J. He, Z. Jia and X. Tao, "Bulk growth and an efficient mid-IR laser of high-quality Er:YSGG crystals," *CrystEngComm*, 21 (2019).

[Hul21] L. Hülshoff, A. Uvarova, C. Guguschev, S. Kalusniak, H. Tanaka, D. Klimm, and C. Kränkel, "Czochralski growth and laser operation of Er- and Yb-doped mixed sesquioxide crystals," Laser Congress 2021 (ASSL,LAC), (Optica Publishing Group, 2021), ATh1A.2.

[Ino65] M. Inokuti, F. Hirayama, "Influence of energy transfer by the exchange mechanism on donor luminescence," *The journal of chemical physics*, *43*(6), 1978-1989, (1965).

[Ish11] A. Ishida, Y. Sugiyama, Y. Isaji, K. Kodama, Y. Takano, H. Sakata, M. Rahim, A. Khiar, M. Fill, F. Felder, and H. Zogg, "2 W high efficiency PbS mid-infrared surface emitting laser," Applied Physics Letters, 99, 121109 (2011).

[Iva14] M. Ivanov, Y. Kopylov, V. Kravchenko, L.I. Jiang, A. Medvedev, and P.A.N Yubai, "Highly transparent ytterbium doped yttrium lanthanum oxide ceramics," *Journal of Rare Earths*, 32(3), pp.254-258 (2014).

[Jen96] T. Jensen, A. Diening, G. Huber, and B.H.T. Chai, "Investigation of diode-pumped 2.8-µm Er:LiYF$_4$ lasers with various doping levels," *Optics Letters*, 21, 585-587 (1996).

[Jin17] W. Jing, P. Loiko, J.M. Serres, Y. Wang, E. Vilejshikova, M. Aguiló, F. Díaz, U. Griebner, H. Huang, V. Petrov and X. Mateos, "Synthesis, spectroscopy, and efficient laser operation of “mixed” sesquioxide Tm:(Lu,Sc)$_2$O$_3$ transparent ceramics," *Optical Material Express*, 7, 4192-4202 (2017).

[Jin18] W. Jing, P. Loiko, J.M. Serres, Y. Wang, E. Kifle, E. Vilejshikova, M. Aguiló, F. Díaz, U. Griebner, H. Huang, V. Petrov and X. Mateos, "Synthesis, spectroscopic characterization and laser operation of Ho^{3+} in “mixed” (Lu,Sc)$_2$O$_3$ ceramics," *Journal of Luminescence*. 203, 145-151 (2018).

[Jin21] W. Jing, P. Loiko, L. Basyrova, Y. Wang, H. Huang, P. Camy, U. Griebner, V. Petrov, J.M. Serres, R.M. Sole, M. Aguilo, F. Díaz and X. Mateos, "Spectroscopy and laser operation of highly-doped 10 at.% Yb:(Lu,Sc)$_2$O$_3$ ceramics," *Optical Materials*, 117, 111128-1-7 (2021).

[Joh72] L.F. Johnson and H.J. Guggenheim, "New laser lines in the visible from Er^{3+} ions in BaY$_2$F$_8$," *Applied Physics Letters*, 20, 474–477 (1972).

[Joh73] L.F. Johnson and H.J. Guggenheim, "Laser emission at 3 µm from Dy^{3+} in BaY$_2$F$_8$," *Applied Physics Letters*, 23, 96 (1973).

[Jud62] B. R. Judd, "Optical absorption intensities of rare-earth ions," *Physical Reviews,* 127(3), 750-761 (1962).

[Kam03] A.A. Kaminskii, K. Ueda, A.F. Konstantinova, H. Yagi, T. Yanagitani, A.V. Butashin, V.P. Orekhova, J. Lu, K. Takaichi, T. Uematsu, and M. Musha,. "Lasing and refractive indices of nanocrystalline ceramics of cubic Yttrium Oxide Y$_2$O$_3$ doped with Nd^{3+} and Yb^{3+} ions," *Crystallography Reports*, *48*, pp.1041-1043 (2003).

[Kam13] A.A. Kaminskii, "Laser crystals: their physics and properties," (Springer, 2013).

[Kam96] A. Kaminskii, "Crystalline Lasers: Physical Processes and Operating Schemes (1st ed.)," *CRC Press* (1996).

[Kar21] D.N Karimov, I.I. Buchinskaya, N.A. Arkharova, A.G. Ivanova, A.G. Savelyev, N.I. Sorokin and P.A. Popov, "Growth Peculiarities and Properties of KR_3F_{10} (R = Y, Tb) Single Crystals," *Crystals* 11(3), 285 (2021).

[Kau17] H. Kaushal, V. Jain and S. Kar, Free Space Optical Communication (Springer India), vol. 7 of Optical Networks, chap. 1. (2017).

[Kaz02] S.A. Kazanskii, and A.I. Ryskin, "Group-III Ion Clusters in Activated Fluorite-Like Crystals," *Physics of the Solid State*, 44(8), 1415-1425 (2002).

[Kif19] E. Kifle, P. Loiko, U. Griebner, V. Petrov, P. Camy, A. Braud, M. Aguiló, F. Díaz and X. Mateos, "Diamond saw dicing of thulium channel waveguide lasers in monoclinic crystalline films," *Optics Letters* 44(7), 1596–1599 (2019).

[Kim10] S.S. Kim, C. Young, B. Vidakovic, S.G.A. Gabram-Mendola, C.W. Bayer and B. Mizaikoff, "Potential and Challenges for Mid-Infrared Sensors in Breath Diagnostics," *IEEE Sensors Journal*, 10(1), 145-158 (2010).

[Kim11] W. Kim, C. Baker, G. Villalobos, J. Frantz, B. Shaw, A. Lutz, B. Sadowski F. Kung, M. Hunt, J. Sanghera and I. Aggarwal, "Synthesis of high purity Yb^{3+}-doped Lu_2O_3 powder for high power solid-state lasers," *Journal of the American Ceramic Society,* 94(9), 3001-3005 (2011).

[Kis64] P. Kisliuk, W.F. Krupke and J.B. Gruber, "Spectrum of Er^{3+} in single crystals of Y_2O_3," *Journal of Chemical Physics*, 40 3606-3610 (1964).

[Kli08] D. Klimm, M. Rabe, R. Bertram, R. Uecker and L. Parthier, "Phase diagram analysis and crystal growth of solid solutions $Ca_{1-x}Sr_xF_2$," *Journal of Crystal Growth,* 310(1), 152-155 (2008).

[Kno92] K. Knowles and H.P. Jenssen, "Upconversion versus Pr-deactivation for efficient 3 µm laser operation in Er," *IEEE Journal of Quantum Electronics*, 28(4), 1197 (1992).

[Kom86] G. Kommichau, H. Neumann, W. Schmitz and B. Schumann, "Thermal expansion of SrF_2 at elevated temperatures," *Crystal Research and Technology*, 21(12), 1583-1587 (1986).

[Koo12] P. Koopmann, "Thulium- and holmium-doped sesquioxides for 2 µm lasers," (PhD thesis, Institut für Laser-Physik, Universität Hamburg) (2012).

[Kra15] C. Kränkel, "Rare-earth-doped sesquioxides for diode-pumped high-power lasers in the 1-, 2-, and 3-μm spectral range," *IEEE Journal of Selected Topics in Quantum Electronics*, 21(1), 250-262 (2015).

[Kra21] C. Kränkel, A. Uvarova, É. Haurat, L. Hülshoff, M. Brützam, C. Guguschev, S. Kalusniak, and D. Klimm, "Czochralski growth of mixed cubic sesquioxide crystals in the ternary system Lu_2O_3–Sc_2O_3–Y_2O_3," *Acta Crystallographica Section B: Structural Science, Crystal Engineering and Materials*, *77*(4), pp.550-558 (2021).

[Kra22] C. Kränkel, A. Uvarova, C. Guguschev, S. Kalusniak, L. Hülshoff, H. Tanaka and D. Klimm, "Rare-earth doped mixed sesquioxides for ultrafast lasers [Invited]," *Optical Material Express*, 12, 1074-1091 (2022).

[Kre09] A. Krell, J. Klimke, and T. Hutzler, "Transparent compact ceramics: Inherent physical issues," *Optical Materials*, *31*(8), 1144-1150 (2009).

[Kuz20] S.V. Kuznetsov, V.A. Konyushkin, A.N. Nakladov, E.V. Chernova, P.A. Popov, A.A. Pynenkov, K.N. Nishchev and P.P. Fedorov, “Thermophysical properties of single crystals of CaF_2–SrF_2–RF_3 (R=Ho, Pr) fluorite solid solutions,” *Inorganic Materials*, 56(9), 975–981 (2020).

[Lab00] C. Labbe, J.L. Doualan, S. Girard, R. Moncorgé and M. Thuau, "Absolute excited state absorption cross section measurements in Er^{3+}: $LiYF_4$ for laser applications around 2.8 μm and 551 nm," *Journal of Physics: Condensed Matter*, 12(30), 6943 (2000).

[Lab02] C. Labbe, J.L. Doualan, P. Camy, R. Moncorgé and M. Thuau, "The 2.8 μm laser properties of Er^{3+} doped CaF_2 crystals," *Optics Commuications*, 209(1-3), 193–199 (2002).

[Lab18a] C. Labbé, J.L. Doualan, R. Moncorgé, A. Braud and P. Camy, "Excited-state absorption and fluorescence dynamics of Er^{3+}:KY_3F_{10}," *Optical Materials*, 79, 279-288 (2018).

[Lab18b] C. Labbe, J.L. Doualan, R. Moncorgé, A. Braud and P. Camy, "Excited-state absorption and fluorescence dynamics in Er:CaF_2," *Journal of Luminescence*, 200, 74-80 (2018).

[Lab99] C. Labbe, "Etude par absorption dans les etats excites de l'ion erbium Er^{3+} dans les matrices fluorees applications lasers a 2.8 µm," (Doctoral dissertation, Normandie Université) (1999).

[Lam15] S. Lambert-Girard, M. Allard, M. Piché, and F. Babin, "Differential optical absorption spectroscopy lidar for mid-infrared gaseous measurements," *Applied Optics*, 54, 1647-1656 (2015).

[Lam70] J.H. Lambert, "I.H. Lambert Photometria, sive, De mensura et gradibus luminis, colorum et umbrae [microform]. Augustae Vindelicorum," V.E. Klett, 1728-1777. (1760).

[Lav01] L. Laversenne, Y. Guyot, C. Goutaudier, M.T. Cohen-Adad and G.J.O.M. Boulon, "Optimization of spectroscopic properties of Yb^{3+}-doped refractory sesquioxides: cubic Y_2O_3, Lu_2O_3 and monoclinic Gd_2O_3," *Optical materials*, 16(4), 475-483 (2001).

[Li12] T. Li, K. Beil, C. Kränkel, and G. Huber, "Efficient high-power continuous wave Er:Lu_2O_3 laser at 2.85 µm," *Optics Letters,* 37, 2568-2570 (2012).

[Li16] C. Li, J. Liu, S. Jiang, S. Xu,W. Ma, J.Wang, X. Xu and L. Su, "2.8 µm passively Q-switched Er:CaF_2 diode-pumped laser," *Optical Materials Express*, 6(5), 1570–1575 (2016).

[Li18] Y. Li, D. Lu, Z. Pan, H. Yu, H. Zhang, and J. Wang, "High-efficiency 3 µm Er:YGG crystal lasers," *Optics Letters*, 43, 5873-5876 (2018).

[Li21] E. Li, H.Uehara, W. Yao, S. Tokita, F. Potemkin, and R. Yasuhara, "High-efficiency, continuous-wave Fe:ZnSe mid-IR laser end pumped by an Er:YAP laser," *Optics Express*, 29, 44118-44128 (2021)

[Liu18] J. Liu, X. Feng, X. Fan, Z. Zhang, B. Zhang, J. Liu and L. Su, "Efficient continuous-wave and passive Q-switched mode-locked Er^{3+} : CaF_2–SrF_2 lasers in the mid-infrared region," *Optics Letters*, 43, 2418-2421 (2018).

[Liu19a] J. Liu, F. Zhang, Z. Zhang, J. Liu, H. Zhang and L. Su, "Watt-level continuous-wave and high-repetition-rate mid-infrared lasers based on a Er^{3+}-doped $Ca_{0.8}Sr_{0.2}F_2$ crystal," *Applied Physics Express*, 12, 115505 (2019).

[Liu19b] J. Liu, J. Song, B. Mei, W. Li and S. Wang, "Fabrication and mid-infrared property of Er:CaF_2 transparent ceramics," *Materials Research Bulletin*, 111, 158-164 (2019).

[Loi09] P.A. Loiko, K.V. Yumashev, N.V. Kuleshov, V.G. Savitski, S. Calvez, D. Burns and A.A. Pavlyuk, "Thermal lens study in diode pumped N_g- and N_p-cut Nd:$KGd(WO_4)_2$ laser crystals," *Optics Express;* 17(26), 23536–23543 (2009).

[Loi12] P. Loiko, “Анизотропия оптических свойств кристаллов двойных калий-редкоземельных вольфраматов и термических искажений лазерных элементов на их основе” (Doctoral dissertation, Belarusian National Technical University) (2012).

[Loi17] P. Loiko, S. Manjooran, K. Yumashev and A. Major, "Polarization anisotropy of thermal lens in Yb:$KY(WO_4)_2$ laser crystal under high-power diode pumping," *Applied Optics*, 56(10), 2937–2945 (2017).

[Loi18] P. Loiko, R. Soulard, G. Brasse, J.-L. Doualan, B. Guichardaz, A. Braud, A. Tyazhev, A. Hideur and P. Camy, "Watt-level Tm:LiYF$_4$ channel waveguide laser produced by diamond saw dicing," *Optics Express* 26 24653-24662 (2018).

[Loi18a] P. Loiko, R. Soulard, G. Brasse, J.-L. Doulan, A. Braud, A. Tyazhev, A. Hideur and P. Camy, "Tm Ho, LiYF$_4$ planar waveguide laser at 2.05 μm," *Optics Letters*, 43 4341–4344 (2018).

[Loi19] P. Loiko, R. Soulard, E. Kifle, L. Guillemot, G. Brasse, A. Benayad, J.L. Doualan, A. Braud, M. Aguiló, F. Díaz and X. Mateos, "Ytterbium calcium fluoride waveguide laser," *Optics Express*, 27(9), 12647-12658, (2019).

[Loi21] P. Loiko, G. Brasse, L. Basyrova, A. Benayad, J. L. Doualan, C. Meroni, A. Braud, E. Dunina, A. Kornienko, M. Baranov and D. Gozhalskii and P. Camy, "Spectroscopy of Tm^{3+}-doped CaF$_2$ waveguiding thin films grown by Liquid Phase Epitaxy," *Journal of Luminescence*, 238; 118109 (2021).

[Loi21a] P. Loiko, L. Basyrova, R. Maksimov, V. Shitov, M. Baranov, F. Starecki, X. Mateo and P. Camy, "Comparative study of Ho:Y$_2$O$_3$ and Ho:Y$_3$Al$_5$O$_{12}$ transparent ceramics produced from laser-ablated nanoparticles," *Journal of Luminescence*, 240, 118460 (2021).

[Lu02] J. Lu, K. Takaichi, T. Uematsu, A. Shirakawa, M. Musha, K.I. Ueda, H. Yagi, T. Yanagitani and A.A. Kaminskii, "Yb^{3+}:Y$_2$O$_3$ ceramics–a novel solid-state laser material," *Japanese Journal of Applied Physics*, 41(12A), L1373 (2002).

[Lu03] J. Lu, J.F. Bisson, K. Takaichi, T. Uematsu, A. Shirakawa, M. Musha, K. Ueda, H. Yagi, T. Yanagitani and A.A. Kaminskii, "Yb^{3+}:Sc$_2$O$_3$ ceramic laser," *Applied Physics Letters*, 83(6), 1101-1103 (2003).

[Luk08] M. Lukač, V. Zdenko, M. Kažič and T. Sult, "Novel Fractional Treatments with VSP Erbium YAG Aesthetic Lasers," *Journal of the Laser and Health Academy*, 6(1) (2008).

[Luo19] S. Luo, R. Moncorgé, J.-L. Doualan, H. Xu, Z. Cai, C. Labbé, B. Xu, A. Braud and P. Camy, "Simulation of dual-wavelength pumped 3.5 μm CW laser operation of Er:CaF$_2$ and Er:KY$_3$F$_{10}$ in waveguide configuration," *Journal of Optical Society of America B* 36, 275-284 (2019).

[Luo19a] H. Luo, Y. Xu, J. Li and Y. Liu, "Gain-switched dysprosium fiber laser tunable from 2.8 to 3.1 μm," *Optics Express*, 27(19), 27151–27158 (2019).

[Luo19b] H. Luo, J. Li, Y. Gao, Y. Xu, X. Li and Y. Liu, "Tunable passively Q-switched dy^{3+}-doped fiber laser from 2.71 to 3.08 μm using pbs nanoparticles," *Optics Letters*, 44(9), 2322–2325 (2019).

[Lup08] A. Lupei, V. Lupei, C. Gheorghe and A. Ikesue, "Excited states dynamics of Er^{3+} in Sc_2O_3 ceramic," *Journal of Luminescence*, 128 918-920 (2008).

[Luz15] E. Luzhansky, F.-S. Choa, S. Merritt, A. Yu and M. Krainak, "Mid-IR free-space optical communication with quantum cascade lasers," Proc. SPIE 9465, Laser Radar Technology and Applications XX; and Atmospheric Propagation XII, 946512 (2015).

[Lv15] S. Lv, Y.Wang, Z. Zhu, Z. You, J. Li, H.Wang, C. Tu, "Role of Er^{3+} concentration in spectroscopic and laser performance of $CaYAlO_4$ crystal," *Optical Materials*, 42, (2015).

[Ma16a] W. Ma, L. Su, X. Xu, J. Wang, D. Jiang, L. Zheng, X. Fan, C. Li, J. Liu and J. Xu, "Effect of erbium concentration on spectroscopic properties and 2.79 μm laser performance of Er:CaF_2 crystals," *Optical Materials Express,* 6(2), 409–415(2016).

[Ma16b] W. Ma, X. Qian, J. Wang, J. Liu, X. Fan, J. Liu, L. Su and J. Xu, "Highly efficient dual-wavelength mid-infrared CW laser in diode end-pumped Er:SrF_2 single crystals," *Scientific Reports*, 6(1), 36635 (2016).

[Mac87] J. Machan, R. Kurtz, M. Bass, M. Birnbaum and M. Kokta, "Simultaneous, multiple wavelength lasing of (Ho, Nd):$Y_3Al_5O_{12}$," *Applied Physics Letters*, 51, 1313 (1987).

[Mah07] S.P. Mahulikar, H.R. Sonawane and G. Arvind Rao, "Infrared signature studies of aerospace vehicles," *Progress in Aerospace Sciences*, 43(8), 218–245 (2007).

[Maj18] M.R. Majewski, R.I. Woodward, and S.D. Jackson, "Dysprosium-doped zblan fiber laser tunable from 2.8 μm to 3.4 μm, pumped at 1.7 μm," *Optics Letters*, 43(5), 971–974 (2018).

[Mar17] D.V. Martyshkin, V.V. Fedorov, M. Mirov, I. Moskalev, S. Vasilyev, V. Smolski, A. Zakrevskiy and S.B. Mirov, "High Power (9.2 W) CW 4.15 μm Fe:ZnSe laser," in Conference on Lasers and Electro-Optics, OSA Technical Digest (online) (Optical Society of America, 2017), STh1L.6 (2017).

[McF95] R. A. McFarlane, M. Lui and D. Yap, "Rare earth doped fluoride waveguides fabricated using molecular beam epitaxy," *IEEE Journal of Selected Topics in Quantum Electronics*. 1(1), 82–91 (1995).

[Mes16] M. Messner, A. Heinrich, C. Hagen, and K. Unterrainer, "High brightness diode pumped Er:YAG laser system at 2.94 μm with nearly

1kW peak power", *Proc. SPIE 9726, Solid State Lasers XXV: Technology and Devices*, 972602 (2016).

[Mic16] M. Michalska, J. Mikolajczyk, J. Wojtas and J. Swiderski, "Mid-infrared, super-flat, supercontinuum generation covering the 2–5 µm spectral band using a fluoroindate fibre pumped with picosecond pulses," *Scientific Reports*, 6(1), pp.1-6. (2016).

[Mil70] S.A. Miller, H.E. Rast and H.H. Caspers, "Lattice vibrations of $LiYF_4$," *The Journal of Chemical Physics*, 52, 4172–4175 (1970).

[Mir10] S. Mirov, V. Fedorov, I. Moskalev, D. Martyshkin and C. Kim, "Progress in Cr^{2+} and Fe^{2+} doped mid-IR laser materials," *Laser & Photonics Review*, 4, 21–41 (2010).

[Mir18] S.B. Mirov, I.S. Moskalev, S. Vasilyev, V. Smolski, V.V. Fedorov, D. Martyshkin, J. Peppers, M. Mirov, A. Dergachev and V. Gapontsev, "Frontiers of Mid-IR Lasers Based on Transition Metal Doped Chalcogenides," *IEEE Journal of Selected Topics in Quantum Electronics*, 24(5), 1-29 (2018).

[Mom11] K. Momma and F. Izumi, "VESTA 3 for three-dimensional visualization of crystal, volumetric and morphology data," *Journal of applied crystallography*, 44(6), p1272-1276 (2011).

[Mon13] R. Moncorge, A. Braud, P. Camy and J.L. Doualan, "Fluoride laser crystals," In Handbook of Solid-State Lasers, Woodhead Publishing, 28-53 (2013).

[Moo81] D.S. Moore and J.C. Wright, "Laser spectroscopy of defect chemistry in CaF_2:Er^{3+}," *Journal of Chemical Physics*, 74(3), 1626-1636 (1981).

[Mor91] M. Mortier, J.Y. Gesland, M. Rousseau, M.A. Pimenta, L.O. Ladeira, J. C. Machado da Silva and G. Barbosa, "Raman scattering investigations of KY_3F_{10}," *Journal of Raman Spectroscopy*, 22, 393-396 (1991).

[Mos16] I. Moskalev, S. Mirov, M. Mirov, S. Vasilyev, V. Smolski, A. Zakrevskiy and V. Gapontsev, "140 W Cr:ZnSe laser system," *Optics Express* 24, 21090-21104 (2016).

[Mun06] J.H. Mun, A. Jouini, A. Novoselov, A. Yoshikawa, T. Kasamoto, H. Ohta, H. Shibata, M. Isshiki, Y. Waseda, G. Boulon, and T. Fukuda, Thermal and optical properties of Yb^{3+}-doped Y_2O_3 single crystal grown by the micro-pulling-down method. *Japanese journal of applied physics*, *45*(7R), p.5885 (2006).

[Naf71] R.H. Nafziger, "High-Temperature Phase Relations in the System BaF_2-SrF_2," *Journal of American Ceramic Society,* 54(9), 467-467 (1971).

[Nas61] K. Nassau, "Application of the Czochralski method to divalent metal fluorides," *Journal of Applied Physics*, 32(10), 1820-1821 (1961).

[Nic08] I. Nicoara, M. Munteanu, E. Preda and M. Stef, "Some dielectric and optical properties of ErF_3-doped CaF_2 crystals," *Journal of Crystal Growth*, 310(7–9), 2020-2025 (2008).

[Nie18] H. Nie, B. Shi, H. Xia, J. Hu, B. Zhang, K. Yang and J.L. He, "High repetition-rate kHz electro-optically Q-switched Ho, Pr:YLF 2.9 µm bulk laser," *Optics Express* 26, 33671 (2018).

[Nik05] A.E. Nikiforov, A.Y. Zakharov, M.Y. Ugryumov, S.A. Kazanskii, A.I. Ryskin and G.S. Shakurov, "Crystal fields of hexameric rare-earth clusters in fluorites," *Physics of the Solid State*, 47(8), 1431-1435 (2005).

[Neu86] H. Neumann, G.W. Kommichau, W. Schmitz and B. Schumann, "Thermal expansion of BaF_2 from 296 to 1173 K," *Journal of Material Science Letters*, 5, 1131–1132 (1986).

[New21] G.A. Newburgh, and M. Dubinskii, "Power and efficiency scaling of Er:ZBLAN fiber laser," *Laser Physics Letters*, 18(9), 095102 (2021).

[Nor17] S. Normani, "Nd,Lu:CaF_2 for high-energy lasers," (Doctoral dissertation, Normandie Université) (2017).

[Nor23a] S. Normani, P. Loiko, L. Basyrova, A. Benayad, A. Braud, E. Dunina, L. Fomicheva, A. Kornienko, A. Hideur and P. Camy, "Mid-infrared emission properties of erbium-doped fluorite-type crystals," *Optical Materials Express*, 13, 1836-1851 (2023).

[Nor23b] S. Normani, P. Loiko, Z. Pan, E. Dunina, L. Fomicheva, A.Kornienko, A. Braud, W. Chen, U. Griebner, V. Petrov, and P. Camy, "Spectroscopy and 2.8 µm laser operation of disordered Er:CLNGG crystals," *Optics Letters*, 48, 2567-2570 (2023).

[Nor23c] S. Normani, L. Basyrova, P. Loiko, A. Benayad, A. Braud, A. Hideur and P. Camy, "Mid-infrared laser operation of Er^{3+}-doped BaF_2 and $(Sr,Ba)F_2$ crystals," *Optics Letters*, 48, 431-434 (2023).

[Ofe62] G. S. Ofelt, "Intensities of crystal spectra of rare-earth ions," *Journal of Chemical Physics*, 37(3), 511-520 (1962).

[Osi71] V.V. Osiko and I.A. Shcherbakov, "Calculation of point-defect equilibrium in CaF_2–NdF_3 crystals," *Soviet Physics Solid state*, 13, 820–824 (1971).

[Paj19] L. Pajewski, L. Sójka, S. Lamrini, T.M. Benson, A.B. Seddon and S. Sujecki, "Gain-switched Dy^{3+}: ZBLAN fiber laser operating around 3 µm," J*ournal of Physics: Photonics* 2, 014003 (2019).

[Pan00] J.-C. Panitz, J.-C. Mayor, B. Grob and W. Durisch, "A Raman spectroscopic study of rare earth mixed oxides," *Journal of Alloys and Compounds*, 303, 340-344 (2000).

[Pan06] A. Pandey, A. Pandey, M. K. Roy and H.C. Verma, "Sol–gel synthesis and characterization of Eu^{+++}/Y_2O_3 nanophosphors by an alkoxide precursor," *Materials Chemistry and Physics*, 96(2–3), 466-470 (2006).

[Par20] S. Parker, M. Cronshaw, E. Anagnostaki, V. Mylona, E. Lynch and M. Grootveld, "Current Concepts of Laser – Oral Tissue Interaction," *Dentistry Journal*, 8(3), 61 (2020).

[Pay92] S.A. Payne, L.L. Chase, L.K. Smith, W.L. Kway and W.F. Krupke, "Infrared cross-section measurements for crystals doped with Er^{3+}, Tm^{3+} and Ho^{3+}," *IEEE Journal of Quantum Electronics* 28, 2619-2630 (1992).

[Pet08] V. Petit, P. Camy, J.-L. Doualan, X. Portier and R. Moncorgé, "Spectroscopy of Yb^{3+}:CaF_2: From isolated centers to clusters," *Physical Review B: Condensed Matter and Materials Physics*, 78, 085131 (2008).

[Pet08a] P.O. Petit, J. Petit, P. Goldner, and B. Viana, "Inhomogeneous broadening of optical transitions in Yb: $CaYAlO_4$," *Optical Materials*, *30*(7), pp.1093-1097 (2008).

[Pet11] R. Peters, C. Kränkel, S.T. Fredrich-Thornton, K. Beil, K. Petermann, G. Huber, O.H. Heckl, C.R.E. Baer, C.J. Saraceno, T. Südmeyer and U. Keller, "Thermal analysis and efficient high power continuous-wave and mode-locked thin disk laser operation of Yb-doped sesquioxides," Applied Physics B, 102, 509-514 (2011).

[Per18] D.A. Permin, S.V. Kurashkin, A.V. Novikova, A.P. Savikin, E.M. Gavrishchuk, S.S. Balabanov, N.M. Khamaletdinova, "Synthesis and luminescence properties of Yb-doped Y_2O_3, Sc_2O_3 and Lu_2O_3 solid solutions nanopowders," *Optical Materials,* 77, 240-245 (2018).

[Pet01] W. Petrich "Mid-infrared and Raman spectroscopy for medical diagnostics, " *Applied Spectroscopy Reviews*, 36:2-3, 181-237 (2001).

[Pet21] V. Petrov, V.V. Badikov, D.V. Badikov, K. Kato, G.S. Shevyrdyaeva, K. Miyata, M. Mero, L. Wang, Z. Heiner and V.L. Panyutin, "Barium nonlinear optical crystals for the mid-IR: characterization and some applications," *Journal of Optical Society of America B*, 38, B46-B58 (2021).

[Pic19] N. Picqué and T.W. Hänsch, "Mid-IR Spectroscopic Sensing," Optics & Photonics News, 30(6), 26-33 (2019).

[Pol01] M. Pollnau and S.D. Jackson, "Erbium 3 μm fiber lasers," *IEEE Journal of Selected Topics in Quantum Electronics*, 7(1), 30-40 (2001).

[Pol03] M. Pollnau, "Analysis of heat generation and thermal lensing in erbium 3-µm lasers," *IEEE Journal of Quantum Electronics*, 39(2), 350–357 (2003).

[Pol05] M. Pollnau, "Dynamics of Solid-State Coherent Light Sources: Upconversion Luminescence Dynamics," In Frontiers of Optical Spectroscopy: Investigating Extreme Physical Conditions with Advanced Optical Techniques, Springer Netherlands, 571-589 (2005).

[Pol96] M. Pollnau, W. Lüthy, H.P. Weber, T. Jensen, G. Huber, A. Cassanho, H.P. Jenssen, and R.A. McFarlane, "Investigation of diode-pumped 2.8-µm laser performance in Er:BaY_2F_8," *Optics Letters*, 21, 48-50 (1996).

[Pol97] M. Pollnau, R. Spring, S. Wittwer, W. Luthy and H.P. Weber, "Investigations on the slope efficiency of a pulsed 2.8 µm Er^{3+}:$LiYF_4$ laser," *Journal of the Optical Society of America, Part B: Optical Physics*, 14(4), 974-978 (1997).

[Pon83] L. Pontonnier, S. Ale, J. J. Capponi, M. Brunel and F. de Bergevin, "An approach to the local arrangement of the fluorine atoms in the anionic conductors with the fluorite structure $Na_{0.5-x}Y_{0.5+x}F_{2+2x}$," *Solid State Ionics* 9, 549-553 (1983)

[Pon87] L. Pontonnier, S. Aléonard, M.T. Roux and A. Hammou, "Propriétés électriques des solutions solides à structure fluorine excédentaire en anions $Na_{0.5-x}Y_{0.5+x}F_{2+2x}$," *Journal of Solid State Chemistry* 69(1), 10-18 (1987).

[Pop08] P. A. Popov, P. P. Fedorov, S. V. Kuznetsov, V. A. Konyushkin, V. V. Osiko and T. T. Basiev, "Thermal conductivity of single crystals of $Ca_{1-x}Yb_xF_{2+x}$ solid solutions," *Doklady Physics,* 53(4), 198-200 (2008).

[Pop21] P. A. Popov, A. A. Krugovykh, V. A. Konyushkin, A. N. Nakladov, S. V. Kuznetsov and P. P. Fedorov, "Thermal Conductivity of $Sr_{1-x}Ba_xF_2$ Single Crystals," *Inorganic Materials*, 57(6), 629–633 (2021).

[Pus18] A.V. Pushkin, E.A. Migal, H. Uehara, K. Goya, S. Tokita, M.P. Frolov, Y.V. Korostelin, V.I. Kozlovsky, Y.K. Skasyrsky and F.V. Potemkin, "Compact, highly efficient, 2.1 W continuous-wave mid-infrared Fe:ZnSe coherent source, pumped by an Er:ZBLAN fiber laser," *Optics Letters* 43(24), 5941–5944 (2018).

[Qia11] X. Qiao, H. Huang, H. Yang, L. Zhang, L. Wang, D. Shen, J. Zhang and D. Tang, "Fabrication, optical properties and LD-pumped 2.7 µm laser performance of low Er^{3+} concentration doped Lu_2O_3 transparent ceramics," *Journal of Alloys and Compounds*, 640, 51-55 (2015).

[Ran04] I.M. Ranieri, A.H.A. Bressiani, S.P. Morato and S.L. Baldochi, "The phase diagram of the system LiF–GdF_3," *Journal of Alloys and Compounds*, 379 95-98 (2004).

[Ren06] S. Renard, P. Camy, J.L. Doualan, R. Moncorge, M. Couchaud and B. Ferrand, "Tm:CaF_2 planar waveguides grown by liquid phase epitaxy on CaF_2 substrates showing signal enhancement at 1.92 μm," *Optical Materials*, 28 1289–1291 (2006).

[Rev07] D.G. Revin, J.W. Cockburn, M.J. Steer, R.J. Airey, M. Hopkinson, A.B. Krysa, L.R. Wilson and S. Menzel, "InGaAs/AlAsSb/InP quantum cascade lasers operating at wavelength close to 3 μm," *Applied Physics Letters*, 90, 021108 (2007).

[Ren08] S. Renard, P. Camy, A. Braud, J.L. Doualan, and R. Moncorgé, "CaF_2 doped with Tm^{3+}: A cluster model," *Journal of Alloys and Compounds*, 451(1-2), 71–73 (2008).

[Ric64] I. Richman, "Longitudinal optical phonons in CaF_2, SrF_2, and BaF_2," *The Journal of Chemical Physics*, 41(9), (1964) 2836-2837.

[Rig21] G.C. Righini, M. Ferrari, in Integrated Optics: Volume 2: Characterization, devices, and applications. Stevenage: Institution of Engineering and Technology (2021).

[Rob67] M. Robinson and D. P. Devor, "Thermal switching of laser emission of Er^{3+} at 2.69 μm and Tm^{3+} at 1.86 μm in mixed crystals of CaF_2:ErF_3:TmF_3," *Applied Physics Letters*, 10(5), 167-170 (1967).

[Rom06] Y. Romanyuk, "Liquid-phase epitaxy of doped. KYWO4 2 layers for waveguide lasers," (Ph.D. thesis, Ecole Polytechnique Fédérale de Lausanne) (2005).

[Rog97] P. Rogin and J. Hulliger, "Liquid phase epitaxy of $LiYF_4$," *Journal of Crystal Growth*, 179 (1997) 551-558.

[Rub66] J.J. Rubin and L.G. Van Uitert, "Growth of sapphire and ruby by the Czochralski technique," *Materials Research Bulletin*, 1(3), 211-214 (1966).

[Rub86] J. Rubin, A. Brenier, R. Moncorge and C. Pedrini, "Excited-state absorption and energy transfer in Er^{3+} doped $LiYF_4$," *Journal of Luminescence*, 36(1), 39-47 (1986).

[Sal97] S. Salaün, M.T. Fornoni, A. Bulou, M. Rousseau, P. Simon and J.Y. Gesland "Lattice dynamics of fluoride scheelites: I. Raman and infrared study of $LiYF_4$ and $LiLuF_4$ (Ln = Ho, Er, Tm and Yb)," *Journal of Physics: Condensed Matter*; 9(32):6941 (1997).

[San11] T. Sanamyan, M. Kanskar, Y. Xiao, D. Kedlaya, and M. Dubinskii, "High power diode-pumped 2.7-µm $Er^{3+}:Y_2O_3$ laser with nearly quantum defect-limited efficiency," *Optics Express*, 19, A1082-A1087 (2011).

[San99] T. Sandrock, A. Diening and G. Huber, "Laser emission of erbium-doped fluoride bulk glasses in the spectral range from 2.7 to 2.8 ?m," *Optics Letters*, 24, 382-384 (1999).

[Sat09] S. Sato, R. Takahashi, M. Kobune and H. Gotoh, "Basic properties of rare-earth oxides," *Applied Catalysis A: General*, 356(1), 57-63 (2009).

[Sau18] P. Saudemont, J. Quanico, Y.M. Robin, A. Baud, J. Balog, B. Fatou, D. Tierny, Q. Pascal, K. Minier, M. Pottier, C. Focsa, M. Ziskind, Z. Takats, M. Salzet and I. Fournier, "Real-Time Molecular Diagnosis of Tumors Using Water-Assisted Laser Desorption/Ionization Mass Spectrometry Technology," Cancer Cell, (2018).

[Sch05] K.L. Schepler, R.D. Peterson, P.A. Berry and J.B. McKay, "Thermal effects in Cr^{2+}:ZnSe thin disk lasers," *IEEE Journal of Selected Topics in Quantum Electronics*, 11(3), 713-720 (2005).

[Sch13] M. Schellhorn, D.Parisi, S. Veronesi, G. Bolognesi, M. Eichhorn and M.Tonelli, "In-band pumped $Ho^{3+}:KY_3F_{10}$ 2 µm laser," *Optics Letters* 38(4), 504 - 506 (2013).

[Sch15] J. Scheuermann, R. Weih, M. von Edlinger, L. Nähle, M. Fischer, Johannes Koeth, M. Kamp and S. Höfling, "Single-mode interband cascade lasers emitting below 2.8 µm," *Applied Physics Letters*, 106(16), 161103 (2015).

[Sch84] B. Schumann and H. Neumann, "Thermal expansion of CaF_2 from 298 to 1173 K," *Crystal Research and Technology*, 19(1), K13-K14 (1984).

[Sch85] L.J. Schowalter, R.W. Fathauer, R.P. Goehner, L.G. Turner, R.W. DeBlois, S. Hashimoto, J.L. Peng, W.M. Gibson, and J.P. Krusius, "Epitaxial growth and characterization of CaF_2 on Si," *Journal of Applied Physics*, 58, 302–308 (1985).

[Sin85] S. Sinharoy, R.A. Hoffman, J.H. Rieger, R.F.C. Farrow and A.J. Noreika, "Epitaxial growth of CaF_2 on GaAs (100)," *Journal of Vacuum Science and Technology*, A 3, 842–845 (1985).

[Sel20] R. Selvaraj, N.J. Vasa, S.M.S Nagendra and B. Mizaikoff, "Advances in Mid-Infrared Spectroscopy-Based Sensing Techniques for Exhaled Breath Diagnostics," *Molecules*, 25(9), 2227 (2020).

[Sem07] M.P. Semtsiv, M. Wienold, S. Dressler and W.T. Masselink, "Shortwavelength ((λ~3.05 µm) InP-based strain compensated quantum cascade laser," *Applied Physics Letters*, 90, 051111, (2007).

[Ser16] J.M. Serres, V. Jambunathan, P. Loiko, X. Mateos, H. Yu, H. Zhang, J. Liu, A. Lucianetti, T. Mocek, K. Yumashev and U. Griebner, "Microchip laser operation of Yb-doped gallium garnets," *Optical Material Express*, 6(1), 46-57 (2016).

[Sha76] R.D. Shannon, "Revised effective ionic radii and systematic studies of interatomic distances in halides and chalcogenides," *Acta crystallographica section A: crystal physics, diffraction, theoretical and general crystallography*, 32(5), 751-767 (1976).

[Shi01] K. Shimamura, H. Sato, A. Bensalah, V. Sudesh, H. Machida, N. Sarukura and T. Fukuda, "Crystal growth of fluorides for optical applications," *Crystal Research and Technology: Journal of Experimental and Industrial Crystallography* 36(8-10), 801-813 (2001).

[Shi22] R. Shi and A.V. Mudring, "Phonon-Mediated Nonradiative Relaxation in Ln3+-Doped Luminescent Nanocrystals," *ACS Materials Letters*, 4(10), 1882-1903 (2022).

[Shi23] C. Shi, H. Huang, M. Li, Y. Bao, and Z. Li, "Passively Q-switched 3 µm erbium-doped solid state lasers using gold nanorods as broadband saturable absorber," *Optics & Laser Technology*, Volume 160, (2023).

[Sor02] N.I. Sorokin, B.P. Sobolev and M.W. Breiter, "Anion transport in superionic conductors $Na_{0.5-x}R_{0.5+x}F_{2+2x}$ (Rare cations of rare-earth elements) at elevated temperatures," *Russian Journal of Electrochemistry* 38(5), 516-521 (2002).

[Sor92] N.I. Sorokin, A.K. Ivanov-Shits, L.L. Vistin and B.P. Sobolev, "Anionic conductivity in $Na_{0.5-x}R_{0.5+x}F_{2+2x}$ (R = Dy-Lu; Y; $x \cong 0.1$) single crystals with fluorite-type structure," *Kristallografiya*, 37(2), 421-426 (1992).

[Sou19] R. Soulard, M. Salhi, G. Brasse, P. Loiko, J.-L. Doualan, L. Guillemot, A. Braud, A. Tyazhev, A. Hideur and P. Camy, "Laser operation of highly-doped Tm:$LiYF_4$ epitaxies: towards thin-disk lasers," *Optics Express*, 27, 9287–9301 (2019).

[Sta07] C.R. Stanek, K.J. McClellan, B. P. Uberuaga, K.E. Sickafus, M.R. Levy and R.W. Grimes, "Determining the site preference of trivalent dopants in bixbyite sesquioxides by atomic-scale simulations," *Physical Review B*, 75(13), 134101 (2007).

[Sta13] F. Starecki, W. Bolanos, A. Braud, J.-L. Doualan, G. Brasse, A. Benayad, V. Nazabal, B. Xu, R. Moncorg ́e and P. Camy, "Red and orange Pr3+:LiYF4 planar waveguide laser," *Optics Letters*, 38 455–457 (2013).

[Sto92] R. C. Stoneman, and L. Esterowitz, "Efficient resonantly pumped 2.8-µm $Er^{3+:}$GSGG laser," *Optics Letters*, 17, 816-818 (1992).

[Sul13] J. Šulc, M. Němec, R. Švejkar, H. Jelínková, M.E. Doroshenko, P.P. Fedorov and V.V. Osiko, "Diode-pumped Er:CaF$_2$ ceramic 2.7 μm tunable laser," *Optics Letters,* 38(17), 3406–3409 (2013).

[Su18] L. Su, X. Guo, D. Jiang, Q. Wu, Z. Qin, and G. Xie, "Highly-efficient mid-infrared CW laser operation in a lightly-doped 3 at.% Er:SrF$_2$ single crystal," *Optics Express*, 26(5), 5558-5563 (2018).

[Sub20] K. Subbotin, P. Loiko, S. Slimi, A. Volokitina, A. Titov, D. Lis, E. Chernova, S. Kuznetsov, R.M. Solé, U. Griebner, V. Petrov, M. Aguiló, F. Díaz, P. Camy, E. Zharikov and X. Mateos, "Monoclinic zinc monotungstate Yb^{3+},Li^{+}:ZnWO4: Part I. Czochralski growth, structure refinement and Raman spectra," *Journal of Luminescence* 228 117601 (2020).

[Su21] C. Su, Y. Liu, T. Feng, W. Qiao, Y. Zhao, Y. Liang, and T. Li, "Optical modulation of the MXene Ti$_3$C$_2$T$_x$ saturable absorber for Er:Lu$_2$O$_3$ laser," (2021).

[Sul13] J. Šulc, M. Němec, R. Švejkar, H. Jelínková, M. E. Doroshenko, P. P. Fedorov and V. V. Osiko, "Diode-pumped Er:CaF$_2$ ceramic 2.7 μm tunable laser," *Optics Letters*, 38(17), 3406–3409 (2013).

[Sve18] R. Švejkar, J. Šulc, M. Němec, P. Boháček, H. Jelínková, B. Trunda, L. Havlák, M. Nikl and K.Jurek, "Line-tunable Er:GGAG laser," *Optics Letters*, 43, 3309-3312 (2018).

[Sve19] R Švejkar J. Šulc and H. Jelínková, "Er:Y$_2$O$_3$ high-repetition rate picosecond 2.7 μm laser," *Laser Physics Letters*, 16, 075802 (2019).

[Sve20] R. Švejkar, J. Šulc, M. Němec and H. Jelínková, "Passively Mode-Locked High-Repetition Rate Er:YLF Laser at 2.81 μm Generating 72 ps Pulses," Conference on Lasers and Electro-Optics Europe & European Quantum Electronics Conference (CLEO/Europe-EQEC), Munich, Germany, 1-1 (2019).

[Tak05] K. Takaichi, H. Yagi, A. Shirakawa, K. Ueda, S. Hosokawa, T. Yanagitani and A.A. Kaminskii, "Lu$_2$O3:Yb^{3+} ceramics–a novel gain material for high-power solid-state lasers," *Physica Status Solidi (A)*, 202(1), R1-R3 (2005).

[Tak07] K. Takaichi, H. Yagi, P. Becker, A. Shirakawa, K. Ueda, L. Bohatý, T. Yanagitani, and A.A. Kaminskii, "New data on investigation of novel laser ceramic on the base of cubic scandium sesquioxide: two-band tunable CW generation of Yb^{3+}: Sc$_2$O$_3$ with laser-diode pumping and the dispersion of refractive index in the visible and near-IR of undoped Sc$_2$O$_3$," *Laser Physics Letters*, *4*(7), 507 (2007).

[Tal75] D.R. Tallant and C.W .John "Selective laser excitation of charge compensated sites in $CaF_2:Er^{3+}$," *The Journal of Chemical Physics*, 63.5, 2074-2085 (1975).

[Tan94] P. A. Tanner, V. R. K. Kumar, C. K. Jayasankar and M. F. Reid, "Analysis of spectral data and comparative energy level parametrizations for Ln^{3+} in cubic elpasolite crystals," *Journal of Alloys and Compounds*, 215(1-2), 349-370 (1994).

[Ter11] N. Ter-Gabrielyan, V. Fromzel and M. Dubinskii, "Performance analysis of the ultra-low quantum defect Er^{3+}: Sc_2O_3 laser," *Optical Materials Express*, 1(3), 503-513 (2011).

[Tho61] R.E. Thoma, C.F. Weaver, H.A. Freidman, H. Insley, L.A. Harris and H.A. Yakel, "Phase equilibria in the system LiF–YF_3," *The Journal of Physical Chemistry*, 65(7), 1096-1099 (1961).

[Tho63] R.E. Thoma, G.M. Hebert, H. Insley, and C.F. Weaver, "Phase equilibria in the system sodium fluoride-yttrium fluoride," *Inorgic Chemistry*, 2(5), 1005-1012 (1963).

[Tho66] R.E. Thoma, H. Insley, and G.M. Hebert, "The sodium fluoride-lanthanide trifluoride systems," *Inorganic Chemistry*, 5(7), 1222-1229 (1966).

[Tia20] Q. Tian, P. Yin, T. Zhang, L. Zhou, B. Xu, Z. Luo, H. Liu, Y. Ge, J. Zhang, P. Liu, and X. Xu, "MXene $Ti_3C_2T_x$ saturable absorber for passively Q-switched mid-infrared laser operation of femtosecond-laser–inscribed Er:Y_2O_3 ceramic channel waveguide," *Nanophotonics, Vol. 9 (Issue 8)*, 2495-2503 (2020).

[Tis91] B.M. Tissue, N.J. Cockroft, L. Lu, D.C. Nguyen, and W.M. Yen, "Comparison of the spectra and dynamics of $Er^{3+}:Y_2{-}xScxO_3$ (x = 0, 1, 2)," *Journal of Luminescence*, 48–49, 477-480 (1991).

[Tka01] A.M. Tkachuk, S.E. Ivanova, M.-F. Joubert, Y. Guyot, and S. Guy, "Luminescence self-quenching from $^4F_{3/2}$, $^2P_{3/2}$ and $^4D_{3/2}$ neodymium levels in double sodium–yttrium fluoride crystals," *Journal of Luminescence*, 94–95, 343-347 (2001).

[Tka04] A.M. Tkachuk, S.E. Ivanova, M-F. Joubert, Y. Guyot and V.P. Gapontzev, "Population of excited erbium levels in Er^{3+}: $Na_{0.4}Y_{0.6}F_{2.2}$ (Er: NYF) laser crystals," *Journal of Alloys and Compounds*, 380(1-2), 130-135 (2004).

[Tka04a] A.M. Tkachuk, S.É. Ivanova, M.F. Joubert and Y. Guyot, "Spectroscopic study of double sodium-yttrium fluoride crystals doped with erbium $Na_{0.4}Y_{0.6}F_{2.2}:Er^{3+}$: I. Intensities of luminescence spectra and kinetics of luminescence," *Optics and spectroscopy*, 97(2), 251-269 (2004).

[Tka11] A.M. Tkachuk, S.E. Ivanova, A.A. Mirzaeva and F. Pellé, "Study of spectroscopic characteristics of holmium-doped double sodium-yttrium fluoride crystals $Na_{0.4}Y_{0.6}F_{2.2}$:Ho^{3+}," *Optics and Spectroscopy*, 111, 919-935 (2011).

[Tka15] A. Tkachuk, S. Ivanova, A. Mirzaeva, M. Joubert and Y. Guyot, "Luminescence self-quenching in praseodymium-doped double sodium-yttrium fluoride cubic crystals (NaYF:Pr)," *Optics & Spectroscopy*, 118(3) (2015).

[Toc21] G. Toci, A. Pirri, B. Patrizi, R.N. Maksimov, V.V. Osipov, V.A. Shitov and M. Vannini, "Yb3+:(LuxY1-x)2O3 mixed sesquioxide ceramics for laser applications. Part II: laser performances", *Journal of Alloys and Compdaunds*, 853 (2021).

[Tod13] N.D. Todorov, M.V. Abrashev, V. Marinova, M. Kadiyski, L. Dimowa and E. Faulques, "Raman spectroscopy and lattice dynamical calculations of Sc 2 O 3 single crystals," *Physical Review B*, 87(10), 104301(2013).

[Tou12] E. Tournié and A.N. Baranov, "Chapter 5 - Mid-Infrared Semiconductor Lasers: A Review," *Semiconductors and Semimetals*, 86, 183-226, (2012).

[Tra10] I. Trabelsi, R. Maâlej, M. Dammak, A. Lupei and M. Kamoun, "Crystal field analysis of Er^{3+} in Sc_2O_3 transparent ceramics," *Journal of Luminescence*, 130(6), 927-931 (2010).

[Tut19] E. Tütüncü and B.Mizaikoff, "Cascade laser sensing concepts for advanced breath diagnostics," *Analytical and Bioanalytical Chemistry*, 411(9), 1679-1686 (2019).

[Uba08] A. Ubaldini and M.M. Carnasciali, "Raman characterisation of powder of cubic RE_2O_3 (RE= Nd, Gd, Dy, Tm, and Lu), Sc_2O_3 and Y_2O_3," *Journal of Alloys and Compounds*, 454(1-2), 374-378 (2008).

[Ueh18] H. Uehara, S. Tokita, J. Kawanaka, D. Konishi, M. Murakami, S. Shimizu, and R. Yasuhara "Optimization of laser emission at 2.8 µm by Er:Lu_2O_3 ceramics," *Optics Express*, 5;26(3):3497-3507 (2015).

[Umy96] A.F. Umyskov, Y.D. Zavartsev, A.I. Zagumennyi, V.V. Osiko and P.A. Studenikin, "Efficient 3 µm Cr^{3+}:Yb^{3+}:Ho^{3+}:YSGG crystal laser," *Quantum Electron*, 26, 771 (1996).

[Uva23] A. Uvarova, P. Loiko, S. Kalusniak, E. Dunina, L. Fomicheva, A. Kornienko, S. Balabanov, A. Braud, P. Camy and C. Kränkel, "Stimulated-emission cross-sections of trivalent erbium ions in the cubic sesquioxides Y_2O_3, Lu_2O_3, and Sc_2O_3," *Optical Materials Express*, 13, 1385-1400 (2023).

[Var62] F. Varsanyi and G.H. Dieke, "Energy levels of hexagonal $ErCl_3$," *The Journal of Chemical Physics*, 36(11), 2951-2961 (1962).

[Vas12] V. Vasyliev, E.G. Villora, M. Nakamura, Y. Sugahara and K. Shimamura, "UV-visible Faraday rotators based on rare-earth fluoride single crystals: $LiREF_4$ (RE = Tb, Dy, Ho, Er and Yb), PrF_3 and CeF_3," *Optical Express*, 20 14460-14470 (2012).

[Ves20] K. Veselský, J. Šulc, H. Jelínková, M.E. Doroshenko, V.A. Konyushkin and A.N. Nakladov, "Spectroscopic and laser properties of a broadly tunable diode-pumped Tm^{3+}:CaF_2–SrF_2 laser," *Laser Physics Letters*, 17(2), 025802 (2020).

[Vil16] P. Villars (Chief Editor), PAULING FILE in: Inorganic Solid Phases, SpringerMaterials (online database), Springer, Heidelberg (ed.) SpringerMaterials.

[Vod00] K.L. Vodopyanov, F. Ganikhanov, J.P. Maffetone, I. Zwieback and W. Ruderman, "$ZnGeP_2$ optical parametric oscillator with 3.8–12.4-µm tunability," *Optics Letters*, 5, 841-843 (2000).

[Vod01] K.L. Vodopyanov, "OPOs target the longwave infrared," *Laser Focus World*, 37, 225–232 (2001).

[Vog03] A. Vogel and V. Venugopalan, "Mechanisms of Pulsed Laser Ablation of Biological Tissues," *Chemical Reviews,* 103(2), 577-644 (2003).

[Vor08] V.I. Voronov, Yu. Kozlovsky, V. Korostelin, A.I. Landman, Yu.P. Podmar'kov, Ya.K. Skasyrsky and M.P. Frolov, "A continuous-wave Fe^{2+}:ZnSe laser," *Quantum Electronics*, 38(12), 1113–1116 (2008).

[Vod20] K.L. Vodopyanov, "Laser-based mid-infrared sources and applications," John Wiley & Sons, 2020.

[Wan18] Y. Wang, W. Jing, P. Loiko, Y. Zhao, H. Huang, X. Mateos, S. Suomalainen, A. Härkönen, M. Guina, U. Griebner and V. Petrov, "Sub-10 optical-cycle passively mode-locked Tm:$(Lu_{2/3}Sc_{1/3})_2O_3$ ceramic laser at 2 µm," *Optics Express* 26(8), 10299-10304 (2018).

[Wan18] L. Wang, H. Huang X. Ren, J. Wang, D. Shen, Y. Zhao, W. Zhou, P. Liu and D. Tang, "Nanosecond Pulse Generation at 2.7 µm From a Passively Q-Switched Er:Y_2O_3 Ceramic Laser," *IEEE Journal of Selected Topics in Quantum Electronics*, 24(5). 1-6 (2018).

[Wan19] Y. Wang, F. Jobin, S. Duval, V. Fortin, P. Laporta, M. Bernier, G. Galzerano and R. Vallée, "Ultrafast Dy^{3+}: fluoride fiber laser beyond 3 µm," *Optics Letters*, 44(2), 395–398 (2019).

[Web18] M.J. Weber, "Handbook of optical materials," (CRC press, 2018).

[Wil98] U. Willamowski, D. Ristau and E. Welsch, "Measuring the absolute absorptance of optical laser components," *Applied Optics,* 37(36), 8362–8370 (1998).

[Woo17] M. Woolman, A. Gribble, E. Bluemke, J. Zou, M. Ventura, N. Bernards, M. Wu, H.J. Ginsberg, S. Das, A. Vitkin and A. Zarrine-Afsar "Optimized Mass Spectrometry Analysis Workflow with Polarimetric Guidance for ex vivo and in situ Sampling of Biological Tissues," *Scientific Reports*, 7, 468 (2017).

[Woo18] R. Woodward, M. Majewski and S. Jackson, "Mode-locked dysprosium fiber laser: Picosecond pulse generation from 2.97 to 3.30 μ m," *APL Photonics 3(11)*, 116106 (2018).

[Woo19] R. Woodward, M. Majewski, N. Macadam, G. Hu, T. Albrow-Owen, T. Hasan and S. Jackson, "Q-switched Dy: ZBLAN fiber lasers beyond 3 μm: comparison of pulse generation using acousto-optic modulation and inkjet-printed black phosphorus," *Optics Express*, 27(10), 15032–15045 (2019).

[Wyb65] B. G. Wybourne, "Spectroscopic Properties of Rare Earths," Interscience (Wiley), New York, (1965).

[Wys97] C. Wyss, W. Lüthy, H.P. Weber, P. Rogin and J. Hulliger, "Emission properties of an optimised 2.8 μm Er^{3+}:YLF laser," *Optics Communications*, 139(4-6), 215–218 (1997).

[Xu22] C. Xu, J. Zhang, X. Zhao, H. Zhao, F. Ling, S. Jia, G. Farrell, S. Wang and P. Wang, "Two-watt mid-infrared laser emission in robust fluorozirconate fibers," *Optics Letters*, 47, 1399-1402 (2022)

[Yan16] D. Yan, X. Xu, H. Lu, Y. Wang, P. Liu and J. Zhang, "Fabrication and properties of Y_2O_3 transparent ceramic by sintering aid combinations," *Ceramics International,* 42(15), 16640-16643 (2016).

[Yan20] J. Yang, J. Hu, H. Luo, J. Li, J. Liu, X. Li and Y. Liu, "Fe_3O_4 nanoparticles as a saturable absorber for a tunable Q-switched dysprosium laser around 3 μm," *Photonics Research*, 8(1), 70–77 (2020).

[Yao12] Y. Yao, A. Hoffman and C. Gmachl, "Mid-infrared quantum cascade lasers," *Nature Photon* 6, 432–439 (2012).

[Yao14] B.Q Yao, Y.J. Shen, X.M. Duan, T.Y. Dai, Y.L. Ju and Y.Z. Wang, "A 41-W $ZnGeP_2$ optical parametric oscillator pumped by a Q-switched Ho: YAG laser," *Optics Letters*, 39(23), 6589-6592 (2014).

[Yao19] Y. Yao, Na Cui, Q. Wang, L. Dong, S. Liu, D. Sun, H. Zhang, D. Li, B. Zhang, and J. He, "Highly efficient continuous-wave and $ReSe_2$ Q-switched ~3 μm dual-wavelength Er:YAP crystal lasers," *Optics Letters*, 44, 2839-2842 (2019).

[Yao20a] W.Yao, H.Uehara, H. Kawase, H. Chen, and R.Yasuhara, "Highly efficient Er:YAP laser with 6.9 W of output power at 2920 nm," *Optics Express*, 28, 19000-19007 (2020).

[Yao20b] W. Yao, H. Uehara, S. Tokita, H. Chen, D. Konishi, M. Murakami, and R. Yasuhara, "LD-pumped 2.8 μm Er: Lu_2O_3 ceramic laser with 6.7 W output power and >30% slope efficiency," *Applied Physics Express*, 14(1), 012001 (2020).

[Yin17] K. Yin, B. Zhang, L. Yang and J. Hou, "15.2 W spectrally flat all-fiber supercontinuum laser source with >1 W power beyond 3.8 μm," *Optics letters*, 42(12), 2334-2337 (2017).

[You18] L. You, D.Z. Lu, Z.B. Pan, H.H. Yu, H.J. Zhang and J.Y. Wang, "High-efficiency 3 μm Er:YGG crystal lasers," *Optics Letters*, 43, 5873–5876 (2018).

[You19] Z. You, Zhenyu, J. Li, Y. Wang, H.Chen, Z. Zhu and C.Tu, "Spectroscopic and laser properties of Er:LuGG crystal at ~2.8 μm," *Applied Physics Express*,12(5), 052019 (2019).

[Zel13] D.E. Zelmon, J.M. Northridge, N.D. Haynes, D. Perlov and K. Petermann, "Temperature-dependent Sellmeier equations for rare-earth sesquioxides," *Applied Optics*, 52(16), 3824-3828 (2013).

[Zha12] P. Zhang, Y. Hang and L. Zhang, "Deactivation effects of the lowest excited state of Ho^{3+} at 2.9 μm emission introduced by Pr^{3+} ions in $LiLuF_4$ crystal," *Optics Letters*, 37, 5241 (2012).

[Zha18] Z. Zhang, F.Ma, X.Guo, J.Wang, X.Qian, J. Liu, J.Liu and L.Su, "Mid-infrared spectral properties and laser performance of Er^{3+} doped $Ca_xSr_{1-x}F_2$ single crystals," *Optical Materials Express*, 8, 3820-3828 (2018).

[Zha19] Y. Zhang, B. Xu, Q. Tian, Z. Luo, H. Xu, Z. Cai, D. Sun, Q. Zhang, P. Liu, X. Xu and J. Zhang, "Sub-15-ns Passively Q-Switched Er:YSGG Laser at ~2.8 μm With Fe:ZnSe Saturable Absorber," *IEEE Photonics Technology Letters*, 31(7), 565-568 (2019).

[Zha20] Y. Zhao, L. Wang, W. Chen, Z. Pan, Y. Wang, P. Liu, X. Xu, Y. Liu, D. Shen, J. Zhang, M. Guina, X. Mateos, P. Loiko, Z. Wang, X. Xu, J. Xu, M. Mero, U. Griebner and V. Petrov, "SESAM mode-locked $Tm:LuYO_3$ ceramic laser generating 54-fs pulses at 2048 nm," *Applied Optics*, 59(33), 10493-10497 (2020).

[Zha20a] L. Zhang, J. Yang, H. Yu and W. Pan, "High performance of La-doped Y2O3 transparent ceramics," *Journal of Advanced Ceramics*, 9, 493-502.(2020).

[Zha21] X. Zhang, H. Zhao, S. Gao and Q. Zeng, "First-principles study of electronic structure and optical properties of Er: Lu_2O_3," *Journal of Rare Earths*, 39(4), 453-459 (2021).

[Zha22] N. Zhang, Z. Wang, S. Liu, W. Jing, H. Huang, Z. Huang, K. Tian, Z. Yang, Y. Zhao, U. Griebner, V. Petrov and W. Chen, "Watt-level femtosecond Tm-doped “mixed” sesquioxide ceramic laser in-band pumped by a Raman fiber laser at 1627 nm," *Optics Express*, 30, 23978-23985 (2022).

[Zha22a] Y. Zhao, M. Zong, J. Zheng, Z. Zhang, Q. Peng, S. Jiang, J. Liu, J. Liu and L. Su, "Indium Tin Oxide Nanowire Arrays as a Saturable Absorber for Mid-Infrared Er:$Ca_{0.8}Sr_{0.2}F_2$ Laser," *Nanomaterials*, 12(3):454 (2022).

[Zha23] H. Zhang, Y. Liu, T. Feng, S. Zhao and W. Qiao, "Optical modulation properties of the Ni-based layered double hydroxides for dual-wavelength Q-switched Er: YAP laser at 2.7 μm," *Optical Materials*, 137, 113499 (2023).

[Zha75] E.V. Zharikov, V.I. Zhekov, L.A. Kulevskii, T.M. Murina, V.V. Osiko, A.M. Prokhorov, A.D. Savel'ev, V.V. Smirnov, B.P. Starikov and M.I. Timoshechkin, "Stimulated emission from Er^{3+} ions in yttrium aluminum garnet crystals at $\lambda = 2.94$ μm," *Soviet Journal of Quantum Electronics*, 4(8), 1039 (1975).

[Zon21] M. Zong, Z. Zhang, J. Liu, J. Liu, and L. Su, "LD pumped high-power mid-infrared solid state lasers based on 1.3at.%Er^{3+}: CaF_2 crystal (Invited)," *Infrared and Laser Engineering*, 50(8), (2021).

[Zon22] M. Zong, Y. Wang, Z. Zhang, J. Liu, L. Zhao, J. Liu, and L. Su, "High-power 2.8 μm lasing in a lightly-doped Er: CaF_2 crystal," *Journal of Luminescence*, 250, 119089 (2022).

Erbium doped materials for bulk and waveguide laser sources emitting around 2.8 µm

Abstract: The main objective of this thesis work, which is a part of the ANR SPLENDID2 project, is to explore a wide range of luminescent inorganic materials, presenting a low phonon energy and in various shapes, for the realization of high-power, ultrafast, and short pulse laser sources and high repetition rate optical amplifiers, operating around 2.8 µm, which is a spectral range of interest for many applications. This thesis work has focused on the growth of single crystalline thin films by liquid phase epitaxy of Er^{3+}-doped $LiYF_4$ and CaF_2 for the development of laser waveguides and characterization of their physicochemical, microstructural, and spectroscopic properties. In addition, an in-depth characterization of the spectroscopic properties of several Er^{3+}-doped fluoride single-crystals and transparent ceramics of sesquioxides was performed. Moreover, particular attention has been given to materials presenting inhomogeneous spectral broadening, leading to wide and smooth emission bands around 2.8 µm, which are favorable for the development of pulsed tunable lasers with short pulse durations.

Keywords: fluorides; erbium ions; crystalline thin films; liquid phase epitaxy; transparent ceramics; sesquioxides; optical spectroscopy; luminescence; laser materials; inhomogeneous spectral broadening; solid-state lasers; waveguide lasers; mid-infrared.

Matériaux dopés erbium sous la forme de cristaux massifs et de guide d'ondes pour la réalisation de sources laser émettant autour de 2,8 µm

Résumé : L'objectif principal de ce travail de thèse, qui s'inscrit dans le cadre du projet ANR SPLENDID2, est d’explorer un large panel de matériaux inorganiques luminescents, à basse énergie de phonons et sous différentes formes, pour la réalisation de sources lasers et d’amplificateurs optiques ultrarapides, à faible durée d’impulsion et de haute puissance, fonctionnant autour de 2.8 µm, qui est un domaine spectral d’intérêt pour de nombreuses applications. Ce travail de thèse a plus particulièrement porté sur la croissance de couches minces monocristallines par épitaxie en phase liquide de $LiYF_4$ et de CaF_2 dopés Er^{3+} pour l’élaboration de guides d’ondes laser et sur leur caractérisation du point de vue physico-chimique, microstructurale et spectroscopique. D’autre part, une caractérisation approfondie des propriétés spectroscopiques de plusieurs cristaux massifs de fluorures et de céramiques transparentes de sesquioxydes dopés Er^{3+}, a été menée. Par ailleurs, une attention particulière a été accordée aux matériaux présentant un élargissement spectral inhomogène, se traduisant par des bandes d'émission larges et lisses autour de 2,8 µm, favorables au développement de lasers impulsionnels, accordables et présentant de faibles durées d’impulsions.

Mots clés : cristaux de fluorures, ions erbium ; couches minces cristallines ; épitaxie en phase liquide ; céramiques transparentes ; sesquioxydes ; spectroscopie optique ; luminescence ; élargissement inhomogène ; matériaux laser ; lasers solides ; guide d'ondes lasers ; moyen-infrarouge.